

Low-Dimensional Magnetic Systems

GUEST EDITORS: ROBERTO ZIVIERI, GIANCARLO CONSOLO, EDUARDO MARTINEZ,
AND JOHAN ÅKERMÁN





Low-Dimensional Magnetic Systems

Advances in Condensed Matter Physics

Low-Dimensional Magnetic Systems

Guest Editors: Roberto Zivieri, Giancarlo Consolo,
Eduardo Martinez, and Johan Åkerman



Copyright © 2012 Hindawi Publishing Corporation. All rights reserved.

This is a special issue published in “Advances in Condensed Matter Physics.” All articles are open access articles distributed under the Creative Commons Attribution License, which permits unrestricted use, distribution, and reproduction in any medium, provided the original work is properly cited.

Editorial Board

A. Alexandrov, UK
Dario Alfe, UK
Bohdan Andraka, USA
Daniel Arovas, USA
A. Bansil, USA
Ward Beyermann, USA
Luis L. Bonilla, Spain
Mark Bowick, USA
Gang Cao, USA
Ashok Chatterjee, India
R. N. P. Choudhary, India
Kim Chow, Canada
Oleg Derzhko, Ukraine
Thomas Peter Devereaux, USA
Gayanath Fernando, USA
Jörg Fink, Germany
Yuri Galperin, Norway
Russell Giannetta, USA
Gabriele F. Giuliani, USA
James L. Gole, USA

P. Guptasarma, USA
M. Zahid Hasan, USA
Yurij Holovatch, Ukraine
Chia-Ren Hu, USA
David Huber, USA
Nigel E. Hussey, UK
Philippe Jacquod, USA
Jan Alexander Jung, Canada
Dilip Kanhere, India
Feo V. Kusmartsev, UK
Robert Leisure, USA
Heiner Linke, USA
Rosa Lukaszew, USA
Dmitrii Maslov, USA
Yashowanta N. Mohapatra, India
Abhijit Mookerjee, India
Victor V. Moshchalkov, Belgium
Charles Myles, USA
Donald Naugle, USA
Vladimir A. Osipov, Russia

Rolfe Petschek, USA
S. J. Poon, USA
Ruslan Prozorov, USA
Leonid Pryadko, USA
Charles Rosenblatt, USA
Alfonso San-Miguel, France
Mohindar S. Seehra, USA
Sergei Sergeenkov, Russia
Ivan Smalyukh, USA
Daniel L. Stein, USA
Michael C. Tringides, USA
Sergio E. Ulloa, USA
Attila Virosztek, Hungary
Markus R. Wagner, Germany
Nigel Wilding, UK
Gary Wysin, USA
Fajun Zhang, Germany
Gergely Zimanyi, USA

Contents

Low-Dimensional Magnetic Systems, Roberto Zivieri, Giancarlo Consolo, Eduardo Martinez, and Johan Åkerman

Volume 2012, Article ID 671416, 1 page

Micromagnetic Study of Synchronization of Nonlinear Spin-Torque Oscillators to Microwave Current and Field, M. Carpentieri, G. Finocchio, A. Giordano, B. Azzerboni, and F. Lattarulo

Volume 2012, Article ID 951976, 5 pages

Hamiltonian and Lagrangian Dynamical Matrix Approaches Applied to Magnetic Nanostructures,

Roberto Zivieri and Giancarlo Consolo

Volume 2012, Article ID 765709, 16 pages

On the Formulation of the Exchange Field in the Landau-Lifshitz Equation for Spin-Wave Calculation in Magnonic Crystals, M. Krawczyk, M. L. Sokolovskyy, J. W. Klos, and S. Mamica

Volume 2012, Article ID 764783, 14 pages

On the Travelling Wave Solution for the Current-Driven Steady Domain Wall Motion in Magnetic Nanostrips under the Influence of Rashba Field, Vito Puliafito and Giancarlo Consolo

Volume 2012, Article ID 105253, 8 pages

Micromagnetic Investigation of Periodic Cross-Tie/Vortex Wall Geometry, Michael J. Donahue

Volume 2012, Article ID 908692, 8 pages

Static Properties and Current-Driven Dynamics of Domain Walls in Perpendicular Magnetocrystalline Anisotropy Nanostrips with Rectangular Cross-Section, Eduardo Martinez

Volume 2012, Article ID 954196, 21 pages

Heterostructures for Realizing Magnon-Induced Spin Transfer Torque, P. B. Jayathilaka, M. C. Monti, J. T. Markert, and Casey W. Miller

Volume 2012, Article ID 168313, 7 pages

Thermodynamics of the Classical Planar Ferromagnet Close to the Zero-Temperature Critical Point: A Many-Body Approach, L. S. Campana, A. Cavallo, L. De Cesare, U. Esposito, and A. Naddeo

Volume 2012, Article ID 619513, 15 pages

Spin-Wave Band Structure in 2D Magnonic Crystals with Elliptically Shaped Scattering Centres,

Śławomir Mamica, Maciej Krawczyk, and Jarosław Wojciech Kłos

Volume 2012, Article ID 161387, 6 pages

Gap Structure and Gapless Structure in Fractional Quantum Hall Effect, Shosuke Sasaki

Volume 2012, Article ID 281371, 13 pages

Semiclassical Description of Anisotropic Magnets for Spin $S = 1$, Khikmat Muminov and Yousef Yousefi

Volume 2012, Article ID 749764, 3 pages

Editorial

Low-Dimensional Magnetic Systems

Roberto Zivieri,¹ Giancarlo Consolo,² Eduardo Martinez,³ and Johan Åkerman⁴

¹ *Department of Physics, University of Ferrara, 44122 Ferrara, Italy*

² *Department of Sciences for Engineering and Architecture, University of Messina, 98166 Messina, Italy*

³ *Department of Applied Physics, University of Salamanca, 37008 Salamanca, Spain*

⁴ *Department of Physics, University of Gothenburg, 41296 Gothenburg, Sweden*

Correspondence should be addressed to Roberto Zivieri, zivieri@fe.infn.it

Received 2 August 2012; Accepted 2 August 2012

Copyright © 2012 Roberto Zivieri et al. This is an open access article distributed under the Creative Commons Attribution License, which permits unrestricted use, distribution, and reproduction in any medium, provided the original work is properly cited.

The interest in the nanoscale properties of low-dimensional magnetic systems has grown exponentially during the last decades and has attracted the attention of both experimentalists and theorists. The state of the art of these investigations has indeed allowed to give valuable insights into the underlying physics of complex magnetization dynamics driven by magnetic fields, electric currents and thermal effects. At the same time, such studies have found, in relatively short times, several applications at industrial level in the field of spintronics and magnonics as magnetic memories, microwave oscillators, modulators, sensors, logic gates, diodes and transistors.

The goal of this special issue is to offer a variety of recent developments on this topic by gathering contributions arising from several specialists in the field of nanomagnetism. The strength of this issue lies indeed on its “variety”: the properties of these systems are, in fact, investigated from the viewpoint of physicists, engineers and mathematicians. Also, the issue encloses studies carried out at both mesoscopic and atomic scales, as well as results of both theoretical approaches (analytical, numerical and, in some cases, even “hybrid”) and experimental observations.

The covered topics range from the micromagnetic modeling of domain wall motion, dynamics of vortex structures, phase-locking phenomena in spintronic oscillators, experimental techniques for realizing heterostructures based on magnon-induced spin transfer torque, band structure and exchange field in the Landau-Lifshitz equation for magnonic crystals, gap and gapless structures in fractional quantum Hall effect, semiclassical description of anisotropic magnets and classical critical behaviour of Heisenberg ferromagnets. More specifically, within the subject dealing with domain

walls, for example, the structure of complex cross-tie/vortex wall structures in soft films has been studied in detail by using micromagnetic simulations whereas the influence of the Rashba spin-orbit coupling on the current-induced dynamics has been investigated analytically. Regarding the exchange interaction governing the dynamics in magnonic crystals, a full analytical calculation of the exchange field acting on spin-wave dynamics from the microscopic Heisenberg model has been performed. Attention has been also devoted to the study of thermodynamics in the case of classical planar ferromagnets close to the zero-temperature critical point.

Two reviews are also included in this special issue. The first one deals with two hybrid micromagnetic tools, based on Hamiltonian and Lagrangian approaches, to model the spin-dynamics in laterally confined magnetic systems. The second one is mostly devoted to the micromagnetic analysis of static and dynamic properties of magnetic domain walls in materials exhibiting perpendicular anisotropy.

Acknowledgments

This issue is the result of generous contributions to this new journal from our colleagues. We are sincerely grateful to all of them for all their efforts. With papers by leading experts in the field of micro- and nanomagnetism, we hope that this special issue will form a timely, open-access resource for experts and novice alike.

*Roberto Zivieri
Giancarlo Consolo
Eduardo Martinez
Johan Åkerman*

Research Article

Micromagnetic Study of Synchronization of Nonlinear Spin-Torque Oscillators to Microwave Current and Field

M. Carpentieri,¹ G. Finocchio,² A. Giordano,² B. Azzerboni,² and F. Lattarulo³

¹ *Dipartimento di Elettronica, Informatica e Sistemistica, University della Calabria, Via P. Bucci 42C, 87036 Rende, Italy*

² *Dipartimento di Fisica della Materia e Ingegneria Elettronica, University degli studi di Messina, C.da di Dio, 98100 Messina, Italy*

³ *Dipartimento di Elettrotecnica ed Elettronica, Politecnico di Bari, Via Orabona 4, 70125 Bari, Italy*

Correspondence should be addressed to M. Carpentieri, mcarpentieri@deis.unical.it

Received 30 March 2012; Revised 17 July 2012; Accepted 23 July 2012

Academic Editor: Giancarlo Consolo

Copyright © 2012 M. Carpentieri et al. This is an open access article distributed under the Creative Commons Attribution License, which permits unrestricted use, distribution, and reproduction in any medium, provided the original work is properly cited.

The nonautonomous dynamics of spin-torque oscillators in presence of both microwave current and field has been numerically studied in nanostructured devices. When both microwave current and field are applied at the same frequency, integer phase locking at different locking ratio is found. In the locking region, a study of the intrinsic phase shift between the locking force (current or field) and the giant magnetoresistive signal as a function of the bias current is also exploited.

1. Introduction

In the last years, the effects due to a direct transfer of the spin angular momentum [1–4] in nanomagnets (magnetization reversal [5, 6] or persistent oscillation of the magnetization [7, 8]) have opened new perspectives in the field of nanotechnology. In particular, one of the most promising applications is the possibility to obtain a competitive generation of nanoscale microwave oscillators, namely, spin-transfer torque oscillators (STOs) [9, 10]. Nowadays, STO is promising from a technological point of view being one of the smallest auto-oscillators observed in nature. It exhibits properties such as frequency tunability on bias current and field and narrow linewidth. To find practical application, STOs have to improve their output power. Some years ago, some researchers demonstrated that synchronized oscillators provided increased output power [11, 12]. This effect, which is receiving a great deal of attention due to its potential applications in telecommunications, has been studied both experimentally and theoretically for the purpose of understanding and realizing mutual synchronization between two or more STOs for microwave source applications. Later, other studies showed the synchronization of serially connected

STOs governed by phase locking to a microwave current offering a valid approach to fabricate STOs for output power levels closer to $1\ \mu\text{W}$ [13, 14].

The synchronization phenomenon is based on the well-known property that when the external frequency f_{RF} of a “weak” microwave current or field is close to the free running oscillation frequency f_0 of the STO, the self-oscillation mode moves and locks to the external frequency. Locking phenomena are also present for the ratio $r = f_{\text{RF}}/f_0$ close to all integers ($r = 1, 2, 3$, etc.) and several rational values [15].

We recently studied the injection locking phenomenon based on the application of a microwave field on perpendicular materials [16]. These systems mainly operate under “weak” microwave signal regime (the power of the microwave signal is negligible compared to the self-oscillation one) [9, 16–18].

In this work, by means of a micromagnetic study, the nonautonomous dynamical behavior of STO in presence of microwave signal composed by the simultaneous application of microwave current density J_{AC} and field h_{AC} (both at the same frequency) is studied. Also, the influence of a static field on the frequency behavior is investigated.

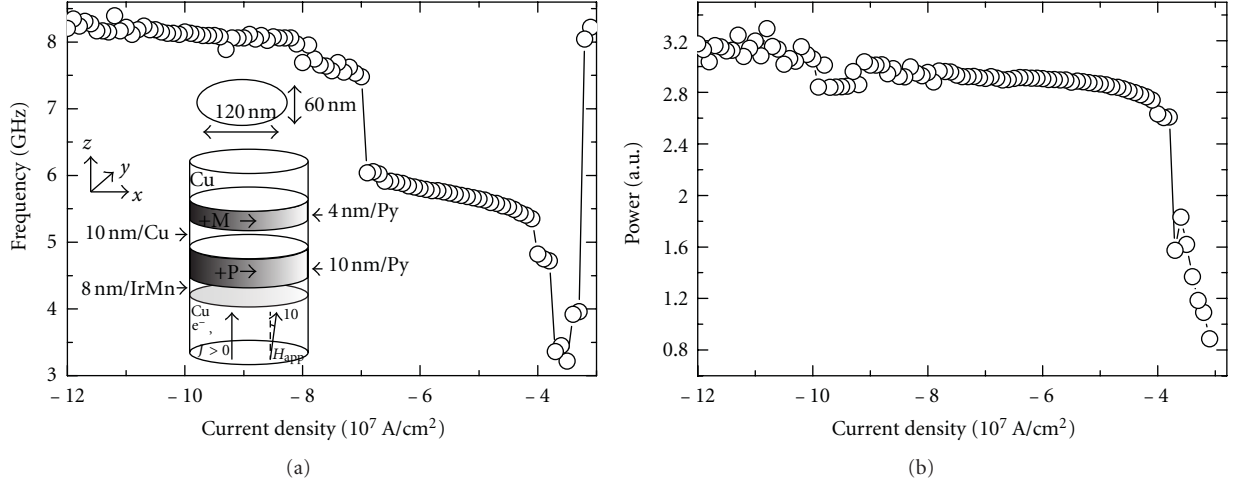


FIGURE 1: (a) Frequency and (b) power amplitude versus dc current density when an out-of-plane field of 250 mT tilted 10° versus x -direction is applied. No microwave source is applied. Inset of (a): sketch of the structure.

2. Device and Numerical Details

We studied the dynamical behavior of exchange bias spin-valves composed by IrMn(8 nm)/Py(10 nm) (polarizer)/Cu(10 nm)/Py(4 nm) (free layer) with elliptical cross-sectional area ($120 \text{ nm} \times 60 \text{ nm}$) (see inset of Figure 1(a)). A Cartesian coordinate system has been introduced, where the x - and the y -axes are, respectively, related to the easy and hard in-plane axes of the ellipse. Our numerical experiment is based on the numerical solution of the Landau-Lifshitz-Gilbert-Slonczewski (LLGS) equation [1–3]. In addition to the standard effective field (external, exchange, and self-magnetostatic), the Oersted field and the magnetostatic coupling with the polarizer are taken into account. The resulting equation (LLG + S) is expressed as

$$\frac{d\mathbf{m}}{d\tau} = -\mathbf{m} \times \mathbf{h}_{\text{eff}} + \frac{\alpha}{M_s} \left(\mathbf{m} \times \frac{d\mathbf{m}}{d\tau} \right) - \chi \mathbf{m} \times (\mathbf{m} \times \mathbf{p}), \quad (1)$$

where $\mathbf{m} = \mathbf{M}/M_s$ and $\mathbf{h}_{\text{eff}} = \mathbf{H}_{\text{eff}}/M_s$ are the dimensionless magnetization vector and the effective field, respectively, $\tau = \gamma_0 M_s t$ is the dimensionless time, γ_0 is the gyromagnetic ratio, and M_s is the saturation magnetization of the free layer. The first term on the right-hand side of (1) represents the precessional torque around the effective field, whereas the second one is the phenomenological dissipation term, α being the so-called Gilbert parameter. The third term in (1) is the dimensionless Slonczewski spin-transfer torque, where $\mathbf{p} = \mathbf{P}/M_s$ represents the dimensionless magnetization in the pinned layer, and the prefactor χ is given by

$$\chi = \frac{\mu_B}{\gamma_0} \frac{J_{\text{app}}}{M_s^2 e d} g(\mathbf{m}, \mathbf{p}), \quad (2)$$

where e and μ_B are the electric charge and the Bohr magneton respectively, J_{app} is the current per unit area (density current), and d is the thickness of the free layer, and $g(\mathbf{m}, \mathbf{p})$ is the polarization function depending on the relative orientation of the magnetizations [1–3].

For a complete model description of the numerical techniques see also [19–22]. Typical parameters for the Py have been used: saturation magnetization $M_s = 650 \times 10^3 \text{ A/m}$, exchange constant $A = 1.3 \times 10^{-11} \text{ J/m}$, damping parameter $\alpha = 0.02$, and polarization factor $\eta = 0.3$ [1–3]. The bias field is applied out-of-plane (z -direction) with a tilted angle of 10° along the x -axis. The polarizer is considered fixed along the x -direction. To study the locking, we consider a microwave current $J_{\text{RF}} = J_M \sin(2\pi f_{\text{AC}} t + \pi/2)$ ($J_M \leq 2 \times 10^7 \text{ A/cm}^2$) and a microwave field linearly polarized at $\pi/4$ in the x - y plane $\mathbf{h}_{\text{RF}} = h_M \sin(2\pi f_{\text{AC}} t + \pi/4) \hat{x} + h_M \sin(2\pi f_{\text{AC}} t + \pi/4) \hat{y}$ ($h_M \leq 3 \text{ mT}$). This microwave field can be generated by using the experimental technique developed in [25]. All the computations have been performed with no thermal effects.

3. Micromagnetic Results and Discussion

In order to characterize the device behavior, first of all we analyzed the STO in the free running regime. We observe dynamical regime in a wide range of current density for bias field larger than 180 mT. Here we discuss in detail data for a bias field of 250 mT, but qualitative similar results have been also observed for 200 and 300 mT.

In order to characterize the oscillator regime of the device, we swapped the dc current exceeding the critical current value (to obtain dynamics regime, threshold current density was $J = 3 \times 10^7 \text{ A/cm}^2$) up to current values, where oscillation regime is degraded by noise. Frequency and power behavior of the nano-oscillator with respect to the current density is shown in Figures 1(a) and 1(b) (no microwave signal). The frequency curve f_0 as a function of J presents red shift from the critical current up to $J_1 = -3.5 \times 10^7 \text{ A/cm}^2$, where the dynamics is characterized by an in-plane oscillation axis. For $|J| > |J_1|$ the magnetization precesses around an out-of-plane axis and the blue shift is achieved. The discontinuities observed in the oscillation frequency are related to jumps of the oscillation axis that

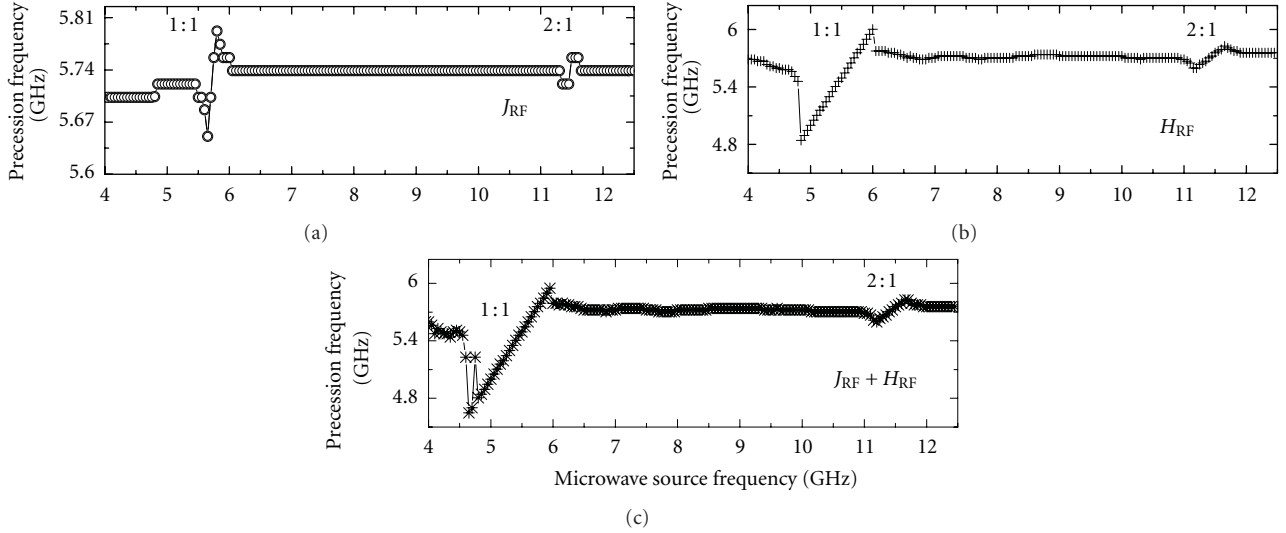


FIGURE 2: Response of the STO self-oscillation for $H_{DC} = 250 \text{ mT}$ and $J_{DC} = -5 \times 10^7 \text{ A/cm}^2$ as a function of the microwave source frequency when (a) $J_{RF} = 2 \times 10^7 \text{ A/cm}^2$, (b) $H_{RF} = 1 \text{ mT}$, and (c) RF current $J_{RF} = 1 \times 10^7 \text{ A/cm}^2$ and RF field $H_{RF} = 1 \text{ mT}$ are applied together at the same frequency. The locking regions for the frequency ratio of 1 : 1 and 2 : 1 are also visible.

correspond to transitions between strongly nonlinear oscillation modes. Similar discontinuities have been also observed in some experimental work [23]. In addition, we performed micromagnetic simulations increasing the out-of-plane static field up to 600 mT, and we observed that for out-of-plane bias field larger than 400 mT the red-shift zone disappears, jumps are softer, and the synchronization data achieved are similar to results already published in the literature (see e.g., [10] for a review). At larger field ($>600 \text{ mT}$), the polarizer is moved from the x -direction towards the out-of-plane z -direction that might generate additional noise showing not coherent precessional states.

Figure 1(b) shows the power versus current behavior. Nonlinear power strongly increases at low current and for current values greater than $4 \times 10^7 \text{ A/cm}^2$ is about constant.

We systematically studied the locking to the first harmonic (the same of the self-oscillation) in the blue shift region as a function of the J_M and h_M . Figure 2 shows the precession frequency of the GMR signal as a function of the microwave source frequency in two cases: RF current only and RF current and field together (for $H_{DC} = 250 \text{ mT}$ and $J_{DC} = -5 \times 10^7 \text{ A/cm}^2$). We found different locking regions at the locking ratio 1 : 1, 2 : 1, and 3 : 1 (in the last case only when the microwave field component is applied, not shown here). Typically, the locking region is much larger when the microwave force is a field (or a combination of current and field). In fact, in the case of current we found a locking region of about 150 MHz (1 : 1) and 50 MHz (2 : 1), whereas no locking on the third harmonic is found. Microwave field provides a locking region larger than 1 GHz and, since driving force breaks the oscillation symmetry, the 1 : 1 synchronization region has a specific asymmetric shape. Then, whereas for small forcing signal the synchronization region can be described by an analytical theory (symmetric tongue where the locking region increases linearly with force

amplitude) [24], it cannot be described analytically when increasing the forcing signal and their precise determination requires necessarily specific numerical techniques.

Figure 3(a) summarizes the Arnold tongue ($J = -5 \times 10^7 \text{ A/cm}^2$) computed up to $J_M = 1 \times 10^7 \text{ A/cm}^2$ ($h_M = 0 \text{ mT}$) and then increasing h_M up to 3 mT with $J_M = 1 \times 10^7 \text{ A/cm}^2$ held unchanged. The border lines have been computed considering the lower (in the left part) and higher (in the right part) microwave frequency where the phase locking is achieved. In the low regime of microwave source, the Arnold tongue is related to the only application of the microwave current, which can be considered as a “weak” microwave signal. In fact, such a signal gives rise to symmetric synchronization region (no hysteresis is observed) with a locking band linearly dependent on the force locking.

When both microwave current and field are applied simultaneously at the same frequency, the nonautonomous response becomes more complicated. The presence of an additional weak microwave field gives rise to increasing of the locking region from 150 MHz at $h_M = 0 \text{ mT}$ to 1.3 GHz for $h_M = 1 \text{ mT}$. As can be observed the locking region is strongly asymmetric. This is caused by the strong nonlinearity of the dependence of the auto-oscillation frequency on the oscillation power [25].

Figure 3(b) shows the phase difference between the magnetization oscillation and the microwave source (negative angle means magnetization in delay with respect to microwave source, Ψ being the phase of the natural precession of the magnetization and Ψ_e the force phase) when the microwave component is applied at the same frequency of the free precession one. As shown, typically in both cases (microwave field or current), the phase increases with current and decreases after a maximum value. The phase shift depends on the initial detuning, and it goes to

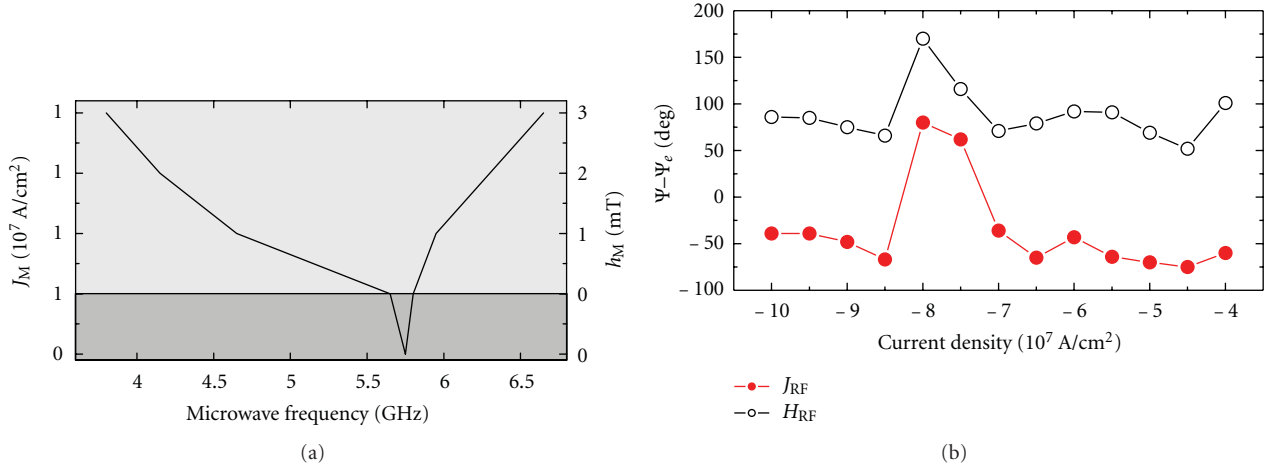


FIGURE 3: (a) Arnold tongue computed for $H_{DC} = 250$ mT and $J = -5 \times 10^7$ A/cm² varying the magnitude of RF current and field. (b) Phase difference between external force (current or field) and output magnetization as a function of dc current when an RF source at the same frequency of the free precessional one is applied. Filled-red circle: RF current, white circle: RF field.

zero only if there is no detuning, that is, in the center of the synchronization region. It should be remembered that the phase difference depends on the initial phase of the force and the way it affects the oscillator. We emphasize here that the phase locking implies that phase difference will be kept bounded inside a finite range of detuning, that is, within the synchronization region. In this case the microwave current and field give the same qualitative behavior to the oscillator, but the phase difference is translated by an angle of about 120° . As expected, phase difference between microwave source and the magnetization precession follows the frequency behavior. It initially decreases with dc current amplitude (precession frequency decreases) and then increases with dc current (precession frequency increases) up to current values of the order of 7×10^7 A/cm². After that current value, phase shift jumps about 180° , typically this is due to the different oscillation mode from in-plane to out-of-plane mode. Lastly, the phase difference gradually increases following the frequency slow rising with dc current magnitude [26].

In the locking region an intrinsic phase shift Ψ_i , computed as the difference between the phase of the self-oscillation Ψ and the phase of the microwave current Ψ_e , is found.

Figure 4 summarizes Ψ_i as a function of the microwave frequency, as can be observed a linear relationship between Ψ_i and f_{AC} is achieved with a range of Ψ_i which can cross 0 or $\pi/2$ depending on the bias current density. As reported by Slavin and Tiberkevich [10], analytical formulation of the phase difference in the locking region is given by

$$\Phi_0 = \arcsin\left(\frac{f_{AC} - f_0}{\Delta f}\right) - \arctan(v), \quad (3)$$

where $v = (N/(G_+ - G_-))$ is the nonlinear frequency shift. We found N which is characterized from two different values of nonlinear frequency shift $N = 2\pi(df/dp)$, p is the oscillation power, and G_+ and G_- are the non-linear

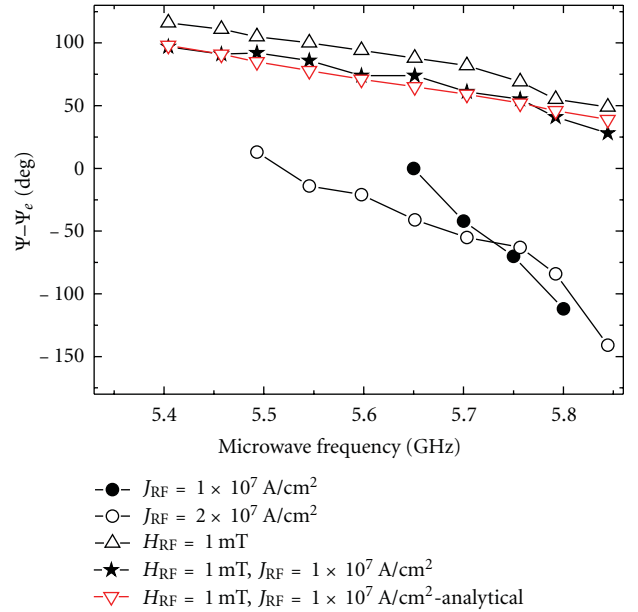


FIGURE 4: Intrinsic phase shift Ψ_i between the phase of self-oscillation and microwave source (current or field) in the locking region for $J_{DC} = 5 \times 10^7$ A/cm².

damping coefficients as in [10]. Phase difference is strongly dependent on the frequency in the locking region [27]. For all the cases, the phase difference decreases from left to right in the Arnold tongue. In particular, the slope of the curve is strong for RF current locking whereas it is more soft for RF field, a result also in substantial agreement with the analytical theory. Considering (3) for RF applied field, the locking bandwidth and nonlinear frequency shift are larger with respect to ac current. A good agreement between analytical and numerical data is found.

4. Conclusions

In summary, we have studied micromagnetically the non-linear behavior of spin-torque nano-oscillators in locking regime driven by microwave current and field. We found a large locking region at different harmonics when RF field is applied. The effect of the static applied field is also studied. Finally, we showed and explained the intrinsic phase shift due to the difference between microwave source and magnetization precession inside the locking region, also comparing our numerical data with a recent analytical theory.

Acknowledgments

This paper was supported by Spanish Project under Contract no. MAT2011-28532-C03-01. The authors would like to thank Sergio Greco for his support with this paper.

References

- [1] J. C. Slonczewski, "Current-driven excitation of magnetic multilayers," *Journal of Magnetism and Magnetic Materials*, vol. 159, no. 1-2, pp. L1–L7, 1996.
- [2] J. C. Slonczewski, "Excitation of spin waves by an electric current," *Journal of Magnetism and Magnetic Materials*, vol. 195, no. 2, pp. L261–L268, 1999.
- [3] J. C. Slonczewski, "Currents and torques in metallic magnetic multilayers," *Journal of Magnetism and Magnetic Materials*, vol. 247, no. 3, pp. 324–338, 2002.
- [4] L. Berger, "Emission of spin waves by a magnetic multilayer traversed by a current," *Physical Review B*, vol. 54, no. 13, pp. 9353–9358, 1996.
- [5] I. N. Krivorotov, N. C. Emley, J. C. Sankey, S. I. Kiselev, D. C. Ralph, and R. A. Buhrman, "Time-domain measurements of nanomagnet dynamics driven by spin-transfer torques," *Science*, vol. 307, no. 5707, pp. 228–231, 2005.
- [6] D. C. Ralph and M. D. Stiles, "Spin transfer torques," *Journal of Magnetism and Magnetic Materials*, vol. 320, no. 7, pp. 1190–1216, 2008.
- [7] S. I. Kiselev, J. C. Sankey, I. N. Krivorotov et al., "Microwave oscillations of a nanomagnet driven by a spin-polarized current," *Nature*, vol. 425, no. 6956, pp. 380–383, 2003.
- [8] A. A. Tulapurkar, Y. Suzuki, A. Fukushima et al., "Spin-torque diode effect in magnetic tunnel junctions," *Nature*, vol. 438, no. 7066, pp. 339–342, 2005.
- [9] W. H. Rippard, M. R. Pufall, S. Kaka, S. E. Russek, and T. J. Silva, "Direct-current induced dynamics in $\text{Co}_{90}\text{Fe}_{10}/\text{Ni}_{80}\text{Fe}_{20}$ point contacts," *Physical Review Letters*, vol. 92, no. 2, Article ID 027201, 4 pages, 2004.
- [10] A. Slavin and V. Tiberkevich, "Nonlinear auto-oscillator theory of microwave generation by spin-polarized current," *IEEE Transactions on Magnetism*, vol. 45, no. 4, pp. 1875–1918, 2009.
- [11] S. Kaka, M. R. Pufall, W. H. Rippard, T. J. Silva, S. E. Russek, and J. A. Katine, "Mutual phase-locking of microwave spin torque nano-oscillators," *Nature*, vol. 437, no. 7057, pp. 389–392, 2005.
- [12] F. B. Mancoff, N. D. Rizzo, B. N. Engel, and S. Tehrani, "Phase-locking in double-point-contact spin-transfer devices," *Nature*, vol. 437, no. 7057, pp. 393–395, 2005.
- [13] J. Grollier, V. Cros, and A. Fert, "Synchronization of spin-transfer oscillators driven by stimulated microwave currents," *Physical Review B*, vol. 73, no. 6, Article ID 060409(R), 4 pages, 2006.
- [14] W. H. Rippard, M. R. Pufall, S. Kaka, T. J. Silva, S. E. Russek, and J. A. Katine, "Injection locking and phase control of spin transfer nano-oscillators," *Physical Review Letters*, vol. 95, no. 6, Article ID 067203, pp. 1–4, 2005.
- [15] S. Urazhdin, P. Tabor, V. Tiberkevich, and A. Slavin, "Fractional synchronization of spin-torque nano-oscillators," *Physical Review Letters*, vol. 105, no. 10, Article ID 104101, 4 pages, 2010.
- [16] M. Carpentieri, G. Finocchio, B. Azzerboni, and L. Torres, "Spin-transfer-torque resonant switching and injection locking in the presence of a weak external microwave field for spin valves with perpendicular materials," *Physical Review B*, vol. 82, no. 9, Article ID 094434, 8 pages, 2010.
- [17] G. Consolo, V. Puliafito, G. Finocchio et al., "Combined frequency-amplitude nonlinear modulation: theory and applications," *IEEE Transactions on Magnetism*, vol. 46, no. 9, pp. 3629–3634, 2010.
- [18] R. Bonin, G. Bertotti, C. Serpico, I. D. Mayergoyz, and M. D'Aquino, "Analytical treatment of synchronization of spin-torque oscillators by microwave magnetic fields," *European Physical Journal B*, vol. 68, no. 2, pp. 221–231, 2009.
- [19] A. Romeo, G. Finocchio, M. Carpentieri, L. Torres, G. Consolo, and B. Azzerboni, "A numerical solution of the magnetization reversal modeling in a permalloy thin film using fifth order Runge-Kutta method with adaptive step size control," *Physica B*, vol. 403, no. 2-3, pp. 464–468, 2008.
- [20] E. Martinez, L. Torres, L. Lopez-Diaz, M. Carpentieri, and G. Finocchio, "Spin-polarized current-driven switching in permalloy nanostructures," *Journal of Applied Physics*, vol. 97, no. 10, Article ID 10E302, 3 pages, 2005.
- [21] Martinez et al., "standard problem #4 report," The free layer has been discretized in computational cells of $5 \times 5 \times 4 \text{ nm}^3$. The time step used was 32 fs, <http://www.ctcms.nist.gov/~rdm/mumag.org.html>.
- [22] M. Carpentieri, L. Torres, B. Azzerboni, G. Finocchio, G. Consolo, and L. Lopez-Diaz, "Magnetization dynamics driven by spin-polarized current in nanomagnets," *Journal of Magnetism and Magnetic Materials*, vol. 316, no. 2, pp. 488–491, 2007.
- [23] I. N. Krivorotov, D. V. Berkov, N. L. Gorn et al., "Large-amplitude coherent spin waves excited by spin-polarized current in nanoscale spin valves," *Physical Review B*, vol. 76, no. 2, Article ID 024418, 14 pages, 2007.
- [24] P. Maffezzoni, "Computing the synchronization regions of injection-locked strongly nonlinear oscillators for frequency division applications," *IEEE Transactions on Computer-Aided Design of Integrated Circuits and Systems*, vol. 29, no. 12, pp. 1849–1857, 2010.
- [25] P. Tabor, V. Tiberkevich, A. Slavin, and S. Urazhdin, "Hysteretic synchronization of nonlinear spin-torque oscillators," *Physical Review B*, vol. 82, no. 2, Article ID 020407, 4 pages, 2010.
- [26] Y. Zhou, J. Persson, S. Bonetti, and J. Akerman, "Tunable intrinsic phase of a spin torque oscillator," *Applied Physics Letters*, vol. 92, no. 9, Article ID 092505, 3 pages, 2008.
- [27] G. Finocchio, G. Siracusano, V. Tiberkevich, I. N. Krivorotov, L. Torres, and B. Azzerboni, "Time-domain study of frequency-power correlation in spin-torque oscillators," *Physical Review B*, vol. 81, no. 18, Article ID 184411, 6 pages, 2010.

Review Article

Hamiltonian and Lagrangian Dynamical Matrix Approaches Applied to Magnetic Nanostructures

Roberto Zivieri¹ and Giancarlo Consolo²

¹ CNISM Unit of Ferrara and Department of Physics, University of Ferrara, Via Saragat 1, 44122 Ferrara, Italy

² Department of Sciences for Engineering and Architecture, University of Messina, C.da di Dio, Villaggio S.Agata, 98166 Messina, Italy

Correspondence should be addressed to Roberto Zivieri, zivieri@fe.infn.it

Received 30 March 2012; Accepted 23 April 2012

Academic Editor: Eduardo Martinez Vecino

Copyright © 2012 R. Zivieri and G. Consolo. This is an open access article distributed under the Creative Commons Attribution License, which permits unrestricted use, distribution, and reproduction in any medium, provided the original work is properly cited.

Two micromagnetic tools to study the spin dynamics are reviewed. Both approaches are based upon the so-called dynamical matrix method, a hybrid micromagnetic framework used to investigate the spin-wave normal modes of confined magnetic systems. The approach which was formulated first is the Hamiltonian-based dynamical matrix method. This method, used to investigate dynamic magnetic properties of conservative systems, was originally developed for studying spin excitations in isolated magnetic nanoparticles and it has been recently generalized to study the dynamics of periodic magnetic nanoparticles. The other one, the Lagrangian-based dynamical matrix method, was formulated as an extension of the previous one in order to include also dissipative effects. Such dissipative phenomena are associated not only to intrinsic but also to extrinsic damping caused by injection of a spin current in the form of spin-transfer torque. This method is very accurate in identifying spin modes that become unstable under the action of a spin current. The analytical development of the system of the linearized equations of motion leads to a complex generalized Hermitian eigenvalue problem in the Hamiltonian dynamical matrix method and to a non-Hermitian one in the Lagrangian approach. In both cases, such systems have to be solved numerically.

1. Introduction

In these last years, great attention has been given to the study of magnetization dynamics in laterally confined magnetic systems. It is well known that spin excitations are quantized due to the lateral confinement. The oscillations are the so-called normal modes, which represent a pattern of motion given by all the parts of the system oscillating sinusoidally with the same frequency and with the same phase relation. In this last decade, analytical models have given important contributions to understand the frequency spectrum of normal modes for different ground-state magnetizations [1–11]. However, some limitations due to the assumptions made for the determination of the equilibrium state, the boundary conditions, and the calculation of the energy contributions to normal modes dynamics are still present.

On the other hand, a lot of efforts have been devoted to develop micromagnetic codes having the aim of calculating

very precisely different ground states of nanometric particles [12]. Due to their accuracy, the developed micromagnetic methods have contributed to give additional information about the spin dynamics. The first micromagnetic calculations were typically based upon codes developed to calculate in the first place the ground state of a given magnetic particle. Then the time evolution of the average magnetization of a particle could be obtained and, from a subsequent postprocessing of these data (mainly using the Fourier transform of the magnetization), information could be extracted about mode frequencies and spatial profiles [13]. In the simplest application of the method, the limit of these calculations was the observation of modes with nonzero magnetization only. More recently, a micromagnetic method was extended to the detailed calculation of eigenfrequencies and eigenvectors under the effect of an oscillatory in-plane small magnetic field [14]. Another recent micromagnetic method was also developed to study the quantized spin excitations in laterally

confined systems [15]. This is the so-called Hamiltonian-based dynamical matrix method (HDMM).

The HDMM was first formulated for isolated magnetic nanoelements and then it has been generalized to the case of interacting nanoelements [16]. It is the prototype of finite-difference methods and represents an eigenvalue/eigenvector problem. The scope of this method is to find the frequencies and profiles of the spin modes which are associated to the eigenvalues and the eigenvectors, respectively, of a dynamical matrix. It can be considered the analogous of the dynamical matrix formalism used to find atomic vibrations (phonons) in crystalline solids. The dynamical matrix contains the second derivatives of the density energy coming from a second order expansion of the density energy around the equilibrium. This method was already used to study the spin excitations in magnetic multilayers with ferro- or anti-ferromagnetic coupling [17, 18]. Due to the translational invariance, the number of independent dynamic variables was reduced to twice the number of the layers. The calculated second derivatives are evaluated at equilibrium. The eigenvalue/eigenvector problem can be set as a complex generalized Hermitian eigenvalue problem. The method presents several advantages: a single calculation yields the frequencies and eigenvectors of all modes of any symmetry, it is applicable to a particle of any shape (within the nanometric range), and the computation time is affordable. This means that by means of this micromagnetic approach, it is possible to determine, after a single iteration, the frequencies and the profiles of all spin-modes, independently of the ground-state magnetization (e.g., vortex state, vortex in the presence of an external magnetic field, onion state, quasi-saturated state). The main restriction of the method is its applicability to confined magnetic systems whose spin dynamics is assumed purely precessional with no dissipative effects. Of course, this is true only in a first approximation, since in real magnetic systems the intrinsic damping process plays an important rule. In order to select the representative modes of the spectrum and to compare them with the ones observed by means of the experimental techniques, the differential scattering cross-section has to be evaluated both for noninteracting and interacting magnetic particles.

The first applications of the HDMM were on chains of dipolarly interacting rectangular dots representing a one-dimensional array [19] and of two-dimensional (2D) arrays formed by circular nanometric disks [20]. Very recently, this method was applied to study the collective mode dynamics in arrays of holes embedded into a thin ferromagnetic film. This calculation was done by including in the energy density computation also the exchange interaction between micromagnetic cells belonging to two adjacent primitive cells [21].

In order to overcome the above-mentioned restrictions of the HDMM, Consolo et al. formulated very recently the so-called Lagrangian-based dynamical matrix method (LDMM) [22]. Such a method explicitly takes into account the intrinsic “positive” Gilbert damping and the current-induced spin-transfer-torque “negative” dissipation. Since the magnetic system so obtained is no more conservative, a Lagrangian formalism is necessary. Unlike the HDMM,

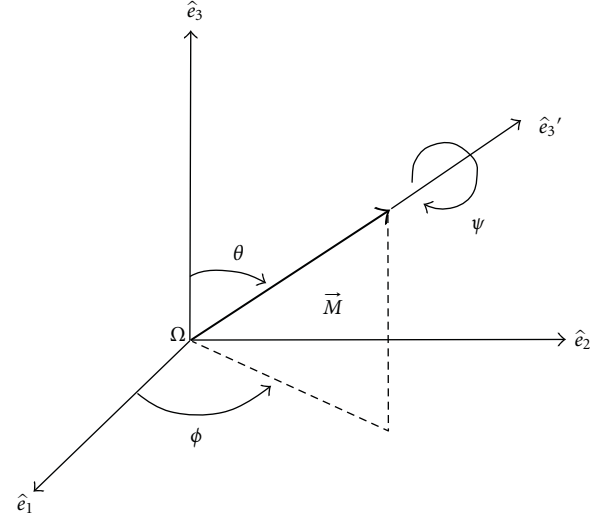


FIGURE 1: Reference frame used in the theory.

the LDMM cannot be cast as a classical (nongeneralized) eigenvalue/eigenvector problem, but it has to be formulated as a complex generalized non-Hermitian eigenvalue problem. The first application of the method was done on a magnetic nanopillar stack of circular cross-section subject to an external magnetic field directed a few degree away from the normal to the plane [22]. The analysis was then extended to the case of external magnetic fields of variable intensity and orientation with respect to the plane of the nanopillar [23].

It is important to notice that both formalisms have been developed up to now in the linear approximation, namely, considering small angular deviations of the magnetization from equilibrium so that each spin excitation is a normal mode of the system.

The reference frame used in the micromagnetic calculations performed both by means of HDMM and LDMM is illustrated in Figure 1. The z -axis is along the normal to the particle and the x - y plane lies on the particle plane. According to this reference frame, the configuration of the vector \vec{M} , representative of the magnetic dipole momentum, is identified through the polar angles, θ and ϕ , and the intrinsic rotation ψ . As it will appear clear in the section devoted to the Lagrangian approach, this latter angle does not enter in the equation of motion, being the corresponding Lagrange equation associated to a first integral of the motion (the conservation of the angular momentum). So that, as it is expected, because the modulus of the magnetization vector is preserved in time, the dynamics can be described through two degrees of freedom only (typically θ and ϕ).

If we assume that the magnetization vector \vec{M} is placed along the generic direction given by the unitary vector \hat{e}_3' , it can be expressed in Cartesian coordinates by

$$\vec{M}(t) = M_s (\sin \theta(t) \cos \phi(t), \sin \theta(t) \sin \phi(t), \cos \theta(t)), \quad (1)$$

being M_s the saturation magnetization value (the modulus of the magnetization vector) and the time dependence of the angles θ and ϕ expressed as

$$\begin{aligned}\theta(t) &= \Theta + \delta\theta(t), \\ \phi(t) &= \Phi + \delta\phi(t).\end{aligned}\quad (2)$$

In (2), we indicate by (Θ, Φ) the static (equilibrium) orientation of the magnetization obtained by solving the stationary problem ($\dot{\vec{M}} = 0$) for whatever effective field and magnetization distributions. Instead, $\delta\theta(t)$ and $\delta\phi(t)$ are the small polar and azimuthal deviations from equilibrium, respectively.

In the micromagnetic calculations, the magnetic system is subdivided into rectangular cells. Each micromagnetic cell is identified by a single index $k(j)$ that varies from 1 to N , where N denotes the number of cells. Hence, \vec{M}_k is the magnetization in the k th cell and $\vec{r}_{ij} = \vec{r}_i - \vec{r}_j$ is the in-plane distance between the i th cell and the j th cell. The index has been assigned so that the first line of the rectangular matrix ($X \times Y$) corresponds to $k = 1, \dots, Y$ and the second line to $k = Y + 1, \dots, 2Y$, and so on and so forth. $X(Y)$ is the number of cells along $x(y)$, while Z is the number of cells along z for a sample of thickness equal to d . We define for each cell the reduced magnetization $\vec{m}_k = \vec{M}_k/M_s$. Hence, in a polar reference frame for each cell

$$\vec{m}_k(t) = (\sin \theta_k(t) \cos \phi_k(t), \sin \theta_k(t) \sin \phi_k(t), \cos \theta_k(t)), \quad (3)$$

where ϕ_k is the azimuthal angle and θ_k is the polar angle of the magnetization. The total energy density of the system, obtained by dividing the total energy by the volume of the cell, is a function of ϕ_k and θ_k : $E = E(\theta_k, \phi_k)$ where k varies from 1 to N .

In the following sections we describe in detail the two micromagnetic methods. We do not illustrate the applications of these methods to magnetic nanoparticles, because this aspect is not the purpose of this paper. We give a summary of the paper. In Section 2, we outline the formalism at the basis of the HDMM. First, we introduce the different contributions to the energy density and then we derive the system of linear and homogeneous equations of motion for the isolated particle from the Hamilton equations. Finally, we present the generalization of the HDMM to the case of interacting elements. In Section 3, the formalism at the basis of the LDMM is presented. First, the Lagrangian equations for a macrospin system are derived. Then a generalization is given by considering N interacting momenta in an isolated magnetic element.

2. HDMM

This section deals with the review of the HDMM formalism. As stated above, the HDMM is a micromagnetic approach that can be applied only to fully conservative systems which are supposed to have, in a first approximation, a purely (undamped) precessional motion of the magnetization about the effective field. It is a finite-difference

micromagnetic method developed in the linear regime of spin dynamics by considering small deviations from the equilibrium magnetization. In the first subsection, the different contributions of the energy density entering into the dynamical matrix are calculated and the equations of motion for an isolated magnetic element are cast in the form of a linear and homogeneous system that can be solved as a complex generalized Hermitian eigenvalue problem. In the last subsection, it is shown the generalization of the HDMM to interacting magnetic nanoparticles by including into the dynamical matrix the Bloch condition.

2.1. Energy Density. First, we give the explicit expressions of the different interactions entering into the total micromagnetic energy density E of a given confined magnetic system simulated by using the HDMM: Zeeman energy, exchange energy, demagnetizing energy, and anisotropy energy, respectively [24]. The energy density is defined as $E = \tilde{E}/V$ where \tilde{E} is the energy of the system and V its volume. In the presence of an external magnetic field \vec{H} , the Zeeman energy density can be written in the form

$$E_{\text{ext}} = -\mu_0 M_s \vec{H} \cdot \sum_{k=1}^N \vec{m}_k, \quad (4)$$

being μ_0 the vacuum permeability. In micromagnetic theory, the exchange energy can be expressed as a volume integral of the form

$$\tilde{E}_{\text{exch}} = A \int_{\text{part}} \sum_{j=1}^3 (\vec{\nabla} m_j)^2 dV, \quad (5)$$

where the subscript “part” denotes the volume of a general magnetic particle, A is the exchange stiffness constant, and $\vec{\nabla}$ is the gradient applied to a given component of the magnetization. In this case the exchange contribution is independent of z . Using the first-neighbours model, the exchange energy density can be written as follows:

$$E_{\text{exch}} = A \sum_{k=1}^N \sum_{n=1}^4 \frac{1 - \vec{m}_k \cdot \vec{m}_n}{a_{kn}^2}, \quad (6)$$

where the variable a_{kn} is the distance between the centers of two adjacent cells of index k and n , respectively, k varies over all micromagnetic cells, and the sum over n ranges over the neighbours of the k -th cell. If the micromagnetic cells k are situated at the edges, one must impose boundary conditions. The cells on the edges interact with an external row of cells that have the same fixed magnetization, in this case the corresponding term in the sum must be weighted twice.

In order to calculate the demagnetizing energy density, we have followed the method of the demagnetizing tensor. In the following, we use also the term dipolar in place of the term demagnetizing, because the higher-order terms of the expansion vanish in the practical cases examined. Generally, within the framework of the demagnetizing tensor

method, the demagnetizing energy density can be written as follows:

$$E_{\text{dmg}} = \frac{1}{2} \mu_0 \sum_{kj} \vec{M}_k \cdot \underline{\underline{N}} \vec{M}_j$$

$$= \mu_0 \frac{M_s^2}{2} \sum_{kj} (m_{xk}, m_{yk}, m_{zk}) \times \begin{pmatrix} N_{xx} & N_{xy} & N_{xz} \\ N_{yx} & N_{yy} & N_{yz} \\ N_{zx} & N_{zy} & N_{zz} \end{pmatrix} \begin{pmatrix} m_{xj} \\ m_{yj} \\ m_{zj} \end{pmatrix}. \quad (7)$$

This equation includes the self-energy and $N_{\alpha\beta} = N_{\alpha\beta}(\vec{r}_{kj})$ with $\alpha, \beta = x, y, z$ are the elements of demagnetizing tensor. Each component of the demagnetizing tensor is related to the interaction between two rectangular surfaces S and S' . Under the assumption made for the calculation of the demagnetizing field for uniform magnetization, by using a version of Gauss's theorem, the demagnetizing tensor can be written as

$$\underline{\underline{N}}(\vec{r}_{kj}) = \frac{1}{V} \int_{S_k} d\vec{S} \int_{S'_j} \frac{d\vec{S}'}{|\vec{r} - \vec{r}'|}, \quad (8)$$

where $V = l_c^2 d$ is the volume of the micromagnetic cell with l_c the cell size and d is the cell height. Because of the four-fold C_4 symmetry and since $\vec{r}_{kj} \equiv (x, y, z)$, all components can be expressed only as a function of $N_{xx}(x, y, z)$ and $N_{xy}(x, y, z)$ components with suitable permutations of the variables x, y, z .

The magnetocrystalline uniaxial anisotropy can be labeled with the symbol E_{ani} . It is an energy density function, for a given micromagnetic cell, of the angle α_k between the magnetization of the single cell \vec{m}_k and the easy axis of generic direction given by the unit vector \hat{u} . We write

$$E_{\text{ani}} = \sum_{k=1}^N K^{(1)} \sin^2 \alpha_k = \sum_{k=1}^N K^{(1)} (1 - \cos^2 \alpha_k)$$

$$= \sum_{k=1}^N K^{(1)} [1 - (\vec{m}_k \cdot \hat{u})^2], \quad (9)$$

where $K^{(1)}$ is the first-order anisotropy uniaxial coefficient.

As the dynamical matrix components are expressed in terms of the second derivatives of the energy density, it is necessary to calculate them from the above expressions. First, we calculate the second derivatives of the magnetization with respect to the polar and azimuthal angles of the given micromagnetic cell that represent the degrees of freedom of the system. Indeed, the second derivatives of the magnetization appear in the final expressions of the second derivatives of the energy density. In particular

$$\frac{\partial^2 \vec{m}_k}{\partial \delta \phi_k^2} = (-\sin \theta_k \cos \phi_k, -\sin \theta_k \sin \phi_k, 0),$$

$$\frac{\partial^2 \vec{m}_k}{\partial \delta \phi_k \partial \delta \theta_k} = (-\cos \theta_k \sin \phi_k, \cos \theta_k \cos \phi_k, 0), \quad (10)$$

$$\frac{\partial^2 \vec{m}_k}{\partial \delta \theta_k^2} = (-\sin \theta_k \cos \phi_k, -\sin \theta_k \sin \phi_k, -\cos \theta_k).$$

The second derivatives of the energy density are calculated at equilibrium. For the sake of simplicity, in the following, the derivatives are calculated with respect to $\delta \theta_k$ and $\delta \theta_l$ implying that one or two of the two generic variables could be also $\delta \phi$.

The second derivative of Zeeman energy density becomes

$$\frac{\partial^2 E_{\text{ext}}}{\partial \delta \theta_k \partial \delta \theta_l} = \begin{cases} -\mu_0 M_s \vec{H} \cdot \frac{\partial^2 \vec{m}_k}{\partial \delta \theta_k \partial \delta \theta_l} & l = k \\ 0 & l \neq k. \end{cases} \quad (11)$$

As outlined previously, for the calculation of the exchange contribution, the nearest-neighbour model is taken into account. It is useful to give also the expression of the first derivative due to some important manipulations that have to be performed. The first derivative with respect to $\delta \theta_k$ includes in the sum a term in which $i = k$ and thus $n \neq k$ and also the other terms with $n = k$ and with i one of the nearest neighbours. Thanks to a proper change of indices in the second term, the following equation is obtained:

$$\frac{\partial E_{\text{exch}}}{\partial \delta \theta_k} = -A \sum_{n=1}^4 \frac{1}{a_{kn}^2} \frac{\partial \vec{m}_k}{\partial \delta \theta_k} \cdot \vec{m}_n - A \sum_{n=1}^4 \frac{1}{a_{kn}^2} \vec{m}_n \cdot \frac{\partial \vec{m}_k}{\partial \delta \theta_k}$$

$$= -2A \sum_{n=1}^4 \frac{1}{a_{kn}^2} \frac{\partial \vec{m}_k}{\partial \delta \theta_k} \cdot \vec{m}_n, \quad (12)$$

where the sum over n is made up over the nearest-neighbour micromagnetic cells of the k -th cell. In the special case of the adopted first neighbours model, the second derivatives are

$$\frac{\partial^2 E_{\text{exch}}}{\partial \delta \theta_k \partial \delta \theta_l} = \begin{cases} -2A \sum_{n=1}^4 \frac{1}{a_{kn}^2} \frac{\partial^2 \vec{m}_k}{\partial \delta \theta_k \partial \delta \theta_l} \cdot \vec{m}_n & l = k \\ -2A \frac{1}{a_{kl}^2} \frac{\partial \vec{m}_k}{\partial \delta \theta_k} \cdot \frac{\partial \vec{m}_l}{\partial \delta \theta_l} & l, k: \text{nearest-neighbour} \\ 0 & k \neq l \text{ and not nearest-neighbour.} \end{cases} \quad (13)$$

We now pass to the calculation of the derivatives of the demagnetizing energy density. Due to their rather complicated form, we give in the following the expression not only of the second derivatives of the demagnetizing energy density but also of the first derivatives with respect to the generic

variable $\delta\theta_i$. The first derivative of the demagnetizing energy density (7) is

$$\begin{aligned} \frac{\partial E_{\text{dmg}}}{\partial \delta\theta_i} &= \mu_0 M_s^2 \left[\frac{1}{2} \sum_{k \neq i} \vec{m}_k \cdot \underline{N}(k, i) \frac{\partial \vec{m}_i}{\partial \delta\theta_i} + \frac{1}{2} \sum_{j \neq i} \frac{\partial \vec{m}_i}{\partial \delta\theta_i} \right. \\ &\quad \left. \cdot \underline{N}(k, i) \vec{m}_j + \frac{1}{2} \frac{\partial}{\partial \delta\theta_i} (\vec{m}_i \cdot \hat{N}(i, i) \vec{m}_i) \right] \\ &= \mu_0 M_s^2 \sum_{\substack{k=1 \\ k \neq i}}^N \vec{m}_k \cdot \underline{N}(k, i) \frac{\partial \vec{m}_i}{\partial \delta\theta_i} + \vec{m}_i \cdot \underline{N}(i, i) \frac{\partial \vec{m}_i}{\partial \delta\theta_i}. \end{aligned} \quad (14)$$

In the sum, the contribution of the terms with the same index $k = j = i$ has been separated; moreover, we have taken into account that the tensor \underline{N} fulfils $\underline{N}(k, i) = \underline{N}(i, k)$ and is symmetric ($N_{\alpha\beta} = N_{\beta\alpha}$).

Thanks to the previous consideration, it is possible to write

$$\frac{\partial \vec{m}_k}{\partial \delta\theta_k} \cdot \underline{N}(k, i) \vec{m}_i = \vec{m}_i \cdot \underline{N}(k, i) \frac{\partial \vec{m}_k}{\partial \delta\theta_k}, \quad (15)$$

and therefore,

$$\begin{aligned} \frac{\partial}{\partial \delta\theta_i} (\vec{m}_i \cdot \underline{N}(i, i) \vec{m}_i) &= \frac{\partial \vec{m}_i}{\partial \delta\theta_i} \cdot \underline{N}(i, i) \vec{m}_i + \vec{m}_i \cdot \underline{N}(i, i) \frac{\partial \vec{m}_i}{\partial \delta\theta_i} \\ &= 2 \vec{m}_i \cdot \underline{N}(i, i) \frac{\partial \vec{m}_i}{\partial \delta\theta_i}. \end{aligned} \quad (16)$$

The second derivative must take into account the two cases: $i \neq l, i = l (j = i)$, namely,

$$\frac{\partial^2 E_{\text{dmg}}}{\partial \delta\theta_i \partial \delta\theta_i} = \begin{cases} M_s^2 \left(\sum_{k=1}^N \vec{m}_k \cdot \underline{N}(k, l) \frac{\partial^2 \vec{m}_l}{\partial \delta\theta_l \partial \delta\theta_i} \right. \\ \quad \left. + \frac{\partial \vec{m}_l}{\partial \delta\theta_l} \cdot \underline{N}(k, l) \frac{\partial \vec{m}_i}{\partial \delta\theta_i} \right) & l = i \\ M_s^2 \frac{\partial \vec{m}_l}{\partial \delta\theta_l} \cdot \underline{N}(k, l) \frac{\partial \vec{m}_i}{\partial \delta\theta_i} & l \neq i. \end{cases} \quad (17)$$

The $k = i$ term resulting from the derivative of the second term (in the expression of the first derivative given above) has been included in the sum over k .

The last step is the calculation of the term associated with the anisotropy energy density. The second derivative of the anisotropy energy density can be written as

$$\begin{aligned} \frac{\partial^2 E_{\text{ani}}}{\partial \delta\phi_j \partial \delta\theta_k} &= \begin{cases} -2K^{(1)} \left[\left(\frac{\partial \vec{m}_k}{\partial \delta\phi_j} \cdot \hat{u} \right) \cdot \left(\frac{\partial \vec{m}_k}{\partial \delta\theta_k} \cdot \hat{u} \right) + (\vec{m}_k \cdot \hat{u}) \right. \\ \quad \left. \cdot \left(\frac{\partial^2 \vec{m}_k}{\partial \delta\phi_j \partial \delta\theta_k} \cdot \hat{u} \right) \right] & \text{for } \delta\theta, \delta\phi \ k = j \\ -2K^{(1)} \left[\left(\frac{\partial \vec{m}_k}{\partial \delta\phi_k} \cdot \hat{u} \right)^2 + (\vec{m}_k \cdot \hat{u}) \cdot \left(\frac{\partial^2 \vec{m}_k}{\partial \delta\phi_k^2} \cdot \hat{u} \right) \right] & \text{for } \delta\phi, \delta\phi \text{ or } \delta\theta, \delta\theta \ k = j \\ 0 & k \neq j. \end{cases} \end{aligned} \quad (18)$$

2.2. Equations of Motion for an Isolated Magnetic Particle. The derivatives calculated previously are included into the dynamic equations. Indeed, the equations of motion can be cast into a linear and homogeneous system in which the second derivatives of the energy density calculated at equilibrium appear explicitly. It is well known that the equation of motion for a magnetic spin system which undergoes a purely precessional motion is the Landau-Lifshitz equation [25], expressed as a torque equation involving the effective field and the magnetization itself. Since our aim is to find the energy density in a conservative system, we derive the equations of motion from the Hamilton equations.

2.2.1. HDMM for a Macrospin System. The equation of motion for the magnetic systems under investigation will be derived by following semiclassical approach. Also, the model will be first derived by considering the so-called macrospin approximation, where the material is thought as uniformly magnetized and represented by a single dipole momentum.

As known from classical mechanics, in the presence of fixed constraints and conservative sources, the system Hamiltonian \mathcal{H} coincides with the total mechanical energy \tilde{E} , namely, $\mathcal{H} \equiv \tilde{E} = T - U$, where T is the kinetic energy and U is the potential expressed as the opposite of the potential energy V . By defining the Lagrangian variables of the problem with q_n , where $n = 1, 2, \dots$ is the number of degrees of freedom corresponding to the dynamic variables, and the corresponding conjugate momenta with p_n , the Hamilton equations in the $2n$ canonical variables (q_n, p_n) take the form [15]

$$\begin{aligned} \frac{\partial q_n}{\partial t} &= \frac{\partial \mathcal{H}}{\partial p_n}, \\ \frac{\partial p_n}{\partial t} &= -\frac{\partial \mathcal{H}}{\partial q_n}. \end{aligned} \quad (19)$$

The direction of the magnetic dipole moment of the k th cell is given by (3). For the specific case, the dynamic variables

referred to the k -cell are the small deviations from equilibrium of the azimuthal and polar angles given by

$$q_1 = \delta\phi, \quad q_2 = \delta\theta, \quad (20)$$

where 1 (2) labels the first (second) variable.

To determine the conjugate momenta, the expression of the angular momentum is needed. We recall the relation between the angular momentum \vec{l}_Ω and the magnetic momentum $\vec{\mu}$ by referring to a rigid body with a fixed point Ω (see Figure 1), namely,

$$\vec{l}_\Omega = \frac{1}{\gamma} \vec{\mu} = \frac{v_c M_s}{\gamma} \vec{m}, \quad (21)$$

where γ is the gyromagnetic ratio and v_c the volume of the magnetic moment to the case. Indeed, since q_1 represents a rotation about the z -axis of the magnetic dipole, its conjugate momentum p_1 corresponds to the z component of the variation of the angular momentum, namely,

$$p_1 = \delta l_z = \frac{v_c M_s}{\gamma} \delta m_z = -\frac{v_c M_s}{\gamma} \sin \theta \delta \theta, \quad (22a)$$

where $\vec{m} = (\sin \theta \cos \phi, \sin \theta \sin \phi, \cos \theta)$ is the unit magnetization vector, normalized to the saturation magnetization M_s . Following an analogous argument, the other momentum p_2 can be determined. Indeed, q_2 is a rotation of the dipole moment about an axis of unitary vector $\hat{\phi}' = -\sin \phi \hat{e}_1 + \cos \phi \hat{e}_2$ in the x - y plane at an angle $\hat{\phi}' = \phi + \pi/2$ from the x -axis. Therefore, p_2 corresponds to the projection of the variation of the angular momentum along the $\hat{\phi}'$ vector, namely,

$$\begin{aligned} p_2 &= \delta \vec{l}_\Omega \cdot \hat{\phi}' = \frac{v_c M_s}{\gamma} (\delta \vec{m} \cdot \hat{\phi}') \\ &= -\frac{v_c M_s}{\gamma} \left(\frac{\partial \vec{m}}{\partial \phi} \delta \phi + \frac{\partial \vec{m}}{\partial \theta} \delta \theta \right) \cdot \hat{\phi}' \\ &= \frac{v_c M_s}{\gamma} \sin \theta \delta \phi. \end{aligned} \quad (22b)$$

By substituting (20), (22a), and (22b) into the first Hamilton equation (cf. (19)), the following system of equations is obtained:

$$\begin{aligned} \dot{\delta\phi} &= -\frac{\gamma}{v_c M_s \sin \theta} \mathcal{H}_{\delta\theta}, \\ \dot{\delta\theta} &= \frac{\gamma}{v_c M_s \sin \theta} \mathcal{H}_{\delta\phi}, \end{aligned} \quad (23)$$

where the dot notation stands for the time derivative and, at the right-hand side, the first derivatives of the energy with respect to the mechanical variables appear. By introducing the energy density $E = \tilde{E}/V$ (keeping in mind that $\mathcal{H} = \tilde{E}$) and expanding it in a power Taylor expansion around the equilibrium up to the second order, it yields

$$E = E_0 + \frac{1}{2} [E_{\phi\phi} (\delta\phi)^2 + 2E_{\phi\theta} \delta\phi \delta\theta + E_{\theta\theta} (\delta\theta)^2], \quad (24)$$

where E_0 is the constant zero-order term that is inessential, the first-order terms vanish at equilibrium, and $E_{\alpha\beta}$ represent the second derivatives calculated at equilibrium ($E_{\alpha\beta} = \partial^2 E / \partial \alpha \partial \beta$ with $\alpha, \beta = \phi, \theta$). By using (23) and (24), we obtain

$$\begin{aligned} \dot{\delta\phi} &= -\frac{\gamma}{M_s \sin \theta} [E_{\theta\phi} \delta\phi + E_{\theta\theta} \delta\theta], \\ \dot{\delta\theta} &= \frac{\gamma}{M_s \sin \theta} [E_{\phi\phi} \delta\phi + E_{\phi\theta} \delta\theta]. \end{aligned} \quad (25)$$

By inserting the time dependence in the form $e^{i\omega t}$, where ω is the angular frequency of the given collective mode, the system of equations of motion reads

$$\begin{aligned} -\frac{E_{\theta\phi}}{\sin \theta} \delta\phi - \frac{E_{\theta\theta}}{\sin \theta} \delta\theta - \tilde{\lambda} \delta\phi &= 0, \\ \frac{E_{\phi\phi}}{\sin \theta} \delta\phi + \frac{E_{\phi\theta}}{\sin \theta} \delta\theta - \tilde{\lambda} \delta\theta &= 0. \end{aligned} \quad (26)$$

The linear and homogeneous system of equations expressed in (26) can be written as an eigenvalue problem

$$\underline{\underline{C}} \vec{v} = \tilde{\lambda} \vec{v}, \quad (27)$$

with $\tilde{\lambda} = i(M_s/\gamma)\omega$ the complex eigenvalues of the problem,

$$\underline{\underline{C}} = \begin{bmatrix} -\frac{E_{\theta\phi}}{\sin \theta} & -\frac{E_{\theta\theta}}{\sin \theta} \\ \frac{E_{\phi\phi}}{\sin \theta} & \frac{E_{\phi\theta}}{\sin \theta} \end{bmatrix}, \quad (28)$$

being $\underline{\underline{C}}$ a real, but not symmetric, matrix and $\vec{v} = (\delta\phi, \delta\theta)^T$.

However, the system of motion equations (26) can be also recast as a complex generalized Hermitian eigenvalue problem

$$\underline{\underline{A}} \vec{v} = \lambda \underline{\underline{B}} \vec{v}, \quad (29)$$

where $\underline{\underline{B}}$ is a Hessian matrix expressed by the second derivatives of the energy density at equilibrium. In particular

$$\begin{aligned} \underline{\underline{B}} &= \begin{bmatrix} E_{\phi\phi} & E_{\phi\theta} \\ E_{\theta\phi} & E_{\theta\theta} \end{bmatrix}, \\ \underline{\underline{A}} &= \begin{bmatrix} 0 & i \sin \theta \\ -i \sin \theta & 0 \end{bmatrix}. \end{aligned} \quad (30)$$

It should be noticed that the matrix $\underline{\underline{A}}$ is Hermitian, whereas $\underline{\underline{B}}$ is real and symmetric, so that all the corresponding eigenvalues $\lambda = \gamma/M_s \omega$ are real quantities.

2.2.2. HDMM for an Isolated System Composed by N Interacting Magnetic Momenta. Equation (24) can be generalized to the case of N interacting magnetic momenta (where each momentum is identified with a micromagnetic cell) taking the form

$$E = E_0 + \frac{1}{2} \sum_{n=1}^N \sum_{l=1}^N [E_{\phi_n \phi_l} \delta\phi_n \delta\phi_l + 2E_{\phi_n \theta_l} \delta\phi_n \delta\theta_l + E_{\theta_n \theta_l} \delta\theta_n \delta\theta_l]. \quad (31)$$

In (31), the total energy density is given by $E = E_{\text{ext}} + E_{\text{exch}} + E_{\text{dmg}} + E_{\text{ani}}$ where the different contributions are expressed in (4), (6), (7), and (9), respectively. By substituting (31) into (23), we get

$$\begin{aligned}\delta\dot{\phi}_k &= -\frac{\gamma}{M_s \sin \theta_k} \sum_{l=1}^N [E_{\theta_k \phi_l} \delta\phi_l + E_{\theta_k \theta_l} \delta\theta_l], \\ \delta\dot{\theta}_k &= \frac{\gamma}{M_s \sin \theta_k} \sum_{l=1}^N [E_{\phi_k \phi_l} \delta\phi_l + E_{\phi_k \theta_l} \delta\theta_l].\end{aligned}\quad (32)$$

By introducing the time dependence in the form $e^{i\omega t}$, the system of equations of motion is composed by the following $2N$ linear and homogeneous equations for $k = 1 \dots N$:

$$\begin{aligned}\sum_{l=1}^N \left(-\frac{E_{\theta_k \phi_l}}{\sin \theta_k} \right) \delta\phi_l + \sum_{l=1}^N \left(-\frac{E_{\theta_k \theta_l}}{\sin \theta_k} \right) \delta\theta_l - \tilde{\lambda} \delta\phi_k &= 0, \\ \sum_{l=1}^N \left(\frac{E_{\phi_k \phi_l}}{\sin \theta_k} \right) \delta\phi_l + \sum_{l=1}^N \left(\frac{E_{\phi_k \theta_l}}{\sin \theta_k} \right) \delta\theta_l - \tilde{\lambda} \delta\theta_k &= 0.\end{aligned}\quad (33)$$

The unknown factors $\delta\phi_l, \delta\theta_l$ represent the eigenvectors of the problem and are expressed by the small angular deviation from the equilibrium position of the azimuthal (ϕ_l) and polar (θ_l) angles in the l th micromagnetic cell. The system above has a solution only if the determinant is zero. By suitable exchanges of rows (columns), the linear and homogeneous system of equations expressed in (33) can be written as an eigenvalue problem in analogy with the case of a macrospin system

$$\underline{\underline{C}} \vec{v} = \tilde{\lambda} \vec{v}. \quad (34)$$

In (34), \vec{v} is the set of the unknown factors representing the eigenvectors of the problem that take the form

$$\vec{v} = (\delta\phi_1, \delta\theta_1, \delta\phi_2, \delta\theta_2, \dots, \delta\phi_N, \delta\theta_N)^T. \quad (35)$$

$\underline{\underline{C}}$ is the matrix whose elements are expressed as

$$\left. \begin{aligned} C_{2k-1,2l-1} &= -\frac{E_{\theta_k \phi_l}}{\sin \theta_k} \\ C_{2k-1,2l} &= -\frac{E_{\theta_k \theta_l}}{\sin \theta_k} \\ C_{2k,2l-1} &= \frac{E_{\phi_k \phi_l}}{\sin \theta_k} \\ C_{2k,2l} &= \frac{E_{\phi_k \theta_l}}{\sin \theta_k} \end{aligned} \right\} k = 1 \dots N, l = 1 \dots N. \quad (36)$$

Analogously to the case of a macrospin system, the matrix $\underline{\underline{C}}$ is real but not symmetric, also in this case the eigenvalues (and not only the eigenvectors) are complex. This matrix can be indeed seen as composed by two submatrices 2×2 for each pair of values (k, l) . In the diagonal submatrices ($k = l$) the following relation is verified:

$$C_{2k-1,2k-1} = -C_{2k,2k}. \quad (37)$$

For the elements of two different submatrices (k, l) and (l, k) , that are not diagonal ($k \neq l$), the following symmetries hold:

$$\begin{aligned}\sin \theta_k C_{2k-1,2l-1} &= -\sin \theta_l C_{2l,2k}, \\ \sin \theta_k C_{2k-1,2l} &= \sin \theta_l C_{2l-1,2k}, \\ \sin \theta_k C_{2k,2l-1} &= \sin \theta_l C_{2l,2k-1}, \\ \sin \theta_k C_{2k,2l} &= -\sin \theta_l C_{2l-1,2k-1}.\end{aligned}\quad (38)$$

As for the macrospin approximation, the equation of motion can be recast as a complex generalized Hermitian eigenvalue problem

$$\underline{\underline{A}} \vec{v} = \lambda \underline{\underline{B}} \vec{v}, \quad (39)$$

where $\underline{\underline{B}}$ is a Hessian matrix expressed by the second derivatives of the energy density at equilibrium. $\underline{\underline{B}}$ is given by

$$\left. \begin{aligned} B_{2k-1,2l-1} &= E_{\phi_k \phi_l} \\ B_{2k-1,2l} &= E_{\phi_k \theta_l} \\ B_{2k,2l-1} &= E_{\theta_k \phi_l} \\ B_{2k,2l} &= E_{\theta_k \theta_l} \end{aligned} \right\} k = 1 \dots N, l = 1 \dots N, \quad (40)$$

where the matrix $\underline{\underline{B}}$ is, again, real and symmetric. Moreover, since the static magnetization corresponds to a minimum of the energy and the matrix $\underline{\underline{B}}$ is its Hessian, the matrix $\underline{\underline{B}}$ is also positive defined. Instead, the matrix $\underline{\underline{A}}$ has the following form:

$$\underline{\underline{A}} = \begin{bmatrix} 0 & i \sin \theta_1 & 0 & 0 & \dots \\ -i \sin \theta_1 & 0 & 0 & 0 & \dots \\ 0 & 0 & 0 & i \sin \theta_2 & \dots \\ 0 & 0 & -i \sin \theta_2 & 0 & \dots \\ \dots & \dots & \dots & \dots & \dots \end{bmatrix}. \quad (41)$$

The matrix $\underline{\underline{A}}$ is Hermitian. This allows us to solve the system as a complex generalized Hermitian eigenvalue problem which admits only real eigenvalues. To further reduce the computational time, it is possible to evaluate only some eigenvalues and eigenvectors that are in a specific range.

Once the eigenvectors \vec{v} are obtained, the dynamic magnetization $\delta \vec{m}_k$ in the k th micromagnetic cell expressed in Cartesian coordinates and in unit of M_s is given by

$$\begin{aligned}\delta \vec{m}_k &= (-\sin \theta_k \sin \phi_k \delta\phi_k + \cos \theta_k \cos \phi_k \delta\theta_k, \\ &\sin \theta_k \cos \phi_k \delta\phi_k + \cos \theta_k \sin \phi_k \delta\theta_k, -\sin \theta_k \delta\theta_k).\end{aligned}\quad (42)$$

For each solution of the eigenvalue problem, the collection of all $\delta \vec{m}_k$ defines the mode profile. It must be remarked that $\delta \vec{m}_k$ is a complex vector, because $\delta\theta_k, \delta\phi_k$ are, in general, complex.

2.3. Equations of Motion for Interacting Magnetic Particles. Let us suppose to have a 2D periodic array of interacting nanodots characterized by the primitive vectors \vec{a}_1 and \vec{a}_2 ;

for example, for the specific case of a rectangular lattice their values are

$$\vec{a}_1 = \lambda_x \hat{x}, \quad \vec{a}_2 = \lambda_y \hat{y}, \quad (43)$$

where λ_x and λ_y represent the periodicity along x -axis and y -axis, respectively. The primitive vectors of the reciprocal lattice are \vec{b}_1 and \vec{b}_2

$$\begin{aligned} \vec{b}_1 &= 2\pi \frac{(\vec{a}_2 \times \vec{a}_1) \times \vec{a}_2}{(\vec{a}_1 \times \vec{a}_2)^2}, \\ \vec{b}_2 &= 2\pi \frac{(\vec{a}_1 \times \vec{a}_2) \times \vec{a}_1}{(\vec{a}_1 \times \vec{a}_2)^2}. \end{aligned} \quad (44)$$

For the special case of a rectangular lattice the vectors become

$$\begin{aligned} \vec{b}_1 &= \frac{2\pi}{\lambda_x} \hat{x}, \\ \vec{b}_2 &= \frac{2\pi}{\lambda_y} \hat{y}. \end{aligned} \quad (45)$$

Due to the analogy with the Bloch wave (analogy, not equality, because the wave function has not a physical meaning, contrarily to the magnetization), it is possible to write the following periodicity rule valid for the dynamic magnetization:

$$\delta \vec{m}(\vec{r} + \vec{R}) = e^{i\vec{K} \cdot \vec{R}} \delta \vec{m}(\vec{r}), \quad (46)$$

where \vec{R} is a vector of the particle lattice given by

$$\vec{R} = i_1 \vec{a}_1 + i_2 \vec{a}_2, \quad i_1, i_2 \in \mathbb{Z}, \quad i_1, i_2 = -\frac{N_1}{2} \dots \frac{N_1}{2} - 1, \quad (47)$$

and \vec{r} can be confined into the first primitive cell centered in the first dot. The Bloch vector takes the following values:

$$\vec{K} = \frac{n_1}{N_1} \vec{b}_1 + \frac{n_2}{N_2} \vec{b}_2, \quad n_i \in \mathbb{Z}, \quad n_i = -\frac{N_i}{2} \dots \frac{N_i}{2} - 1. \quad (48)$$

$N_1, N_2 \in \mathbb{N}$ indicate the number of primitive cells n in direction \vec{a}_1 and \vec{a}_2 , respectively. In this scheme, both N_1 and N_2 are taken as even numbers. In order to confirm the hypothesis on the dynamic magnetization N_1, N_2 must be very large.

If the magnetizations of different primitive cells and the different micromagnetic cells were independent, that is no periodicity rule were present, then one would have a dynamic system with variables $\theta_{k\vec{R}}$ and $\phi_{k\vec{R}}$, where the k index changes inside the magnetic particle and \vec{R} can assume the values indicated in (47). In this case, the linear and homogeneous system of $2N$ equations of motion is

$$\begin{aligned} \sum_{l, \vec{R}'} \left(-\frac{E_{\theta_{k\vec{R}} \phi_{l\vec{R}'}}}{\sin \theta_{k\vec{R}}} \right) \delta \phi_{l\vec{R}'} + \sum_{l, \vec{R}'} \left(-\frac{E_{\theta_{k\vec{R}} \theta_{l\vec{R}'}}}{\sin \theta_{k\vec{R}}} \right) \delta \theta_{l\vec{R}'} - \lambda \delta \phi_{k\vec{R}} &= 0, \\ \sum_{l, \vec{R}'} \left(\frac{E_{\phi_{k\vec{R}} \phi_{l\vec{R}'}}}{\sin \theta_{k\vec{R}}} \right) \delta \phi_{l\vec{R}'} + \sum_{l, \vec{R}'} \left(\frac{E_{\phi_{k\vec{R}} \theta_{l\vec{R}'}}}{\sin \theta_{k\vec{R}}} \right) \delta \theta_{l\vec{R}'} - \lambda \delta \theta_{k\vec{R}} &= 0, \end{aligned} \quad (49)$$

where $k = 1 \dots N$ and the sums over l and \vec{R}' are on the same values. Instead, thanks to the Bloch condition expressed in (46), one can consider the equations only at $\vec{R} = 0$; moreover, taking into account the same condition, the variables appearing for $\vec{R}' \neq 0$ can be replaced by using the same condition. Now, when rewriting the system, the index \vec{R} is omitted when it has value equal to 0 or it is irrelevant. Owing to these considerations, the system given in (49) can be rewritten in the form [16]

$$\begin{aligned} \sum_{l=1}^N \left(-\frac{\sum_{\vec{R}'} E_{\theta_k \phi_{l\vec{R}'}} e^{i\vec{K} \cdot \vec{R}'}}{\sin \theta_k} \right) \delta \phi_l + \sum_{l=1}^N \left(-\frac{\sum_{\vec{R}'} E_{\theta_k \theta_{l\vec{R}'}} e^{i\vec{K} \cdot \vec{R}'}}{\sin \theta_k} \right) \delta \theta_l \\ - \tilde{\lambda} \delta \phi_k = 0, \\ \sum_{l=1}^N \left(\frac{\sum_{\vec{R}'} E_{\phi_k \phi_{l\vec{R}'}} e^{i\vec{K} \cdot \vec{R}'}}{\sin \theta_k} \right) \delta \phi_l + \sum_{l=1}^N \left(\frac{\sum_{\vec{R}'} E_{\phi_k \theta_{l\vec{R}'}} e^{i\vec{K} \cdot \vec{R}'}}{\sin \theta_k} \right) \delta \theta_l \\ - \tilde{\lambda} \delta \theta_k = 0. \end{aligned} \quad (50)$$

Equation (50) is similar to (33) by making the following replacement:

$$E_{\alpha_k \beta_l} \longrightarrow \sum_{\vec{R}'} e^{i\vec{K} \cdot \vec{R}'} E_{\alpha_{k0} \beta_{l\vec{R}'}} \quad (51)$$

and recalling that now the energy is referred to the whole system of particles. Like for the case of the isolated magnetic particle, also for the case of interacting magnetic particles the system of linear and homogeneous equations given in (50) can be written as an eigenvalue problem which in turn can be cast as a complex generalized Hermitian eigenvalue problem.

The symmetry for the matrix elements that was valid for a single primitive cell now is not respected except for $\vec{K} = 0$ or $\vec{K} = \vec{G}/2$ with \vec{G} a translational reciprocal vector:

$$\begin{aligned} \sum_{\vec{R}'} e^{i\vec{K} \cdot \vec{R}'} E_{\alpha_{k0} \beta_{l\vec{R}'}} &= \sum_{\vec{R}'} e^{i\vec{K} \cdot \vec{R}'} E_{\beta_{l\vec{R}'} \alpha_{k0}} = \sum_{\vec{R}'} e^{i\vec{K} \cdot \vec{R}'} E_{\beta_{l0} \alpha_{k-\vec{R}'}} \\ &= \sum_{\vec{R}'} e^{-i\vec{K} \cdot \vec{R}'} E_{\beta_{l0} \alpha_{k\vec{R}'}} \\ &\neq \sum_{\vec{R}'} e^{i\vec{K} \cdot \vec{R}'} E_{\beta_{l0} \alpha_{k\vec{R}'}} \quad \vec{K} \neq \vec{0}, \vec{K} \neq \frac{\vec{G}}{2}, \end{aligned} \quad (52)$$

with $\vec{R}' = -\vec{R}$. The primitive cell has at the centre a single dot that occupies only a part of it. The interdot exchange coupling is zero. Thanks to the last consideration and to the fact that derivatives of Zeeman, exchange, anisotropy, energy density are referred only to the cell of the first variable (α_{k0}) with $\alpha_{k\vec{R}} = \theta_{k\vec{R}}, \phi_{k\vec{R}}$ or at most to the nearest neighbour, all terms of the sum in (51) with $\vec{R}' \neq 0$ are zero. Hence, for these energy density terms, the equations are the same as those of the single particle case and the same occurs for their corresponding derivatives appearing in the equations of motion. The only energy density term that differs from the

one obtained for the isolated element is the demagnetizing energy density. For a system of interacting nanoparticles, the demagnetizing energy density can be written as

$$E_{\text{dmg}} = \frac{1}{2} \mu_0 \sum_{\vec{R}, \vec{R}', k, k'} \vec{m}_k(\vec{R}) \underline{\underline{N}}(\vec{R}, \vec{R}', k, k') \vec{m}_{k'}(\vec{R}'). \quad (53)$$

Due to its rather complex expression, it is useful to give the derivation also of the first derivative of E_{dmg} like for the case of the isolated nanoelement.

In order to calculate the first derivative, the properties of the demagnetizing tensor must be considered

$$\begin{aligned} \langle \nu | N | \omega \rangle &= \langle \omega | N^\dagger | \nu \rangle^* = \langle \omega | N^\dagger | \nu \rangle \\ &= \langle \omega | N^t | \nu \rangle = \langle \omega | N | \nu \rangle, \end{aligned} \quad (54a)$$

since N is real and symmetric and

$$\begin{aligned} \underline{\underline{N}}(\vec{R}, \vec{R}', k, k') &= \underline{\underline{N}}(\vec{R}' - \vec{R} + \vec{r}_{k'} - \vec{r}_k) \\ &= \underline{\underline{N}}(-\vec{R}' + \vec{R} - \vec{r}_{k'} + \vec{r}_k) = \underline{\underline{N}}(\vec{R}', \vec{R}, k', k), \end{aligned} \quad (54b)$$

thanks to the inversion symmetry. Hence, the first derivative of the energy is

$$\begin{aligned} \frac{\partial E_{\text{dmg}}}{\partial \delta \alpha_k(\vec{0})} &= \mu_0 \frac{M_s^2}{2} \left[\sum_{\substack{\vec{R}', k' \\ (\vec{R}', k') \neq (\vec{0}, k)}} \vec{m}_{k'}(\vec{R}') \cdot \underline{\underline{N}}(\vec{R}', \vec{0}, k', k) \frac{\partial \vec{m}_k(\vec{0})}{\partial \delta \alpha_k(\vec{0})} \right. \\ &\quad + \sum_{\substack{\vec{R}', k' \\ (\vec{R}', k') \neq (\vec{0}, k)}} \frac{\partial \vec{m}_k(\vec{0})}{\partial \delta \alpha_k(\vec{0})} \cdot \underline{\underline{N}}(\vec{0}, \vec{R}', k', k) \vec{m}_{k'}(\vec{R}') \\ &\quad \left. + \frac{\partial}{\partial \delta \alpha_k(\vec{0})} (\vec{m}_k(\vec{0}) \cdot \underline{\underline{N}}(\vec{0}, \vec{0}, k, k) \vec{m}_k(\vec{0})) \right] \\ &= \mu_0 M_s^2 \left[\sum_{\substack{\vec{R}', k' \\ (\vec{R}', k') \neq (\vec{0}, k)}} \vec{m}_{k'}(\vec{R}') \cdot \underline{\underline{N}}(\vec{R}', \vec{0}, k', k) \frac{\partial \vec{m}_k(\vec{0})}{\partial \delta \alpha_k(\vec{0})} \right. \\ &\quad \left. + \vec{m}_k(\vec{0}) \cdot \underline{\underline{N}}(\vec{0}, \vec{0}, k, k) \frac{\partial \vec{m}_k(\vec{0})}{\partial \delta \alpha_k(\vec{0})} \right]. \end{aligned} \quad (55)$$

The second derivative takes the form

$$\begin{aligned} \frac{\partial^2 E_{\text{dmg}}}{\partial \delta \alpha_k(\vec{0}) \partial \delta \beta_k(\vec{R})} &= \left\{ \begin{aligned} &\mu_0 M_s^2 \left[\sum_{\vec{R}', k'} \vec{m}_{k'}(\vec{R}') \cdot \underline{\underline{N}}(\vec{R}', \vec{0}, k', k) \right. \\ &\quad \times \frac{\partial^2 \vec{m}_k(\vec{0})}{\partial \delta \alpha_k(\vec{0}) \partial \delta \beta_k(\vec{0})} \\ &\quad + \frac{\partial \vec{m}_k(\vec{0})}{\partial \delta \beta_k(\vec{0})} \\ &\quad \left. \cdot \underline{\underline{N}}(\vec{0}, \vec{0}, k, k) \frac{\partial \vec{m}_k(\vec{0})}{\partial \delta \alpha_k(\vec{0})} \right] \end{aligned} \right. \quad \vec{R} = \vec{0}, l = k \\ &\quad \left[\mu_0 M_s^2 \frac{\partial \vec{m}_l(\vec{0})}{\partial \delta \beta_l(\vec{0})} \cdot \underline{\underline{N}}(\vec{R}, \vec{0}, l, k) \frac{\partial \vec{m}_k(\vec{0})}{\partial \delta \alpha_k(\vec{0})} \right] \quad (\vec{R}, l) \neq (\vec{0}, k). \end{aligned} \quad (56)$$

In the sum it is included the case in which $(\vec{R}', k') = (\vec{0}, k)$ that is generated from the derivative of the second term in the expression of the first derivative given above. Now it is possible to calculate the terms that enter into the system of (50), starting with the one corresponding to $l = k$

$$\begin{aligned} \sum_{\vec{R}} e^{i\vec{K} \cdot \vec{R}} E_{\alpha_{k0} \beta_{l\vec{R}}} &= \sum_{\vec{R}} e^{i\vec{K} \cdot \vec{R}} E_{\alpha_{k0} \beta_{k\vec{R}}} \\ &= \mu_0 M_s^2 \left[\sum_{\vec{R}', k'} \vec{m}_{k'}(\vec{0}) \cdot \underline{\underline{N}}(\vec{R}', \vec{0}, k', k) \right. \\ &\quad \times \frac{\partial^2 \vec{m}_k(\vec{0})}{\partial \delta \alpha_k(\vec{0}) \partial \delta \beta_k(\vec{0})} + \frac{\partial \vec{m}_k(\vec{0})}{\partial \delta \beta_k(\vec{0})} \\ &\quad \left. \cdot \underline{\underline{N}}(\vec{0}, \vec{0}, k, k) \frac{\partial \vec{m}_k(\vec{0})}{\partial \delta \alpha_k(\vec{0})} \right] \\ &\quad + \mu_0 M_s^2 \sum_{\vec{R} \neq \vec{0}} e^{i\vec{K} \cdot \vec{R}} \frac{\partial \vec{m}_k(\vec{0})}{\partial \delta \beta_k(\vec{0})} \\ &\quad \cdot \underline{\underline{N}}(\vec{R}, \vec{0}, k, k) \frac{\partial \vec{m}_k(\vec{0})}{\partial \delta \alpha_k(\vec{0})} \\ &= \mu_0 M_s^2 \sum_{\vec{R}} \left[\sum_{k'} \vec{m}_{k'}(\vec{0}) \cdot \underline{\underline{N}}(\vec{R}, \vec{0}, k', k) \right. \\ &\quad \times \frac{\partial^2 \vec{m}_k(\vec{0})}{\partial \delta \alpha_k(\vec{0}) \partial \delta \beta_k(\vec{0})} \end{aligned}$$

$$\begin{aligned}
& + e^{i\vec{k} \cdot \vec{R}} \frac{\partial \vec{m}_k(\vec{0})}{\partial \delta \beta_k(\vec{0})} \\
& \cdot \underline{N}(\vec{R}, \vec{0}, k, k) \frac{\partial \vec{m}_k(\vec{0})}{\partial \delta \alpha_k(\vec{0})} \Big].
\end{aligned} \quad (57a)$$

Equation (57a) is obtained by taking into account (46), by including the term corresponding to $\vec{R} = 0$ into the sum performed over $\vec{R} \neq 0$ and by considering that both the static magnetization and the dynamic magnetization do not depend on \vec{R} . Indeed, second derivatives are calculated at equilibrium and the exponential $e^{i\vec{k} \cdot \vec{R}}$ appears on both the numerator and the denominator of the derivative.

When $l \neq k$, the term turns out to be

$$\begin{aligned}
& \sum_{\vec{R}} e^{i\vec{k} \cdot \vec{R}} E_{\alpha_{k0}\beta_{l\vec{R}}} \\
& = \mu_0 M_s^2 \left[\sum_{\vec{R}} e^{i\vec{k} \cdot \vec{R}} \frac{\partial \vec{m}_l(\vec{0})}{\partial \delta \beta_l(\vec{0})} \cdot \underline{N}(\vec{R}, \vec{0}, l, k) \frac{\partial \vec{m}_k(\vec{0})}{\partial \delta \alpha_k(\vec{0})} \right].
\end{aligned} \quad (57b)$$

Due to the properties of the demagnetizing tensor, the symmetry

$$\sum_{\vec{R}'} e^{i\vec{k} \cdot \vec{R}'} E_{\alpha_{k0}\beta_{l\vec{R}'}} = \sum_{\vec{R}'} e^{i\vec{k} \cdot \vec{R}'} E_{\alpha_{l0}\beta_{k\vec{R}'}} \quad (58)$$

is fulfilled when $l = k$, but it is not fulfilled when $l \neq k$.

The formalism previously developed for interacting particles can be extended to a system of 2D antidots (ADs). In this case, it is necessary to add the exchange interaction between primitive cells [21]. In extended magnetic system like AD arrays, in addition to the usual nearest-neighbours exchange interaction between micromagnetic cells, the exchange contribution across the nearest-neighbours micromagnetic cells belonging to adjacent surface primitive cells must be taken into account. Hence, we recall the exchange energy density of (6)

$$E_{\text{exch}} = A \sum_k \sum_n \frac{(1 - \vec{m}_k \cdot \vec{m}_n)}{a_{kn}^2}. \quad (59)$$

Here, the first sum runs over all the micromagnetic cells of the primitive cell and the second sum runs over the nearest neighbours of the k th micromagnetic cell. When the k th micromagnetic cell is on one of the edges (vertices) of the given primitive cell, the interaction with one (two) micromagnetic cell(s) belonging to the correct nearest primitive cell must be added.

3. LDMM

This section is devoted to the review of the LDMM approach through which we derive the generalized Lagrange equation

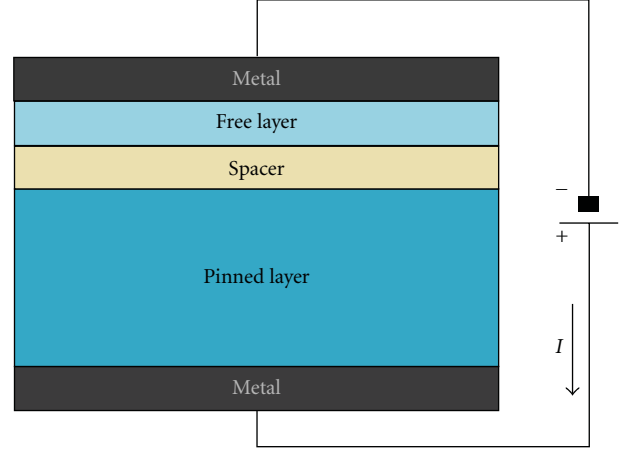


FIGURE 2: A schematic of a spin-valve nanopillar device.

in the presence of two dissipative effects arising from the “positive” intrinsic damping and the “negative” one induced by the current-driven spin-transfer torque [22]. As for the Hamiltonian approach, we limit our study to the dynamics taking place in the linear and autonomous regime.

3.1. Description of the Magnetic System and Equation of Motion. The magnetic systems in which such competing phenomena take place are generally referred to as spin-valve nanopillars. These are heterostructures composed by two ferromagnetic layers, having generally different thicknesses, separated by a nonmagnetic (metallic or insulating) spacer, which is used to decouple the exchange interactions between them. The thinner magnetic layer is generally referred to as “Free Layer” (FL), whereas the thicker one is called “Fixed Layer” or “Pinned Layer” (PL). By means of an external voltage source and metallic contacts applied at the top and bottom of the structure, a current flow traverses the structure along the normal-to-plane direction (see Figure 2).

In this kind of device, conservative effects arise from the previously mentioned classical micromagnetic contributions (exchange, demagnetizing, magnetocrystalline anisotropy, and Zeeman fields) together with the Ampere (or Oersted) field due to the current flow. This latter contribution, however, will be neglected for simplicity. In fact, the main goal of this section is to describe why and how a Lagrangian approach needs to be taken into account when nonconservative forces act in the system. The inclusion of more sophisticated effects, such as the Ampere field, will become relevant when this approach will be further generalized to describe the dynamics occurring in the nonlinear regime of spin-wave generation.

Let us now briefly recall the governing equation of motion. When no dissipative contributions are taken into account, a persistent precessional motion of the magnetization vector \vec{M} takes place. It is described by classical Landau-Lifshitz equation $\dot{\vec{M}} = \gamma(\vec{H}_{\text{eff}} \times \vec{M})$, where \vec{H}_{eff} is the effective field which accounts for all the above-mentioned contributions.

On the other hand, nonconservative contributions arise from the material intrinsic dissipation and the spin-transfer torque induced by the current flow [26]. The former accounts for the phenomenologically introduced intrinsic Gilbert dissipation [27], the phenomenon by which the precessional motion of \vec{M} , excited by a given stimulus, relaxes towards its equilibrium state. The relaxation rate is proportional to a scalar quantity, called Gilbert constant α . The torque exerted on the magnetization is generally represented by $\vec{T}_{\text{ID}} = (\alpha/M_S)(\vec{M} \times \dot{\vec{M}})$.

Concerning the dissipative effects induced by the current flow, it has been extensively shown that this bias current can become spin-polarized in the direction of the magnetization vector of the thicker magnetic layer and can then transfer this induced spin angular momentum to the magnetization of the thinner magnetic layer. For a proper direction of the bias current I , this spin-transfer mechanism creates a torque which opposes to that induced by the Gilbert damping, creating an effective negative damping. The corresponding spin-transfer torque, derived by Slonczewski [28], can be expressed as $\vec{T}_{\text{ST}} = (\sigma I/M_S)[\vec{M} \times (\vec{M} \times \vec{p})]$, where the unit vector \vec{p} defines the direction of the spin polarization (in turn defined by the magnetization vector of the PL) and the constant σ modulates the strength of the spin-torque effect. It is equal to $\sigma = \varepsilon g_0 \mu_B / 2e M_S d$, where ε is the spin-torque efficiency (defined in [29]), g_0 is the Landé factor, μ_B is the Bohr magneton, e is the absolute value of the electronic charge, d is the thickness of the magnetic layer, and S is the current-carrying area [30].

It should be mentioned that, because of the larger value of both saturation magnetization and thickness, the PL is not substantially affected by any current-driven magnetization dynamics, so that it is generally treated as it were fixed (or pinned) along its equilibrium direction. On the contrary, the FL's properties allow it to describe more easily several kinds of dynamics (e.g., switching [31], precession [32], domain-wall motion [33], gyrotropic motion of vortex state [34]), as it were “free” to move.

Under these circumstances, the magnetization dynamics of the FL is governed by the Landau-Lifshitz-Gilbert-Slonczewski (LLGS) equation

$$\dot{\vec{M}} = \gamma(\vec{H}_{\text{eff}} \times \vec{M}) + \frac{\alpha}{M_S}(\vec{M} \times \dot{\vec{M}}) + \frac{\sigma I}{M_S}[\vec{M} \times (\vec{M} \times \vec{p})]. \quad (60)$$

It has to be remarked that the equality (with opposite sign) of the two torques ($\vec{T}_{\text{ID}} = -\vec{T}_{\text{ST}}$), achievable by means of a proper intensity and sign of current (the positive one, $I > 0$, which corresponds to a current flow moving from the PL to the FL), which in turn implies the fully compensation of the two dissipation mechanisms, yields the system in an out-of-equilibrium zero-dissipation stationary state (a *limit cycle*, using the notation of dynamic systems) (see Figure 3). In such a regime, the excitation of microwave spin waves becomes physically conceivable.

To derive the mathematical formulation of the LDMM, for the sake of simplicity, we write, first, the generalized Lagrange equation for the case of an isolated magnetic

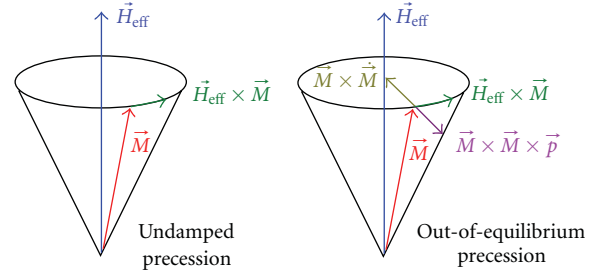


FIGURE 3: Schematic representation of undamped (in the absence of both Gilbert and current-induced damping) and out-of-equilibrium (in the presence of both Gilbert and current-induced damping) precessions. In this latter case, a limit cycle is described as well since the torques due to the intrinsic dissipation and the spin-transfer-induced one (for a proper intensity and direction of the current) balance each other.

particle within the macrospin approximation. After that, we will generalize this approach for the case of an isolated particle composed by N interacting momenta.

3.1.1. LDMM for a Macrospin System. We will preliminarily assume that the dynamics of the magnetization vector could be described through three degrees of freedom (θ, ϕ, ψ), as shown in Figure 1. In such a framework the generalized Lagrange equations read

$$\begin{aligned} \frac{d}{dt} \left(\frac{\partial L}{\partial \dot{\phi}} \right) - \frac{\partial L}{\partial \phi} + \frac{\partial \mathfrak{I}_{\text{ST}}}{\partial \dot{\phi}} + \frac{\partial \mathfrak{I}_{\text{ID}}}{\partial \dot{\phi}} &= 0, \\ \frac{d}{dt} \left(\frac{\partial L}{\partial \dot{\theta}} \right) - \frac{\partial L}{\partial \theta} + \frac{\partial \mathfrak{I}_{\text{ST}}}{\partial \dot{\theta}} + \frac{\partial \mathfrak{I}_{\text{ID}}}{\partial \dot{\theta}} &= 0, \\ \frac{d}{dt} \left(\frac{\partial L}{\partial \dot{\psi}} \right) - \frac{\partial L}{\partial \psi} + \frac{\partial \mathfrak{I}_{\text{ST}}}{\partial \dot{\psi}} + \frac{\partial \mathfrak{I}_{\text{ID}}}{\partial \dot{\psi}} &= 0, \end{aligned} \quad (61)$$

where $L = T + U$ represents the Lagrangian of the system given by the sum of the kinetic energy T and the potential U , whereas \mathfrak{I}_{ST} and \mathfrak{I}_{ID} are the dissipation functions related to the spin torque and the intrinsic damping, respectively.

Taking advantage of the explicit formulations of the energy contributions given in Section 2.1, we can rewrite the previous system by accounting for the relationship among the potential, the kinetic energy, and the conservative part $\tilde{E} = T - U$ of the total mechanical energy (which in the conservative limit coincides with the Hamiltonian of the system \mathcal{H} in the presence of fixed constraints). By substituting L with $2T - \tilde{E}$, we thus obtain

$$\begin{aligned} 2 \frac{d}{dt} \left(\frac{\partial T}{\partial \dot{\phi}} \right) - \frac{d}{dt} \left(\frac{\partial \tilde{E}}{\partial \dot{\phi}} \right) - 2 \frac{\partial T}{\partial \phi} + \frac{\partial \tilde{E}}{\partial \phi} + \frac{\partial \mathfrak{I}_{\text{ST}}}{\partial \dot{\phi}} + \frac{\partial \mathfrak{I}_{\text{ID}}}{\partial \dot{\phi}} &= 0, \\ 2 \frac{d}{dt} \left(\frac{\partial T}{\partial \dot{\theta}} \right) - \frac{d}{dt} \left(\frac{\partial \tilde{E}}{\partial \dot{\theta}} \right) - 2 \frac{\partial T}{\partial \theta} + \frac{\partial \tilde{E}}{\partial \theta} + \frac{\partial \mathfrak{I}_{\text{ST}}}{\partial \dot{\theta}} + \frac{\partial \mathfrak{I}_{\text{ID}}}{\partial \dot{\theta}} &= 0, \\ 2 \frac{d}{dt} \left(\frac{\partial T}{\partial \dot{\psi}} \right) - \frac{d}{dt} \left(\frac{\partial \tilde{E}}{\partial \dot{\psi}} \right) - 2 \frac{\partial T}{\partial \psi} + \frac{\partial \tilde{E}}{\partial \psi} + \frac{\partial \mathfrak{I}_{\text{ST}}}{\partial \dot{\psi}} + \frac{\partial \mathfrak{I}_{\text{ID}}}{\partial \dot{\psi}} &= 0. \end{aligned} \quad (62)$$

To solve the proposed problem, we need thus to explicitly find the expressions of the variables T , \tilde{E} , \mathfrak{I}_{ID} and \mathfrak{I}_{ST} , shown in (62), in Lagrangian coordinates.

The kinetic energy T associated to the precessional motion of the magnetization vector can be computed by referring to the case of a rigid body with a fixed point Ω (see Figure 1). In this case, the rotational kinetic energy density is expressed as

$$T = \frac{1}{2} \vec{l}_\Omega \cdot \vec{\omega}, \quad (63)$$

where \vec{l}_Ω is the angular momentum and $\vec{\omega}$ is the angular velocity vector. Notice that in the following the kinetic energy T , the dissipation functions \mathfrak{I}_{ID} and \mathfrak{I}_{ST} , the work dw , and the energy losses dw/dt are referred to their corresponding quantities per unit volume. In addition, we recall the definition of the energy density $E = \tilde{E}/V$ given in Section 2.1. By virtue of the relationship between angular momentum \vec{l}_Ω and magnetic dipole momentum $\vec{\mu}$ ($\vec{l}_\Omega = (1/\gamma)\vec{\mu}$), and considering that this latter is directed along \vec{e}_3 (see Figure 1), the previous scalar product involves, in turn, the only component of \vec{l}_Ω along \vec{e}_3 . It leads to

$$T = \frac{1}{2} \frac{M_S}{\gamma} (\dot{\phi} \cos \theta + \dot{\psi}). \quad (64)$$

Equation (64) therefore represents the rotational kinetic energy $T = T(\theta, \phi, \psi)$ expressed in Lagrangian coordinates with $M_S = \mu/V$. The conservative part E of the energy density accounts for all the standard micromagnetic contributions discussed previously. As shown in Section 2.1, all the contributions appearing in E only depend on the Lagrangian variables θ, ϕ , but not on their derivatives, namely, $E = E(\theta, \phi)$.

To derive the Lagrangian formulation of the dissipative contributions, let us start from the classical definition of the work dw carried out by a magnetic system subject to a nonconservative force. As it is known, such a force has to be derived from the gradient of a dissipation function \mathfrak{I} and the rate of energy losses associated to a dissipative torque can be thus expressed as

$$\frac{dw}{dt} = \pm \dot{\vec{M}} \cdot \frac{\partial \mathfrak{I}}{\partial \dot{\vec{M}}}, \quad (65)$$

where the plus (minus) sign accounts for torques which act as “drain” (“source”) of energy and refers to the case $\mathfrak{I} = \mathfrak{I}_{\text{ID}}$ ($\mathfrak{I} = \mathfrak{I}_{\text{ST}}$).

So, by multiplying the LLGS equation (60) by \vec{H}_{eff} and assuming that the energy losses rates are small compared to the conservative (precessional) part, namely, $\dot{\vec{M}} \simeq -\gamma\mu_0(\vec{M} \times \vec{H}_{\text{eff}})$, we deduce the following expressions for the dissipative function densities

$$\mathfrak{I}_{\text{ID}} = \frac{\alpha}{2\gamma M_0} \dot{\vec{M}}^2, \quad (66)$$

$$\mathfrak{I}_{\text{ST}} = \frac{\sigma J}{\gamma M_0} \vec{p} \cdot (\vec{M} \times \dot{\vec{M}}). \quad (67)$$

It should be noticed that (66), which appears in the usual form of a Rayleigh-like dissipation function, is a positive-definite form, as expected for a power dissipated through a viscous friction mechanism, whatever the magnetization configuration (α , γ , and M_S are positive constants). On the other hand, the spin-torque dissipation function of (67) is a non-Rayleigh one and strongly depends, apart from the direction of the current flow J , on the relative magnetization configuration of the ferromagnetic layers (\vec{M} and \vec{p}).

Finally, taking into account the expression of the time-independent unit vector $\vec{p} = (\sin \Theta_{\text{PL}} \cos \Phi_{\text{PL}}, \sin \Theta_{\text{PL}} \sin \Phi_{\text{PL}}, \cos \Theta_{\text{PL}})$, the explicit expressions of the dissipative functions densities are

$$\mathfrak{I}_{\text{ID}} = \frac{\alpha M_S}{2\gamma} (\dot{\theta}^2 + \dot{\phi}^2 \sin^2 \theta) = \mathfrak{I}_{\text{ID}}(\theta, \phi), \quad (68)$$

$$\mathfrak{I}_{\text{ST}} = \frac{\sigma J M_S}{\gamma} [f_1(\phi) \dot{\theta} + f_2(\theta, \phi) \dot{\phi}] = \mathfrak{I}_{\text{ST}}(\theta, \phi),$$

where

$$f_1(\phi) = \sin \Theta_{\text{PL}} \sin(\Phi_{\text{PL}} - \phi), \quad (69)$$

$$f_2(\theta, \phi) = \sin^2 \theta \cos \Theta_{\text{PL}} - \cos \theta \sin \theta \sin \Theta_{\text{PL}} \cos(\Phi_{\text{PL}} - \phi). \quad (70)$$

We proceed by evaluating first the third Lagrange equation

$$2 \frac{d}{dt} \left(\frac{\partial T}{\partial \dot{\psi}} \right) - \frac{d}{dt} \left(\frac{\partial E}{\partial \dot{\psi}} \right) - 2 \frac{\partial T}{\partial \psi} + \frac{\partial E}{\partial \psi} + \frac{\partial \mathfrak{I}_{\text{ST}}}{\partial \dot{\psi}} + \frac{\partial \mathfrak{I}_{\text{ID}}}{\partial \dot{\psi}} = 0. \quad (71)$$

In (71), we notice that the kinetic energy is the only term dependent on the intrinsic rotation, and, in particular, on its velocity $\dot{\psi}$, so that the previous equation reduces to

$$2 \frac{d}{dt} \left(\frac{\partial T}{\partial \dot{\psi}} \right) = 0, \quad (72)$$

which stands for a first integral of motion representing the conservation of the (only component of the) angular momentum

$$2 \frac{\partial T}{\partial \dot{\psi}} = \frac{M_S}{\gamma} = \text{constant} \equiv \vec{l}_\Omega \cdot \vec{e}_3. \quad (73)$$

Such a first integral also points out that our system can be described through only two degrees of freedom, as expected for the characterization of the dynamics of a vector having constant modulus which undergoes a precession (with a fixed point) onto a sphere. Taking into account this result, in the following we will use the parameters θ, ϕ .

The first two Lagrange equations read

$$2 \frac{d}{dt} \left(\frac{\partial T}{\partial \dot{\phi}} \right) - \frac{d}{dt} \left(\frac{\partial E}{\partial \dot{\phi}} \right) - 2 \frac{\partial T}{\partial \phi} + \frac{\partial E}{\partial \phi} + \frac{\partial \mathfrak{I}_{\text{ST}}}{\partial \dot{\phi}} + \frac{\partial \mathfrak{I}_{\text{ID}}}{\partial \dot{\phi}} = 0,$$

$$2 \frac{d}{dt} \left(\frac{\partial T}{\partial \dot{\theta}} \right) - \frac{d}{dt} \left(\frac{\partial E}{\partial \dot{\theta}} \right) - 2 \frac{\partial T}{\partial \theta} + \frac{\partial E}{\partial \theta} + \frac{\partial \mathfrak{I}_{\text{ST}}}{\partial \dot{\theta}} + \frac{\partial \mathfrak{I}_{\text{ID}}}{\partial \dot{\theta}} = 0, \quad (74)$$

which, substituting the corresponding expressions (the conservative part E of the total energy density will be discussed later on in the text), become

$$\begin{aligned} -\frac{M_s}{\gamma} \sin \theta \dot{\theta} + \frac{\partial E}{\partial \phi} + \frac{\sigma J M_s}{\gamma} f_2 + \frac{\alpha M_s}{\gamma} \dot{\phi} \sin^2 \theta &= 0, \\ \frac{M_s}{\gamma} \dot{\phi} \sin \theta + \frac{\partial E}{\partial \theta} + \frac{\sigma J M_s}{\gamma} f_1 + \frac{\alpha M_s}{\gamma} \dot{\theta} &= 0. \end{aligned} \quad (75)$$

Since in the present LDMM approach we are interested in the characterization of the linear dynamics of these magnetic current-driven auto-oscillatory systems, we adopt the classical formalism of small oscillations. By following this procedure, we linearize the system of (75) by considering small perturbations $(\delta\theta, \delta\phi)$ around the equilibrium configuration of the FL (Θ, Φ) , as done in (2), and expand the energy terms in Taylor series up to the second perturbative order.

By means of such a formalism, the system given in (75) leads to the set of generalized Lagrange equations

$$\begin{aligned} -\frac{M_s}{\gamma} \sin \Theta \delta\dot{\theta} + \frac{\partial E}{\partial \delta\phi} + \frac{\sigma J M_s}{\gamma} \\ \times [\chi(\Theta, \Phi) \delta\theta + \eta(\Theta, \Phi) \delta\phi + \nu(\Theta, \Phi)] \\ + \frac{\alpha M_s}{\gamma} \delta\dot{\phi} \sin^2 \Theta = 0, \\ \frac{M_s}{\gamma} \delta\dot{\phi} \sin \Theta + \frac{\partial E}{\partial \delta\theta} + \frac{\sigma J M_s}{\gamma} [\zeta(\Theta, \Phi) \delta\phi + \beta(\Theta, \Phi)] \\ + \frac{\alpha M_s}{\gamma} \delta\dot{\theta} = 0, \end{aligned} \quad (76)$$

where

$$\begin{aligned} \chi(\Theta, \Phi) &= \sin 2\Theta \cos \Theta_{\text{PL}} - \cos 2\Theta \sin \Theta_{\text{PL}} \cos(\Phi_{\text{PL}} - \Phi), \\ \eta(\Theta, \Phi) &= \cos \Theta \sin \Theta \sin \Theta_{\text{PL}} \sin(\Phi - \Phi_{\text{PL}}), \\ \nu(\Theta, \Phi) &= \sin \Theta (\sin \Theta \cos \Theta_{\text{PL}} - \cos \Theta \sin \Theta_{\text{PL}} \cos(\Phi_{\text{PL}} - \Phi)), \\ \zeta(\Theta, \Phi) &= -\sin \Theta_{\text{PL}} \cos(\Phi_{\text{PL}} - \Phi), \\ \beta(\Theta, \Phi) &= \sin \Theta_{\text{PL}} \sin(\Phi_{\text{PL}} - \Phi). \end{aligned} \quad (77)$$

Furthermore, by developing also the energy density E in Taylor series around the equilibrium state in analogy with what was done in (24) for HDMM, we notice that only the second derivatives appear in the equation. Indeed, the inessential constant term can be neglected and the first derivatives vanish at equilibrium. Moreover, considering that the new Lagrangian variables $(\delta\theta, \delta\phi)$ have to exhibit a time dependence proportional to $\exp(i\omega t)$ (being $\omega/2\pi$

the frequency of the spin-wave eigenmode), we end up with

$$\begin{aligned} \delta\phi \left[E_{\phi\phi} + \frac{\sigma J M_s}{\gamma} \eta \right] + \delta\theta \left[E_{\phi\theta} + \frac{\sigma J M_s}{\gamma} \chi \right] \\ = \delta\phi \left[-i\omega \frac{\alpha M_s}{\gamma} \sin^2 \Theta \right] + \delta\theta \left[i\omega \frac{M_s}{\gamma} \sin \Theta \right], \\ \delta\phi \left[E_{\theta\phi} + \frac{\sigma J M_s}{\gamma} \zeta \right] + \delta\theta [E_{\theta\theta}] \\ = \delta\phi \left[-i\omega \frac{M_s}{\gamma} \sin \Theta \right] + \delta\theta \left[-i\omega \frac{\alpha M_s}{\gamma} \right], \end{aligned} \quad (78)$$

where the subscripts stand for partial derivative with respect to the indicated variables, whose explicit expressions can be found in the Section 2.1. The terms involving $\beta(\Theta, \Phi)$ and $\nu(\Theta, \Phi)$ have been disregarded since they do not exhibit an explicit time dependence.

By setting $\lambda = \gamma/M_s \omega$ and $\tilde{\sigma} = \sigma M_s/\gamma$, (78) can be recast in the form of a complex generalized non-Hermitian eigenvalue problem

$$\underline{\underline{A}} \vec{v} = \lambda \underline{\underline{B}} \vec{v}, \quad (79)$$

with

$$\begin{aligned} \underline{\underline{A}} &= \begin{bmatrix} -i\alpha \sin^2 \Theta & i \sin \Theta \\ -i \sin \Theta & -i\alpha \end{bmatrix}, \\ \underline{\underline{B}} &= \begin{bmatrix} E_{\phi\phi} + \tilde{\sigma} J \eta & E_{\phi\theta} + \tilde{\sigma} J \chi \\ E_{\theta\phi} + \tilde{\sigma} J \zeta & E_{\theta\theta} \end{bmatrix}, \\ \vec{v} &= [\delta\phi, \delta\theta]^T. \end{aligned} \quad (80)$$

As expected, if no damping and current are taken into account ($\alpha = 0, J = 0$ A/m²), the system in (79) so obtained recovers exactly the fully conservative HDMM one, where the matrix $\underline{\underline{A}}$ is Hermitian, whereas the matrix $\underline{\underline{B}}$ is real and symmetric (see (40)), and all the corresponding eigenvalues are real.

In the presence of dissipative effects due to damping and spin torque, the symmetry of the problem is strongly reduced and the corresponding eigenvalues will be, in general, complex quantities: the real part represents the mode frequency, whereas the imaginary part defines the mode decay rate. With this information in hands, it will be possible to establish, after a single iteration, the subset of the spin-wave normal modes which becomes unstable after the application of a spin-polarized current. In detail, for any applied current below the excitation threshold, the imaginary parts of all eigenvalues have to be positive, recalling the behavior of a damped oscillator. On the contrary, for current values above the excitation threshold, the imaginary parts of the activated normal modes switch to a negative value, giving rise to the instability mechanism which determines, in the time domain, the growth of the precession cone and, in turn, the change of the generated frequency.

Finally, it should be mentioned that, unlike HDMM, LDMM cannot be recast in a nongeneralized eigenvalue problem form.

3.1.2. LDMM for an Isolated System Composed by N Interacting Magnetic Momenta. Let us consider now the magnetic system of our micromagnetic calculations composed by a finite number N of interacting magnetic momenta. Within our nanoscale numerical approach, each magnetic momentum is identified by means of a micromagnetic cell. The generalization of (78) to N cells ($k = 1, \dots, N$) leads to a system of $2N$ scalar and linear equations as follows:

$$\begin{aligned} & \lambda \left\{ \sum_{l=1}^N [E_{\phi_k \phi_l} \delta \phi_l + E_{\phi_k \theta_l} \delta \theta_l] + \delta \theta_k [\tilde{\sigma} J \chi_k] + \delta \phi_k [\tilde{\sigma} J \eta_k] \right\} \\ &= \delta \phi_k [-i\alpha \sin^2 \Theta_k] + \delta \theta_k [i \sin \Theta_k], \\ & \lambda \left\{ \sum_{l=1}^N [E_{\theta_k \phi_l} \delta \phi_l + E_{\theta_k \theta_l} \delta \theta_l] + \delta \phi_k [\tilde{\sigma} J \zeta_k] \right\} \\ &= \delta \phi_k [-i \sin \Theta_k] + \delta \theta_k [-i\alpha]. \end{aligned} \quad (81)$$

The system in (81) can be analogously formulated as a complex generalized non-Hermitian eigenvalue problem (in the same form as (79)), where

$$\begin{aligned} \underline{\underline{A}} &= \begin{bmatrix} -i\alpha \sin^2 \Theta_1 & i \sin \Theta_1 & 0 & 0 & \dots \\ -i \sin \Theta_1 & -i\alpha & 0 & 0 & \dots \\ 0 & 0 & -i\alpha \sin^2 \Theta_2 & i \sin \Theta_2 & \dots \\ 0 & 0 & -i \sin \Theta_2 & -i\alpha & \dots \\ \dots & \dots & \dots & \dots & \dots \end{bmatrix}, \\ \underline{\underline{B}} &= \begin{bmatrix} E_{\phi_1 \phi_1} + \tilde{\sigma} J \eta_1 & E_{\phi_1 \theta_1} + \tilde{\sigma} J \chi_1 & E_{\phi_1 \phi_2} & E_{\phi_1 \theta_2} & \dots \\ E_{\theta_1 \phi_1} + \tilde{\sigma} J \zeta_1 & E_{\theta_1 \theta_1} & E_{\theta_1 \phi_2} & E_{\theta_1 \theta_2} & \dots \\ E_{\phi_2 \phi_1} & E_{\phi_2 \theta_1} & E_{\phi_2 \phi_2} + \tilde{\sigma} J \eta_2 & E_{\phi_2 \theta_2} + \tilde{\sigma} J \chi_2 & \dots \\ E_{\theta_2 \phi_1} & E_{\theta_2 \theta_1} & E_{\theta_2 \phi_2} + \tilde{\sigma} J \zeta_1 & E_{\theta_2 \theta_2} & \dots \\ \dots & \dots & \dots & \dots & \dots \end{bmatrix}, \\ \vec{v} &= [\delta \phi_1, \delta \theta_1, \delta \phi_2, \delta \theta_2, \dots, \delta \phi_N, \delta \theta_N]^T. \end{aligned} \quad (82)$$

It is also interesting to notice that both matrices $\underline{\underline{A}}$ and $\underline{\underline{B}}$ appearing in (80) and (82) admit a decomposition which allows to separate the conservative part from the nonconservative one

$$\begin{aligned} \underline{\underline{A}} &= \underline{\underline{A}}_c + \underline{\underline{A}}_{nc} \\ \underline{\underline{B}} &= \underline{\underline{B}}_c + \underline{\underline{B}}_{nc}, \end{aligned} \quad (83)$$

where

$$\begin{aligned} \underline{\underline{A}}_c &= \begin{bmatrix} 0 & i \sin \Theta_1 & 0 & 0 & \dots \\ -i \sin \Theta_1 & 0 & 0 & 0 & \dots \\ 0 & 0 & 0 & i \sin \Theta_1 & \dots \\ 0 & 0 & -i \sin \Theta_2 & 0 & \dots \\ \dots & \dots & \dots & \dots & \dots \end{bmatrix}, \\ \underline{\underline{A}}_{nc} &= \begin{bmatrix} -i\alpha \sin^2 \Theta_1 & 0 & 0 & 0 & \dots \\ 0 & -i\alpha & 0 & 0 & \dots \\ 0 & 0 & -i\alpha \sin^2 \Theta_2 & 0 & \dots \\ 0 & 0 & 0 & -i\alpha & \dots \\ \dots & \dots & \dots & \dots & \dots \end{bmatrix}, \\ \underline{\underline{B}}_c &= \begin{bmatrix} E_{\phi_1 \phi_1} & E_{\phi_1 \theta_1} & E_{\phi_1 \phi_2} & E_{\phi_1 \theta_2} & \dots \\ E_{\theta_1 \phi_1} & E_{\theta_1 \theta_1} & E_{\theta_1 \phi_2} & E_{\theta_1 \theta_2} & \dots \\ E_{\phi_2 \phi_1} & E_{\phi_2 \theta_1} & E_{\phi_2 \phi_2} & E_{\phi_2 \theta_2} & \dots \\ E_{\theta_2 \phi_1} & E_{\theta_2 \theta_1} & E_{\theta_2 \phi_2} & E_{\theta_2 \theta_2} & \dots \\ \dots & \dots & \dots & \dots & \dots \end{bmatrix}, \\ \underline{\underline{B}}_{nc} &= \begin{bmatrix} \tilde{\sigma} J \eta_1 & \tilde{\sigma} J \chi_1 & 0 & 0 & \dots \\ \tilde{\sigma} J \zeta_1 & 0 & 0 & 0 & \dots \\ 0 & 0 & \tilde{\sigma} J \eta_2 & \tilde{\sigma} J \chi_2 & \dots \\ 0 & 0 & \tilde{\sigma} J \zeta_1 & 0 & \dots \\ \dots & \dots & \dots & \dots & \dots \end{bmatrix}. \end{aligned} \quad (84)$$

The results of this approach have been successfully compared with those coming from another micromagnetic framework which integrates the LLGS equation in the time domain by using a finite-difference scheme [22, 23, 35]. In these works, we evaluated the accuracy of the LDMM approach in determining the excitation threshold and studied in detail the reorientational phase transition which takes place when the direction of the external magnetic field is varied.

Finally, we would like to mention that the extension of the LDMM approach to model the more realistic (and attractive) nonlinear and nonautonomous dynamics [30, 36–41] is currently under study.

Acknowledgments

The research leading to these results has received funding from the European Community's Seventh Framework Programme (FP7/2007–2013) under Grant agreement no. 228673 (MAGNONICS). The authors acknowledge the Project MAT2011-28532-C03-01 from Spanish government.

References

- [1] K. Y. Guslienko and A. N. Slavin, "Spin-waves in cylindrical magnetic dot arrays with in-plane magnetization," *Journal of Applied Physics*, vol. 87, no. 9, pp. 6337–6339, 2000.
- [2] B. A. Ivanov and C. E. Zaspel, "Magnon modes for thin circular vortex-state magnetic dots," *Applied Physics Letters*, vol. 81, no. 7, pp. 1261–1263, 2002.
- [3] C. E. Zaspel, B. A. Ivanov, J. P. Park, and P. A. Crowell, "Excitations in vortex-state permalloy dots," *Physical Review B*, vol. 72, no. 2, Article ID 024427, 2005.
- [4] R. Zivieri and F. Nizzoli, "Theory of spin modes in vortex-state ferromagnetic cylindrical dots," *Physical Review B*, vol. 71, no. 1, Article ID 014411, 2005.

- [5] R. Zivieri and F. Nizzoli, "Erratum: theory of spin modes in vortex-state ferromagnetic cylindrical dots," *Physical Review B*, vol. 74, no. 21, Article ID 219901, 2006.
- [6] B. A. Ivanov and C. E. Zaspel, "High frequency modes in vortex-state nanomagnets," *Physical Review Letters*, vol. 94, no. 2, Article ID 027205, 2005.
- [7] R. Zivieri and R. L. Stamps, "Theory of spin wave modes in tangentially magnetized thin cylindrical dots: a variational approach," *Physical Review B*, vol. 73, no. 14, Article ID 144422, 2006.
- [8] R. Zivieri, G. Santoro, and A. Franchini, "Localized spin modes in ferromagnetic cylindrical dots with in-plane magnetization," *Journal of Physics Condensed Matter*, vol. 19, no. 30, Article ID 305012, 2007.
- [9] R. Zivieri and F. Nizzoli, "Dipolar magnetic fields of spin excitations in vortex-state cylindrical ferromagnetic dots," *Physical Review B*, vol. 78, no. 6, Article ID 064418, 2008.
- [10] V. Novosad, M. Grimsditch, K. Y. Guslienko, P. Vavassori, Y. Otani, and S. D. Bader, "Spin excitations of magnetic vortices in ferromagnetic nanodots," *Physical Review B*, vol. 66, no. 5, Article ID 052407, pp. 524071–524074, 2002.
- [11] R. Zivieri and F. Nizzoli, "Spin excitations in vortex-state magnetic cylindrical dots: from nanometric to micrometric size," in *Electromagnetic, Magnetostatic, and Exchange-Interaction Vortices in Confined Magnetic Structures*, E.O. Kamenetskii, Ed., Transworld Research Network, Kerala, India, 2009.
- [12] "OOMMF user's guide," NIST, Gaithersburg, Md, USA.
- [13] "LLG micromagnetic simulator," llgmicro@mindsping.com.
- [14] F. Boust and N. Vukadinovic, "Micromagnetic simulations of vortex-state excitations in soft magnetic nanostructures," *Physical Review B*, vol. 70, no. 17, Article ID 172408, pp. 1–4, 2004.
- [15] M. Grimsditch, L. Giovannini, F. Montoncello, F. Nizzoli, G. K. Leaf, and H. G. Kaper, "Magnetic normal modes in ferromagnetic nanoparticles: a dynamical matrix approach," *Physical Review B*, vol. 70, no. 5, Article ID 054409, 7 pages, 2004.
- [16] L. Giovannini, F. Montoncello, and F. Nizzoli, "Effect of interdot coupling on spin-wave modes in nanoparticle arrays," *Physical Review B*, vol. 75, no. 2, Article ID 024416, 2007.
- [17] R. Zivieri, L. Giovannini, and F. Nizzoli, "Acoustical and optical spin modes of multilayers with ferromagnetic and antiferromagnetic coupling," *Physical Review B*, vol. 62, no. 22, pp. 14950–14955, 2000.
- [18] G. Gubbiotti, G. Carlotti, A. Montecchiari et al., "Brillouin light scattering study of ferromagnetically coupled Cu/Fe(110)/Cu/Fe(110)/Cu/Si(111) heterostructures: Bilinear exchange magnetic coupling," *Physical Review B*, vol. 62, no. 23, pp. 16109–16115, 2000.
- [19] R. Zivieri, F. Montoncello, L. Giovannini et al., "Effect of interdot separation on collective magnonic modes in Chains of rectangular dots," *IEEE Transactions on Magnetics*, vol. 47, no. 6, pp. 1563–1566, 2011.
- [20] S. Tacchi, F. Montoncello, M. Madami et al., "Band diagram of spin waves in a two-dimensional magnonic crystal," *Physical Review Letters*, vol. 107, no. 12, Article ID 127204, 2011.
- [21] R. Zivieri, S. Tacchi, F. Montoncello et al., "Bragg diffraction of spin waves from a two-dimensional antidot lattice," *Physical Review B*, vol. 85, no. 1, Article ID 012403, 2012.
- [22] G. Consolo, G. Gubbiotti, L. Giovannini, and R. Zivieri, "Lagrangian formulation of the linear autonomous magnetization dynamics in spin-torque auto-oscillators," *Applied Mathematics and Computation*, vol. 217, no. 21, pp. 8204–8215, 2011.
- [23] G. Consolo, L. Giovannini, and R. Zivieri, "Excitation of magnetic normal modes by spin-torque: a Lagrangian approach," *Journal of Applied Physics*, vol. 111, Article ID 07C916, 3 pages, 2012.
- [24] F. Montoncello and F. Nizzoli, "Application of the dynamical matrix approach to the investigation of spin excitations in nanometric dots," in *Magnetic Properties of Laterally Confined Nanometric Structures*, p. 131, Transworld Research Network, Kerala, India, 2006.
- [25] L. D. Landau and E. M. Lifshitz, "Theory of the dispersion of magnetic permeability in ferromagnetic bodies," *Physik. Z. Sowjetunion*, vol. 8, p. 153, 1935.
- [26] A. Slavin and V. Tiberkevich, "Nonlinear auto-oscillator theory of microwave generation by spin-polarized current," *IEEE Transactions on Magnetics*, vol. 45, no. 4, pp. 1875–1918, 2009.
- [27] T. L. Gilbert, "A phenomenological theory of damping in ferromagnetic materials," *IEEE Transactions on Magnetics*, vol. 40, no. 6, pp. 3443–3449, 2004.
- [28] J. C. Slonczewski, "Current-driven excitation of magnetic multilayers," *Journal of Magnetism and Magnetic Materials*, vol. 159, no. 1-2, pp. L1–L7, 1996.
- [29] J. C. Slonczewski, "Excitation of spin waves by an electric current," *Journal of Magnetism and Magnetic Materials*, vol. 195, no. 2, pp. L261–L268, 1999.
- [30] G. Consolo, B. Azzerboni, G. Gerhart, G. A. Melkov, V. Tiberkevich, and A. N. Slavin, "Excitation of self-localized spin-wave bullets by spin-polarized current in in-plane magnetized magnetic nanocontacts: a micromagnetic study," *Physical Review B*, vol. 76, no. 14, Article ID 144410, 2007.
- [31] G. Consolo, G. Finocchio, L. Torres, M. Carpentieri, L. Lopez-Diaz, and B. Azzerboni, "Spin-torque switching in Py/Cu/Py and Py/Cu/CoPt spin-valve nanopillars," *Journal of Magnetism and Magnetic Materials*, vol. 316, no. 2, pp. 492–495, 2007.
- [32] S. Bonetti, V. Tiberkevich, G. Consolo et al., "Experimental evidence of self-localized and propagating spin wave modes in obliquely magnetized current-driven nanocontacts," *Physical Review Letters*, vol. 105, no. 21, Article ID 217204, 2010.
- [33] G. Consolo, C. Currò, E. Martinez, and G. Valenti, "Mathematical modeling and numerical simulation of domain wall motion in magnetic nanostrips with crystallographic defects," *Applied Mathematical Modelling*, vol. 36, no. 10, pp. 4876–4886, 2012.
- [34] G. Consolo, L. Lopez-Diaz, L. Torres, G. Finocchio, A. Romeo, and B. Azzerboni, "Nanocontact spin-transfer oscillators based on perpendicular anisotropy in the free layer," *Applied Physics Letters*, vol. 91, no. 16, Article ID 162506, 2007.
- [35] A. Romeo, G. Finocchio, M. Carpentieri, L. Torres, G. Consolo, and B. Azzerboni, "A numerical solution of the magnetization reversal modeling in a permalloy thin film using fifth order Runge-Kutta method with adaptive step size control," *Physica B*, vol. 403, no. 2-3, pp. 464–468, 2008.
- [36] G. Finocchio, I. Krivorotov, M. Carpentieri et al., "Magnetization dynamics driven by the combined action of ac magnetic field and dc spin-polarized current," *Journal of Applied Physics*, vol. 99, no. 8, Article ID 08G507, 2006.
- [37] G. Consolo, L. Lopez-Diaz, L. Torres, G. Finocchio, A. Romeo, and B. Azzerboni, "Nanocontact spin-transfer oscillators based on perpendicular anisotropy in the free layer," *Applied Physics Letters*, vol. 91, no. 16, Article ID 162506, 2007.
- [38] Y. Zhou, V. Tiberkevich, G. Consolo et al., "Oscillatory transient regime in the forced dynamics of a nonlinear auto oscillator," *Physical Review B*, vol. 82, no. 1, Article ID 012408, 2010.

- [39] G. Consolo, V. Puliafito, G. Finocchio et al., “Combined frequency-amplitude nonlinear modulation: theory and applications,” *IEEE Transactions on Magnetics*, vol. 46, no. 9, pp. 3629–3634, 2010.
- [40] V. Puliafito, G. Consolo, L. Lopez-Diaz, and B. Azzerboni, “Micromagnetic analysis of nonlinear dynamics in spintronic analog modulators,” *IEEE Transactions on Magnetics*, vol. 45, no. 11, pp. 5239–5242, 2009.
- [41] G. Consolo and V. Puliafito, “Analytical and micromagnetic study of nonlinear amplitude modulation in spintronic modulators,” *IEEE Transactions on Magnetics*, vol. 46, no. 6, pp. 2063–2066, 2010.

Research Article

On the Formulation of the Exchange Field in the Landau-Lifshitz Equation for Spin-Wave Calculation in Magnonic Crystals

M. Krawczyk, M. L. Sokolovskyy, J. W. Klos, and S. Mamica

Department of Nanomaterials Physics, Faculty of Physics, Adam Mickiewicz University, Umultowska 85, 61-614 Poznań, Poland

Correspondence should be addressed to M. Krawczyk, krawczyk@amu.edu.pl

Received 17 February 2012; Revised 7 May 2012; Accepted 10 May 2012

Academic Editor: Roberto Zivieri

Copyright © 2012 M. Krawczyk et al. This is an open access article distributed under the Creative Commons Attribution License, which permits unrestricted use, distribution, and reproduction in any medium, provided the original work is properly cited.

The calculation of the magnonic spectra using the plane-wave method has limitations, the origin of which lies in the formulation of the effective magnetic field term in the equation of motion (the Landau-Lifshitz equation) for composite media. According to ideas of the plane-wave method the system dynamics is described in terms of plane waves (a superposition of a number of plane waves), which are continuous functions and propagate throughout the medium. Since in magnonic crystals the sought-for superposition of plane waves represents the dynamic magnetization, the magnetic boundary conditions on the interfaces between constituent materials should be inherent in the Landau-Lifshitz equations. In this paper we present the derivation of the two expressions for the exchange field known from the literature. We start from the Heisenberg model and use a linear approximation and take into account the spacial dependence of saturation magnetization and exchange constant present in magnetic composites. We discuss the magnetic boundary conditions included in the presented formulations of the exchange field and elucidate their effect on spin-wave modes and their spectra in one- and two-dimensional planar magnonic crystals from plane-wave calculations.

1. Introduction

For the first time the exchange effects were discovered independently by W. Heisenberg and P.A.M. Dirac in 1926. They proposed the energy operator (Hamiltonian) for the exchange interaction between two particles with spins \mathbf{S}_1 and \mathbf{S}_2 in the following form:

$$\mathcal{H}_{\text{ex}} = -2J_{12}\mathbf{S}_1 \cdot \mathbf{S}_2, \quad (1)$$

where J_{12} is the exchange integral. Because the exchange interaction is the fundamental one for magnetic materials than it is crucial for the calculations of the spin dynamics. An equation commonly used to describe the magnetization dynamics is the following Landau-Lifshitz (LL) equation:

$$\frac{\partial \mathbf{M}(\mathbf{r}, t)}{\partial t} = -\gamma\mu_0[\mathbf{M}(\mathbf{r}, t) \times (\mathbf{H}_{\text{ex}}(\mathbf{r}, t) + \dots)] + \dots, \quad (2)$$

where \mathbf{H}_{ex} is the exchange field acting on the magnetization vector \mathbf{M} . This equation is a macroscopic where all terms are in a form of continuous functions of a position vector \mathbf{r} .

The derivation of an exchange field in a uniform ferromagnetic material from the microscopic Heisenberg

Hamiltonian (1) can be found in many textbooks, for example, [1–5]. We will follow ideas presented in these books but for composite materials, that is, when the structure consists of two or more constituent ferromagnetics being in direct contact.

On the interface between two ferromagnetic materials, the boundary conditions (BCs) on dynamical component of the magnetization vector should be imposed. Such boundary conditions were proposed by Hoffman, then developed, and investigated by other authors [6–14]. From the LL equation together with the set of BCs, the spin-wave (SW) dispersion and profiles can be calculated. In many papers the calculation of the SW spectra in composite magnetic materials is based on the solution of the LL equation defined for a uniform material and then matched at the boundaries [7, 12, 13, 15–19]. In this paper we are interested in other method used to calculate the dispersion relation of the spin waves in magnetic composites with periodic distribution of constituent materials, and it is the plane-wave method (PWM). This method is widely used in calculations of the frequency spectra of an electromagnetic, elastic or electron waves propagating in a photonic crystal, phononic crystal or semiconductor

periodic heterostructures, respectively. In this method, described in details in Section 3, boundary conditions at interfaces between constituent materials should be inherently included into the equation of motion, that is, by properly defined exchange field.

Composites with a periodic arrangement of two (or more) different materials are extensively studied from many years. In the past, structures with periodicity in one dimension were investigated, these are multilayered structures which found many applications, for example, as a Bragg mirror or in GMR devices [20, 21]. Starting from 1987 and the discovery of photonic band gaps in photonic crystals [22, 23], the research was rapidly extended to other composites with periodicity in two and three dimensions. Among them there are phononic crystals, plasmonic crystals and also magnonic crystals (MCs) [24–30]. MCs can be regarded as magnetic analog of the photonic crystal, which uses the spin waves, instead of electromagnetic waves, to carry the information. MCs constitute one of the main building blocks of magnonic—promising direction of research focused on practical applications of spin waves [29–36]. For the development of magnonics, the computational methods have to be developed as well. The calculation of SW's dispersion in MCs can be performed with different methods, for example, with micromagnetic simulations or dynamical matrix method but because of their complexity the computations are very time consuming [37–42]. It is important to develop other analytical and semianalytical methods, like a PWM which even though approximate will allow for efficient calculation of the dispersion of SWs in MCs with big insight into physical processes.

Semiconductor periodic heterostructures (SHs) allow to tailor the electron and heat transport in nanoscale [43–45]. SHs are often described in effective mass approximation with the use of the envelope function instead of single electron functions. Effective mass equations derived from the Schrödinger equations are not unique, and many possible definitions of the kinetic energy operator were proposed. An extensive discussion about proper definition of the kinetic energy operator for the electron envelop function in SHs with position-dependent effective mass can be found in literature [46–58]. The calculation of the SW spectra in continuous model, that is, from the LL equation (2), undergoes similar difficulties, as we will show in this paper. However, this topic related to the calculations of the spin-wave dynamics in MCs is weakly presented in literature. In this paper we would like to fill this gap with a detailed consideration of different forms of the exchange field and then look at their consequences in the SW spectra of a MC calculated using the PWM.

In this study we will show in details the derivation from the microscopic model different forms of the exchange field used for SW calculations in MCs. Then we will analyze differences in SW spectra in one- (1D) and two-dimensional (2D) thin films of MCs calculated with PWM for three different expressions of the exchange field. We will discuss the boundary condition implemented in each formulation. The paper consists of five sections. In Section 2 we show the derivation of two forms of the exchange field from the

Heisenberg Hamiltonian in linear approximation for magnetic composites with pointing at surface terms neglected. Then in Section 3 we introduce the PWM method and derive a final algebraic eigenvalue equations for different definitions of the exchange field. In Section 4 we present the results of the PWM calculations of SW spectra for these different forms of the exchange field for MCs. We will consider 1D and 2D MC. The paper finished with Section 5 where conclusions of our investigation are drawn.

2. Expression of the Exchange Field in Inhomogeneous Media

We split the derivation of the expression of the exchange field in inhomogeneous materials into two steps. First, in Section 2.1 we obtain the formula for the exchange energy density from the microscopic Heisenberg Hamiltonian. Here the crucial step is a transformation from the discrete model to the continuous one. In the second step, Section 2.2 the formula for the exchange field will be derived from the exchange energy density. In this step a linear approximation will be introduced, and the space dependence of magnetic material parameters will be considered.

2.1. Exchange Energy Functional. We start our calculations from the Heisenberg Hamiltonian \mathcal{H}_l which defines exchange energy of the spin \mathbf{S}_l on the lattice point l as follows:

$$\mathcal{H}_l = -2 \sum_{m \in (\text{n.n.})} J_{lm} \mathbf{S}_l \cdot \mathbf{S}_m, \quad (3)$$

where \mathbf{S}_m is the total spin vector on lattice point m , and the summation is performed over all nearest neighbors (n.n.) of a l th spin. J_{lm} is an exchange integral between the spins located at l and m . When we introduce normalized unit vector $\boldsymbol{\alpha}_l$ for the spin vector \mathbf{S}_l

$$\boldsymbol{\alpha}_l = \frac{\mathbf{S}_l}{|\mathbf{S}_l|}, \quad (4)$$

then (3) will read

$$\mathcal{H}_l = -2|\mathbf{S}_l| \sum_{m \in (\text{n.n.})} J_{lm} |\mathbf{S}_m| \boldsymbol{\alpha}_l \cdot \boldsymbol{\alpha}_m. \quad (5)$$

According to the definition in (4), $\boldsymbol{\alpha}_l \cdot \boldsymbol{\alpha}_m = \cos \varphi$, where φ is an angle between spin vectors on lattice points l and m (see Figure 1).

Let us assume that the angle φ between the nearest spin vectors is small and moreover that the spin vectors are continuous and smooth functions of a position vector \mathbf{r} , that is, $\boldsymbol{\alpha} = \boldsymbol{\alpha}(\mathbf{r})$ [2]. Formally we can do it through averaging \mathbf{S} over the unit cell; that is, we introduce magnetization vector $\mathbf{M}(\mathbf{r})$ as follows:

$$\mathbf{M}(\mathbf{r}_l) = \bar{N} \mu_B g \mathbf{S}_l, \quad \text{where } \bar{N} = \frac{N}{V} \quad (6)$$

defines a number of spins (N) in the unit cell volume (V). μ_B is Bohr magneton, and g is a g factor (for free electrons $g \approx 2$). According to these definitions

$$\boldsymbol{\alpha}_l = \frac{\mathbf{S}_l}{|\mathbf{S}_l|} \equiv \frac{\mathbf{M}(\mathbf{r}_l)}{M(\mathbf{r}_l)} \quad (7)$$

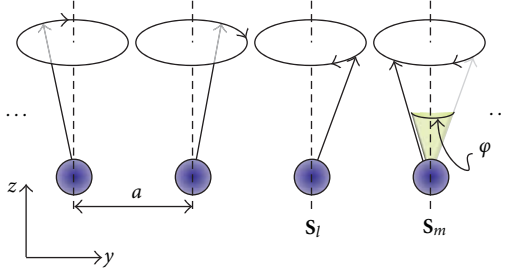


FIGURE 1: The discrete lattice of spins. The angle between neighboring spins: S_l and S_m is φ . We assume that φ and the spin deviation from the z axis are small.

and we can write $\alpha(\mathbf{r})$ as a continuous function of the position vector as follows:

$$\alpha(\mathbf{r}) = \frac{\mathbf{M}(\mathbf{r})}{M(\mathbf{r})}. \quad (8)$$

Having the continuous function of a position vector in hand, we can expand a unit vector α in a lattice point m ($\alpha(\mathbf{r}_m) \equiv \alpha_m \equiv \alpha'$) in the Taylor series:

$$\alpha' = \alpha_l + \sum_i (\partial_{x_i} \alpha_l) dx_i + \frac{1}{2} \sum_{i,j} (\partial_{x_i} \partial_{x_j} \alpha_l) dx_i dx_j + \dots, \quad (9)$$

where $x_i = x, y$ or z , and dx_i is the distance between nearest spins along x_i axis. ∂_{x_i} is an abbreviation of the partial derivative with respect to the Cartesian x_i component. After limiting expansion up to the quadratic terms (it means that we assumed a small variation of $\alpha(\mathbf{r})$ in space) we can substitute this into (5) as follows:

$$\begin{aligned} \mathcal{H}_l = & -2|S_l| \sum_{m \in (\text{n.n.})} J_{lm} |S_m| \\ & - 2|S_l| \sum_{m \in (\text{n.n.})} J_{lm} |S_m| \sum_i \alpha_l \cdot (\partial_{x_i} \alpha_l) dx_i \\ & - |S_l| \sum_{m \in (\text{n.n.})} J_{lm} |S_m| \sum_{i,j} \alpha_l \cdot (\partial_{x_i} \partial_{x_j} \alpha_l) dx_i dx_j. \end{aligned} \quad (10)$$

The second term on the right side is equal to zero because α is a unit vector, and the only possibility to change it is a rotation: unit vectors α_l fulfill obvious relation: $\alpha_l \cdot \alpha_l = 1$. Differentiate this equation with respect to x_i results in the following:

$$(\partial_{x_i} \alpha_l) \cdot \alpha_l = 0. \quad (11)$$

It means that $\partial_{x_i} \alpha$ is zero or is orthogonal to the vector α (i.e., $\alpha_l \cdot (\partial_{x_i} \alpha_l) \equiv 0$, see (11)). The Hamiltonian can be now rewritten as follows:

$$\begin{aligned} \mathcal{H}_l = & -2|S_l| \sum_{m \in (\text{n.n.})} J_{lm} |S_m| \\ & - |S_l| \sum_{m \in (\text{n.n.})} J_{lm} |S_m| \sum_{i,j} \alpha_l \cdot (\partial_{x_i} \partial_{x_j} \alpha_l) dx_i dx_j. \end{aligned} \quad (12)$$

For a homogeneous material the length of the spins is preserved, $|S_l| = |S_m|$ in each lattice point, and the exchange integral is constant, that is, $J_{lm} = J$ for each n.n. l and m ($l \neq m$), (this assumption is valid for inhomogeneous material when two atomic planes (for n.n. exchange interactions) at the interfaces are removed from consideration.) With this homogenization, we obtain from (12) the following expression:

$$\mathcal{H}_l = -2Z|S|^2 J - |S|^2 J \sum_{m \in (\text{n.n.})} \sum_{i,j} \alpha_l \cdot (\partial_{x_i} \partial_{x_j} \alpha_l) dx_i dx_j, \quad (13)$$

where Z is a number of the nearest neighbors. For crystals with cubic crystallographic structures (i.e., for simple cubic (sc), body-centered cubic (bcc), and face-centered cubic (fcc) lattice types) the distance between n.n. is equal along all directions, $|dx_i| = a$. Using this property, the summation over nearest neighbors $\sum_{m \in (\text{n.n.})} (\dots) dx_i dx_j$ for $i \neq j$ is equal to 0 for each lattice type. So, we can obtain the following Hamiltonian:

$$\mathcal{H}_l = -2Z|S|^2 J - 2|S|^2 J a^2 \sum_i \alpha_l \cdot (\partial_{x_i} \partial_{x_i} \alpha_l). \quad (14)$$

Equation (11) can be again differentiate with respect to x_j , and the result is

$$\alpha_l \cdot (\partial_{x_i} \partial_{x_j} \alpha_l) = -(\partial_{x_i} \alpha_l) \cdot (\partial_{x_j} \alpha_l). \quad (15)$$

With this equality we can rewrite (14) for the exchange energy into the following form:

$$\mathcal{H}_l = -2Z|S|^2 J + 2|S|^2 J a^2 \sum_i (\partial_{x_i} \alpha_l)^2. \quad (16)$$

To define energy density, \mathcal{E}_{ex} as a continuous function of the position vector, we have to sum over all spins in the unit cell and divide it by the volume of this unit cell. In that way we obtain density of the following exchange energy:

$$\mathcal{E}_{\text{ex}} = \lambda M^2 + A \sum_i (\partial_{x_i} \alpha(\mathbf{r}))^2, \quad (17)$$

where

$$A = \frac{2nJS^2}{a} \quad (18)$$

and $n = 1, 2$, or 4 for sc, bcc, or fcc lattice, respectively; [2], $\alpha(\mathbf{r})$ is defined in (8) and

$$\lambda = \frac{-2ZJ}{N\mu_B^2 g^2}. \quad (19)$$

To calculate the total exchange energy, E_{ex} , stored in a magnetic material, we have to integrate density of the energy (17) over the volume of the material [3] as follows:

$$\begin{aligned} E_{\text{ex}} = & \int_V \mathcal{E}_{\text{ex}} d^3 r = \int_V \lambda M^2 d^3 r + \int_V A \sum_i (\partial_{x_i} \alpha(\mathbf{r}))^2 d^3 r \\ = & \int_V \lambda M^2 d^3 r \\ & + \int_V A \left[\left(\partial_x \frac{\mathbf{M}}{M} \right)^2 + \left(\partial_y \frac{\mathbf{M}}{M} \right)^2 + \left(\partial_z \frac{\mathbf{M}}{M} \right)^2 \right] d^3 r. \end{aligned} \quad (20)$$

The SW can be regarded as coherent precession of the magnetization vector around its equilibrium direction. Based on this observation most SW calculation are performed in linear approximation. This approximation was already used once in our paper, it is in (10). Now we will use it again to simplify the expression (20) for the total exchange energy.

2.1.1. Exchange Energy in Form I. In linear approximation the magnetization vector

$$\mathbf{M}(\mathbf{r}) = M_x(\mathbf{r})\hat{x} + M_y(\mathbf{r})\hat{y} + M_z(\mathbf{r})\hat{z} \quad (21)$$

can be separated into two parts: a static and dynamic components. We assume that the magnetization component along the direction of the applied magnetic field, in our case it is the z -axis, is constant in time (but can be still position dependent), and its value is close to the length of the total magnetization vector as follows:

$$M_0 = M_0(\mathbf{r}) \equiv M_z \approx |\mathbf{M}| \approx \text{const}(t). \quad (22)$$

The time-depending components of the magnetization vector; M_x and M_y will be denoted by m_x and m_y , respectively. We will define the dynamic magnetization vector as $\mathbf{m} = (m_x, m_y)$ being a two-dimensional vector in the plane perpendicular to the direction of the saturation magnetization.

The exchange energy, (20), with the help of approximation (22) can be rewritten in the following form:

$$E_{\text{ex}} = \int_V \lambda M_0^2 d^3r + \int_V A \left(\nabla \frac{\mathbf{m}}{M_0} \right)^2 d^3r. \quad (23)$$

This consists of the formula for the exchange energy, which we will call as Form I.

2.1.2. Exchange Energy in Form II. In the following we will make further assumptions to obtain another expression for the exchange field. We can write that

$$\begin{aligned} \left(\partial_x \frac{\mathbf{m}}{M_0} \right)^2 &= \left(\frac{(\partial_x \mathbf{m})M_0 - (\partial_x M_0)\mathbf{m}}{M_0^2} \right)^2 \\ &= \frac{(\partial_x \mathbf{m})^2 M_0^2 + (\partial_x M_0)^2 \mathbf{m}^2 - M_0(\partial_x M_0)(\partial_x \mathbf{m}^2)}{M_0^4} \end{aligned} \quad (24)$$

were in the last component of the nominator we have used $2\mathbf{m} \cdot \partial_x \mathbf{m} = \partial_x(\mathbf{m}^2)$. The same calculations can be applied to other components of the ∇ operator in the exchange energy functional (23). The following expression for the exchange energy can be obtained:

$$\begin{aligned} E_{\text{ex}} &= \int_V \lambda M_0^2 d^3r + \int_V \frac{A}{M_0^2} (\nabla \mathbf{m})^2 d^3r \\ &+ \int_V \frac{A}{M_0^4} (\nabla M_0)^2 \mathbf{m}^2 d^3r - \int_V \frac{A}{M_0^3} (\nabla M_0) \cdot (\nabla \mathbf{m}^2) d^3r. \end{aligned} \quad (25)$$

In MCs the saturation magnetization is a function of the position vector with a step increase at interfaces. For

bicomponent MCs (i.e., consisting of two ferromagnetic materials: A and B), $M_0(\mathbf{r})$ can be defined with the help of the characteristic function $S(\mathbf{r})$:

$$M_0(\mathbf{r}) = (M_{0,A} - M_{0,B})S(\mathbf{r}) + M_{0,B}, \quad (26)$$

were

$$S(\mathbf{r}) = \begin{cases} 1 & \text{for } \mathbf{r} \text{ in material A,} \\ 0 & \text{for } \mathbf{r} \text{ in material B,} \end{cases} \quad (27)$$

and $M_{0,A}$ and $M_{0,B}$ are saturation magnetizations in materials A and B, respectively. We can see that in last two terms in (25) there are derivatives of M_0 with respect to the position which according to (26) are derivatives from the step function, that is, $\nabla M_0 = (M_{0,A} - M_{0,B})\delta(\mathbf{r} - \mathbf{r}_{\text{interface}})$, where δ is the Dirac delta function, and $\mathbf{r}_{\text{interface}}$ is a position vector which define the interface. It means that these two terms are connected with the exchange energy contributed only at interfaces and which are related to the jump of the saturation magnetization value (in PWM calculations we will assume parallel magnetizations in both materials). It can be shown that these two terms result in internal magnetic field components localized on interfaces and that these components introduce singularities in the equation of motion. To avoid these singularities we neglect these two terms. (It can be shown by direct calculation of functional derivatives according to (29), that these terms introduce non-Hermitian (or non-anti-Hermitian) elements into equation of motion, that is, $(\mathbf{m}/M_0)\nabla((2A/\mu_0 M_0^2)\nabla M_0)$, and again its physical interpretation is questionable.)

To summarize, we have derived two different formulas for the exchange energy in linear approximation, which are equivalent in the case of homogeneous material. These are

$$\text{Form I: } E_{\text{ex}} = \int_V \lambda M_0^2 d^3r + \int_V A \left(\nabla \frac{\mathbf{m}}{M_0} \right)^2 d^3r, \quad (28)$$

$$\text{Form II: } E_{\text{ex}} = \int_V \lambda M_0^2 d^3r + \int_V \frac{A}{M_0^2} (\nabla \mathbf{m})^2 d^3r.$$

In this derivation we have neglected the interface anisotropy terms [9, 11]. These effects, which can be present in real materials, have a microscopic origin and are limited to the very thin area around interfaces (one or two atomic planes). In continuous effective models such effects can be included by proper effective boundary conditions imposed on dynamical component of the magnetization vector.

2.2. Exchange Field. Exchange field can be derived from the exchange energy functionals (28) as a first variational derivative with respect to the magnetization vector [4, 59] as follows:

$$\mathbf{H}_{\text{ex}}(\mathbf{r}) = -\frac{1}{\mu_0} \frac{\delta E_{\text{ex}}}{\delta \mathbf{M}} = -\frac{1}{\mu_0} \left[\frac{\delta E_{\text{ex}}}{\delta m_x}, \frac{\delta E_{\text{ex}}}{\delta m_y}, \frac{\delta E_{\text{ex}}}{\delta M_0} \right]. \quad (29)$$

This equation is written in SI units. Those variational derivatives can be calculated from Euler formula [4] as follows:

$$\frac{\delta E_{\text{ex}}}{\delta m_x} = \frac{\partial \eta}{\partial m_x} - \nabla \left(\frac{\partial \eta}{\partial (\nabla m_x)} \right) = \frac{\partial \eta}{\partial m_x} - \sum_i \frac{\partial}{\partial x_i} \left(\frac{\partial \eta}{\partial (\partial_{x_i} m_x)} \right), \quad (30)$$

where $E_{\text{ex}} = \int_V \eta d^3r$ and $\eta = \lambda M_0^2(\mathbf{r}) + A(\mathbf{r})(\nabla \mathbf{m}(\mathbf{r})/M_0(\mathbf{r}))^2$ or $\eta = \lambda M_0^2(\mathbf{r}) + \left(\frac{A(\mathbf{r})}{M_0^2(\mathbf{r})} \right) (\nabla \mathbf{m}(\mathbf{r}))^2$ for Form I and Form II of the exchange energy, respectively (see (28)). We will perform those calculations independently for each form of the exchange energy defined in (28). During calculations we will take into account the inhomogeneity in the material, that is, spacial dependence of material parameters: $A(\mathbf{r})$ and $M_0(\mathbf{r})$.

2.2.1. Form I of the Exchange Field. For Form I of the exchange energy functional $\eta = \lambda M_0^2(\mathbf{r}) + A(\mathbf{r})(\nabla(\mathbf{m}(\mathbf{r})/M_0(\mathbf{r})))^2$ and we will calculate functional derivative directly from (30). First we calculate the derivative with respect of \mathbf{m} as follows:

$$\begin{aligned} \frac{\partial \eta}{\partial m_x} &= \frac{(\partial A(\mathbf{r}) \nabla(\mathbf{m}(\mathbf{r})/M_0(\mathbf{r})))^2}{\partial m_x} \\ &= \frac{A(\mathbf{r})}{M_0(\mathbf{r})^2} \nabla \left(\frac{\mathbf{m}(\mathbf{r})}{M_0(\mathbf{r})} \right) \cdot \nabla (M_0(\mathbf{r})). \end{aligned} \quad (31)$$

This term includes the derivative of saturation magnetization, which is a step function on the interface between two magnetic materials—(26). This part of the magnetic field is localized purely at interfaces similarly as was found already in (25). This term will introduce singularity into equation of motions, and it will be neglected.

After this assumption the exchange magnetic field in the Form I will be obtained solely from the second term in (30), that is,

$$\begin{aligned} \mu_0 \mathbf{H}_{\text{ex}} &= \nabla \frac{\partial \eta}{\partial \nabla \mathbf{m}(\mathbf{r})} = \nabla \frac{\partial A(\mathbf{r})(\nabla(\mathbf{m}(\mathbf{r})/M_0(\mathbf{r})))^2}{\partial \nabla \mathbf{m}(\mathbf{r})} \\ &= \nabla \left[A(\mathbf{r}) 2 \left(\nabla \frac{\mathbf{m}(\mathbf{r})}{M_0(\mathbf{r})} \right) \cdot \left(\frac{\partial \nabla(\mathbf{m}(\mathbf{r})/M_0(\mathbf{r}))}{\partial \nabla \mathbf{m}(\mathbf{r})} \right) \right] \quad (32) \\ &= \nabla \left[\frac{2A(\mathbf{r})}{M_0(\mathbf{r})} \right] \nabla \frac{\mathbf{m}(\mathbf{r})}{M_0(\mathbf{r})}. \end{aligned}$$

2.2.2. Form II of the Exchange Field. For exchange energy written in the Form II as defined in (28), $\eta = \lambda M_0^2(\mathbf{r}) + (A(\mathbf{r})/M_0^2(\mathbf{r}))(\nabla \mathbf{m}(\mathbf{r}))^2$. We can calculate functional derivatives according to (30) and write \mathbf{H}_{ex} in a compact form without any further approximations. In this case $\partial \eta / \partial m_x = 0$ because the first term in η is independent on $\partial_{x_i} m_x$. So

the functional derivative of E_{ex} with respect to m_x take the following form:

$$\begin{aligned} \frac{\delta E_{\text{ex}}}{\delta m_x} &= - \sum_i \frac{\partial}{\partial x_i} \left(\frac{\partial (A/M_0^2)(\nabla \mathbf{m})^2}{\partial (\partial_{x_i} m_x)} \right) \\ &= - \sum_i \frac{\partial}{\partial x_i} \left[\frac{A}{M_0^2} \frac{\partial \mathfrak{A}}{\partial (\partial_{x_i} m_x)} \right] \\ &= - \frac{\partial}{\partial x} \left[\frac{2A}{M_0^2} (\partial_x m_x) \right] - \frac{\partial}{\partial y} \left[\frac{2A}{M_0^2} (\partial_y m_x) \right] \\ &\quad - \frac{\partial}{\partial z} \left[\frac{2A}{M_0^2} (\partial_z m_x) \right], \end{aligned} \quad (33)$$

where \mathfrak{A} denotes $[(\partial_x m_x)^2 + (\partial_x m_y)^2 + (\partial_y m_x)^2 + (\partial_y m_y)^2 + (\partial_z m_x)^2 + (\partial_z m_y)^2]$. The same procedure can be repeated for the y component of the magnetization. Finally the exchange field can be written in the following form, that is, Form II:

$$\mu_0 \mathbf{H}_{\text{ex}}(\mathbf{r}) = \nabla \left[\frac{2A(\mathbf{r})}{M_0^2(\mathbf{r})} \right] \nabla \mathbf{m}(\mathbf{r}). \quad (34)$$

2.2.3. Summary of the Exchange Field Forms. We have shown the derivation of two different expressions for the exchange field in nonuniform ferromagnetic materials in linear approximation. These are

Form I: $\mathbf{H}_{\text{ex}}(\mathbf{r}) = \nabla l_{\text{ex,I}}(\mathbf{r}) \nabla \tilde{\mathbf{m}}(\mathbf{r})$,

$$\text{where } \tilde{\mathbf{m}}(\mathbf{r}) \equiv \frac{\mathbf{m}(\mathbf{r})}{M_0(\mathbf{r})}, \quad l_{\text{ex,I}} = \frac{2A(\mathbf{r})}{\mu_0 M_0(\mathbf{r})}; \quad (35)$$

Form II: $\mathbf{H}_{\text{ex}}(\mathbf{r}) = \nabla l_{\text{ex,II}}(\mathbf{r}) \nabla \mathbf{m}(\mathbf{r})$,

$$\text{where } l_{\text{ex,II}} = \frac{2A(\mathbf{r})}{\mu_0 M_0^2(\mathbf{r})}.$$

We can also add to this list the exchange field in Form III, which is derived directly from the exchange energy functional (28) (independent of the form which will be used) under assumption of the homogeneous material, that is, when the space dependence of A and M_0 is not taken into account during calculations of a functional derivative (30)

$$\text{Form III: } \mathbf{H}_{\text{ex}}(\mathbf{r}) = \frac{l_{\text{ex,I}}(\mathbf{r})}{M_0(\mathbf{r})} \nabla^2 \mathbf{m}(\mathbf{r}). \quad (36)$$

From the parameters introduced just above: $l_{\text{ex,I}}$ and $l_{\text{ex,II}}$, only the second one (i.e., from Form II) has an additional physical meaning; that is, its square root defines the exchange length [3]. (In Form III the coefficient in the exchange field is the same as in Form II, but M_0 was excluded from new parameter due to simplification in the latter calculus, see (42).)

It is worth to note at this moment that differential operators in the definition of the exchange field, (35)-(36), work on dynamical components of the magnetization vector, $\mathbf{m}(\mathbf{r})$ in Forms II and III, while on its normalized function in Form I, $\tilde{\mathbf{m}}(\mathbf{r})$. This will make different equations and should be kept in mind during the interpretation of the eigenvectors

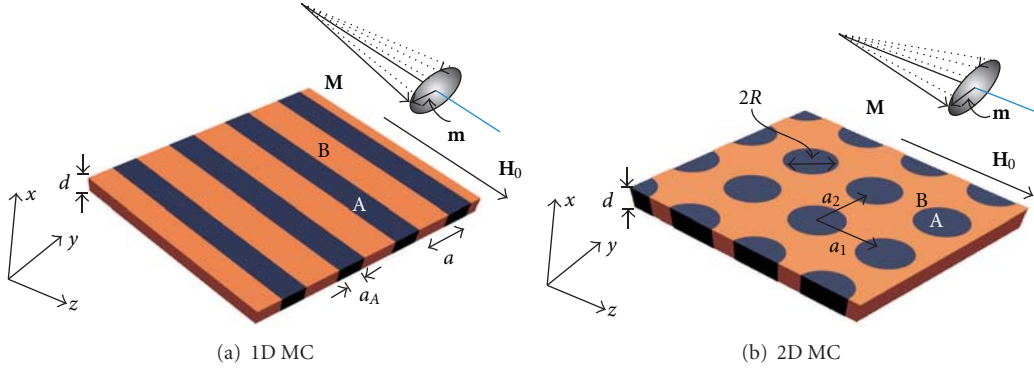


FIGURE 2: Structure of a 1D MC (a) and 2D MC (b) considered in this manuscript. 2D MC is formed by cylindrical dots A arranged in a square lattice immersed into a ferromagnetic matrix B. The external magnetic field \mathbf{H}_0 is applied in the direction of the z -axis. Spin waves are assumed to form standing waves in the infinite (y, z) plane or along y axis in (b) and (a), respectively. The thickness of MCs, d , is much smaller than the lattice constant a and the diameter of dots, $2R$ or width of stripes a_A .

found in PWM and boundary conditions implemented in the exchange field definitions.

Those three different formulas for the exchange field will be investigated for the calculation of the magnonic band structure in thin plates of 1D and 2D MCs with PWM.

3. Plane Wave Method

The PWM is a useful tool used for study systems with discrete translational symmetry, including electronic, photonic, phononic and magnonic crystals [24, 27, 28, 60–66]. This method can be applied to any type of lattice and various shapes of scattering centers. The method is being constantly improved, with its field of application extending to new problems also in magnonic field [67]. Recently, the PWM has been used for the calculation of the SW spectra of 1D and 2D MCs of finite thickness [68, 69], and the magnonic spectra of thin films of 2D antidot lattices (ADLs) based on a square lattice [70, 71]. The PWM gives also a possibility for calculations of the surface effects and defect states but this requires so-called supercell formulation. The PWM in the supercell formulations was recently used to study the surface and defect influence on magnonic spectra in 2D MCs [69, 72]. For completeness we will briefly outline the PWM and explain the approximations used in this method.

We will consider slabs of 1D or 2D MCs (Figure 2) where the dynamics of the magnetization vector $\mathbf{M}(\mathbf{r}, t)$ can be described by the LL equation as follows:

$$\frac{\partial \mathbf{M}(\mathbf{r}, t)}{\partial t} = -\gamma \mu_0 [\mathbf{M}(\mathbf{r}, t) \times \mathbf{H}_{\text{eff}}(\mathbf{r}, t)] + \frac{\xi}{M_s} \left[\mathbf{M} \times \frac{\partial \mathbf{M}}{\partial t} \right], \quad (37)$$

where γ is the gyromagnetic ratio, μ_0 is permeability of vacuum; as in the case of free electrons, we will assume $\gamma \mu_0 = 2.21 \times 10^5 \text{ m(A s)}^{-1}$. t is a time, the last term on the right describes relaxation with dimensionless damping factor ξ . The damping will be neglected in this study, while an application of the PWM for calculation of the time life of SWs in 2D MCs can be found in [67]. \mathbf{H}_{eff} is an effective

magnetic field, which in our study will consist of three components:

$$\mathbf{H}_{\text{eff}}(\mathbf{r}, t) = \mathbf{H}_0 + \mathbf{H}_{\text{ms}}(\mathbf{r}, t) + \mathbf{H}_{\text{ex}}(\mathbf{r}, t). \quad (38)$$

\mathbf{H}_0 is a homogeneous in space and directed along the z -axis bias magnetic field, $\mathbf{H}_{\text{ex}}(\mathbf{r}, t)$ is an exchange field; its proper definitions were derived in preceding section in (35). $\mathbf{H}_{\text{ms}}(\mathbf{r}, t)$ is the demagnetizing field. In the magnetostatic approximation (with retardation effects neglected), the demagnetizing field must fulfill the magnetostatic Maxwell's equations [59] as follows:

$$\begin{aligned} \nabla \times \mathbf{H}_{\text{ms}}(\mathbf{r}, t) &= 0; \\ \nabla \cdot (\mathbf{H}_{\text{ms}}(\mathbf{r}, t) + \mathbf{M}(\mathbf{r}, t)) &= 0. \end{aligned} \quad (39)$$

We will calculate the demagnetizing field by decomposing this field into the static and dynamic components, $\mathbf{H}_{\text{ms}}(\mathbf{r})$ and $\mathbf{h}_{\text{ms}}(\mathbf{r}, t)$, respectively. We will assume that the static part will have values different from zero only in the direction of the external magnetic field: $\mathbf{H}_{\text{ms}}(\mathbf{r}) = H_{\text{ms}}(\mathbf{r}) \hat{z}$. The time dependence of the dynamic component of the demagnetizing field has the same form as that of the dynamic component of the magnetization vector: $\mathbf{h}_{\text{ms}}(\mathbf{r}, t) = \mathbf{h}_{\text{ms}}(\mathbf{r}) e^{i\omega t}$, ω being an angular frequency of the SW.

In PWM calculations we shall consider a saturated magnetization in the whole magnonic crystal. This allows us to use linear approximation and a global coordinate system in which the y - and z -axes define the plane of periodicity, and the x -axis is normal to the surface of a thin plate of the MC. In the case of linear spin waves the component of the magnetization vector parallel to the static magnetic field (in this study the static magnetic field is always assumed to be oriented along the z -axis) is constant in time, and its magnitude is much greater than that of the perpendicular components: $|\mathbf{m}(\mathbf{r}, t)| \ll M_z(\mathbf{r})$ ($\mathbf{M}(\mathbf{r}, t) = M_z(\mathbf{r}) \hat{z} + \mathbf{m}(\mathbf{r}, t)$). Thus, the linear approximation, introduced in the derivation of the exchange field in the previous section, can be used again, by neglecting all terms with squared $\mathbf{m}(\mathbf{r}, t)$ and $\mathbf{h}_{\text{ms}}(\mathbf{r}, t)$ and assuming $M_z \approx M_0$. We will only search for

solutions of the LL equation corresponding to monochromatic spin waves: $\mathbf{m}(\mathbf{r}, t) = \mathbf{m}(\mathbf{r}) \exp(i\omega t)$.

Using the linear approximation, we derive the following system of equations for m_x and m_y (and \tilde{m}_x and \tilde{m}_y) from (37) for exchange field in various formulations defined in (35). For Form I of the exchange field we get

$$\begin{aligned} i \frac{\omega}{\gamma \mu_0} \tilde{m}_{x(y)}(\mathbf{r}) = & -_{(+)} [\nabla \cdot l_{\text{ex,I}} \nabla] \tilde{m}_{y(x)}(\mathbf{r}) \\ & +_{(-)} \tilde{m}_{y(x)}(\mathbf{r}) (H_0 + H_{\text{ms,z}}) -_{(+)} M_0 \tilde{h}_{\text{ms,y}(x)}(\mathbf{r}), \end{aligned} \quad (40)$$

for Form II:

$$\begin{aligned} i \frac{\omega}{\gamma \mu_0} m_{x(y)}(\mathbf{r}) = & -_{(+)} M_0 [\nabla \cdot l_{\text{ex,II}} \nabla] m_{y(x)}(\mathbf{r}) \\ & +_{(-)} m_{y(x)}(\mathbf{r}) (H_0 + H_{\text{ms,z}}) -_{(+)} M_0 h_{\text{ms,y}(x)}(\mathbf{r}) \end{aligned} \quad (41)$$

and for Form III:

$$\begin{aligned} i \frac{\omega}{\gamma \mu_0} m_{x(y)}(\mathbf{r}) = & -_{(+)} l_{\text{ex,I}} \nabla^2 m_{y(x)}(\mathbf{r}) \\ & +_{(-)} m_{y(x)}(\mathbf{r}) (H_0 + H_{\text{ms,z}}) -_{(+)} M_0 h_{\text{ms,y}(x)}(\mathbf{r}). \end{aligned} \quad (42)$$

In (40) we introduce $\tilde{h}_{\text{ms,y}(x)}(\mathbf{r})$, which is a value of the demagnetizing field normalized to the saturation magnetization, M_0 . The formula for normalized demagnetizing field is obtained under the same approximations as used in the derivation of the exchange field and will have the same expression as $h_{\text{ms,y}(x)}$.

In MCs the material parameters, namely, A and M_0 , are periodic functions of the in-plane position vector $\mathbf{r} = (y, z)$ for 2D MC ($\mathbf{r} = (y, 0)$ for 1D MC), with a period equal to the lattice vector \mathbf{a} (a) as follows:

$$M_0(\mathbf{r} + \mathbf{a}) = M_0(\mathbf{r}), \quad A(\mathbf{r} + \mathbf{a}) = A(\mathbf{r}). \quad (43)$$

Also parameters used in formulas for the exchange field, $l_{\text{ex,I}}(\mathbf{r})$ and $l_{\text{ex,II}}(\mathbf{r})$, fulfill the same relation. In MCs composed of two materials each of these material parameters can be expressed by two terms: $M_{0,A}$, $M_{0,B}$ and A_A , A_B , representing its respective values in each constituent material. The lattice vector \mathbf{a} in a square lattice is any superposition of two primitive vectors: $\mathbf{a}_1 = a\hat{z}$, $\mathbf{a}_2 = a\hat{y}$ with integer coefficients, where a is the lattice constant (see Figure 2(b)).

To solve the LL equation we will use Bloch's theorem, which asserts that a solution of a differential equation with periodic coefficients can be represented as a product of a plane-wave envelope function and a periodic function. For dynamical components of the magnetization vector and its normalized values, those are

$$\begin{aligned} \mathbf{m}(\mathbf{r}) &= \sum_{\mathbf{G}} \mathbf{m}_{\mathbf{q}}(\mathbf{G}) e^{i(\mathbf{q}+\mathbf{G}) \cdot \mathbf{r}}, \\ \tilde{\mathbf{m}}(\mathbf{r}) &= \sum_{\mathbf{G}} \tilde{\mathbf{m}}_{\mathbf{q}}(\mathbf{G}) e^{i(\mathbf{q}+\mathbf{G}) \cdot \mathbf{r}}, \end{aligned} \quad (44)$$

respectively. For 2D MCs $\mathbf{G} = (G_y, G_z)$ denotes a reciprocal lattice vector of the structure considered; in the case of square lattice $\mathbf{G} = (2\pi/a)(n_y, n_z)$, n_y and n_z are integers. The Bloch wave vector $\mathbf{q} = (q_y, q_z)$ refers to those spin waves which according to Bloch's theorem can be limited to the first Brillouin zone (1BZ). For 1D MCs, $\mathbf{G} = (G_y, 0) = ((2\pi/a)n_y, 0)$ and $\mathbf{q} = (q_y, 0)$.

In the next step we perform the Fourier transformation to map the periodic functions M_S , $l_{\text{ex,I}}$, and $l_{\text{ex,II}}$ in (40)-(41) onto the reciprocal space. The transformation formulas are as follow:

$$\begin{aligned} M_0(\mathbf{r}) &= \sum_{\mathbf{G}} M_0(\mathbf{G}) e^{i\mathbf{G} \cdot \mathbf{r}}, \\ l_{\text{ex,I}}(\mathbf{r}) &= \sum_{\mathbf{G}} l_{\text{ex,I}}(\mathbf{G}) e^{i\mathbf{G} \cdot \mathbf{r}}, \\ l_{\text{ex,II}}(\mathbf{r}) &= \sum_{\mathbf{G}} l_{\text{ex,II}}(\mathbf{G}) e^{i\mathbf{G} \cdot \mathbf{r}}. \end{aligned} \quad (45)$$

In the case of cylindrical dots in 2D MC and stripes in 1D MC, the Fourier components of the saturation magnetization $M_S(\mathbf{G})$ and the exchange parameters, $l_{\text{ex,I}}(\mathbf{G})$, $l_{\text{ex,II}}(\mathbf{G})$, can be calculated analytically. The formula for the saturation magnetization in 2D MC reads as follows:

$$M_0(\mathbf{G}) = \begin{cases} (M_{0,A} - M_{0,B}) \frac{\pi R^2}{a^2} + M_{0,B}, & \text{for } \mathbf{G} = 0, \\ (M_{0,A} - M_{0,B}) 2 \frac{\pi R^2}{a^2} \frac{J_1(GR)}{GR}, & \text{for } \mathbf{G} \neq 0, \end{cases} \quad (46)$$

where J_1 is a Bessel function of the first kind, R is a radius of a dot. G is the length of a reciprocal wave vector \mathbf{G} . For stripes in 1D MC with lattice constant a , $M_0(\mathbf{G})$ has the following form:

$$M_0(\mathbf{G}) = \begin{cases} (M_{0,A} - M_{0,B}) \frac{a_A}{a} + M_{0,B}, & \text{for } \mathbf{G} = 0, \\ (M_{0,A} - M_{0,B}) 2 \frac{a_A}{a} \frac{\sin Ga_A/2}{Ga_A/2}, & \text{for } \mathbf{G} \neq 0, \end{cases} \quad (47)$$

where a_A is the width of the stripe of material A. The formulas for other periodic functions of the position vector, that is, $l_{\text{ex,I}}(\mathbf{G})$ and $l_{\text{ex,II}}(\mathbf{G})$ have the same form.

We need formulas for the static and dynamic demagnetizing fields, $H_{\text{ms,z}}(\mathbf{r}, x)$, $h_{\text{ms,x}}(\mathbf{r}, x)$, and $h_{\text{ms,y}}(\mathbf{r}, x)$, to finalize the procedure, in which an eigenvalue problem in the reciprocal space is derived from LL equation. According to the ideas presented in [73], for a slab of a 2D magnonic crystal with a uniform magnetization Maxwell's equations can be solved in the magnetostatic approximation with appropriate electromagnetic BCs at both surfaces of the slab, that is, at $x = -d/2$ and $x = d/2$. Those BCs are a continuity of the tangential components of the magnetic field vector and a normal component of the magnetic induction vector. For the considered structure, infinite in the (y, z) plane, analytical

solutions in the form of Fourier series can be obtained for both the static and dynamic demagnetizing fields [68, 70] as follows:

$$H_{ms,z}(\mathbf{r}, x) = - \sum_{\mathbf{G}} \frac{M_s(\mathbf{G})}{G^2} G_z^2 (1 - \cosh(|\mathbf{G}|x) e^{-|\mathbf{G}|d/2}) e^{i\mathbf{G} \cdot \mathbf{r}}, \quad (48)$$

$$h_{ms,y}(\mathbf{r}, x) = - \sum_{\mathbf{G}} \frac{m_y(\mathbf{G})}{|\mathbf{q} + \mathbf{G}|^2} (q_y + G_y)^2 \times (1 - \cosh(|\mathbf{q} + \mathbf{G}|x) e^{-|\mathbf{q} + \mathbf{G}|d/2}) e^{i(\mathbf{q} + \mathbf{G}) \cdot \mathbf{r}}, \quad (49)$$

$$h_{ms,x}(\mathbf{r}, x) = - \sum_{\mathbf{G}} m_x(\mathbf{G}) \cosh(|\mathbf{q} + \mathbf{G}|x) e^{-|\mathbf{q} + \mathbf{G}|d/2} e^{i(\mathbf{q} + \mathbf{G}) \cdot \mathbf{r}}. \quad (50)$$

Similarly to the static component of the demagnetizing field, we take into account dynamical magnetostatic field components which depend on the same component of the magnetization vector, only. Represented in the reciprocal space for the in-plane components, these formulas for the demagnetizing fields are x dependent, that is, vary with position across the thickness of the slab. However, when the slab is thin enough (which is the case of the discussed MC, with $d = 30$ nm), the nonuniformity of the demagnetizing fields across its thickness can be neglected, and the respective field values calculated from (48)–(50) for $x = 0$ can be used in the PWM calculations.

The substitution of the (44)–(50) into (41)–(42) leads to an algebraic eigenvalue problem with eigenvalues $i\omega/\gamma\mu_0 H_0$ as follows:

$$\widehat{M}_\Lambda \mathbf{m}_{\mathbf{q},\Lambda} = i \frac{\omega}{\gamma\mu_0 H_0} \mathbf{m}_{\mathbf{q},\Lambda}, \quad (51)$$

where Λ takes the values I, II, or III in dependence on which form of the exchange field is derived for. The eigenvector $\mathbf{m}_{\mathbf{q},\Lambda}^T = [m_{x,\mathbf{q}}(\mathbf{G}_1), \dots, m_{x,\mathbf{q}}(\mathbf{G}_N), m_{y,\mathbf{q}}(\mathbf{G}_1), \dots, m_{y,\mathbf{q}}(\mathbf{G}_N)]$ for Λ equal II or III, and $\mathbf{m}_{\mathbf{q},\Lambda}^T = [\tilde{m}_{x,\mathbf{q}}(\mathbf{G}_1), \dots, \tilde{m}_{x,\mathbf{q}}(\mathbf{G}_N), \tilde{m}_{y,\mathbf{q}}(\mathbf{G}_1), \dots, \tilde{m}_{y,\mathbf{q}}(\mathbf{G}_N)]$ when a finite number N of reciprocal lattice vectors is used in the Fourier series (44) and (45). For each form of the exchange field, the elements of the matrix \widehat{M}_Λ of the eigenvalue problem (51) can be written in a block-matrix form as follows:

$$\widehat{M}_\Lambda = \begin{pmatrix} \widehat{M}_\Lambda^{xx} & \widehat{M}_\Lambda^{xy} \\ \widehat{M}_\Lambda^{yx} & \widehat{M}_\Lambda^{yy} \end{pmatrix}. \quad (52)$$

The submatrices in (52) for the exchange field in different forms are defined as follows:

$$\begin{aligned} \widehat{M}_{ij}^{xx} &= \widehat{M}_{ij}^{yy} = 0, \\ \widehat{M}_{ij}^{xy} &= \delta_{ij} + M_{ij}^{\text{ex},\Lambda} + \frac{(q_y + G_{y,j})^2}{H_0 |\mathbf{q} + \mathbf{G}_j|^2} \\ &\quad \times (1 - C(\mathbf{q} + \mathbf{G}_j, x)) M_S(\mathbf{G}_i - \mathbf{G}_j) \\ &\quad - \frac{(G_{z,i} - G_{z,j})^2}{H_0 |\mathbf{G}_i - \mathbf{G}_j|^2} M_S(\mathbf{G}_i - \mathbf{G}_j) (1 - C(\mathbf{G}_i - \mathbf{G}_j, x)), \\ \widehat{M}_{ij}^{yx} &= -\delta_{ij} - M_{ij}^{\text{ex},\Lambda} - \frac{1}{H_0} C(\mathbf{q} + \mathbf{G}_j, x) M_S(\mathbf{G}_i - \mathbf{G}_j) \\ &\quad + \frac{(G_{z,i} - G_{z,j})^2}{H_0 |\mathbf{G}_i - \mathbf{G}_j|^2} M_S(\mathbf{G}_i - \mathbf{G}_j) (1 - C(\mathbf{G}_i - \mathbf{G}_j, x)), \end{aligned} \quad (53)$$

where indexes of reciprocal lattice vectors i, j, l are integers which number reciprocal lattice vectors. The additional function used in above equations is defined as follows:

$$C(\mathbf{q}, x) = \cosh(|\mathbf{q}|x) e^{-|\mathbf{q}|d/2}. \quad (54)$$

Matrix elements connected with the exchange field, $M_{ij}^{\text{ex},\Lambda}$, depend on definition used. These elements are as follow:

$$\begin{aligned} M_{i,j}^{\text{ex,I}} &= \frac{(\mathbf{q} + \mathbf{G}_j) \cdot (\mathbf{q} + \mathbf{G}_i)}{H_0} l_{\text{ex,I}}^2 (\mathbf{G}_i - \mathbf{G}_j), \\ M_{i,j}^{\text{ex,II}} &= \sum_l \frac{(\mathbf{q} + \mathbf{G}_j) \cdot (\mathbf{q} + \mathbf{G}_l)}{H_0} l_{\text{ex,II}}^2 (\mathbf{G}_l - \mathbf{G}_j) M_S(\mathbf{G}_i - \mathbf{G}_l), \\ M_{i,j}^{\text{ex,III}} &= \frac{(\mathbf{q} + \mathbf{G}_j)^2}{H_0} l_{\text{ex,I}}^2 (\mathbf{G}_i - \mathbf{G}_j), \end{aligned} \quad (55)$$

for Forms I, II, and III, respectively.

We solve the system of (51) by standard numerical procedures designed for solving complex matrix eigenvalue problems. All the eigenvalues found by these procedures must be tested for convergence though. A satisfactory convergence of numerical solutions of (51) for all the structures considered proves to be assured by the use of 625 and 161 reciprocal lattice vectors for 2D and 1D MC, respectively.

All three forms of the exchange field were used in literature in calculations of the magnonic band structure in MCs, but to our best knowledge there is missed their detailed derivations, and in this paper we would like to fill this gap. In the first paper devoted to MCs by Vasseur et al. [27], the exchange field in the form similar to Form I was postulated. The only difference is that the eigenvector is related to the dynamical component of the magnetization vector \mathbf{m} instead its normalized value $\tilde{\mathbf{m}}$. The same form of the \mathbf{H}_{ex} was used

also in other papers, for example, [67, 72, 74–76] without the derivation of its form and with the dynamical components of the magnetization vector used instead its normalized value. Of course this different definition of the eigenvectors does not influence the dispersion of spin waves found in calculations (i.e., eigenvalues) but change only the interpretation of eigenvectors. In papers [62, 63] another definition of the exchange field, that is, Form II with additional surface term, was used, and a detailed analysis of the results obtained with both formulations was presented for infinite 2D and 3D MCs. The additional component introduced in the LL equation is related to the interface anisotropy as was pointed out in the appendix of [28]. In fact this interface term can be obtained from last two terms in the exchange field defined in (25) and neglected in this study. The strict Form II of the exchange field, for the first time probably, was used by Mills in [9] where he derived the corrected Hoffman boundary conditions. In our recent papers [28, 68, 69], we used Form II for the calculations of the SW spectra in thin films of 1D and 2D MCs. The Form III of the exchange field, that is, characteristic for uniform materials, was also used for calculations of the magnonic band structure in magnetic stripes coupled by dynamic dipole interactions, [77]. Below the influence of different definitions of the exchange field on the magnonic band structure in planar MCs will be investigated.

4. Magnonic Spectra versus Formulation of H_{ex}

In this section we will present results of our calculations performed with PWM for three different forms of the exchange field as defined in (35)–(36). We will present the results for a 1D MC and a 2D MC separately.

4.1. 1D Magnonic Crystals. We chose for our study a 1D MC consisting of Co and permalloy (Py) stripes of equal width 250 nm. The thickness of the film is 20 nm and the length is assumed infinite. Our choice is motivated by recently published papers presenting experimental and theoretical results [68, 75, 76, 78, 79]. The dispersion relation of SWs in such crystal was measured by Brillouin Light Scattering spectroscopy and was calculated from the LL equation using the finite-element method and the PWM. Very weak magnetic field, $\mu H_0 = 0.001$ T, is applied along the stripes.

We assume values of material parameters (spontaneous magnetization and exchange constant for cobalt and permalloy) equal to those presented in the experimental paper [75]. It is for cobalt: $M_{0,\text{Co}} = 1.15 \cdot 10^6$ A/m, $A_{\text{Co}} = 2.88 \cdot 10^{-11}$ J/m and for permalloy: $M_{0,\text{Py}} = 0.658 \cdot 10^6$ A/m, $A_{\text{Py}} = 1.1 \cdot 10^{-11}$ J/m. For the gyromagnetic ratio, we assume average value proposed in [75], $\gamma = 194.6$ GHz/T, that is, the same for cobalt and permalloy. Three types of lines in Figure 3 represent the results of our calculations with the PWM for three different formulations of the exchange field taken from (35)–(36).

The dispersion relations calculated with the three different forms of the exchange field are overlapping almost perfectly (see Figure 3). It means that the effect of exchange

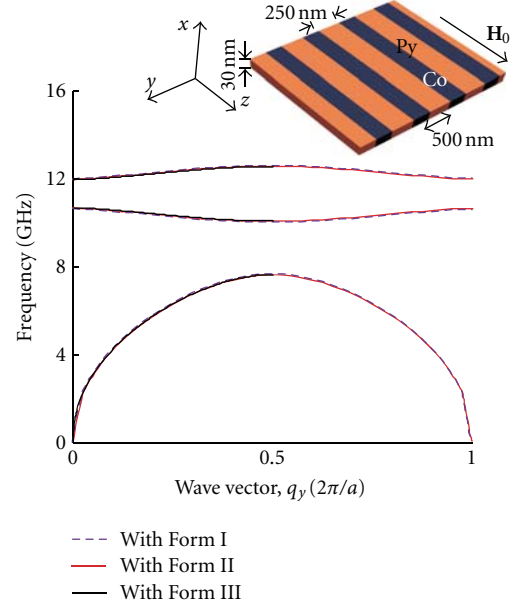


FIGURE 3: Magnonic band structures calculated for three different definitions of the exchange field (as defined in (35)–(36)) for a thin slab of the considered 1D MC. The structure of the MC is schematically shown in the inset; stripes of Co and Py with the same width are arranged periodically with the lattice constant 500 nm. Very weak external magnetic field, $\mu_0 H_0 = 0.001$ T, is directed along stripes. The magnetostatic interaction determine, the magnonic band structure—the definition of the H_{ex} is unimportant.

interactions between Co and Py is minor or even negligible for this structure. It is because the magnetostatic interactions dominate over the exchange interactions for large lattice constant.

To observe effects connected with various definitions of the exchange field in nonuniform materials, the decrease of the role of magnetostatic interaction is necessary. This can be done by decreasing a lattice constant. In Figure 4 we show the magnonic band structure for the 1D MC with 30 nm lattice constant and 15 nm width of Co and Py stripes. We change also the film thickness to 4 nm. The rest of parameters are the same as in previous calculation.

The differences connected with various definition of the exchange field start to be visible already near the BZ border and for higher modes also at the BZ center. The most essential difference can be observed between SW dispersions calculated according to Form I and Forms II and III. For the Form I (dashed line), the magnonic gap is absent between 1st and 2nd band, while for the other two formulations of H_{ex} the gap exists.

In Figures 4(b) and 4(c) the profiles of dynamical magnetization and its first derivatives with respect to y are shown for three lowest modes. The profiles are very similar for all three forms of the exchange field. The shift of the 3rd profile along y -axis for Form I of the exchange field with respect to other two can be observed. In the inset in Figure 4(c), we can see also a discontinuity of the $\partial \mathbf{m} / \partial y$ for the form I and II.

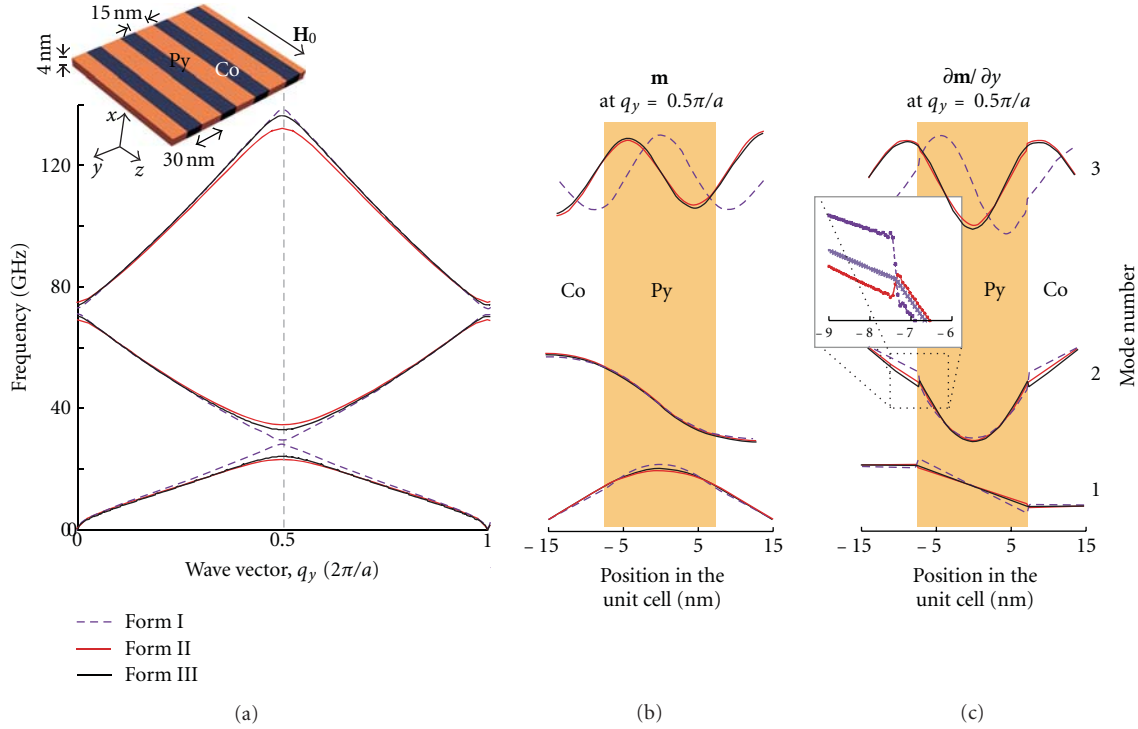


FIGURE 4: Magnonic band structure and profiles of SWs calculated for three different definitions of the exchange field for the 1D MC with the lattice constant of 30 nm and thickness 4 nm (schematically shown in the inset)—for the case of dominating exchange interaction. (a) Magnonic band structure with the Brillouin zone border marked by dashed gray line. In (b) an amplitude of the dynamical component of the magnetization vector, m_x at the border of the 1st Brillouin zone is shown. Its first derivative with respect to the y is shown in (c).

The biggest one is observed for SWs calculated with Form I of the exchange field.

4.2. 2D Magnonic Crystals. Let us consider a thin film of a 2D MC composed of ferromagnetic circular dots in the square lattice and immersed in other ferromagnetic material. First, we will calculate the SW spectrum for Co dots in Py matrix in the exchange interaction dominating regime. This is obtained by assuming small lattice constant $a = 30$ nm and thickness $d = 4$ nm. We chose the dot diameter of 14 nm. The magnonic band structure along y -axis (i.e., perpendicular to the direction of bias magnetic field), and profiles of spin-waves are shown in Figures 5(a) and 5(b), respectively. The bias magnetic field is directed along the z -axis, and it is strong enough to saturate the sample $\mu_0 H_0 = 0.2$ T.

We observed similar dependences as for the case of 1D MC in Figure 4. For the Forms II and III of the exchange field magnonic gaps (at least partial) exist, while for the Form I the bands overlap. We found also differences in the SW profiles, especially for modes with higher frequencies.

4.3. Boundary Conditions. We discussed so far PWM results for various definitions of the exchange field performed for MC consisting of two materials: Co and Py only. We showed also that the different expressions for the exchange field are important only for small lattice constant. In Figures 6(a) and 6(b) we show the magnonic band structure for a 1D and

2D MC, respectively, formed by Fe and yttrium iron garnet (YIG). We chose Fe and YIG because those materials have very different magnetization and exchange constants, which are $M_{S,Fe} = 1.752 \cdot 10^6$ A/m, $A_{Fe} = 2.1 \cdot 10^{-11}$ J/m, $M_{S,YIG} = 0.194 \cdot 10^6$ A/m, and $A_{YIG} = 0.4 \cdot 10^{-11}$ J/m. The structure of the MCs is the same as in previous studies: the lattice constant 30 nm and the film thickness 4 nm for 1D MC and $a = 30$ nm, $R = 7$ nm, thickness 4 nm for 2D MC. We found that the magnonic gap (between 1st and 2nd band) exist in all band structures, also this calculated with Form I. For the 1D MC there is a big difference between the magnonic bands and the gap width calculated with Form II of the exchange field and other two forms. It is interesting to note that at Γ point there is good agreement between various formulations of H_{ex} . In 2D MC the magnonic band structure is more complicated, gaps are smaller than for 1D but exist for all expressions of the exchange field.

Now we can try to answer the question for the physical reasons of different solutions found with Form I, II and III of the exchange field. We have seen significantly different results obtained from Form II, and Form I for Co/Py MC, while the solutions obtained from Forms II and III are close to each other. It is different to Fe/YIG MC where the solution for Form III is much closer to the solution of Form I. Those effects shall be related to BCs for dynamic components of the magnetization vector implemented in various formulations. We can obtain the BC implemented in the differential equation, in our case LL equation, by integrating them over

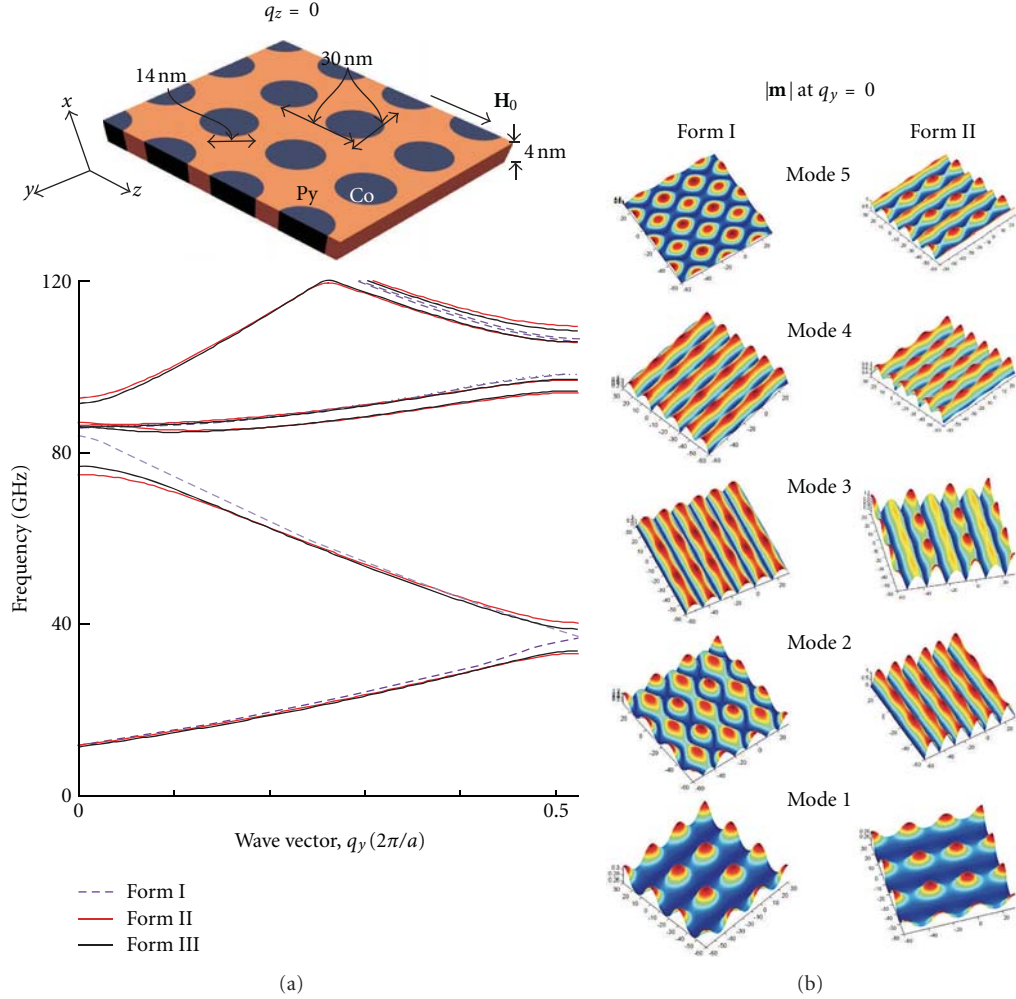


FIGURE 5: (a) Magnonic band structure calculated for three different definitions of the exchange field for 2D MC. The MC is composed of Co dots in square lattice and immersed in Py matrix. The film has a thickness of 4 nm, the lattice constant is 30 nm, and diameter of dots is 14 nm. (b) Modulus of the dynamical component of the magnetization vector calculated for the wave vector from the center of the BZ. The profiles shown are calculated for Form II and Form I of the exchange field.

the interface [9, 14, 27]. Because we are focusing on the exchange BCs, it is enough for the purpose of this study to take only terms connected with the exchange field in (41)-(42). By performing those integrations and taking a limit of a zero thickness, one can obtain the conditions of continuity of \mathbf{m} for Forms II and III, and continuity of the $\tilde{\mathbf{m}}$ for Form I. At this point the difference between calculations performed in [27] and with Form I appears. In [27] the continuity of \mathbf{m} was cast on while here is continuity of its normalized value $\tilde{\mathbf{m}}$. Also the second BC is obtained, that is, continuity of terms proportional to the first derivative of the dynamical component of the magnetization vector with respect to the normal to the interface. One can find that this BC requires the continuity of $l_{\text{ex},2}^2 \partial_n \tilde{\mathbf{m}}$, $l_{\text{ex},\text{II}}^2 \partial_n \mathbf{m}$, and $\partial_n \mathbf{m}$ for the exchange field in Forms I, II, and III, respectively. ∂_n means the derivative along the direction normal to the interface. Those boundary conditions agree with the profiles and its first derivatives found for 1D MC and shown in Figures 4(b) and 4(c),

respectively (see also the inset in Figure 4(c) for the 2nd mode). The continuity of the first derivative at the interface is observed only for Form III, as expected. However, to validate which form of the exchange field is proper one and which describe properly the real physical system is out of scope of this paper. In the literature various boundary conditions were used, for example, [6–14], but the discussion under possibility for implementing them in effective continuous models is only at the beginning stage, and further investigation is required.

5. Conclusions

We presented derivations of the two different expressions for the exchange field used in literature for SW calculations in magnonic crystals with pointing at the surface terms neglected in each case. We compared these formulas with the definition of the exchange field used for SW calculations in

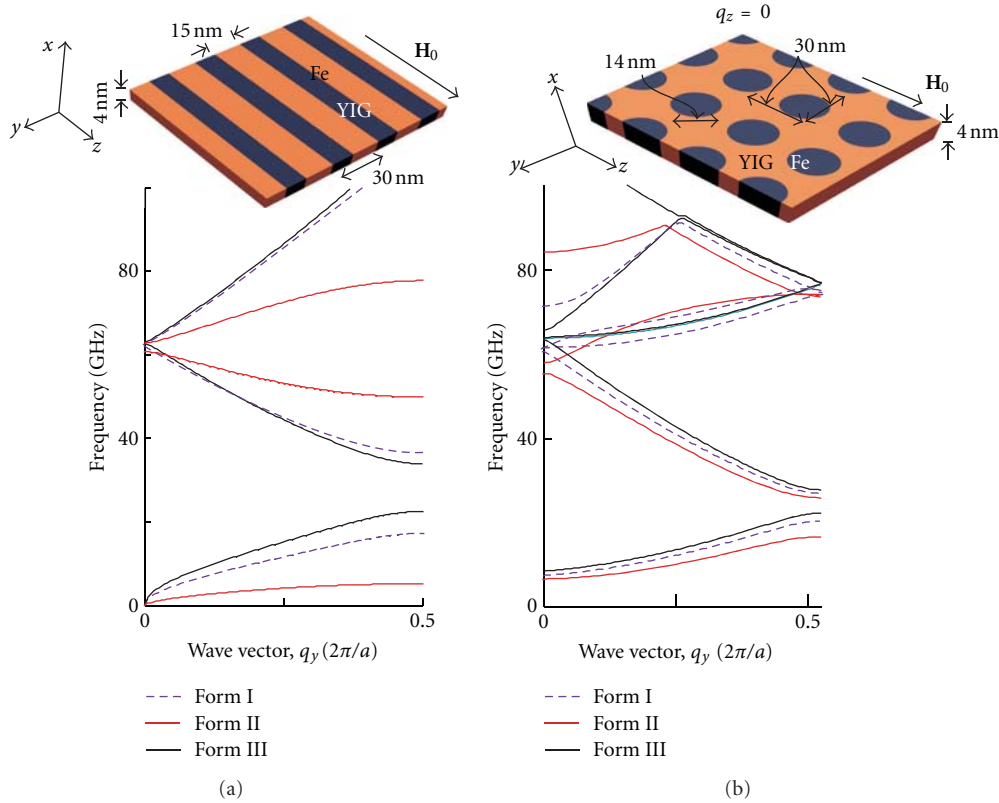


FIGURE 6: Magnonic band structure calculated for various forms of the exchange field. MCs composed of Fe and YIG were studied with a periodicity in (a) 1D and (b) 2D. The lattice constant is 30 nm and the film thickness 4 nm in both cases. The external magnetic field is applied along z-axis and has the value almost 0 for 1D MC and 0.1 T for 2D MC.

a uniform ferromagnetic material. Numerical calculations with PWM were performed to study the influence of these different expressions on the magnonic band structure and profiles of SWs in 1D and 2D planar magnonic crystals. We found that for a large lattice constant the magnonic band structure is independent of the formulation used. It is because the magnetostatic interaction dominates over the exchange one. The situation changed for small lattice constants where in dependence on the form of the exchange field used in calculations the magnonic gap can be present or absent in magnonic band structure. By numerical calculations we showed that various formulations of the exchange field have strong relation to the boundary conditions at the interfaces between two ferromagnetic materials. Further investigation is necessary to elucidate the proper form of the exchange field which fulfill the physical boundary conditions on interfaces imposed on dynamic components of the magnetization vector in magnonic crystals.

Acknowledgments

The authors acknowledge the financial support from the European Community's Seventh Framework Programme FP7/2007-2013 (Grant Agreement no. 228673 for MAGNICS). The calculations presented in this paper were performed in Poznan Supercomputing and Networking Center.

References

- [1] F. Keffer, "Spin waves," in *Handbuch Der Physik*, S. Flügge, Ed., vol. 18, Springer, Berlin, Germany, 1966.
- [2] S. Chikazumi, *Physics of Ferromagnetism*, Oxford University Press, 1997.
- [3] R. Skomsky, *Simple Models of Magnetism*, Oxford University Press, 2008.
- [4] A. G. Gurevich and G. A. Melkov, *Magnetization Oscillations and Waves*, CRC Press, 1996.
- [5] A. I. Akhiezer, V. G. Bariakhtar, and S. V. Peletminskii, *Spin Waves*, North-Holland, 1968.
- [6] F. Hoffmann, "Dynamic pinning induced by nickel layers on permalloy films," *Physica Status Solidi*, vol. 41, no. 2, pp. 807–813, 1970.
- [7] M. Vohl, J. Barnas, and P. Grünberg, "Effect of interlayer exchange coupling on spin-wave spectra in magnetic double layers: theory and experiment," *Physical Review B*, vol. 39, no. 16, pp. 12003–12012, 1989.
- [8] S. L. Vysotskii, G. T. Kazakov, and A. Yu. Filimonov, "Magnetostatic volume waves in exchange-coupled ferrite films," *Technical Physics*, vol. 43, no. 7, pp. 834–845, 1998.
- [9] D. L. Mills, "Spin waves in ultrathin exchange-coupled ferromagnetic multilayers: the boundary condition at the interface," *Physical Review B*, vol. 45, no. 22, pp. 13100–13104, 1992.
- [10] J. F. Cochran and B. Heinrich, "Boundary conditions for exchange-coupled magnetic slabs," *Physical Review B*, vol. 45, no. 22, pp. 13096–13099, 1992.

- [11] J. Barnas, "On the Hoffmann boundary conditions at the interface between two ferromagnets," *Journal of Magnetism and Magnetic Materials*, vol. 102, no. 3, pp. 319–322, 1991.
- [12] V. V. Kruglyak, A. N. Kuchko, and V. I. Finokhin, "Spin-wave spectrum of an ideal multilayer magnet upon modulation of all parameters of the Landau-Lifshitz equation," *Physics of the Solid State*, vol. 46, no. 5, pp. 867–871, 2004.
- [13] V. V. Kruglyak and A. N. Kuchko, "Spectrum of spin waves propagating in a periodic magnetic structure," *Physica B*, vol. 339, no. 2–3, pp. 130–133, 2003.
- [14] A. M. Zyuzin, S. N. Sabaev, and V. V. Radaikin, "Spectra of spin-wave resonance upon dissipative or mixed mechanisms of spin pinning," *Physics of Metals and Metallography*, vol. 102, no. 5, pp. 478–484, 2006.
- [15] B. Hillebrands, "Spin-wave calculations for multilayered structures," *Physical Review B*, vol. 41, no. 1, pp. 530–540, 1990.
- [16] R. L. Stamps and B. Hillebrands, "Dipole-exchange modes in multilayers with out-of-plane anisotropies," *Physical Review B*, vol. 44, no. 10, pp. 5095–5104, 1991.
- [17] Y. V. Gulyaev and S. A. Nikitov, "Magnonic crystals and spin waves in periodic structures," *Doklady Physics*, vol. 46, no. 10, pp. 687–689, 2001.
- [18] Y. V. Gulyaev, S. A. Nikitov, L. V. Zhivotovskii et al., "Ferromagnetic films with magnon bandgap periodic structures: magnon crystals," *JETP Letters*, vol. 77, no. 10, pp. 567–570, 2003.
- [19] J. Ben Youssef, V. Castel, N. Vukadinovic, and M. Labrune, "Spin-wave resonances in exchange-coupled Permalloy/garnet bilayers," *Journal of Applied Physics*, vol. 108, no. 6, Article ID 063909, 2010.
- [20] A. Yariv and P. Yeh, *Optical Waves in Crystals*, Wiley-Interscience, 2003.
- [21] M. N. Baibich, J. M. Broto, A. Fert et al., "Giant magnetoresistance of (001)Fe/(001)Cr magnetic superlattices," *Physical Review Letters*, vol. 61, no. 21, pp. 2472–2475, 1988.
- [22] E. Yablonovitch, "Inhibited spontaneous emission in solid-state physics and electronics," *Physical Review Letters*, vol. 58, pp. 2059–2062, 1987.
- [23] S. John, "Strong localization of photons in certain disordered dielectric superlattices," *Physical Review Letters*, vol. 58, pp. 2486–2489, 1987.
- [24] J. D. Joannopoulos, R. D. Meade, and J. N. Winn, *Photonic Crystals: Molding the Flow of Light*, Princeton University Press, Princeton, NJ, USA, 2nd edition, 2008.
- [25] M. Skorobogatiy and J. Yang, *Fundamentals of Photonic Crystal Guiding*, Cambridge University Press, 2009.
- [26] M. S. Kushwaha, P. Halevi, L. Dobrzynski, and B. Djafari-Rouhani, "Acoustic band structure of periodic elastic composites," *Physical Review Letters*, vol. 71, no. 13, pp. 2022–2025, 1993.
- [27] J. O. Vasseur, L. Dobrzynski, B. Djafari-Rouhani, and H. Puszkarski, "Magnon band structure of periodic composites," *Physical Review B*, vol. 54, no. 2, pp. 1043–1049, 1996.
- [28] M. Krawczyk and H. Puszkarski, "Plane-wave theory of three-dimensional magnonic crystals," *Physical Review B*, vol. 77, no. 5, Article ID 054437, 13 pages, 2008.
- [29] V. Kruglyak, O. Demokritov, and D. Grundler, "Preface: magnonics," *Journal of Physics D*, vol. 43, no. 26, Article ID 260301, 2010.
- [30] B. Lenk, H. Ulrichs, F. Garbs, and M. Münzenberg, "The building blocks of magnonics," *Physics Reports*, vol. 507, no. 4–5, pp. 107–136, 2011.
- [31] S. Neusser and D. Grundler, "Magnonics: spin waves on the nanoscale," *Advanced Materials*, vol. 21, no. 28, pp. 2927–2932, 2009.
- [32] A. A. Serga, A. V. Chumak, and B. Hillebrands, "YIG magnonics," *Journal of Physics D*, vol. 43, no. 26, Article ID 264002, 2010.
- [33] T. Schneider, A. A. Serga, B. Leven, B. Hillebrands, R. L. Stamps, and M. P. Kostylev, "Realization of spin-wave logic gates," *Applied Physics Letters*, vol. 92, no. 2, Article ID 022505, 2008.
- [34] F. Macia, A. D. Kent, and F. C. Hoppensteadt, "Spin-wave interference patterns created by spin-torque nano-oscillators for memory and computation," *Nanotechnology*, vol. 22, no. 9, Article ID 095301, 2011.
- [35] A. Khitun, M. Bao, and K. L. Wang, "Magnonic logic circuits," *Journal of Physics D*, vol. 43, no. 26, Article ID 264005, 2010.
- [36] R. V. Mikhaylovskiy, E. Hendry, and V. V. Kruglyak, "Negative permeability due to exchange spin-wave resonances in thin magnetic films with surface pinning," *Physical Review B*, vol. 82, no. 19, Article ID 195446, 10 pages, 2010.
- [37] M. Donahue and D. Porter, "OOMMF users guide, version 1.0," Tech. Rep., National Institute of Standards and Technology, Gaithersburg, Md, USA, 1999.
- [38] M. R. Scheinfein, "LLG-micromagnetics simulator," 2008, <http://llgmicro.home.mindspring.com/>.
- [39] D. Berkov, "Micromagus-software for micromagnetic simulation," 2008, <http://www.micromagus.de/>.
- [40] T. Fischbacher, M. Franchin, G. Bordignon, and H. Fangohr, "A systematic approach to multiphysics extensions of finite-element-based micromagnetic simulations: Nmag," *IEEE Transactions on Magnetics*, vol. 43, no. 6, pp. 2896–2898, 2007.
- [41] M. Grimsditch, L. Giovannini, F. Montoncello, F. Nizzoli, G. K. Leaf, and H. G. Harper, "Magnetic normal modes in ferromagnetic nanoparticles: a dynamical matrix approach," *Physical Review B*, vol. 70, no. 5, Article ID 054409, 7 pages, 2004.
- [42] M. Grimsditch, L. Giovannini, F. Montoncello et al., "Magnetic normal modes in nano-particles," *Physica B*, vol. 354, no. 1–4, pp. 266–270, 2004.
- [43] A. Luque, A. Martí, E. Antolín et al., "New Hamiltonian for a better understanding of the quantum dot intermediate band solar cells," *Solar Energy Materials and Solar Cells*, vol. 95, no. 8, pp. 2095–2101, 2011.
- [44] J. W. Klos and M. Krawczyk, "Electronic and hole spectra of layered systems of cylindrical rod arrays: solar cell application," *Journal of Applied Physics*, vol. 107, no. 4, Article ID 043706, 5 pages, 2010.
- [45] O. L. Lazarenkova and A. A. Balandin, "Miniband formation in a quantum dot crystal," *Journal of Applied Physics*, vol. 89, no. 10, pp. 5509–5515, 2001.
- [46] J. M. Levy-Leblond, "Position-dependent effective mass and Galilean invariance," *Physical Review A*, vol. 52, no. 3, pp. 1843–1849, 1995.
- [47] J. Thomsen, G. T. Einevoll, and P. C. Hemmer, "Operator ordering in effective-mass theory," *Physical Review B*, vol. 39, no. 17, pp. 12783–12788, 1989.
- [48] U. E. H. Laheld and P. C. Hemmer, "Matching conditions for effective-mass functions at an abrupt heterojunction, tested on an exactly solvable model," *Physica Scripta*, vol. 59, no. 5, pp. 405–410, 1999.
- [49] M. G. Burt, "Direct derivation of effective-mass equations for microstructures with atomically abrupt boundaries," *Physical Review B*, vol. 50, no. 11, pp. 7518–7525, 1994.

- [50] B. A. Foreman, "Effective-mass Hamiltonian and boundary conditions for the valence bands of semiconductor microstructures," *Physical Review B*, vol. 48, no. 7, pp. 4964–4967, 1993.
- [51] M. V. Kisin, B. L. Gelmont, and S. Luryi, "Boundary-condition problem in the Kane model," *Physical Review B*, vol. 58, no. 8, pp. 4605–4616, 1998.
- [52] S. De Franceschi, J. M. Jancu, and F. Beltram, "Boundary conditions in multiband $k \cdot p$ models: a tight-binding test," *Physical Review B*, vol. 59, no. 15, pp. 9691–9694, 1999.
- [53] G. T. Einevoll and L. J. Sham, "Boundary conditions for envelope functions at interfaces between dissimilar materials," *Physical Review B*, vol. 49, no. 15, pp. 10533–10543, 1994.
- [54] M. E. Pistol, "Boundary conditions in the effective-mass approximation with a position-dependent mass," *Physical Review B*, vol. 60, no. 20, pp. 14269–14271, 1999.
- [55] A. V. Rodina, A. Yu. Alekseev, L. Al. Efros, M. Rosen, and B. K. Meyer, "General boundary conditions for the envelope function in the multiband $k \cdot p$ model," *Physical Review B*, vol. 65, no. 12, Article ID 125302, 12 pages, 2002.
- [56] G. T. Einevoll, P. C. Hammer, and J. Thomsen, "Operator ordering in effective-mass theory for heterostructures. I. Comparison with exact results for superlattices, quantum wells, and localized potentials," *Physical Review B*, vol. 42, no. 6, pp. 3485–3496, 1990.
- [57] R. Balian, D. Bessis, and G. A. Mezincescu, "Form of kinetic energy in effective-mass Hamiltonians for heterostructures," *Physical Review B*, vol. 51, no. 24, pp. 17624–17629, 1995.
- [58] G. T. Einevoll, "Operator ordering in effective-mass theory for heterostructures. II. Strained systems," *Physical Review B*, vol. 42, no. 6, pp. 3497–3502, 1990.
- [59] D. D. Stancil and A. Prabhakar, *Spin Waves*, Springer, 2nd edition, 2009.
- [60] D. W. Prather, S. Shi, A. Sharkawy, J. Murakowski, and G. J. Schneider, *Photonic Crystals: Theory, Applications, and Fabrication*, John Wiley & Sons, 2009.
- [61] V. Laude, M. Wilm, S. Benchabane, and A. Khelif, "Full band gap for surface acoustic waves in a piezoelectric phononic crystal," *Physical Review E*, vol. 71, no. 3, Article ID 036607, 7 pages, 2005.
- [62] M. Krawczyk and H. Puzkarski, "Magnonic spectra of ferromagnetic composites versus magnetization contrast," *Acta Physica Polonica A*, vol. 93, no. 5-6, pp. 805–810, 1998.
- [63] M. Krawczyk and H. Puzkarski, "Absolute gaps in magnonic spectra of periodic two-dimensional ferromagnetic composites," *Acta Physicae Superficierum*, vol. 3, pp. 89–102, 1999.
- [64] H. Puzkarski and M. Krawczyk, "Magnonic crystals—the magnetic counterpart of photonic crystals," *Solid State Phenomena*, vol. 94, pp. 125–134, 2003.
- [65] M. Krawczyk and H. Puzkarski, "Magnonic excitations versus three-dimensional structural periodicity in magnetic composites," *Crystal Research and Technology*, vol. 41, no. 6, pp. 547–552, 2006.
- [66] J. O. Vasseur, P. A. Deymier, B. Djafari-Rouhani, Y. Pennec, and A. C. Hladky-Hennion, "Absolute forbidden bands and waveguiding in two-dimensional phononic crystal plates," *Physical Review B*, vol. 77, no. 8, Article ID 085415, 2008.
- [67] R. P. Tiwari and D. Stroud, "Magnetic superlattice with two-dimensional periodicity as a waveguide for spin waves," *Physical Review B*, vol. 81, no. 22, Article ID 220403, 4 pages, 2010.
- [68] M. L. Sokolovskyy and M. Krawczyk, "The magnetostatic modes in planar one-dimensional magnonic crystals with nanoscale sizes," *Journal of Nanoparticle Research*, vol. 13, no. 11, pp. 6085–6091, 2011.
- [69] J. W. Klos, M. Krawczyk, and M. L. Sokolovskyy, "Bulk and edge modes in two-dimensional magnonic crystal slab," *Journal of Applied Physics*, vol. 109, no. 7, Article ID 07D311, 3 pages, 2011.
- [70] S. Neusser, G. Duerr, S. Tacchi et al., "Magnonic minibands in antidot lattices with large spin-wave propagation velocities," *Physical Review B*, vol. 84, no. 9, Article ID 094454, 9 pages, 2011.
- [71] S. Neusser, H. G. Bauer, G. Duerr et al., "Tunable metamaterial response of a $\text{Ni}_{80}\text{Fe}_{20}$ antidot lattice for spin waves," *Physical Review B*, vol. 84, no. 18, Article ID 184411, 11 pages, 2011.
- [72] H. Yang, G. Yun, and Y. Cao, "Point defect states of exchange spin waves in all-ferromagnetic two-dimensional magnonic crystals," *Journal of Applied Physics*, vol. 111, no. 1, Article ID 013908, 2012.
- [73] J. Kaczer and L. Murtinova, "On the demagnetizing energy of periodic magnetic distributions," *Physica Status Solidi*, vol. 23, no. 1, pp. 79–86, 1974.
- [74] Y. Cao, G. Yun, X. Liang, and N. Bai, "Band structures of two-dimensional magnonic crystals with different shapes and arrangements of scatterers," *Journal of Physics D*, vol. 43, no. 30, Article ID 305005, 2010.
- [75] Z. K. Wang, V. L. Zhang, H. S. Lim et al., "Observation of frequency band gaps in a one-dimensional nanostructured magnonic crystal," *Applied Physics Letters*, vol. 94, no. 8, Article ID 083112, 3 pages, 2009.
- [76] Z. K. Wang, V. L. Zhang, H. S. Lim et al., "Nanostructured magnonic crystals with size-tunable bandgaps," *ACS Nano*, vol. 4, no. 2, pp. 643–648, 2010.
- [77] M. Kostylev, P. Schrader, R. L. Stamps et al., "Partial frequency band gap in one-dimensional magnonic crystals," *Applied Physics Letters*, vol. 92, no. 13, Article ID 132504, 2008.
- [78] V. L. Zhang, H. S. Lim, C. S. Lin et al., "Ferromagnetic and antiferromagnetic spin-wave dispersions in a dipole-exchange coupled bi-component magnonic crystal," *Applied Physics Letters*, vol. 99, no. 14, Article ID 143118, 3 pages, 2012.
- [79] C. S. Lin, H. S. Lim, Z. K. Wang, S. C. Ng, and M. H. Kuok, "Band gap parameters of one-dimensional bicomponent nanostructured magnonic crystals," *Applied Physics Letters*, vol. 98, no. 2, Article ID 022504, 3 pages, 2010.

Research Article

On the Travelling Wave Solution for the Current-Driven Steady Domain Wall Motion in Magnetic Nanostrips under the Influence of Rashba Field

Vito Puliafito¹ and Giancarlo Consolo²

¹ Department of Matter Physics and Electronic Engineering, University of Messina, V.le F. Stagno D'Alcontres 31, 98166 Messina, Italy

² Department of Science for Engineering and Architecture, University of Messina, Contrada Di Dio, 98166 Messina, Italy

Correspondence should be addressed to Vito Puliafito, vpuliafito@unime.it

Received 31 March 2012; Revised 17 May 2012; Accepted 19 May 2012

Academic Editor: Roberto Zivieri

Copyright © 2012 V. Puliafito and G. Consolo. This is an open access article distributed under the Creative Commons Attribution License, which permits unrestricted use, distribution, and reproduction in any medium, provided the original work is properly cited.

Spin-orbit Rashba effect applies a torque on the magnetization of a ferromagnetic nanostrip in the case of structural inversion asymmetry, also affecting the steady domain wall motion induced by a spin-polarized current. This influence is here analytically studied in the framework of the extended Landau-Lifshitz-Gilbert equation, including the Rashba effect as an additive term of the effective field. Results of previous micromagnetic simulations and experiments have shown that this field yields an increased value of the Walker breakdown current together with an enlargement of the domain wall width. In order to analytically describe these results, the standard travelling wave ansatz for the steady domain wall motion is here adopted. Results of our investigations reveal the impossibility to reproduce, at the same time, the previous features and suggest the need of a more sophisticated model whose development requires, in turn, additional information to be extracted from ad hoc micromagnetic simulations.

1. Introduction

Magnetization dynamics in nanodevices has been intensely investigated in the last decades as it provides a wide variety of technological applications in the area of storage and logic devices. Formerly, the manipulation of the magnetic configuration was typically achieved by means of external magnetic fields but the contemporary demand of miniaturizing storage devices and of increasing their capacity would have required higher and higher fields. An alternative method, realized by using spin-polarized currents, was outlined by the discovery of spin-transfer torque effect [1, 2]. Theoretical and experimental studies, therefore, examined magnetization dynamics due to the simultaneous action of external magnetic fields and electric currents [3–5] as well as current-driven dynamics at zero field [6, 7].

Among the different geometries used for spintronic devices, a more recent attention is directed to magnetic

nanowires and strips [8–22]. Such thin ferromagnetic structures turn out to be relevant for the realization of oscillators and high-density memories with low energy consumption [9]. In particular, their behavior and applications are strictly connected to the motion of magnetic domain walls (DWs), namely, the continuous transition regions that separate two uniformly and oppositely magnetized domains [9, 10]. Also, in this case, DW dynamics can be activated by means of an external field or an electric current. Independently of the nature of the source term, it has been widely demonstrated that, by varying the strength of such a driving source, the DW motion experiences two different dynamical regimes. At low fields (or currents), the equilibrium wall structure is rigidly shifted along the nanostrip (or nanowire) axis, leading to a “steady” regime of high DW mobility. Above a critical field (or current) value, named Walker breakdown, a regime of lower DW mobility takes place and the internal deformation is so strong that the wall structure is altered giving rise to a

periodical alternation of Bloch and Néel DW structures. Such a dynamics is generally referred to as “precessional” regime [11].

DW motion can be also strongly modified by spin-orbit interaction [12] that takes place in the case of structural inversion asymmetry of the nanodevice. Some previous works [13–18], in particular, pointed out that this effect, induced by the flow of an electric current through the material, acts as an effective field. This contribution, which was named Rashba field, produces two main consequences: (1) a (Bloch-like) DW structure is stabilized as the steady regime turns broadened up to higher current densities so allowing higher DW velocities; (2) the DW width enlarges with the increase of the current-induced Rashba field.

From the theoretical viewpoint, DW motion in ferromagnetic thin layers is ruled by the extended Landau-Lifshitz-Gilbert (ELLG) equation including the current-driven spin-torque effects [20–24]. Travelling wave solutions for the ELLG equation have been recently obtained, providing a strong theoretical support for both experimental and numerical results [20, 22]. It has been also demonstrated that the inclusion of a different dissipation function into the ELLG equation, usually referred to as “dry-friction,” gives a good description of DW dynamics in the presence of crystallographic defects and structural disorder [20, 22].

In this work, we propose to analytically study, by using a one-dimensional mathematical model, the steady DW motion in ferromagnetic nanostrips subject to the action of spin-polarized currents and Rashba fields. In particular, we investigate on the appropriateness of using a standard travelling wave ansatz describing a Bloch DW structure which rigidly shifts under the action of the external source. In order to validate the developed model, these analytical results are then compared, at qualitative level, with those arising from recent numerical and experimental investigations. The model also accounts for the nonlinear dry-friction dissipation function in order to evaluate how such a contribution affects the current-driven steady DW motion in the presence of a Rashba field.

2. The Analytical One-Dimensional Model: Results and Discussion

As depicted in Figure 1, a ferromagnetic nanostrip can be represented by a rectangular prism of length l , width w , and thickness t along \mathbf{c}_x , \mathbf{c}_y , \mathbf{c}_z axes, respectively, with $l \gg w > t$. Let us assume that an electric current density $\mathbf{J} = J\mathbf{c}_x$, constant in time and uniform in space, is applied to the device along the \mathbf{c}_x axis. Under the hypothesis that the Rashba field does not modify the equilibrium configuration obtained in its absence, we assume that a 180° DW of width δ is nucleated at the center of the structure with the magnetization vector that rotates between the state $(0,0,1)$ at $x \rightarrow -\infty$ and the opposite one $(0,0,-1)$ at $x \rightarrow \infty$. These uniformly magnetized states, far away from the wall location, are hence supposed to be directed towards the easy axis $\mathbf{c}_z = \mathbf{e}$, namely, the energetically preferred direction of spontaneous magnetization.

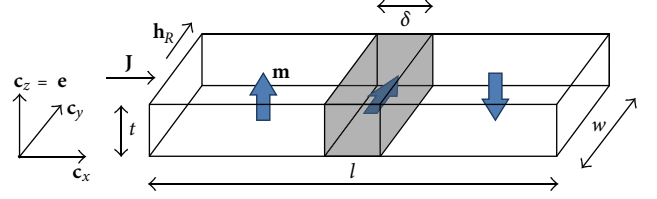


FIGURE 1: Schematics of a ferromagnetic nanostrip exhibiting a Bloch DW.

Current-driven DW dynamics in such a thin layer is described by the ELLG equation [20–24]:

$$\dot{\mathbf{m}} = \gamma(\mathbf{h}_{\text{eff}} \wedge \mathbf{m}) + \mathbf{t}_d + \mathbf{t}_{\text{st}}, \quad (1)$$

where the over-dot denotes time derivation, $\mathbf{m} = \mathbf{M}/M_S$ is the unit vector along the local magnetization and all the field vectors are normalized with respect to the saturation magnetization M_S . The constant $\gamma = M_S\mu_0\gamma_e$ is expressed in terms of the vacuum magnetic permeability μ_0 and the gyromagnetic ratio $\gamma_e = ge/m_e$, being g the Landé factor, e the electron charge, and m_e the electron mass. The first term in the right-hand side of (1) describes the precession of magnetization \mathbf{m} around the direction of the effective magnetic field \mathbf{h}_{eff} , the second term \mathbf{t}_d is the dissipative torque representing energy dissipation, and \mathbf{t}_{st} corresponds to the current-induced spin torque.

The effective magnetic field $\mathbf{h}_{\text{eff}} = -\partial W/\partial \mathbf{m}$, calculated as the variational derivative of the free energy density W , accounts for external \mathbf{h}_{ext} , exchange \mathbf{h}_{exc} , demagnetizing \mathbf{h}_{dmg} , anisotropy \mathbf{h}_{an} , and Rashba \mathbf{h}_R fields:

$$\mathbf{h}_{\text{eff}} = \mathbf{h}_{\text{ext}} + \mathbf{h}_{\text{exc}} + \mathbf{h}_{\text{dmg}} + \mathbf{h}_{\text{an}} + \mathbf{h}_R, \quad (2)$$

As our attention focuses on the influence of the current-induced Rashba field, we will limit our analysis to the zero-field configuration:

$$\mathbf{h}_{\text{ext}} = 0. \quad (3)$$

The exchange field can be written as

$$\mathbf{h}_{\text{exc}} = A \frac{\partial^2 \mathbf{m}}{\partial x^2} \quad (4)$$

being A related to the exchange constant A_{ex} of the material through

$$A = \frac{2A_{\text{ex}}}{\mu_0 M_S^2}. \quad (5)$$

The demagnetizing field can be approximated by considering the only diagonal terms of the corresponding tensor which relates the field to the magnetization [11]:

$$\mathbf{h}_{\text{dmg}} = -N_x(\mathbf{m} \cdot \mathbf{c}_x)\mathbf{c}_x - N_y(\mathbf{m} \cdot \mathbf{c}_y)\mathbf{c}_y - N_z(\mathbf{m} \cdot \mathbf{e})\mathbf{e}, \quad (6)$$

where N_x , N_y , and N_z are the demagnetizing factors satisfying the normalization condition $N_x + N_y + N_z = 1$. These coefficients depend both on the shape (assumed to be

a rectangular prism) and on the dimensions ($w \times t \times \delta$) of the DW.

We also assume that the strip is made by a material exhibiting a high perpendicular magnetic anisotropy, so that we can express

$$\mathbf{h}_{\text{an}} = \beta(\mathbf{m} \cdot \mathbf{e})\mathbf{e}, \quad (7)$$

where $\beta \gg 1$ is proportional to the anisotropy constant K of the material through

$$\beta = \frac{2K}{\mu_0 M_S^2}. \quad (8)$$

Finally, the Rashba field is given by [13–18]:

$$\mathbf{h}_R = \frac{\alpha_R P}{\mu_0 \mu_B M_S^2} (\mathbf{e} \wedge \mathbf{J}) \quad (9)$$

being α_R the Rashba parameter, P the polarization factor of the current, and μ_B the Bohr magneton. The expression (9) can be also written in compact form as

$$\mathbf{h}_R = \chi u \mathbf{c}_y, \quad (10)$$

where χ accounts for the Rashba effect, $\chi = (2e/g\mu_0\mu_B^2 M_S)\alpha_R$, and the spin-torque velocity u accounts for the applied current, $u = (g\mu_B P/2eM_S)J$.

The dissipative torque \mathbf{t}_d is here described by the phenomenological Gilbert-like expression that also includes a dry-friction damping function [19–22]:

$$\mathbf{t}_d = \mathbf{m} \wedge \left[\alpha_G + \frac{\zeta}{|\dot{\mathbf{m}}|} \right] \dot{\mathbf{m}}, \quad (11)$$

Being α_G the classical linear damping coefficient and ζ the phenomenological dry-friction parameter (for more details on the dry-friction formulation, together with its practical justification within the equation of motion, see [20–22]).

The spin transfer torque \mathbf{t}_{st} is given by

$$\mathbf{t}_{\text{st}} = u(-1 + \eta \mathbf{m} \wedge) \frac{\partial \mathbf{m}}{\partial x}, \quad (12)$$

where η is the phenomenological nonadiabatic spin-torque parameter [10].

Taking into account (3)–(12), (1) becomes

$$\begin{aligned} \dot{\mathbf{m}} - \left[\alpha_G + \frac{\zeta}{|\dot{\mathbf{m}}|} \right] (\mathbf{m} \wedge \dot{\mathbf{m}}) \\ = \left(\gamma \mathbf{h}_{\text{eff}} - u \mathbf{m} \wedge \frac{\partial \mathbf{m}}{\partial x} - \eta u \frac{\partial \mathbf{m}}{\partial x} \right) \wedge \mathbf{m} \end{aligned} \quad (13)$$

with

$$\begin{aligned} \mathbf{h}_{\text{eff}} = A \frac{\partial^2 \mathbf{m}}{\partial x^2} + (\beta - N_z)(\mathbf{m} \cdot \mathbf{e})\mathbf{e} \\ - N_x(\mathbf{m} \cdot \mathbf{c}_x)\mathbf{c}_x - N_y(\mathbf{m} \cdot \mathbf{c}_y)\mathbf{c}_y + \chi u \mathbf{c}_y. \end{aligned} \quad (14)$$

Let us now make a transformation from the Cartesian to the spherical frame, so that it is possible to express the local magnetization as:

$$\mathbf{m} = \cos \varphi \sin \vartheta \mathbf{c}_x + \sin \varphi \sin \vartheta \mathbf{c}_y + \cos \vartheta \mathbf{e}. \quad (15)$$

From (13)–(15), we therefore obtain a system of two second-order partial differential equations:

$$\begin{aligned} \dot{\vartheta} + \left[\alpha_G + \left(\dot{\vartheta}^2 + \sin^2 \vartheta \dot{\varphi}^2 \right)^{-1/2} \zeta \right] \sin \vartheta \dot{\varphi} \\ = A \gamma \sin \vartheta \frac{\partial^2 \varphi}{\partial x^2} + 2A \gamma \cos \vartheta \frac{\partial \varphi}{\partial x} \frac{\partial \vartheta}{\partial x} \\ + \gamma (N_x - N_y) \sin \varphi \cos \varphi \sin \vartheta \\ - \eta u \sin \vartheta \frac{\partial \varphi}{\partial x} - u \frac{\partial \vartheta}{\partial x} + \gamma \chi u \cos \varphi \\ \sin \vartheta \dot{\varphi} - \left\{ \left[\alpha_G + \left(\dot{\vartheta}^2 + \sin^2 \vartheta \dot{\varphi}^2 \right)^{-1/2} \zeta \right] \dot{\vartheta} \right\} \\ = -A \gamma \frac{\partial^2 \vartheta}{\partial x^2} + A \gamma \sin \vartheta \cos \vartheta \left(\frac{\partial \varphi}{\partial x} \right)^2 \\ + \gamma \sin \vartheta \cos \vartheta (\beta - N_z + N_x \cos^2 \varphi + N_y \sin^2 \varphi) \\ - u \sin \vartheta \frac{\partial \varphi}{\partial x} + \eta u \frac{\partial \vartheta}{\partial x} - \gamma \chi u \sin \varphi \cos \vartheta. \end{aligned} \quad (16)$$

Since it was demonstrated that the previous system admits analytical solutions in the form of travelling waves [19–22], we search for such solutions apt to describe the DW motion within the steady regime. In particular, in order to reduce the system (16) to a couple of ordinary differential equations, we study the appropriateness of adopting the commonly used travelling wave ansatz $\vartheta = \vartheta(x - vt)$, where the DW velocity v is assumed to be a positive constant, and $\varphi = \varphi_0 = \text{constant}$. By using this strategy, we get

$$\begin{aligned} (u - v)\vartheta' &= \gamma \cos \varphi_0 \left[(N_x - N_y) \sin \varphi_0 \sin \vartheta + \chi u \right] \\ (\alpha_G v - \eta u)\vartheta' + \hat{\zeta} &= -\gamma A \vartheta'' \\ + \gamma \sin \vartheta \cos \vartheta (\beta - N_z + N_x \cos^2 \varphi_0 + N_y \sin^2 \varphi_0) \\ - \gamma \chi u \sin \varphi_0 \cos \vartheta, \end{aligned} \quad (17)$$

where $\hat{\zeta} = \zeta \text{sign}(v\vartheta')$, while the prime denotes the derivative with respect to the travelling wave variable $x - vt$ and the boundary conditions take the Dirichlet form $\vartheta(-\infty) = 0$, $\vartheta(+\infty) = \pi$. We can recast (17)₁ in the following form:

$$\vartheta' = \Gamma_0 (\sin \vartheta + \rho), \quad (18)$$

where

$$\begin{aligned} \rho &= \frac{\gamma \chi u \cos \varphi_0}{(u - v)\Gamma_0} \\ \Gamma_0 &= \frac{\gamma (N_x - N_y) \cos \varphi_0 \sin \varphi_0}{u - v}. \end{aligned} \quad (19)$$

In (19)₁ the parameter ρ accounts for the presence of the Rashba field. For what concerns (19)₂, let us remind that, in the absence of the Rashba field and nonlinear dissipations, we recover the classical definition of DW width $\Gamma_0^{-1} = \delta$ [10, 11, 20] with

$$\delta = \sqrt{\frac{A}{\beta - N_z + N_y + (N_x - N_y)\cos^2\varphi_0}}. \quad (20)$$

Let us also notice that the knowledge of the DW width requires, as shown in (20), the value of the demagnetizing factors (N_x, N_y, N_z). On the other hand, as discussed after (6), the demagnetizing factors can be computed once the DW width is known. This apparent conflict is generally solved by determining the DW width by means of alternative methods (e.g., by extracting it either from the profile of the travelling wave computed numerically and/or analytically, or from experiments).

Substituting (18) in (17)₂, after some algebraic steps, leads to

$$\widehat{M} \sin \vartheta + \widehat{Q} \sin \vartheta \cos \vartheta + \widehat{S} \cos \vartheta + \widehat{P} = 0, \quad (21)$$

where

$$\begin{aligned} \widehat{M} &= \Gamma_0(\alpha_G v - \eta u) \\ \widehat{Q} &= \gamma \left[A \Gamma_0^2 - (\beta - N_z + N_x \cos^2 \varphi_0 + N_y \sin^2 \varphi_0) \right] \\ \widehat{S} &= \gamma \chi u \left(\sin \varphi_0 + \frac{\gamma A \Gamma_0 \cos \varphi_0}{u - v} \right) \\ \widehat{P} &= (\alpha_G v - \eta u) \frac{\gamma \chi u \cos \varphi_0}{u - v} + \zeta, \end{aligned} \quad (22)$$

By performing the average of (21) over the DW width (i.e., for $0 \leq \vartheta \leq \pi$) and taking into account that the terms defined in (22) do not depend on ϑ , it is possible to derive the following expression for the DW velocity v as a function of the current-dependent spin-torque velocity u :

$$v = \frac{(\eta \chi \Gamma_0 / (N_x - N_y)) u^2 + (2 \eta \Gamma_0 / \pi) u - \zeta}{(\alpha_G \chi \Gamma_0 / (N_x - N_y)) u + (2 \alpha_G \Gamma_0 / \pi)}, \quad (23)$$

where it is supposed to deal with a DW of Bloch type ($\varphi_0 = \pi/2$) [19, 20].

As pointed out in some previous works [20–22], the inclusion of a dry-friction dissipation generally yields the steady DW motion to take place for values of the input stimulus which overcome a well-defined threshold. Equation (23) gives also the possibility to determine such a threshold current, defined as the minimum current value which satisfies the condition $v \geq 0$. In order to properly investigate on this aspect (and to emphasize the sole effect of the Rashba field), let us consider the two separate cases corresponding to the presence and the absence of the dry-friction dissipation function.

2.1. DW Dynamics in the Absence of Dry-Friction ($\zeta = 0$). If we exclude the additive dry friction term in the dissipation function, (23) simply reduces to

$$v = \frac{\eta}{\alpha_G} u \quad (24)$$

that, interestingly, matches exactly the current-driven steady DW velocity derived in the absence of the Rashba field [20, 22]. It is also straightforward to notice that, in the perfect adiabatic case ($\eta = 0$), no DW motion occurs. Equation (24) also implies that the threshold current is null:

$$u_{\text{th}} = 0, \quad (25)$$

so that the DW motion takes place for any nonnull value of the applied current. Results coming from (24) and (25), which clearly claim that the Rashba field does not modify the DW velocity (and, in turn, the DW mobility, defined as the ratio between the velocity and the input current) and the threshold current, satisfactorily agree with the recent experimental [14, 15] and numerical [17, 18] investigations. However, since these studies pointed out an increase of the Walker breakdown value and an enlargement of the DW width, we perform further investigations in this direction to validate the appropriateness of our initial conjectures.

In order to determine the Walker breakdown, from the definition (19)₁, we can write

$$\sin 2\varphi_0 = \frac{2\Gamma_0(u - v)}{\gamma(N_x - N_y)} \quad (26)$$

that implies

$$u - \frac{\gamma}{2\Gamma_0} |N_x - N_y| \leq v \leq u + \frac{\gamma}{2\Gamma_0} |N_x - N_y|. \quad (27)$$

Let us remember that the left and the right implications of (27) are representative of the so-called lower and upper Walker breakdown conditions, respectively [20–22]. They define the range of the input source in which the steady DW motion takes place.

By comparing the expression of the DW velocity (24) and the breakdown condition (27) with those derived in the absence of the Rashba field [20, 22], we report no differences which, at first, would lead to conclude that the inclusion of this field contribution has no influence on the DW dynamics at all. Nonetheless, as mentioned previously, the works carried out in [15, 17] have shown that, in a framework with Rashba field and no internal disorder, in spite of the DW mobility that is unchanged, the upper Walker breakdown is increased (the lower breakdown brings a nonnegligible contribution only in the presence of nonlinear dissipations [22]). Since our results do not allow to apparently satisfy this latter property, we therefore ask on the reasons of this discrepancy. We believe that the answer has to be searched in the numerical values of the parameters appearing in the expression of the Walker breakdown. In detail, we can hypothesize that the Rashba field has changed the modulus of the quantity $\gamma|N_x - N_y|/2\Gamma_0$, making it somehow larger. In particular, considering that the expression of Γ_0 (19) is not formally affected, the only way to obtain such an increase is that the demagnetizing factors, strictly related to the DW width, are varied. In order to find out if our conjecture is correct, we search for the expression of the DW profile by

integrating (18). The resolving procedure strictly depends on the parameter ρ that can be recast in the form:

$$\rho = \frac{\chi u}{(N_x - N_y)}. \quad (28)$$

For completeness, let us remember first that, in the case $\rho = 0$, corresponding to the absence of Rashba field, the solution is in the classical form [19, 20]:

$$\vartheta = 2 \arctan \left[e^{\Gamma_0(x-vt)} \right], \quad (29)$$

where Γ_0 indeed equals the inverse of the DW width.

Let us discuss, now, the solutions obtained as a function of the strength of the quantity $|\rho|$.

For $|\rho| < 1$, the solution can be expressed as

$$\vartheta = \arccos \frac{1 - f^2(x - vt)}{1 + f^2(x - vt)}, \quad (30)$$

where the expression of the function f can be found in (99)–(102) of [19] and in (35) of [20]. In this case, the DW profile (30) is distorted with respect to the classical case, as shown in Figure 4 of [19], and, in particular, the DW width increases with increasing ρ . Under this circumstance, therefore, the analytical model confirms the enlargement of the DW width which was highlighted in a previous work [18]. Nevertheless, this increase of the DW width changes, in turn, the values of the demagnetizing factors, in such a way that N_x approaches N_y , leading to an overall decrease of the quantity $|N_x - N_y|$, so lowering the Walker breakdown value. This latter evidence is thus in contradiction with the other expected feature of the dynamics under investigation.

For this reason, we can hypothesize that the correct solution has to be searched for $|\rho| > 1$. The solution in this case is

$$\vartheta = 2 \arctan \left\{ \frac{\sqrt{\rho^2 - 1} \tan \left[\Gamma_0 \sqrt{\rho^2 - 1} (x - vt) + \kappa \right] - 1}{\rho} \right\} \quad (31)$$

being κ the integration constant

$$\kappa = \frac{1}{\sqrt{\rho^2 - 1}} \arctan \left(\frac{\rho + 1}{\sqrt{\rho^2 - 1}} \right) \quad (32)$$

that has to be chosen in such a way the variable ϑ , evaluated at the center of the DW, is null. It should be indeed mentioned that, in this case, the travelling wave solution does not allow to satisfy the Dirichlet boundary conditions, so that the solution is only locally valid, namely, in the proximity of the center of the DW.

In order to estimate the orders of magnitude of the quantities involved in the model and to validate our assumption, we carry out a numerical evaluation of the travelling wave profile. For this reason, we take into account the parameter setup proposed in [17]. In detail, we consider a magnetic nanostrip of thickness $t = 3$ nm and $w = 120$ nm,

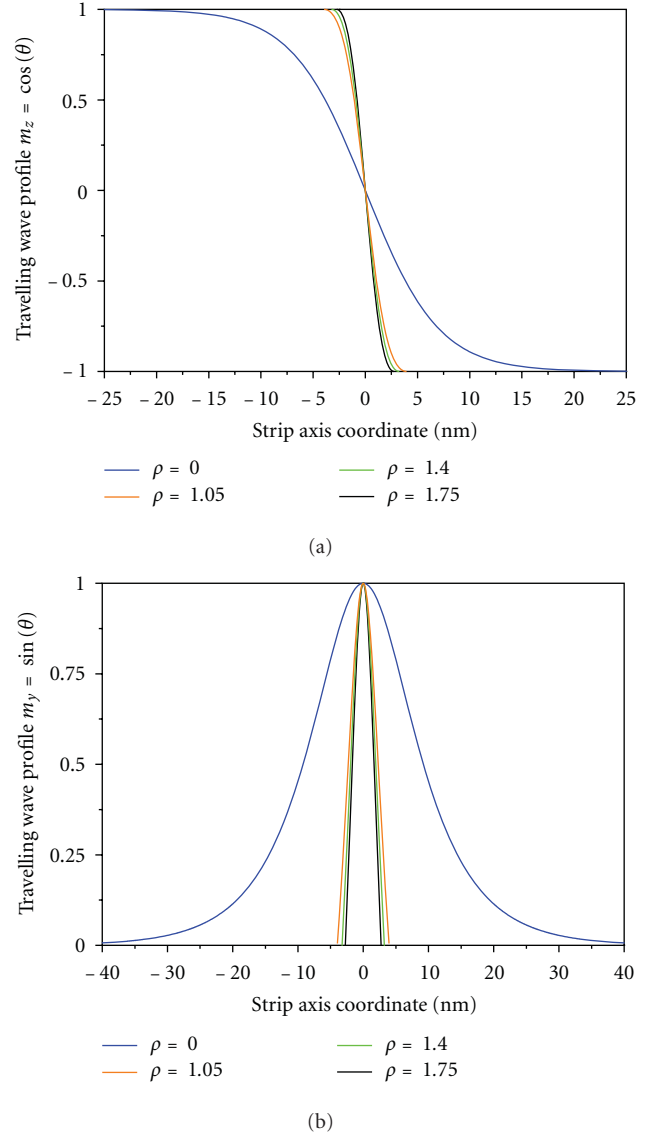


FIGURE 2: Comparison among the travelling wave profiles with and without Rashba field ($|\rho| > 1$ and $\rho = 0$, resp.) computed analytically by using (31)-(32).

saturation magnetization $M_S = 3 \times 10^5$ A/m, Landé factor $g = 2$, exchange constant $A = 10^{-11}$ J/m, anisotropy constant $K = 2 \times 10^5$ J/m³, Gilbert damping constant $\alpha_G = 0.2$, polarization factor $P = 0.5$, nonadiabatic parameter $\eta = 0.4$.

Figure 2 shows the profile of the Bloch DW (characterized by $\varphi_0 = \pi/2$), as its components $m_z = \cos \vartheta$ and $m_y = \sin \vartheta$ (m_x is null everywhere), for $\rho = 0$ (namely, with no Rashba field) and $|\rho| > 1$ (with Rashba field), as deduced from (31)-(32). It is clear that, in this case, the presence of the Rashba field would strongly modify the DW profile and width, making this latter about ten times narrower. It can be also appreciated that the DW width is only slightly affected by variations of ρ , higher than unity.

Starting from these results, we evaluate the new demagnetizing factors corresponding to the modified situation.

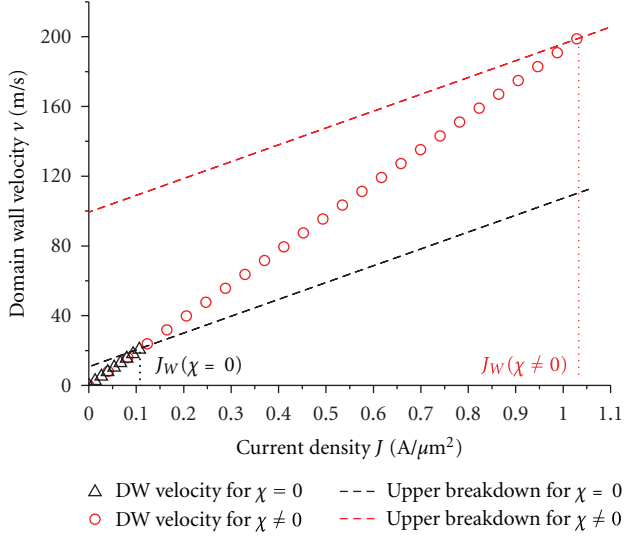


FIGURE 3: Current-driven DW velocity in the steady dynamic regime with and without Rashba field ($\chi \neq 0$ and $\chi = 0$, resp.) computed analytically by using (24) together with the upper breakdown condition (27).

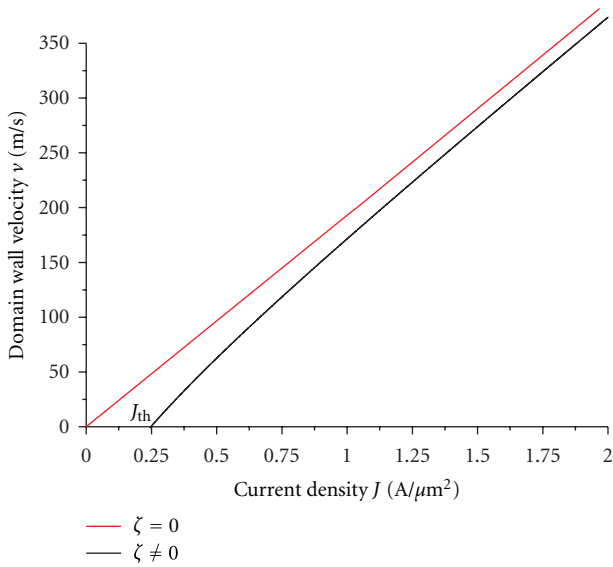


FIGURE 4: Current-driven DW velocities in the steady dynamic regime with and without the inclusion of the dry-friction dissipation function in the mathematical model ($\zeta \neq 0$ and $\zeta = 0$, resp.). The limit of Walker has not been considered in this figure in order to better emphasize the nonlinear behavior of the DW velocity influenced by internal disorder, $\zeta \neq 0$, with respect to the case $\zeta = 0$. Walker breakdown conditions, indeed, are not influenced by ζ .

Because of the DW width is reduced, the difference $|N_x - N_y|$ increases, leading to an increase of the Walker breakdown. For instance, such a difference is equal to 0.046 for $\rho = 0$ and 0.445 for $|\rho| > 1$. The resulting increase of the Walker breakdown value and the enlargement of the range of steady DW motion are depicted in Figure 3 (obtained by using (24) together with (27)). When no Rashba field is considered,

namely, $\chi = 0$ (i.e., $\rho = 0$), the Walker breakdown current is $J_W = 0.11 \text{ A}/\mu\text{m}^2$. Under the influence of the Rashba effect, instead, the upper Walker limit increases, making the steady regime possible up to a higher current $J_W(\chi \neq 0) = 1.04 \text{ A}/\mu\text{m}^2$. From a direct inspection of Figure 3, it should be also noticed that, in both cases, there is no threshold current and the DW mobility is not affected by the Rashba field.

Summarizing, the case $|\rho| > 1$ leads to the expected raise of the Walker breakdown value but negates the enlargement of the DW width.

We can state, therefore, that the classical travelling wave ansatz for the ELLG equation ($\vartheta = \vartheta(x - vt)$ with $v = \text{constant}$ and $\varphi = \text{constant}$) cannot be satisfactorily used to reproduce the overall effects of the Rashba field on the steady DW motion in ferromagnetic nanostrip.

2.2. DW Dynamics in the Presence of Dry Friction ($\zeta \neq 0$). The usage of a dry-friction dissipation function already turned to be useful to model the effects of crystallographic defects, structural disorder, including surface roughness, on the DW motion [20, 21]. In particular, it was demonstrated that the inclusion of such a friction mechanism leads to the appearance of a threshold below which no DW motion can take place, whereas the DW mobility is not affected in the above-threshold regime. In the present work, we would like to test these two properties when the dry-friction dissipation acts simultaneously to the Rashba field. To this aim, (23) is plotted in Figure 4. As it is expected, also in this case, the dry friction causes the motion to occur for current values larger than a given threshold current J_{th} (in the figure, $J_{th} = 0.25 \text{ A}/\mu\text{m}^2$ for $\zeta = 2 \times 10^{-2} \gamma$). On the other hand, the DW velocity, which followed a linear trend in the absence of Rashba field (independently of the presence of dry friction), now exhibits a nonlinear dependence on the input current which approximate, for large current values, the velocity obtained in the case $\zeta = 0$. It is interesting to notice that the same result was qualitatively obtained in experiments [16] as well as in numerical simulations [17] that accounted for thermal effects and roughness. However, the corresponding travelling wave solutions would suffer from the same incompatibility with respect to numerical and experimental observations.

3. Conclusions

In this work, we have analyzed the bias-field-free current-driven DW motion in a ferromagnetic nanostrip subject to the Rashba field and dry-friction dissipation. The study has been mathematically carried out by modifying the extended Landau-Lifshitz-Gilbert equation with the inclusion of the Rashba contribution into the effective field. The standard travelling wave ansatz generally used for the equation of motion, within the steady regime, does not succeed in confirming simultaneously both the key features revealed in recent numerical and experimental observations: increase of the Walker breakdown value and enlargement of the DW width.

This result suggests that the system (16) has to be solved by using a different approach. We believe that, due to the transversal component of the effective field induced by the Rashba field, the hypothesis $\varphi = \text{constant}$, together with the Dirichlet boundary conditions $\vartheta(-\infty) = 0$ and $\vartheta(\infty) = \pi$, does not apply in this case. For this reason, one could consider that the angle φ exhibits an analogous travelling wave dependence $\varphi = \varphi(x - vt)$ and that, due to the symmetry of the problem, Neumann boundary conditions $\vartheta'(\pm\infty) = 0$ and $\varphi'(\pm\infty) = 0$ should be satisfied instead. By imposing such constraints, we get the following nonlinear system of coupled ordinary differential equations:

$$\begin{aligned}
& (u - v)\vartheta' - \left(\vartheta'^2 + \sin^2\vartheta\varphi'^2\right)^{-1/2}\zeta v^2 \sin\vartheta\varphi' \\
& - 2A\gamma \cos\vartheta\vartheta'\varphi' - A\gamma \sin\vartheta\varphi'' \\
& + (\eta u \sin\vartheta - \alpha_G v \sin\vartheta)\varphi' \\
& - \gamma(N_x - N_y) \sin\varphi \cos\varphi \sin\vartheta \\
& - \gamma\chi u \cos\varphi = 0 \\
& \gamma\vartheta'' + (\alpha_G v - \eta u)\vartheta' + \left(\vartheta'^2 + \sin^2\vartheta\varphi'^2\right)^{-1/2}\zeta v^2\vartheta' \\
& - A\gamma \sin\vartheta \cos\vartheta\varphi'^2 + (u - v) \sin\vartheta\varphi' \\
& - \gamma \sin\vartheta \cos\vartheta(\beta - N_z + N_x \cos^2\varphi + N_y \sin^2\varphi) \\
& + \gamma\chi u \sin\varphi \cos\vartheta = 0.
\end{aligned} \tag{33}$$

However, solving this system without simplifying assumptions is not trivial at all. For example, the missing information could be argued from ad hoc micromagnetic simulations which should provide the accurate profile of the travelling wave variable and their dependence on the strength of the Rashba field. Therefore, we strongly encourage numerical investigations in this direction to overcome this issue.

Acknowledgment

G. Consolo gratefully acknowledges support from GNFM-INdAM.

References

- [1] J. C. Slonczewski, "Current-driven excitation of magnetic multilayers," *Journal of Magnetism and Magnetic Materials*, vol. 159, no. 1-2, pp. L1-L7, 1996.
- [2] L. Berger, "Emission of spin waves by a magnetic multilayer traversed by a current," *Physical Review B*, vol. 54, no. 13, pp. 9353-9358, 1996.
- [3] A. N. Slavin and P. Kabos, "Approximate theory of microwave generation in a current-driven magnetic nanocontact magnetized in an arbitrary direction," *IEEE Transactions on Magnetism*, vol. 41, no. 4, pp. 1264-1273, 2005.
- [4] G. Finocchio, O. Ozatay, L. Torres, M. Carpentieri, G. Consolo, and B. Azzerboni, "Micromagnetic modeling of magnetization reversal in nano-scale point contact devices," *IEEE Transactions on Magnetism*, vol. 43, no. 6, pp. 2938-2940, 2007.
- [5] G. Consolo and V. Puliafito, "Analytical and micromagnetic study of nonlinear amplitude modulation in spintronic modulators," *IEEE Transactions on Magnetism*, vol. 46, no. 6, Article ID 5467373, pp. 2063-2066, 2010.
- [6] X. Zhu and J. G. Zhu, "Bias-field-free microwave oscillator driven by perpendicularly polarized spin current," *IEEE Transactions on Magnetism*, vol. 42, pp. 2670-2672, 2006.
- [7] V. Puliafito, B. Azzerboni, G. Consolo, G. Finocchio, L. Torres, and L. L. Diaz, "Micromagnetic modeling of nanocontact spin-torque oscillators with perpendicular anisotropy at zero bias field," *IEEE Transactions on Magnetism*, vol. 44, no. 11, pp. 2512-2515, 2008.
- [8] N. Vernier, D. A. Allwood, D. Atkinson, M. D. Cooke, and R. P. Cowburn, "Domain wall propagation in magnetic nanowires by spin-polarized current injection," *Europhysics Letters*, vol. 65, no. 4, pp. 526-532, 2004.
- [9] D. A. Allwood, G. Xiong, C. C. Faulkner, D. Atkinson, D. Petit, and R. P. Cowburn, "Magnetic domain-wall logic," *Science*, vol. 309, no. 5741, pp. 1688-1692, 2005.
- [10] A. Thiaville, Y. Nakatani, J. Miltat, and Y. Suzuki, "Micromagnetic understanding of current-driven domain wall motion in patterned nanowires," *Europhysics Letters*, vol. 69, no. 6, pp. 990-996, 2005.
- [11] A. Mougins, M. Cormier, J. P. Adam, P. J. Metaxas, and J. Ferré, "Domain wall mobility, stability and Walker breakdown in magnetic nanowires," *Europhysics Letters*, vol. 78, no. 5, Article ID 57007, 2007.
- [12] A. Manchon and S. Zhang, "Theory of spin torque due to spin-orbit coupling," *Physical Review B - Condensed Matter and Materials Physics*, vol. 79, no. 9, Article ID 094422, 2009.
- [13] K. Obata and G. Tatara, "Current-induced domain wall motion in Rashba spin-orbit system," *Physical Review B*, vol. 77, no. 21, Article ID 214429, 2008.
- [14] I. M. Miron, G. Gaudin, S. Auffret et al., "Current-driven spin torque induced by the Rashba effect in a ferromagnetic metal layer," *Nature Materials*, vol. 9, no. 3, pp. 230-234, 2010.
- [15] I. M. Miron, T. Moore, H. Szambolics et al., "Fast current-induced domain-wall motion controlled by the Rashba effect," *Nature Materials*, vol. 10, no. 6, pp. 419-423, 2011.
- [16] J. Ryu, S. B. Choe, and H. W. Lee, "Magnetic domain-wall motion in a nanowire: depinning and creep," *Physical Review B*, vol. 84, Article ID 075469, 2011.
- [17] E. Martinez, "The influence of the Rashba field on the current-induced domain wall dynamics: a full micromagnetic analysis, including surface roughness and thermal effects," *Journal of Applied Physics*, vol. 111, Article ID 07D302, 2012.
- [18] E. Martinez, "Micromagnetic analysis of the Rashba field on current-induced domain wall propagation," *Journal of Applied Physics*, vol. 111, Article ID 033901, 2012.
- [19] P. Podio-Guidugli and G. Tomassetti, "On the steady motions of a flat domain wall in a ferromagnet," *European Physical Journal B*, vol. 26, no. 2, pp. 191-198, 2002.
- [20] G. Consolo, C. Currò, E. Martinez, and G. Valenti, "Mathematical modeling and numerical simulation of domain wall motion in magnetic nanostrips with crystallographic defects," *Applied Mathematical Modelling*, vol. 36, no. 10, pp. 4876-4886, 2012.

- [21] G. Consolo and E. Martinez, “The effect of dry friction on domain wall dynamics: a micromagnetic study,” *Journal of Applied Physics*, vol. 111, Article ID 07D312, 3 pages, 2012.
- [22] G. Consolo and G. Valenti, “Travelling wave solutions of the one-dimensional extended Landau-Lifshitz-Gilbert equation with nonlinear dry and viscous dissipations,” *Acta Applicandae Mathematicae*, 2012.
- [23] L. D. Landau and E. Lifshitz, “On the theory of the dispersion of magnetic permeability in ferromagnetic bodies,” *Physikalische Zeitschrift der Sowietunion*, vol. 8, pp. 153–169, 1935.
- [24] W. F. Brown, *Micromagnetics*, Krieger, Huntington, NY, USA, 1963.

Research Article

Micromagnetic Investigation of Periodic Cross-Tie/Vortex Wall Geometry

Michael J. Donahue

Applied and Computational Mathematics Division, National Institute of Standards and Technology, Gaithersburg, MD 20899-8910, USA

Correspondence should be addressed to Michael J. Donahue, michael.donahue@nist.gov

Received 31 March 2012; Accepted 18 May 2012

Academic Editor: Eduardo Martinez Vecino

Copyright © 2012 Michael J. Donahue. This is an open access article distributed under the Creative Commons Attribution License, which permits unrestricted use, distribution, and reproduction in any medium, provided the original work is properly cited.

A systematic series of micromagnetic simulations on periodic cross-tie/vortex wall structures in an ideal soft film at various widths, thicknesses, and period lengths is performed. For each width and thickness a natural period length is found which has minimal energy density for walls of this type. For each width, a critical thickness is determined below which the natural period length is infinite; for films thinner than this, the pure Néel wall has lower energy than any cross-tie/vortex wall. Details of the origin of the energy reduction in cross-tie/vortex walls as compared to Néel walls are also examined, and canting inside cross-tie and vortex structures in films thicker than $1 \ell_{\text{ex}}$ is explained.

1. Introduction

The predominant types of 180° domain walls in soft films are Néel walls occurring in very thin films, Bloch walls in thicker samples, and numerous transitional structures [1–3]. One of the more interesting transitional structures is the cross-tie/vortex (or simply cross-tie) wall which alternates cross-ties and vortices between counterrotating segments of Néel walls. Cross-tie/vortex walls are observed experimentally [4–6], in micromagnetic simulations [6–9], and in theory [10, 11]. In finite samples, this wall type appears in low remanence closed-flux Landau patterns, as seen in Figure 1. If the structure is long enough, then multiple cross-tie/vortex pairs can appear, as in Figure 2.

To gain insight into the formation and structure of cross-tie/vortex walls, this work presents a systematic collection of micromagnetic simulations performed using the OOMMF micromagnetic package from NIST [12]. An ideally soft material was modeled (anisotropy constant $K = 0 \text{ J/m}^3$) with saturation magnetization $M_s = 860 \text{ kA/m}$ and exchange coefficient $A = 13 \text{ pJ/m}$, to approximate a NiFe alloy. All of the simulations were performed with no applied field.

The component energies in this system are the stray field energy and the exchange energy, with the component fields defined by:

$$\mathbf{H}_{\text{stray field}}(\mathbf{r}) = -\frac{1}{4\pi} \int_V \nabla \cdot \mathbf{M}(\mathbf{r}') \frac{\mathbf{r} - \mathbf{r}'}{|\mathbf{r} - \mathbf{r}'|^3} d^3 r' + \frac{1}{4\pi} \int_S \hat{\mathbf{n}} \cdot \mathbf{M}(\mathbf{r}') \frac{\mathbf{r} - \mathbf{r}'}{|\mathbf{r} - \mathbf{r}'|^3} d^2 r', \quad (1)$$

$$\mathbf{H}_{\text{exchange}}(\mathbf{r}) = \frac{2A}{\mu_0 M_s} \nabla^2 \mathbf{m}(\mathbf{r}), \quad (2)$$

where $\mathbf{m} = \mathbf{M}/M_s$ is the normalized (unit) magnetization. In both cases, energy density $E = -(1/2)\mu_0 \mathbf{M} \cdot \mathbf{H}$, where the $1/2$ factor arises from the dependence of \mathbf{H} on \mathbf{M} . Thus the total energy density in the system is

$$E_{\text{total}} = -\frac{\mu_0}{2} \mathbf{M} \cdot (\mathbf{H}_{\text{stray field}} + \mathbf{H}_{\text{exchange}}). \quad (3)$$

In soft films, the relevant length scale is the magnetostatic-exchange length, defined by

$$\ell_{\text{ex}} = \sqrt{\frac{A}{K_d}}, \quad (4)$$

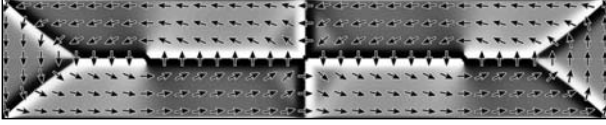


FIGURE 1: Zero-field equilibrium state from a micromagnetic simulation of a magnetically soft thin film rectangle with dimensions $500 \ell_{\text{ex}} \times 100 \ell_{\text{ex}} \times 6 \ell_{\text{ex}}$. The shading indicates the magnetic charge $-\text{div } \mathbf{M}$, with black indicating negative charge and white positive charge.

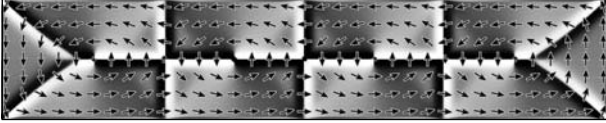


FIGURE 2: Simulation of the same system as in Figure 1, but in an equilibrium configuration featuring three cross-ties alternating with vortices; for this sample this is a lower energy state than the single cross-tie state in Figure 1.

where K_d is the magnetostatic energy density

$$K_d = \frac{1}{2} \mu_0 M_s^2. \quad (5)$$

All lengths reported herein are in units of ℓ_{ex} , and energy densities are reported in units of K_d . However, for the given values of A and M_s , $\ell_{\text{ex}} \doteq 5.289 \text{ nm}$ and $K_d \doteq 464.7 \text{ kJ/m}^3$, so the results may be easily converted to nm and J/m^3 if desired.

2. Simulation Details

Aside from Figures 1 and 2, the simulations in this paper are periodic along the long axis of the wall, as indicated in Figure 3. This allows the structure of the cross-tie/vortex wall to be studied separately from the effects of edge domains. The period length is denoted by X , with Y and Z denoting the sample width and thickness, respectively. Coordinates are introduced such that positions (x, y, z) inside the simulation volume run from $0 \leq x \leq X$, $0 \leq y \leq Y$, and $0 \leq z \leq Z$.

The computational cells are approximately cubic in shape, with each edge dimension not larger than $1/2 \ell_{\text{ex}}$. This size is small enough that the maximum change in magnetization angle from one cell site to the next is kept below about 30° ; this suffices to provide a good rendering of the magnetization on the discretized grid. The y and z cell sizes are adjusted downward if necessary to make the count of cells across each of the y and z dimensions odd, so that there is a unique center cell along each of those dimensions. The x cell size is adjusted downward as necessary so that the count of cells along the x dimension is $\equiv 2 \pmod{4}$ (so allowed cell counts are 2, 6, 10, ...). Taken together, these adjustments allow a unique cell in the center of each of the vortex and cross-tie cores to be identified.

The initial magnetization configuration for each simulation is either taken from the end state of a previous run (if one is available that is close to the dimensions of the

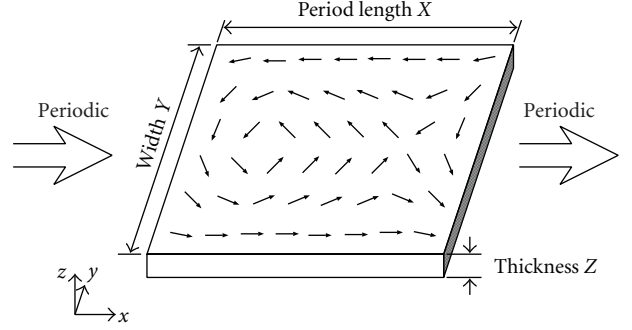


FIGURE 3: Simulations are computed on a rectangular volume representing a thin film strip with thickness Z , width Y , and an infinite length modeled by a periodic length of dimension X .

current run) or else set to a cartoon version of the cross-tie/vortex configuration as illustrated in Figure 3. Either way, the magnetization in the central cell in the vortex core is set to $+z$ (along the film normal) and the central cell in the cross-tie core is set to $-z$. Except as noted, the magnetization in these center cells is held fixed. As discussed in Rave [8], this pinning tends to accelerate convergence of simulations to equilibrium and improves accuracy. Simulations run without this constraint show no discernible difference in the end equilibrium state. Some simulations were also run with the vortex and cross-tie cores both aligned in the $+z$ direction. This raises the energy somewhat, but for most geometries the energy difference is negligible, typically less than one part in 10^5 . For simulations with a period length to film thickness ratio of less than 10:1, however, the difference is larger. For example, in the $X = 25 \ell_{\text{ex}}$, $Y = 200 \ell_{\text{ex}}$, $Z = 8 \ell_{\text{ex}}$ case the energy in the aligned core setting was 3% larger than for the antialigned setting.

Once the initial magnetization is set, the simulation proceeds by energy minimization via a conjugate-gradient procedure, stopping when the reduced torque $|m \times H|/M_s < 1.2 \times 10^{-8}$.

3. Results and Discussion

Each point in Figure 4 marks the average total energy density at equilibrium resulting from a simulation with width $Y = 200 \ell_{\text{ex}}$ at the indicated thickness Z and period length X . There is one cross-tie/vortex pair in each period, so as the period length X grows large the wall becomes primarily two Néel segments interrupted by a cross-tie and vortex at either end. This is evident in the behavior of the curves for large X , as for each thickness Z the curve asymptotically converges to the energy density of the associated Néel wall. For small period lengths ($X < 100 \ell_{\text{ex}}$) the energy density grows sharply as the exchange energy resists compression of the complex cross-tie/vortex structure. For thinner films (Z under about $1 \ell_{\text{ex}}$ for $Y = 200 \ell_{\text{ex}}$), the energy density curves are monotonically decreasing. This means that in a thin infinite strip if the cross-tie and vortex are not pinned by some means, they will spread out indefinitely leaving behind a plain Néel wall. This is consistent with the experimental

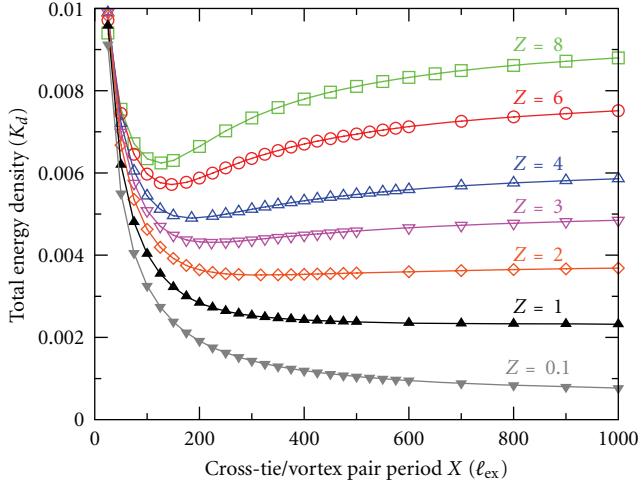


FIGURE 4: Average total energy density as a function of period length X for simulations with width $Y = 200 \ell_{\text{ex}}$ for various thicknesses Z (measured in ℓ_{ex}). Symbols represent simulation results, lines are a guide to the eye. Each of the curves with $Z \geq 2 \ell_{\text{ex}}$ exhibits a minimum value between $125 \ell_{\text{ex}}$ and $320 \ell_{\text{ex}}$. In this range, the curves for $Z \leq 1 \ell_{\text{ex}}$ are monotonically decreasing with X .

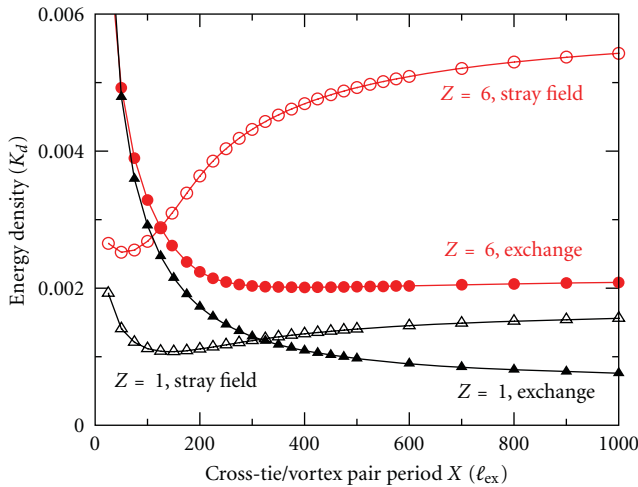


FIGURE 5: Average stray field (open symbols) and exchange energy (filled symbols) densities as a function of period length X for width $Y = 200 \ell_{\text{ex}}$ at thicknesses $Z = 6 \ell_{\text{ex}}$ and $1 \ell_{\text{ex}}$. These curves are a decomposition of the corresponding total energy density curves from Figure 4 into constitutive parts.

result that cross-tie/vortex walls are not observed in ultrathin films. The transition thickness is a function of the strip width Y ; this dependence is explored in Figure 9 below.

For thicker films there is a unique minimum on each curve, which corresponds to a “natural” period length X —this is the period length that minimizes the energy for a cross-tie/vortex wall at the given film thickness and strip width. Note though that each point in Figure 4 is a stable equilibrium configuration under the fixed period assumption. So if the period length is constrained by geometry or other means

such as pinning defects, then period lengths other than the natural length are possible, as seen in Figures 1 and 2.

The energy wells are asymmetric, especially for the midlevel thicknesses, say Z between $2 \ell_{\text{ex}}$ and $4 \ell_{\text{ex}}$. In this regime the penalty for a period longer than the natural period is small, but in all cases periods significantly shorter than the natural period are energetically prohibitive.

Another feature of the curves in Figure 4 is that as the films grow thicker, the energy density increases, the natural period length grows shorter, and the energy well is deeper. These effects can be explained by examining the stray field and exchange component energies of the total energy.

In this regard, note two attributes of the magnetization in these simulations. The first is that the shape anisotropy of thin films constrains the magnetization to lie mostly in-plane (the notable exception being of course the cores of vortex and cross-tie structures). The second is that the magnetization does not vary much along the film normal (z) direction. This is due in part to the dominance of exchange coupling over the relatively short distance between the top and bottom of each film and also due to the relative uniformity of stray field in z . (The latter condition does not hold near the vicinity of the vortex and cross-tie cores, and this leads to nearby z -variation in \mathbf{m} , as will be seen below.)

The second attribute means we can meaningfully consider a situation where the magnetization is held fixed and the thickness of the part is varied. In this setting the first integral in the formula for the stray field (1), which handles the effects of the bulk charge, is seen to vary linearly with thickness Z via the change in the part volume. Ignoring magnetic charges on the top and bottom surfaces in the second integral, we see that it too varies linearly with Z (although in the Landau flux-closure structures considered here this contribution is minor regardless). The net result is that if the magnetization were held fixed, then reducing the film thickness would be expected to reduce the stray field by a similar amount. The exchange field (2), however, does not vary with thickness Z . This means that one can expect exchange to take on a more dominant role as the film thickness is decreased.

These effects are on display in Figure 5, which breaks down the total energy density curves from Figure 4 for two thicknesses into the stray field and exchange components. For both thicknesses we see the dominance of the exchange energy in short-period lengths, giving way to the stray field energy for longer period lengths. Moreover, for each component the energy density is greatly reduced in the thinner strip. If the magnetization configurations were the same for the two thicknesses, then by the above analysis the exchange energy density would stay constant and the stray field energy density would drop by a factor of six. In practice, of course, what happens is that the weak stray field in the thinner film allows the magnetic structures to expand, reducing the exchange energy at the expense of a modest increase in the stray field.

To understand how cross-tie/vortex structures lower the energy density of a Néel wall, return to Figure 1, and focus first on a section of the Néel portion of the wall between the left hand vortex and the cross-tie. Moving from bottom to

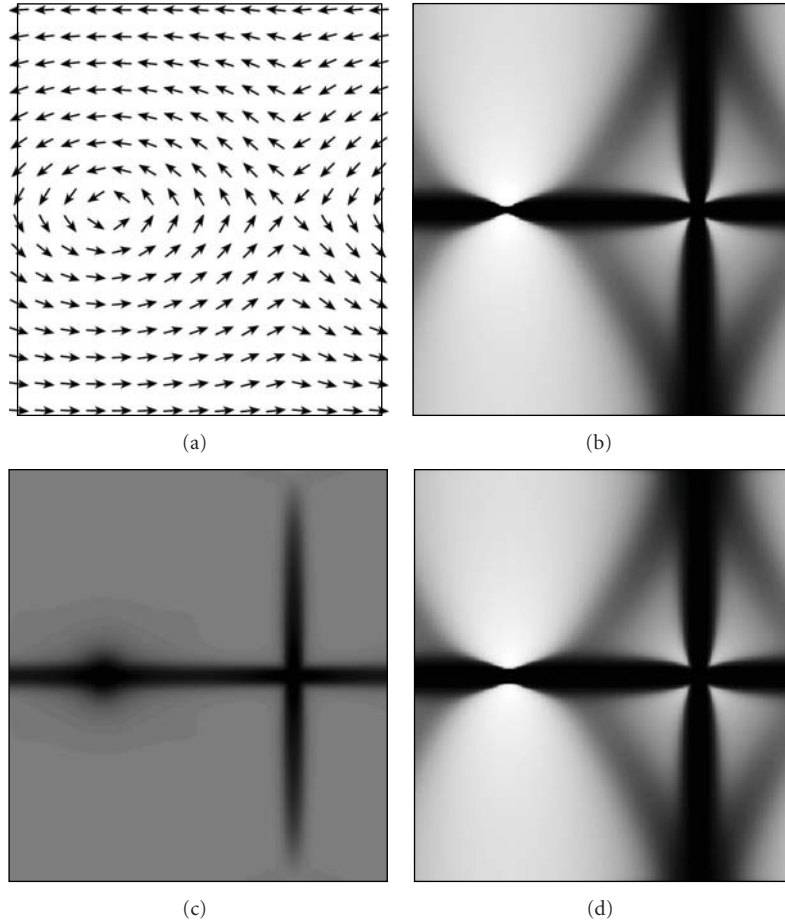


FIGURE 6: Equilibrium configuration for width $Y = 200 \ell_{\text{ex}}$, thickness $Z = 4 \ell_{\text{ex}}$, and X -period length $185 \ell_{\text{ex}}$ (which is the natural period length for this Y and Z). (a) Magnetization pattern, (b) stray-field energy density, (c) exchange energy density, and (d) total energy density. In (b)–(d), the shading scale runs from white (low energy density) to black (high energy density).

top across the wall, the magnetization rotates counterclockwise. This configuration produces negative magnetic charge on the lower half of the strip (dark region) and positive charges on the upper half (light region). (Here “lower” and “upper” refer to the view on the page.) This sets up a stray field running from the positive charges to the negative charges, counter to the magnetization in the center of the wall, making the wall center a high stray field energy density region. On the right hand side of the cross-tie the magnetization rotation direction across the wall is reversed, so that the positive charge region is below the wall and the negative charge region is above. The wall is still a high stray field energy density region, but the checkerboarding of the charge regions reduces the total stray field energy in two ways. The first factor is that by effectively arranging the charge regions into a quadrupole configuration, the extent of their stray field is reduced. The second, larger contribution is seen more clearly in Figure 2. In the checkerboard pattern, stray field between the charge blocks runs not only up and down across the Néel sections of the wall, but also left and right horizontally parallel to the wall. The orientation of the magnetization about each vortex core is such that it aligns with the stray field from the nearby charge blocks, so that the

regions above and below each vortex are regions of low stray field energy density.

This latter effect is shown directly in Figure 6, which is from the (periodic) simulation corresponding to the minimum point on the $Z = 4 \ell_{\text{ex}}$ curve in Figure 4. Parts (b)–(d) of this figure are shaded to indicate the component and total energy densities as a function of position. In part (b), the light-colored low energy density regions above and below the vortex core are clearly visible. Part (c) shows the regions of high exchange energy density. These include the vortex core and center of the wall, as expected. It is interesting that there is also a region of high exchange energy running perpendicular to the wall through the cross-tie core. In an idealized cross-tie, the magnetization rotates around the cross-tie core in the same manner as the magnetization rotates about a vortex core, only with the opposite winding number. In such a configuration the exchange energy is exactly the same as for a vortex (the stray field energy is a different matter, of course), so the high exchange energy spike perpendicular to the wall must arise due to deformation of the cross-tie structure. Most likely the observed buckling in the magnetization along this line is caused by the horizontal stray field from the checkerboard

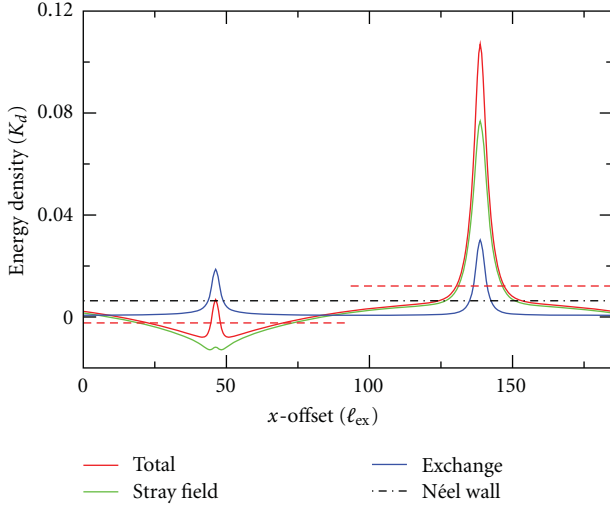


FIGURE 7: Cross-sectional (yz) averages for total, stray field, and exchange energy densities as a function of the x location along the wall for the simulation in Figure 6, and the energy density for a Néel wall in the same geometry. The center of the vortex core is in the cross-section at offset $x = 46 \ell_{\text{ex}}$, and the center of the cross-tie core is at $x = 139 \ell_{\text{ex}}$. The two half-width dashed red lines indicate the average energy density of the cross-tie/vortex wall across each corresponding half-period.

charge regions which flows counter to the magnetization here.

Additional details may be gleaned from Figure 7, which shows cross-sectional averages for Figure 6 and includes a black-dashed line showing the energy density for a pure Néel wall in this geometry. The energy savings in stray field energy around the vortex core, and expense around the cross-tie core, are shown by the green line. On either side of the cross-tie and vortex cores, the magnetization spreads out slightly as compared to a Néel wall, and as a result the exchange energy density (blue line) in those regions is slightly less than the exchange energy density for a Néel wall (not shown). This savings is more than offset by the increase in exchange energy inside the vortex and cross-tie core structures, so that in total the exchange energy for the cross-tie/vortex wall is higher than the exchange energy for the Néel wall. (Another view of this is that the wall structure outside the cores is essentially that of a stretched Néel wall; the stretching reduces the exchange energy, but the stray field energy across the wall is increased by more than the exchange energy reduction.) The dashed red line shows the combined (stray field plus exchange) energy density averaged across each half of the simulation volume. This shows a clear reduction in energy density as compared to the Néel wall for the portion of the simulation about the vortex, and a clear increase about the cross-tie. The average of these two half-lines is the average energy density for the cross-tie/vortex wall as a whole, which is slightly below the energy density for the pure Néel wall. An important point here is that the cross-tie structure by itself costs energy as compared to the Néel wall; the cross-tie/vortex wall formation as a whole is

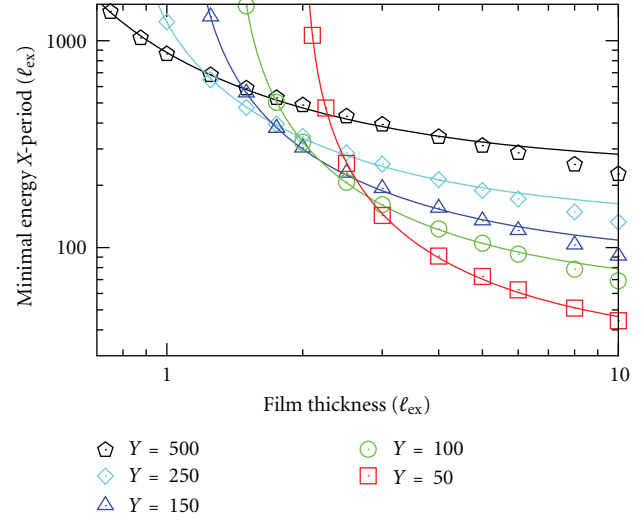


FIGURE 8: Cross-tie/vortex pair period length (X) having the lowest energy density as a function of film thickness (Z) for five strip widths (Y , in ℓ_{ex}), as labeled (log-log scale). Symbols show data from micromagnetic simulations; curves are least-square fits through data to the functional form $X = A/((Z/B) - 1) + C$; the corresponding values for A , B , and C for each curve are given in Table 1.

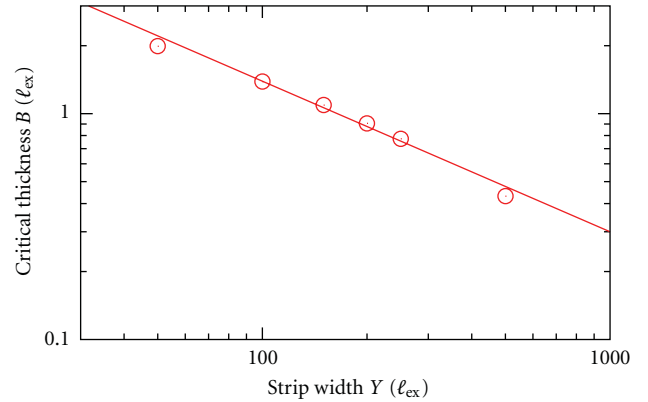


FIGURE 9: Critical thickness at which the Néel wall has lower energy density than a cross-tie/vortex wall of period X , for all X , as a function of strip width Y . Data points are from Table 1, the line is the fit curve $30/Y^{2/3}$.

energetically favorable only because of the stray field energy savings associated with the vortex structure.

The two graphs, Figures 8 and 9, collect information on the natural period lengths from Figure 4 and similar simulation series for several other strip widths. For each strip width Y and thickness Z , a sequence of simulations was performed using a golden section search to locate the precise X -period that minimized the total energy density. In Figure 8 we observe that for each strip width Y , the minimal X -period length data can be fitted fairly well by a curve of the form $X = A/((Z/B) - 1) + C$, where Z is the film thickness and A , B , and C are fit parameters. In this fit only the data for $Z < 8 \ell_{\text{ex}}$ are used; in the thicker films the cross-tie and vortex

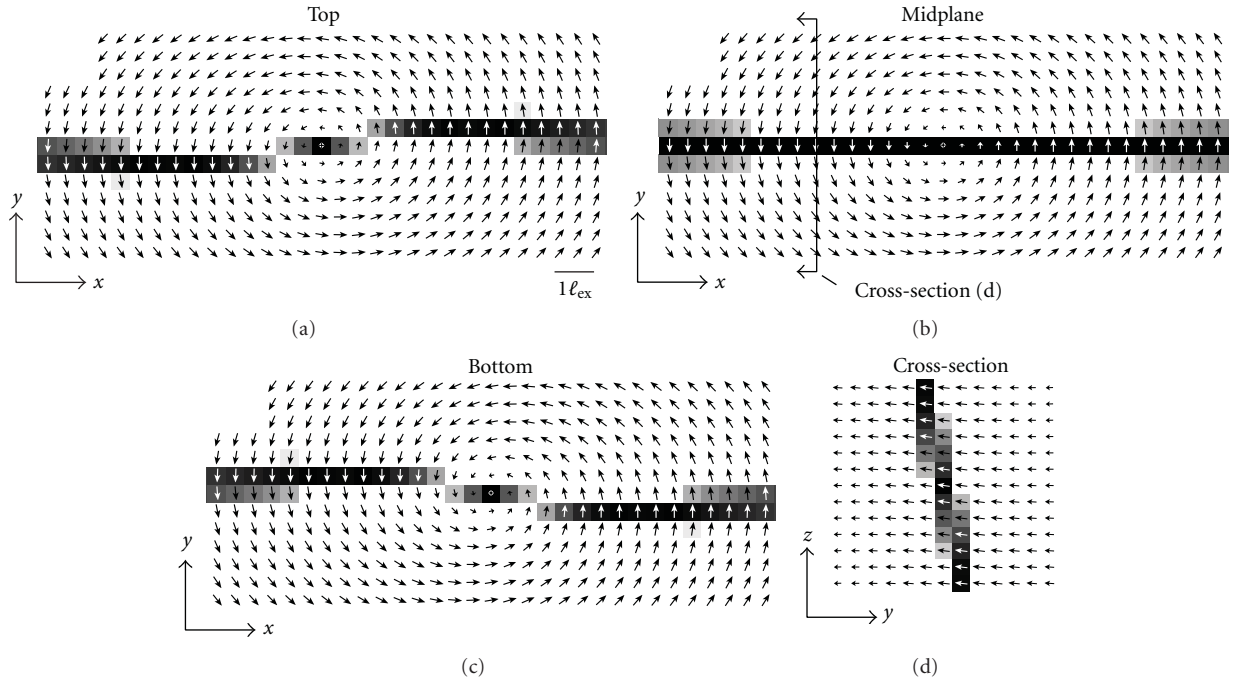


FIGURE 10: Enlarged view of a $15\ell_{\text{ex}} \times 6\ell_{\text{ex}}$ subsection about a vortex in a simulation having X-period length of $147\ell_{\text{ex}}$, width $Y = 200\ell_{\text{ex}}$, and thickness $Z = 6\ell_{\text{ex}}$. Parts (a), (b), and (c) show the top, middle, and bottom planes, respectively, while (d) is a cross-section through the full thickness of the sample at the location marked in (b), roughly $3.5\ell_{\text{ex}}$ to the left of the vortex core. The shading indicates the absolute value of the x-component of the magnetization, with black at $m_x = 0$.

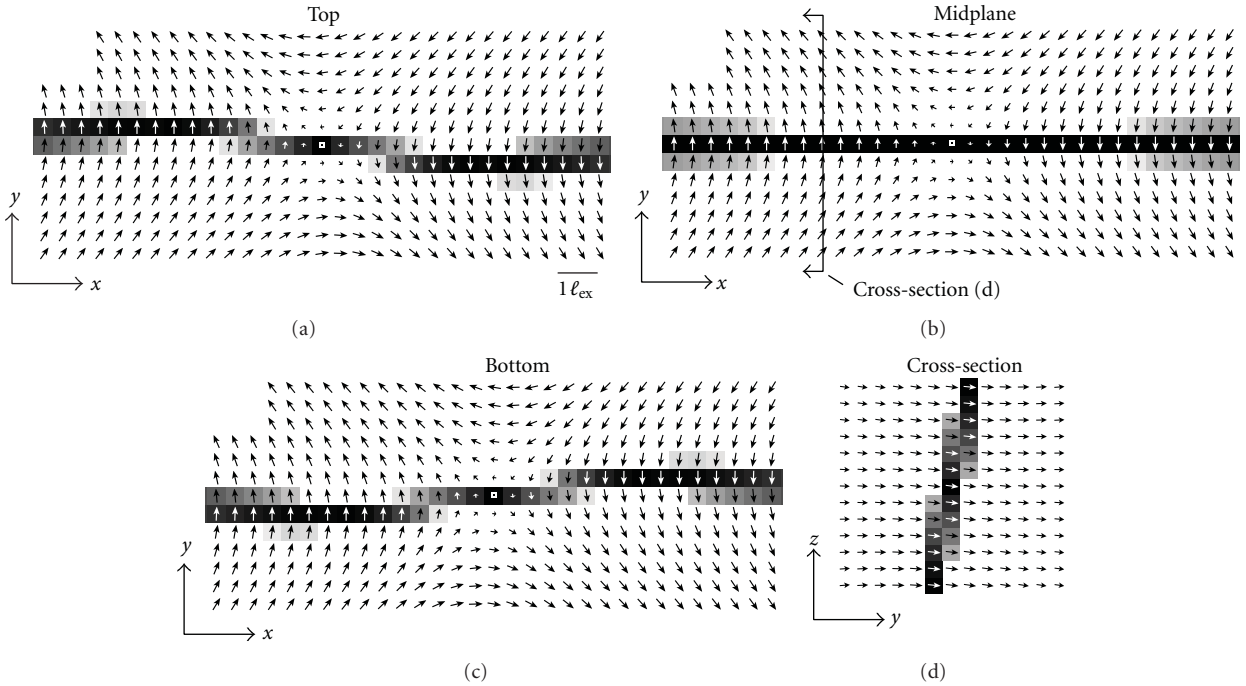


FIGURE 11: Companion image to Figure 10, this enlarged view of a $15\ell_{\text{ex}} \times 6\ell_{\text{ex}}$ subsection is about the cross-tie in the same simulation with X-period length of $147\ell_{\text{ex}}$, width $Y = 200\ell_{\text{ex}}$, and thickness $Z = 6\ell_{\text{ex}}$. Parts (a), (b), and (c) show the top, middle, and bottom planes, respectively, while (d) is a cross-section through the full thickness of the sample at the location marked in (b), roughly $3.5\ell_{\text{ex}}$ to the left of the cross-tie core. The shading indicates the absolute value of the x-component of the magnetization, with black at $m_x = 0$.

TABLE 1: Coefficients to functional form $X = A/((Z/B) - 1) + C$ for various strip widths Y to fit simulation results for minimal energy X -period (see Figure 8).

Strip width (ℓ_{ex})	A (ℓ_{ex})	B (ℓ_{ex})	C (ℓ_{ex})
50	58	1.988	32
100	117	1.386	60
150	177	1.091	87
200	243	0.906	113
250	320	0.774	136
500	832	0.431	245

structures develop significant asymmetry which alters the character of the structure. If this asymmetry did not develop, then the parameter C would describe the asymptotic period length that would be obtained in thick films.

At the other end of the scale, we see that each of the curves in Figure 8 has a pole on the left, which corresponds to parameter B . As discussed above with respect to the $Z = 0.1 \ell_{\text{ex}}$ curve in Figure 4, if a film is thin enough then there is no minimal period length. For each strip width Y , the critical thickness dividing the two regimes corresponds to the location of the pole in Figure 8 (or, equivalently, parameter B). The critical thickness as a function of strip width Y is plotted on a log-log scale in Figure 9. We see from the fitted curve, $Z_{\text{crit}} \approx 30/Y^{2/3}$, that the critical thickness decreases with increasing strip width. From a practical standpoint the natural period length can be quite large. For example, although the $Z = 1 \ell_{\text{ex}}$ curve in Figure 4 appears to be monotonically decreasing, the fit in Table 1 predicts a minimum at $X = 2455 \ell_{\text{ex}}$, or roughly $13 \mu\text{m}$ in NiFe.

As an example of the use of Figure 8, refer again to the finite system of Figures 1 and 2. If we allow for a $50 \ell_{\text{ex}}$ border at each of the left and right sides of the sample to accommodate edge closure domains, then that leaves a $400 \ell_{\text{ex}}$ run in the middle for the cross-tie/vortex wall. From Figure 8, we see that the natural period length for a strip of width $100 \ell_{\text{ex}}$ and thickness $6 \ell_{\text{ex}}$ is just under $100 \ell_{\text{ex}}$. This predicts that a configuration with four cross-tie/vortex periods would have lower energy than either the three period configuration shown in Figure 2 or a five period configuration. Direct simulations on the finite system bear out this result.

In regions where the magnetization lies in-plane, the stray field is nearly uniform through the thickness of the film, and so the magnetization also shows little variation in z . The vortex and cross-tie core regions, however, are delineated by out-of-plane magnetization, and this does produce a z -dependence on the magnetization near the cores. This effect is shown in Figures 10 and 11. (For this simulation, the magnetization in the central cells of the cores was not pinned.) Looking first at the magnetization at the top surface around the vortex core (Figure 10(a)), the magnetization in the vortex core points out of the plane, and the resulting positive magnetic charge interacts with the checkerboard magnetic charge pattern on either side by

pushing the positive charge blocks away (towards $-y$ on the left and $+y$ on the right) and extending the negative charge regions. This causes a “micro-deformation” of the wall [7]; the spacing between the arrows in the diagram is roughly $1/2 \ell_{\text{ex}}$, so the total deformation is about $1 \ell_{\text{ex}}$. Outside the viewed region, at about $12 \ell_{\text{ex}}$ on either side of the core, the wall shifts back to the center line.

On the bottom surface of the film (Figure 10(c)), the surface charge from the core has the opposite charge, and the wall shifts in the opposite direction, while the midplane shows no shift at all (Figure 10(b)). A cross-section through the thickness of the film (Figure 10(d)) shows that the wall is actually canted by about 10° from the vertical. Outside of this view area, the Néel portions of the wall are not canted, but run through the thickness of the film independent of z . Figure 11 shows that the magnetization around the cross-tie core behaves similarly.

This effect relies on the opposite charges on the top and bottom surfaces being sufficiently far apart that they can independently influence the nearby magnetization. For thinner films, the extent of the dipole field from the core diminishes relative to the exchange length and the wall canting is reduced; for films thinner than about $1 \ell_{\text{ex}}$ the effect is not evident.

4. Conclusion

In an ideally soft magnetic thin film, the 180° cross-tie/vortex wall is a periodic structure consisting of alternating cross-ties and vortices sandwiched between Néel wall segments having alternating chiralities. This structure is primarily two dimensional (i.e., independent of z), with the exception of minor canting on either side of both cross-tie and vortex cores in films thicker than $1 \ell_{\text{ex}}$.

In an infinite strip, the cross-tie/vortex wall structure has a natural period length that minimizes the energy density for this class of walls, and this length is a function of both the strip thickness and width. For a given strip width Y , there is a critical thickness Z_{crit} below which the natural period length is infinite. That relation is $Z_{\text{crit}} \approx 30/Y^{2/3}$, with Z_{crit} and Y measured in ℓ_{ex} . In films thicker than Z_{crit} , the energy reduction obtained by a cross-tie/vortex wall as compared to a plain Néel wall is the result of decreased stray field energy across the outboard sides of the vortex cores arising from the checkerboarding of the magnetic charge associated with the Néel wall segments.

Related periodic wall structures are topologically permissible, for example one could replace each vortex in the cross-tie/vortex structure with a counterrotating cross-tie, or replace each cross-tie with a counterrotating vortex. The former is probably energetically ill-favored, but the latter produces the well-known diamond state that frequently sports lower energy than the cross-tie/vortex wall [8].

References

- [1] R. Kirchner and W. Döring, “Thin films: domain walls and related topics,” *Journal of Applied Physics*, vol. 39, pp. 855–856, 1968.

- [2] D. V. Berkov, K. Ramstöck, and A. Hubert, "Solving micromagnetic problems. Towards an optimal numerical method," *Physica Status Solidi*, vol. 137, pp. 207–225, 1993.
- [3] K. Ramstöck, W. Hartung, and A. Hubert, "The phase diagram of domain walls in narrow magnetic strips," *Physica Status Solidi*, vol. 155, no. 2, pp. 505–518, 1996.
- [4] R. Ploessl, J. N. Chapman, A. M. Thompson, J. Zweck, and H. Hoffmann, "Investigation of the micromagnetic structure of cross-tie walls in permalloy," *Journal of Applied Physics*, vol. 73, no. 5, pp. 2447–2452, 1993.
- [5] A. Hubert and R. Schäfer, *Magnetic Domains*, Springer, 1998.
- [6] S. Hou, G. Pan, D. J. Mapps et al., "Magnetic force microscopy and micromagnetic study of cross-tie wall structures in $\text{Co}_{91}\text{Nb}_6\text{Zr}_3$ amorphous thin films," *Journal of Applied Physics*, vol. 87, no. 3, pp. 1096–1102, 2000.
- [7] M. Redjidal, A. Kakay, M. F. Ruane, and F. B. Humphrey, "Cross-tie walls in thin permalloy films," *IEEE Transactions on Magnetics*, vol. 38, no. 5, pp. 2471–2473, 2002.
- [8] W. Rave and A. Hubert, "Magnetic ground state of a thin-film element," *IEEE Transactions on Magnetics*, vol. 36, no. 6, pp. 3886–3899, 2000.
- [9] R. Hertel, "Thickness dependence of magnetization structures in thin Permalloy rectangles," *Zeitschrift für Metallkunde*, vol. 93, no. 10, pp. 957–962, 2002.
- [10] F. Alouges, T. Rivière, and S. Serfaty, "Néel and cross-tie wall energies for planar micromagnetic configurations," *ESAIM*, vol. 8, pp. 31–68, 2002.
- [11] A. DeSimone, H. Knüpfer, and F. Otto, "2-d stability of the Néel wall," *Calculus of Variations and Partial Differential Equations*, vol. 27, no. 2, pp. 233–253, 2006.
- [12] M. J. Donahue and D. G. Porter, "OOMMF user's guide, version 1.0," NISTIR 6376, National Institute of Standards and Technology, Gaithersburg, Md, USA, 1999.

Review Article

Static Properties and Current-Driven Dynamics of Domain Walls in Perpendicular Magnetocrystalline Anisotropy Nanostrips with Rectangular Cross-Section

Eduardo Martinez

Universidad de Salamanca, Plaza de los Caidos s/n, 38008 Salamanca, Spain

Correspondence should be addressed to Eduardo Martinez, edumartinez@usal.es

Received 26 March 2012; Accepted 28 May 2012

Academic Editor: Giancarlo Consolo

Copyright © 2012 Eduardo Martinez. This is an open access article distributed under the Creative Commons Attribution License, which permits unrestricted use, distribution, and reproduction in any medium, provided the original work is properly cited.

The current-induced domain wall motion along thin ferromagnetic strips with high perpendicular magnetocrystalline anisotropy is studied by means of full micromagnetic simulations and the extended one-dimensional model, taking into account thermal effects and edge roughness. A slow creep regime, where the motion is controlled by wall pinning and thermal activation, and a flow regime with linear variation of the DW velocity, are observed. In asymmetric stacks, where the Rashba spin-orbit field stabilizes the domain wall against turbulent transformations, the steady linear regime is extended to higher currents, leading to higher velocities than in single-layer or symmetric stacks. The pinning and depinning at and from a local constriction were also studied. The results indicate that engineering pinning sites in these strips provide an efficient pathway to achieve both high stability against thermal fluctuations and low-current depinning avoiding Joule heating. Finally, the current-driven dynamics of a pinned domain wall is examined, and both the direct and the alternating contributions to the induced voltage signal induced are characterized. It was confirmed that the direct contribution to the voltage signal can be linearly enhanced with the number of pinned walls, an observation which could be useful to develop domain-wall-based nano-oscillators.

1. Introduction

A typical pattern of a ferromagnetic sample consist on a set of domains and domain walls (DWs). The domains are uniformly magnetized regions, and DWs constitute the boundary between them. DWs have been intensively researched in the past, both in bulk or continuous films [1]. However, as many other areas of physics, the study of DWs has been revitalized by the advent of nanotechnology, and at the present, modern nanolithography techniques allow the fabrication of suitable ultra-thin ferromagnetic strips where DWs can be easily nucleated. The development of advance microscopy methods has also permitted them to be imaged and their dynamics to be explored. The traditional way to promote the DW dynamics is done by applying magnetic fields. Recently, a more promising alternative to drive DWs has been proposed. It consists on flowing electrical currents through ferromagnetic strip by using the novel physics of spin-transfer torque. Electrical current passing through a ferromagnetic strip becomes spin polarized along the local

magnetization direction. When the current crosses a DW, spin angular momentum is transferred from the current to the magnetization, thereby inducing a torque which leads to DW motion. This spin-transfer torque phenomenon, which was firstly predicted by Berger [2, 3], has adiabatic and nonadiabatic contributions. The first one, which is expected to be dominant in wide walls, acts as a hard-axis field perpendicular to the magnetization inside the DW and controls the initial DW velocity. The nonadiabatic torque, which is expected to be dominant in thin wall, mimics an easy axis magnetic field and it is the responsible of the terminal DW velocity [4–8]. Although several experimental [9–23] and theoretical [24–29] studies have provided advances in the understanding of current-driven DW dynamics, there are many aspects of the underlying physical mechanism, such as the origin (large gradient of the local magnetization [3], spin-flip scattering [5, 8], or linear momentum transfer [6]) and the strength of the nonadiabatic contribution, which remain still unclear [30].

Apart from its intrinsic fundamental interest, the efficient control of the current-induced DW dynamics along thin strips is nowadays a promising but a technological challenge. Logic [31–33] and storage [34–36] devices based on DW displacement along thin ferromagnetic strips have been proposed during the last decade, where the DW position can be manipulated by means of constrictions which act as local pinning sites for the wall. These DW-based devices require a high efficient current-driven DW propagation, with high velocity under low current. The high stability of a trapped DW at a pinning site against thermal fluctuations, along with a low current DW depinning are also mandatory for recording applications. On the other hand, there exist other potential applications exploiting the current-induced DW dynamics, such as nano-oscillators [37–41] or nanosensors and amplifiers [42].

Most of the experimental and theoretical studies have been focused on soft Permalloy strips, which present several drawbacks for applications. For instance, critical depinning density currents around $1 \text{ A}/\mu\text{m}^2$ are required to promote the DW depinning from thermally stable pinning notches [13, 14, 26], but these currents remain too high for applications due to unwanted Joule heating effects. On the other hand, DWs in typical soft strips usually adopt wide (50–100 nm) and complex out-of-plane vortex configurations with low mobility [14, 15]. The classical one-dimensional model (1DM) of DW propagation provides a approach to understand experiments on soft strips, but its validity is rather limited because it cannot capture the full complexity of the vortex configuration nor its translational deformation, and time-consuming micromagnetic simulations (μM) are needed to interpret experimental measurements in the framework of available theories.

Due to these limitations, the attention is recently shifting to materials with high perpendicular magnetocrystalline anisotropy (PMA) resulting in an out-of-plane easy axis [43–72]. Thin strips made of high PMA ferromagnetic materials are characterized by narrow DWs and combine several key advantages over soft magnetic materials, such as high nonadiabatic effects leading to lower critical current densities and high DW velocities. A pinned DW at constrictions in these high PMA strips also depicts high stability against thermal fluctuations and low current-induced DW depinning against Joule heating. All these observations make high PMA strips very attractive, not only for technological applications, but also as valuable systems to test the microscopic theories of the spin-transfer torque by means of the simple one-dimensional models. This work reviews recent theoretical and numerical results in this class of high PMA materials, and it discusses the relevant implications they entail for the nature of the current-driven DW dynamics and its potential technological applications. The paper is organized as follows. The typology of the DWs in strips with high PMA of rectangular cross-section, along with a brief description of the micromagnetic and the one dimensional models are described in Section 2. The current-driven domain wall dynamics along both a free-defect strip and other with edge roughness is studied in Section 3. Section 4 is dedicated to the analysis of pinning of a DW in a geometrical constriction of the strip, and

its depinning under both static fields and currents. The pinned DW oscillations driven by static currents and the possibility of developing DW-based oscillators are evaluated in Section 5. Finally, the main conclusions of the study, along with the theoretical open questions and future numerical tasks are summarized in Section 6.

2. Geometry, Materials and Models

We focus our attention on thin strips of rectangular cross-section $L_y \times L_z$ with the easy axis along the z -axis ($\vec{u}_K = \vec{u}_z$, see Figure 1(a)). In order to mimic a material with high perpendicular anisotropy, the following parameters have been considered: saturation magnetization $M_s = 3 \times 10^5 \text{ A/m}$, exchange constant $A = 10^{-11} \text{ J/m}$, and anisotropy constant $K = 2 \times 10^5 \text{ J/m}^3$. According to Weller et al. [73], these parameters correspond to a typical CoPtCr alloy. The dimensionless damping parameter was taken to be $\alpha = 0.2$, which is in the same order of magnitude as the materials with high PMA analysed by Metaxas et al. [74]. A standard finite-difference scheme with cubic computational cells of $\Delta x = 3 \text{ nm}$ in side was considered.

Two equilibrium states can be found depending on the width (L_y) and thickness (L_z) of the strip: Bloch DW and Neel DW, which are plotted in Figures 1(b) and 1(c), respectively. In both cases, the magnetization inside the DW rests in the xy -plane, and it points along the y -axis and x -axis for Bloch ($\vec{m}_{\text{DW}} \propto \pm \vec{u}_y$) and Neel ($\vec{m}_{\text{DW}} \propto \pm \vec{u}_x$) configurations, respectively. These magnetic configurations were the initial state of a minimization energy process in order to evaluate which is the equilibrium state with minimum energy for different values of L_y and L_z . Figure 1(d) shows the critical value of L_y as a function of L_z above which the Bloch configuration has smaller energy than the Neel one. The transition between Bloch and Neel configurations moves toward smaller values of L_y as the strip thickness L_z increases.

In order to analyse the DW dynamics from a full-micromagnetic model (μM) point of view, the strip is assumed to be infinite along the x -axis, and a moving computational region centered on the DW with $L_x = 1.2 \mu\text{m}$ in length was performed [26]. Starting from the corresponding equilibrium state at rest, either Bloch or Neel, the response to the action of magnetic fields along the easy axis ($\vec{B}_e = B_e \vec{u}_z$) and/or electrical density currents along the x -axis $\vec{j}_a = j_a \vec{u}_x$, both of them spatially uniform and instantaneously applied at $t = 0$, is micromagnetically (μM) evaluated by numerically solving the Langevin-Landau-Lifshitz-Gilbert equation augmented by the adiabatic and nonadiabatic spin-polarized torques [5, 8, 26]:

$$\begin{aligned} \frac{d\vec{m}}{dt} = & -\gamma_0 \vec{m} \times (\vec{H}_{\text{eff}} + \vec{H}_{\text{th}}) + \alpha \left(\vec{m} \times \frac{d\vec{m}}{dt} \right) \\ & + \frac{\mu_B P}{e M_s} \left[(\vec{j}_a \cdot \nabla) \vec{m} - \xi \vec{m} \times (\vec{j}_a \cdot \nabla) \vec{m} \right], \end{aligned} \quad (1)$$

where $\vec{m}(\vec{r}, t) = \vec{M}/M_s$ is the normalized local magnetization, γ_0 is the gyromagnetic ratio, and \vec{H}_{eff} is the effective field, which includes exchange, self-magnetostatic, uniaxial

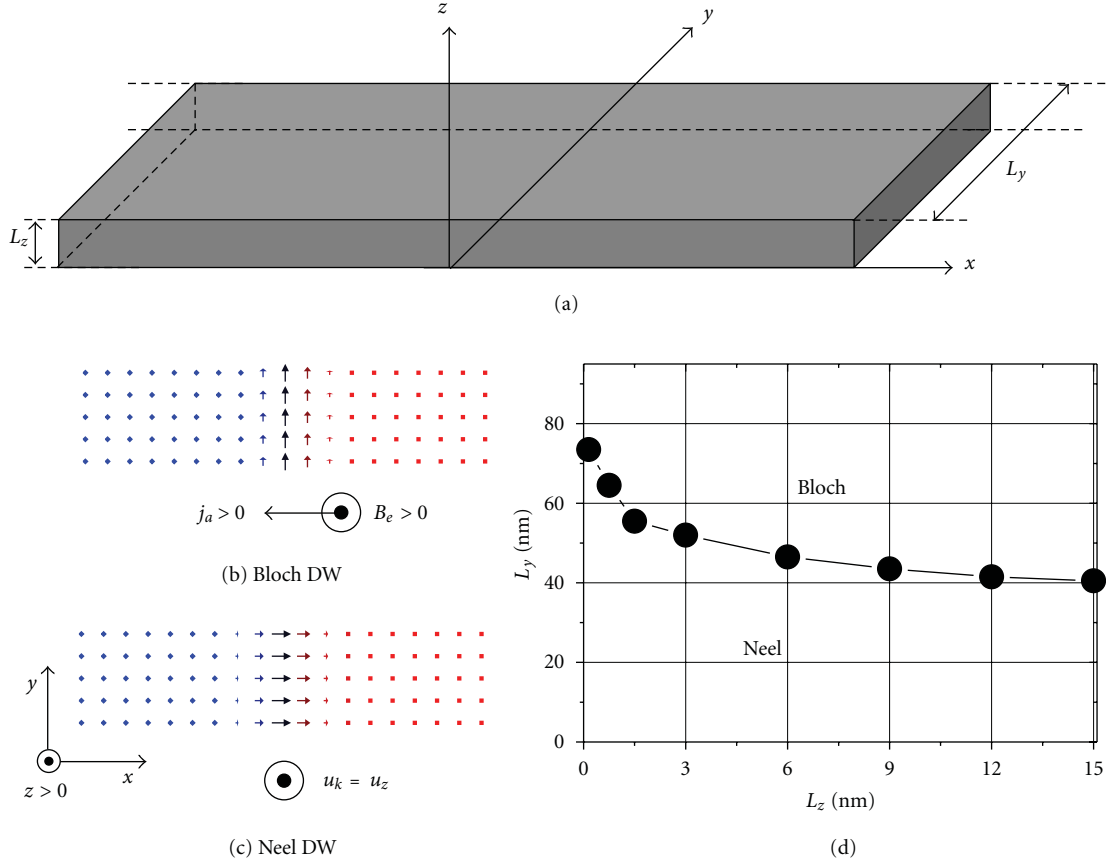


FIGURE 1: (a) Scheme of the rectangular cross-section strip geometry. Equilibrium states for a DW in thin CoPtCr strips: (b) Bloch, (c) Neel. (d) Phase diagram of the equilibrium state as a function of the width L_y and the thickness L_z of the strip (from [41]).

anisotropy ($\vec{u}_K = \vec{u}_z$ is easy axis), and external field contributions [26]. \vec{H}_{th} is the thermal field [26], which is a Gaussian random process with the following statistical properties [75, 76]:

$$\langle H_{th,i}(\vec{r}, t) \rangle = 0, \quad (2)$$

$$\langle H_{th,i}(\vec{r}, t) H_{th,j}(\vec{r}', t') \rangle = 2D_{\mu M} \delta_{ij} \delta(\vec{r} - \vec{r}') \delta(t - t'). \quad (3)$$

Equation (2) indicates that the average of the thermal field taken over different stochastic realizations vanishes in each direction $i : x, y, z$. The thermal field \vec{H}_{th} is assumed to be uncorrelated in time ($\delta(t - t')$) and uncorrelated at different points $\delta(\vec{r} - \vec{r}')$ of the finite difference mesh, as stated by (3). The strength of the thermal field, which follows from the fluctuation-dissipation theorem [75, 76], is given by

$$D_{\mu M} = \frac{\alpha K_B T}{\gamma_0 \mu_0 M_s}, \quad (4)$$

where K_B is the Boltzmann constant, and T represents the temperature.

The last two terms on the right side of (1) represent the adiabatic and the nonadiabatic spin-transfer torques, respectively [5], where μ_B is the Bohr magneton, $e < 0$ the electron's electric charge, and P is the spin polarization

factor of the current, which here is assumed to be $P = 0.5$. The coefficient ξ is a dimensionless constant describing the degree of nonadiabaticity between the spin of conduction electrons and the local magnetization [5]. Equation (1) is numerically solved by means of a fourth-order Runge-Kutta scheme. The micromagnetic results described hereafter were obtained by using a time step of 0.15 ps, and it was verified in several tested cases that a time step of 0.1 ps does not modify the presented results. Although the following micromagnetic results were computed with a cell size of $\Delta x = 3$ nm, it was also checked that the results do not significantly change when the cell size is reduced to half for several tested cases.

On the other hand, the DW dynamics has been also analyzed from the one-dimensional model (1 DM) point of view, which is described by the following equations [15, 29, 63]:

$$(1 + \alpha^2) \frac{\dot{X}}{\Delta} = \alpha \gamma_0 (H_e + H_p(X) + H_{th}(t)) + \frac{1}{2} \gamma_0 H_K \sin(2\Phi) - (1 + \alpha \xi) \frac{1}{\Delta} \frac{\mu_B P}{e M_s} j_a, \quad (5)$$

$$(1 + \alpha^2) \dot{\Phi} = \gamma_0 (H_e + H_p(X) + H_{th}(t)) - \alpha \frac{1}{2} \gamma_0 H_K \sin(2\Phi) - (\xi - \alpha) \frac{1}{\Delta} \frac{\mu_B P}{e M_s} j_a, \quad (6)$$

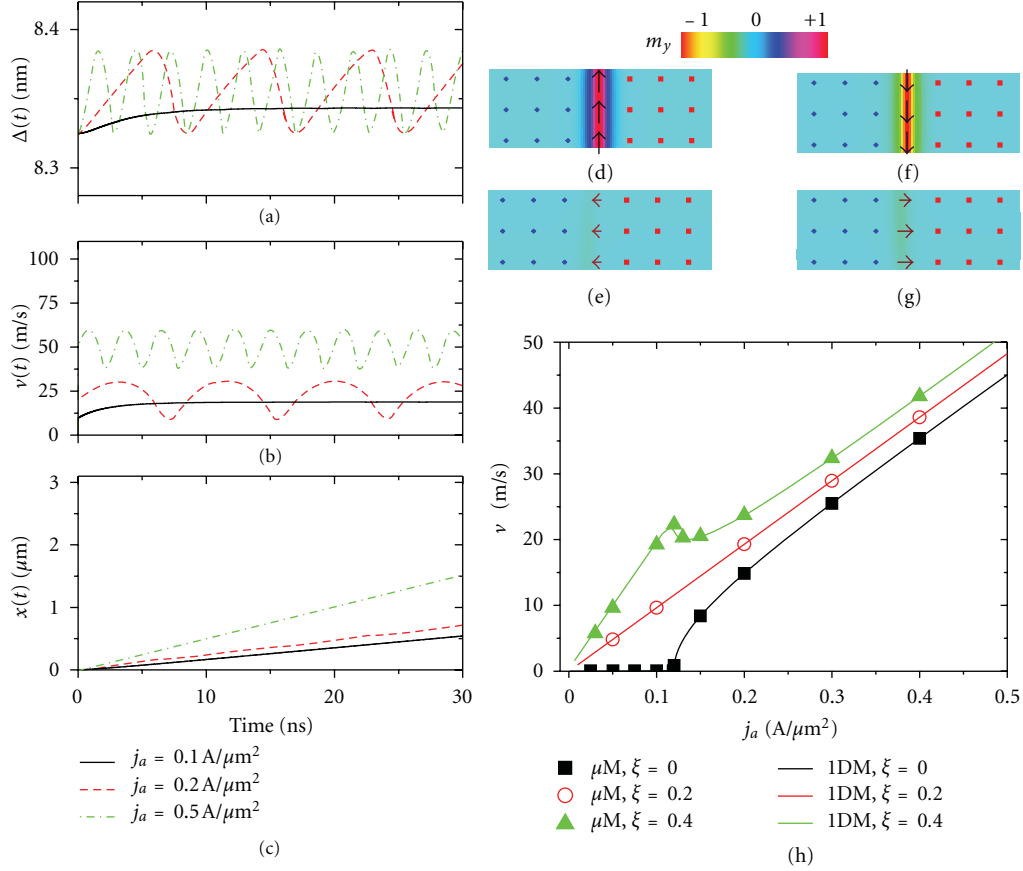


FIGURE 2: Current driven DW dynamics along a perfect strip with $L_y \times L_z = 120 \times 3 \text{ nm}^2$. (a), (b), and (c) depict the micromagnetically (μM) computed temporal evolution of the DW width Δ , the DW velocity v , and the DW position x under three different density currents: $j_a = 0.1 \text{ A}/\mu\text{m}^2$, $j_a = 0.2 \text{ A}/\mu\text{m}^2$, and $j_a = 0.5 \text{ A}/\mu\text{m}^2$ for a nonadiabatic parameter of $\xi = 0.4$. (d)–(g) show typical micromagnetic states of the propagating DW for currents larger than the Walker breakdown ($j_a > j_W(\xi)$). (h) Time-averaged DW velocity as function of j_a for three different values of the nonadiabatic parameter: $\xi = 0$, $\xi = 0.2$ and $\xi = 0.4$. Dots correspond to μM results, whereas lines are predictions from the 1 DM with $\Delta = 8.325 \text{ nm}$ and $H_K = 12533.5 \text{ A/m}$. (Reprinted with permission From [70, 72]. Copyright (2012), American Institute of Physics).

where $X = X(t)$ is the position of the DW centre, $\Phi = \Phi(t)$ is the tilt angle of the DW magnetization, Δ is the DW width, and H_K is the hard-axis anisotropy field of magnetostatic origin. $H_e = B_e/\mu_0$ is the applied field along the easy z -axis, and $H_p(X)$ is the spatial dependent pinning field, which can be expressed as $H_p(X) = -(1/2\mu_0 M_s L_y L_z)(\partial V_{\text{pin}}(X)/\partial X)$, where $V_{\text{pin}}(X)$ is the local pinning potential. $H_{\text{th}}(t)$ is a stochastic random thermal field which describes the effect of thermal fluctuation in the 1 DM [24, 26, 27, 29]. The thermal field is assumed to be a Gaussian-distributed stochastic process with zero mean value ($\langle H_{\text{th}}(t) \rangle = 0$) and uncorrelated in time ($\langle H_{\text{th}}(t) H_{\text{th}}(t') \rangle = 2D_{1D} \delta(t - t')$). The factor D_{1D} represents the strength of the thermal field, which can be obtained from the fluctuation-dissipation theorem ($D = (\alpha K_B T / \mu_0 V_{\text{DW}} M_s \gamma_0)^{1/2}$, where $V_{\text{DW}} = \Delta L_y L_z$ is the DW volume).

3. Current-Driven DW Dynamics

The essential goal for designing recording and logic DW-based devices which can be competitive with nowadays

available technologies is to efficiently improve the velocity of the propagating DW with low currents against unwanted Joule heating effects. This section is dedicated to describe the DW dynamics along high PMA strips driven by spin-polarized current, from the ideal or perfect strips to the realistic ones, where disorder and thermal effects play a significant role.

3.1. Perfect Strips at Zero Temperature. The case of a perfect strip with $L_y \times L_z = 120 \times 3 \text{ nm}^2$ is firstly considered. Figures 2(a), 2(b), and 2(c) depicts the micromagnetically (μM) computed temporal evolution of the DW width Δ , the DW velocity v and the DW position x under three different density currents: $j_a = 0.1 \text{ A}/\mu\text{m}^2$, $j_a = 0.2 \text{ A}/\mu\text{m}^2$ and $j_a = 0.5 \text{ A}/\mu\text{m}^2$ for a nonadiabatic parameter of $\xi = 0.4$. The instantaneous DW width was numerically evaluated considering the Thiele's definition [77], which is given by $1/\Delta(t) = (1/2L_y L_z) \int (\partial \vec{m}(\vec{r}, t) / \partial x)^2 dV$. For $j_a = 0.1 \text{ A}/\mu\text{m}^2$, which is below than the Walker breakdown ($j_W(\xi = 0.4) = 0.12 \text{ A}/\mu\text{m}^2$), the DW moves by preserving its initial Bloch

configuration and reaching a stationary linear behavior with a steady DW velocity. In contrast, for $j_a = 0.2 \text{ A}/\mu\text{m}^2 > j_w(0.4)$, the DW does not reach a steady regime and its internal magnetization precesses periodically around the easy z -axis. Figures 2(d)–2(g) depict typical Bloch and Neel configurations adopted by the DW during the turbulent precessional regime.

The time-averaged DW velocity $\langle v \rangle$ as a function of j_a is shown in Figure 2(h) for three different values of the nonadiabatic parameter: $\xi = 0$ (perfect adiabatic case), $\xi = 0.2$, and $\xi = 0.4$. Dots correspond to μM results and lines to 1DM predictions, where the value of DW width $\Delta = 8.325 \text{ nm}$ was obtained from the micromagnetic configuration of the DW at rest, and the hard axis anisotropy field of magnetostatic origin $H_K = 12533.5 \text{ A/m}$ was deduced from the micromagnetically computed Walker field $B_W = \mu_0 H_W \approx 1.575 \text{ mT}$ ($H_K = 2H_W/\alpha$). In the perfect adiabatic case ($\xi = 0$), there is a threshold density current ($j_w(\xi = 0)$) below which the DW motion is not achieved. Above $j_w(0)$, the motion takes place by means of DW precession similarly to the field-driven case above the Walker breakdown [66, 70]. In the 1DM, the Walker field H_W and the Walker threshold current (j_w) are related by $j_w(\xi) = (1/|\xi - \alpha|) (|e|M_s/P\mu_B)\gamma_0\Delta H_W$, which yields $j_w(0) = 0.12 \text{ A}/\mu\text{m}^2$, in good agreement with full micromagnetic results (μM). In the nonadiabatic case ($\xi > 0$), the DW moves for any positive current along the perfect strip, and it does it without changing its initial structure if the nonadiabatic parameter matches the damping parameter ($\xi = \alpha = 0.2$). Note that $j_w(\xi = \alpha) = \infty$. For any other case ($0 < \xi \neq \alpha$), there is a Walker threshold density current $j_w(\xi)$ above which the DW rotates around the z -axis similarly to the field-driven case. The current DW mobility is defined as $\mu = dv/dj_a$, and it is given by $\mu_{st,j} = (\xi/\alpha)(\mu_B P/|e|M_s)$ and $\mu_{hf,j} = ((1 + \xi\alpha)/(1 + \alpha^2))(\mu_B P/|e|M_s)$ for the steady ($j_a < j_w$) and the high-current ($j_a \gg j_w$) linear regimes [25], respectively.

3.2. Rough Strips at Room Temperature. Former simulations were conducted on a perfect strip, without any defect which could prevent the free DW motion. However, due to the nanolithography fabrication process, realistic strips have defects and imperfections such as edge roughness [78] which oppose to the free DW motion. Due to the electron beam, the edge roughness in real samples can be characterized by an average depth (along the y -axis) and an average length (along the x -axis). In order to mimic the irregularities in the sample geometry originating from electron beam lithography, natural edge roughness is modelled by independently deforming the perfect finite difference mesh at both edges of the strip [26]. Here, a random roughness pattern, where both the depth and the length are assumed to be equal to the typical grain size $D_g = 3 \text{ nm}$, is considered, so each computational cell at the edges of the strip is or not magnetic with 50% of probability. A $6 \mu\text{m}$ -long strip pattern is generated at the beginning of the simulation to be used by the moving $1.2 \mu\text{m}$ -long computational region.

Typical examples of the micromagnetic results for the temporal evolution of the DW position along a rough strip are depicted in Figure 3 for three different currents: (a) $j_a =$

$0.04 \text{ A}/\mu\text{m}^2$, (b) $j_a = 0.1 \text{ A}/\mu\text{m}^2$, and (c) $j_a = 0.2 \text{ A}/\mu\text{m}^2$, considering a nonadiabatic parameter of $\xi = 0.4$ and temporal window of $t_w = 50 \text{ ns}$. The deterministic trajectory ($T = 0$, dashed lines) and ten different stochastic realizations at room temperature ($T = 300 \text{ K}$, solid lines) are shown for each current. Computing ten stochastic realizations each one of 50 ns requires a enormous computational effort in the framework of the full micromagnetic model (μM), and in every specific case we must wonder if this number is sufficient to obtain statistically meaning results. In order to justify this choice, the same problem was also analyzed in the 1DM (see Figure 3(h)), where the number of stochastic realizations and the temporal window can be increased by one or two orders of magnitude with reduced computational effort. It was confirmed that results of extended 1DM simulations with $t_w = 500 \text{ ns}$ and $N = 100$ are quite similar to the ones obtained for $t_w = 50 \text{ ns}$ and $N = 10$, and they are also in quantitative agreement with the full micromagnetic results. This observation allows us to justify that $N = 10$ is sufficient to obtain meaningful statistically results. The deterministic threshold current j_d , defined as the minimum current required to promote the sustained DW propagation at zero temperature, is around $0.1 \text{ A}/\mu\text{m}^2$ for a $L_y \times L_z = 120 \times 3 \text{ nm}^2$ strip with a typical roughness size of $D_g = 3 \text{ nm}$.

For very low currents, the DW does not depart from its initial position (see Figure 3(a)) because the force on the DW due to the applied current ($j_a = 0.04 \text{ A}/\mu\text{m}^2$) is still too low to overcome the energy barrier induced by the roughness, even at room temperature. For larger currents but smaller than the deterministic depinning threshold ($0.05 \text{ A}/\mu\text{m}^2 \leq j_a \leq j_d(\xi)$), the DW also gets pinned due to the roughness, but due to thermal fluctuations, it eventually depins and propagates along the strip (see Figure 3(b)). In this thermally activated field regime ($0.05 \text{ A}/\mu\text{m}^2 \leq j_a \leq j_d(\xi)$), the DW displaces several nanometers from its initial position for some time before reaching a region of higher surface roughness where it becomes pinned again for some time up to thermal fluctuations assist again the DW depinning and propagation. Similar to the field-driven case, the DW follows a creep regime, where it can be seen as a thermally activated interface that is creeping over local pinning sites. For very high currents ($j_a \geq 0.2 \text{ A}/\mu\text{m}^2$), the DW position increases almost linearly as the time elapses for all the stochastic realizations, and it reaches a quite similar final position at the end of the evaluated temporal window ($t_w = 50 \text{ ns}$, see Figure 3(c)). Therefore, in such a high regime, the DW dynamics is governed by the current, which is high enough to overcome the energy barrier of the roughness independently on the thermal effects. It is worthy to note that, independently of the nonadiabatic parameter, the thermally activated DW motion along the rough strip takes place by precessing between Bloch and Neel configurations. These characteristic configurations are shown in Figures 3(d)–3(g). This observation is in contrast to the DW propagation along a perfect strip, where DW propagates rigidly for any finite current if the nonadiabatic parameter is equal to the damping ($\xi = \alpha$).

The statistically averaged DW velocity $[\langle v \rangle]$ as a function of j_a along a rough strip at room temperature ($T = 300 \text{ K}$) is

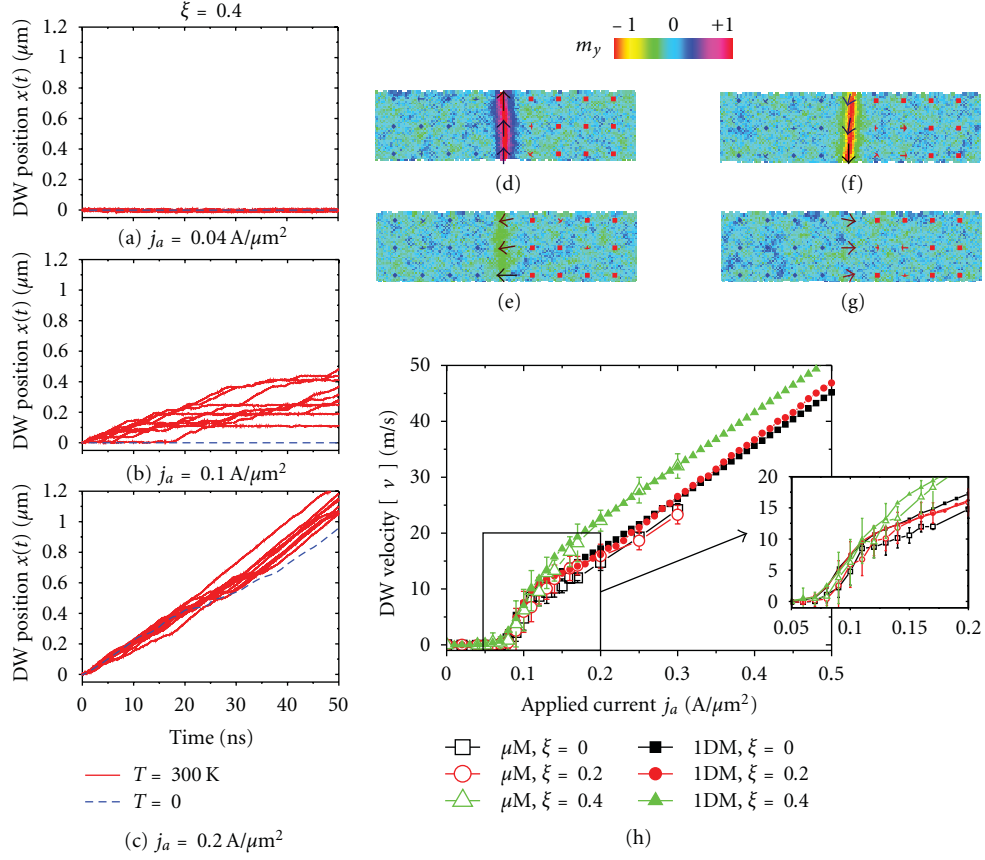


FIGURE 3: Current driven DW dynamics along a rough ($D_g = 3$ nm) strip with $L_y \times L_z = 120 \times 3$ nm². Micromagnetically (μM) computed temporal evolution of the DW position x under three different density currents: (a) $j_a = 0.04$ A/ μm^2 , (b) $j_a = 0.1$ A/ μm^2 and (c) $j_a = 0.2$ A/ μm^2 for a nonadiabatic parameter of $\xi = 0.4$. Blue-dashed lines correspond to the deterministic case ($T = 0$), whereas red-solid lines correspond to ten stochastic realizations at room temperature ($T = 300$ K). (d)–(g) show typical micromagnetic states of the propagating DW along a rough strip at room temperature. (h) Time-averaged DW velocity as function of j_a for three different values of the nonadiabatic parameter: $\xi = 0$, $\xi = 0.2$, and $\xi = 0.4$. Open-dots correspond to μM results (with indication of the standard deviation), whereas solid symbols are the predictions from the 1DM with $\Delta = 8.325$ nm, $H_K = 12533.5$ A/m, and a periodic pinning potential given by $V_{\text{pin}}(X) = V_0 \sin^2(\pi X/p)$ with $V_0 = 1.65 \times 10^{-20}$ J and $p = 30$ nm. The inset shows the results around between $j_a = 0.05$ A/ μm^2 and $j_a = 0.2$ A/ μm^2 (Reprinted with permission From [70]. Copyright (2012), American Institute of Physics).

shown in Figure 3(h) for three different values of the nonadiabatic parameter: $\xi = 0$, $\xi = 0.2$, and $\xi = 0.4$. This statistically averaged DW velocity $[\langle v \rangle]$ was calculated by firstly averaging over a temporal window of $t_w = 50$ ns as $\langle v \rangle_i = (1/t_w) \int_0^{t_w} v(t) dt$, and then, averaging over ten ($N = 10$) stochastic realizations as $[\langle v \rangle] = (1/N) \sum_{i=1}^N \langle v \rangle_i$. Open symbols correspond to μM simulations of a rough strip with $D_g = 3$ nm, and full symbols were obtained in the framework of the 1DM, where the local pinning landscape is modeled by a periodic pinning potential given by $V_{\text{pin}}(X) = V_0 \sin^2(\pi X/p)$. The values of the energy barrier V_0 and the spatial periodicity p were chosen to match a deterministic depinning field similar to the micromagnetic value for $D_g = 3$ nm: $V_0 = 1.65 \times 10^{-20}$ J, and $p = 30$ nm. Figure 3(h) confirms that the velocity-current characteristic predicted by the 1DM is in good qualitative and quantitative agreement with full μM results.

Analogously to the creep and flow regimes seen in former numerical studies and other experimental studies of

field-driven motion, the DW mobility increases at low currents and saturates at higher values (see Figure 3(h)). Therefore, the inclusion of surface roughness along with thermal fluctuations in both μM and 1DM simulations provides a proper explanation to understand experimental observations. Apart from the qualitative agreement with experiments [47, 55], micromagnetic simulations also provide information on the internal DW structure during its motion. In the single layer rough strip, the thermally activated DW translation occurs by DW precession around the z -axis, even for the case of $\xi = \alpha = 0.2$. In the creep regime (0.05 A/ $\mu\text{m}^2 < j_a < 0.1$ A/ μm^2), $[\langle v \rangle]$ increases exponentially with j_a , but it does not depend significantly on nonadiabatic parameter (see Figure 3(h)), so it is dominated by roughness and thermal fluctuations, and ξ does not play a remarkable role. In the high-current flow regime ($j_a \gg 0.1$ A/ μm^2), the DW mobility recovers the deterministic value for the perfect strip ($\mu_{hf,j} = ((1+\xi\alpha)/(1+\alpha^2))(\mu_B P/|e| M_s)$), both for $\xi = 0$ and $\xi = 0.4$ cases. However,

as it is clear in Figure 3(h), the DW mobility in the high-current flow regime for $\xi = \alpha = 0.2$ approaches to the one of the perfect adiabatic case ($\mu_{hf,j} = (1/(1 + \alpha^2))(\mu_B P / |e| M_s)$). These numerical predictions point out that, in a single layer strip, the surface roughness favors the turbulent motion with DW precession between Bloch and Néel configurations. It is also clear in Figure 3(h) that the standard deviation of $\langle v \rangle$ versus j_a is enlarged in the creep regime, whereas it decreases significantly as j_a increases in the high-current flow regime. This fact indicates that at high currents, the DW dynamics becomes insensitive to the roughness, being mainly dominated by the current force.

3.3. Strips Sandwiched in Asymmetric Stacks: The Role of the Spin-Orbit Interaction. Experimental measurements along high PMA strips have been performed in several architectures, ranging from single layer [50, 53] to multilayer stacks [47, 49, 51, 52, 54, 55]. Former section was dedicated to the study of the current-driven DW dynamics along a single layer PMA strip. However, the experiments on DW propagation along a high PMA Cobalt strip sandwiched between two dissimilar nonmagnetic layers (Pt/Co/AlO) are particularly interesting because they have pointed out a high spin-torque efficiency leading to very high DW velocities at reduced currents [51, 55]. The suggested reason for this behavior is the spin-orbit interaction (SOI) on the conduction electrons, which originates from the structural inversion asymmetry (SIA) of the multilayer stack. The SOI allows for the transfer of orbital angular momentum from the crystal lattice to the local magnetization [79], and it is mediated by an effective Rashba magnetic field (\vec{H}_R) which is given by [55, 80, 81]

$$\vec{H}_R = \frac{\alpha_R P}{\mu_0 \mu_B M_s} (\vec{u}_z \times \vec{j}_a), \quad (7)$$

where \vec{u}_z is the unit vector along the perpendicular axis (the z direction) and α_R is the Rashba parameter which describes the strength of the SOI [81]. The aim of the present section consists on analysing the current-driven DW propagation in the presence of the Rashba field. This field is added as a new contribution to the effective field in (1) considering a Rashba parameter of $\alpha_R = 10^{-11}$ eVnm, which is a typical value of a two-dimensional electron gas with SIA [55, 80, 81]. The μM results along a perfect strip are collected in Figure 4, which depicts the temporal evolution of the DW width [77] $\Delta(t)$, the DW velocity $v(t)$, and the DW position $x(t)$, respectively, under three different values of j_a for the case of finite Rashba field ($\alpha_R = 10^{-11}$ eVnm) with $\xi = 0.4$. Contrary to what happens in the absence of Rashba field for currents larger than the Walker breakdown (see Figures 2(a)–2(c)), the DW reaches a stationary behavior for all the studied currents $[0, 1 \text{ A}/\mu\text{m}^2]$, and it propagates rigidly with steady velocity. Typical steady Bloch DW configurations reached under two values of j_a are depicted in Figures 4(d) and 4(e).

The time-averaged DW velocity $\langle v \rangle$ over a temporal window of $t_w = 50$ ns is depicted as a function of j_a in Figure 4(f) for several values of ξ in the case of a perfect strip ($D_g = 0$) at zero temperature ($T = 0$). Open symbols

correspond to the case of finite Rashba field with $\alpha_R = 10^{-11}$ eVnm. The results corresponding to zero-Rashba field ($\alpha_R = 0$, filled symbols) of former Figure 2(h) are also included for comparison. In the perfect adiabatic case ($\xi = 0$), a minimum density current of $j_w(\xi = 0) \approx 0.12 \text{ A}/\mu\text{m}^2$ is required to promote self-sustained DW motion in absence of Rashba field ($\alpha_R = 0$). Above this intrinsic critical current, the DW moves turbulently by precessing clockwise around the z -axis between Bloch and Néel configurations, and for very high currents ($j_a \gg j_w(\xi = 0)$) the DW mobility, which is defined as $\mu = dv/dj_a$, is $\mu_t(\xi = 0) = (1/(1 + \alpha^2))(\mu_B P / |e| M_s)$ [25], which tends to $\mu_t(\xi = 0) = \mu_B P / |e| M_s$ for $\alpha \ll 1$. However, when a finite Rashba field with $\alpha_R = 10^{-11}$ eVnm is taken into account, no DW motion is achieved in the perfect adiabatic case ($\xi = 0$) even for high currents such as $j_a = 1 \text{ A}/\mu\text{m}^2$. Therefore, \vec{H}_R increases the critical intrinsic current in the perfect adiabatic case ($\xi = 0$). For $\xi = \alpha = 0.2$, the DW velocity increases linearly with j_a for any finite value, and the DW mobility is $\mu_s(\xi = \alpha) = \mu_B P / |e| M_s$ independently of the Rashba field. Note that this mobility is similar to the one achieved in the high current turbulent regime ($j_a \gg j_w(\xi)$) for zero-Rashba field independently on ξ . Finally, for $\xi = 0.4$, the DW precesses turbulently and counter-clockwise between Bloch and Néel configurations above the Walker threshold at zero Rashba field ($\alpha_R = 0$), and under currents well above than this threshold the DW mobility approaches again to one observed for both $\xi = 0$ and $\xi = 0.2$ cases ($\mu_t(\xi) \approx \mu_B P / |e| M_s$, for $\alpha \approx \xi \ll 1$). However, there is no Walker breakdown in the presence of the Rashba field ($\alpha_R = 10^{-11}$ eVnm) for $\xi \neq 0$, and the DW mobility maintains the value of the linear low-current steady regime ($\mu_s(\xi > 0) = (\xi/\alpha)(\mu_B P / |e| M_s)$) in the whole analyzed range of density currents.

The effect of the Rashba field under positive current ($j_a > 0$) is equivalent to a homogeneous transverse field along $y > 0$ -axis, and both of them promote the stabilization of the Bloch up DW configuration by raising the energy barrier against transformations to Néel DW. If the current is reversed ($j_a < 0$), the Rashba field points along the negative transverse direction ($y < 0$), and similarly to a negative transverse magnetic field, it firstly promotes the transition from Bloch up to Bloch down. Once this transition is completed, the Bloch down DW moves rigidly in the opposite sense ($x < 0$) [55]. These results indicate that due to the SOI in a asymmetric trilayer stack with SIA ($\vec{H}_R \neq 0$), the linear steady high mobility regime is extended to high currents, and therefore, it allows to achieve rigid DW propagation with higher DW velocities than the ones achieved in a single layer or a symmetric multilayer stack, where the Rashba field due to the SOI is negligible ($\vec{H}_R = 0$) and the maximum velocity is limited by the nonadiabatic parameter.

In order to get a more realistic description, and as it was done for a single layer strip ($\vec{H}_R = 0$), the next step in the study is focused on describing the influence of the edge roughness and thermal fluctuations when the finite Rashba field is taken into account. The effect of \vec{H}_R with $\alpha_R = 10^{-11}$ eVnm on the temporal evolution of $x(t)$ along the rough strip ($D_g = 3$ nm) under different j_a is depicted in

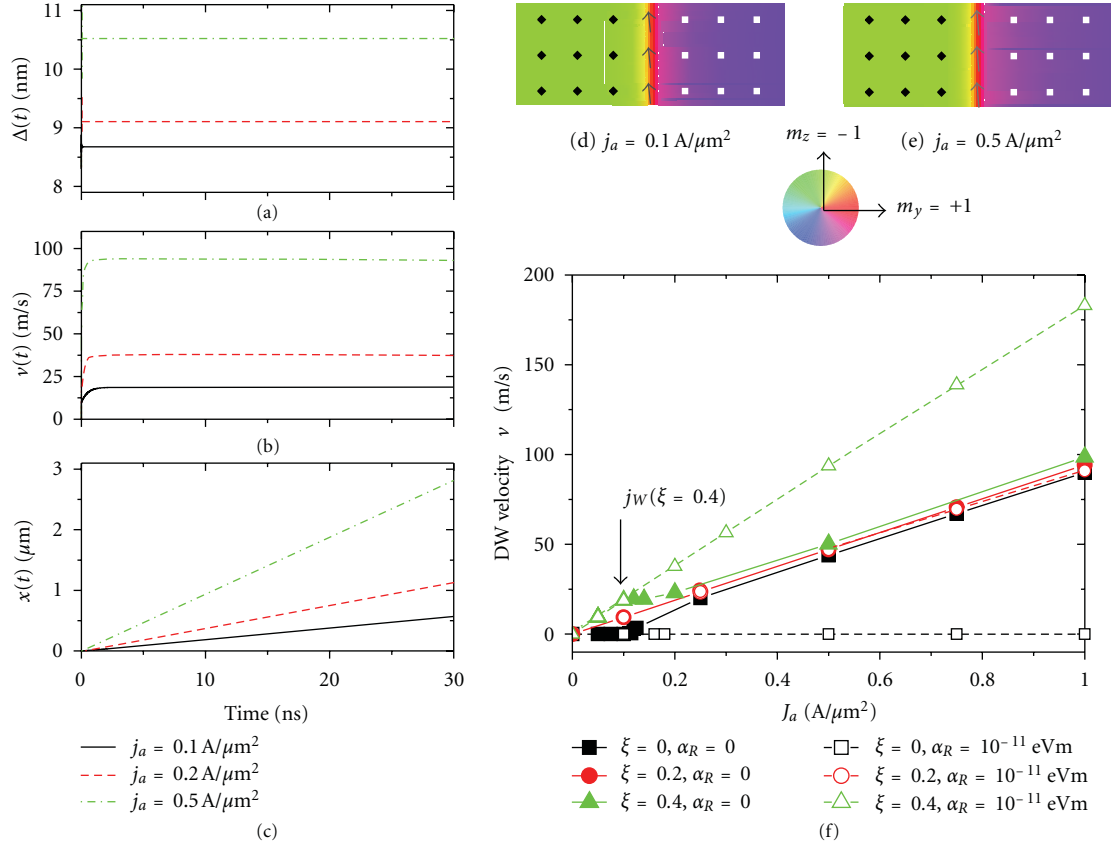


FIGURE 4: μM results of the current driven DW dynamics along a perfect strip with $L_y \times L_z = 120 \times 3 \text{ nm}^2$ in the presence of SOI ($\alpha_R = 10^{-11} \text{ eV}\text{m}$). (a), (b), and (c) depict the micromagnetically (μM) computed temporal evolution of the DW width Δ , the DW velocity v and the DW position x under three different density currents: $j_a = 0.1 \text{ A}/\mu\text{m}^2$, $j_a = 0.2 \text{ A}/\mu\text{m}^2$, and $j_a = 0.5 \text{ A}/\mu\text{m}^2$ for a nonadiabatic parameter of $\xi = 0.4$. (d)-(e) show typical micromagnetic states of the propagating DW in the presence of SOI. (f) Time-averaged DW velocity as function of j_a for three different values of the nonadiabatic parameter: $\xi = 0$, $\xi = 0.2$, and $\xi = 0.4$. Filled and open symbols correspond to the cases with $\alpha_R = 0$ and $\alpha_R = 10^{-11} \text{ eV}\text{m}$, respectively (Reprinted with permission From [72]. Copyright (2012), American Institute of Physics).

Figures 5(a)–5(c). A first quantitative difference with respect to the zero-Rashba field case ($\alpha_R = 0$) studied in Figure 3(h) is that the deterministic depinning threshold current increases to $j_d = 0.6 \text{ A}/\mu\text{m}^2$ in the presence of finite Rashba field with $\alpha_R = 10^{-11} \text{ eV}\text{m}$. At zero temperature ($T = 0$, blue-dashed lines) two different behaviors are clearly observed. If j_a is smaller than the deterministic threshold current ($j_d = 0.6 \text{ A}/\mu\text{m}^2$), the DW eventually departs from its initial position but after a few nanoseconds, it becomes totally pinned after reaching a region with high surface roughness (see Figures 5(a) and 5(b) for $j_a = 0.2 - 0.4 \text{ A}/\mu\text{m}^2$). On the other hand, for $j_a \geq j_d$, the DW position increases linearly as the time elapses in the whole evaluate temporal window ($t_w = 50 \text{ ns}$).

The DW dynamics is substantial different at $T = 300 \text{ K}$. Ten stochastic realizations have been evaluated for each j_a . Even for very small currents (see red-solid lines in Figure 5(a)) there is a non-null probability of DW propagation. If j_a increases below the critical deterministic threshold ($j_a < j_d$), the DW propagates depicting a jerky motion as due to thermal activation over the local energy barrier induced by

the roughness (see red-solid Figure 5(b)). The DW displaces several nanometers from its initial position during some time before reaching a region of high surface roughness, where it is temporally pinned up to thermal fluctuations assist again the DW depinning and its subsequent propagation. Similarly to the deterministic case, if $j_a \geq j_d$, the DW position increases almost linearly as the time elapses for all the realizations (see Figure 5(c)). Therefore, j_a is high enough to overcome the energy barrier of the roughness independently on the thermal effects in such a high current regime. As it is depicted in Figures 5(d)–5(g), the DW Bloch structure is also preserved for all j_a in the presence of the Rashba field at $T = 300 \text{ K}$.

The DW velocity as a function of j_a is shown in Figure 5(h) for $\alpha_R = 10^{-11} \text{ eV}\text{m}$. The time-averaged DW velocity ($\langle v \rangle$) along a rough strip ($D_g = 3 \text{ nm}$) at zero temperature ($T = 0$, blue-squares) are compared to the statistically-averaged DW velocity ($[\langle v \rangle]$) at room temperature ($T = 300 \text{ K}$, red-circles), which was computed by averaging the time-averaged velocity over ten stochastic realizations for each j_a . Error bars indicate the standard

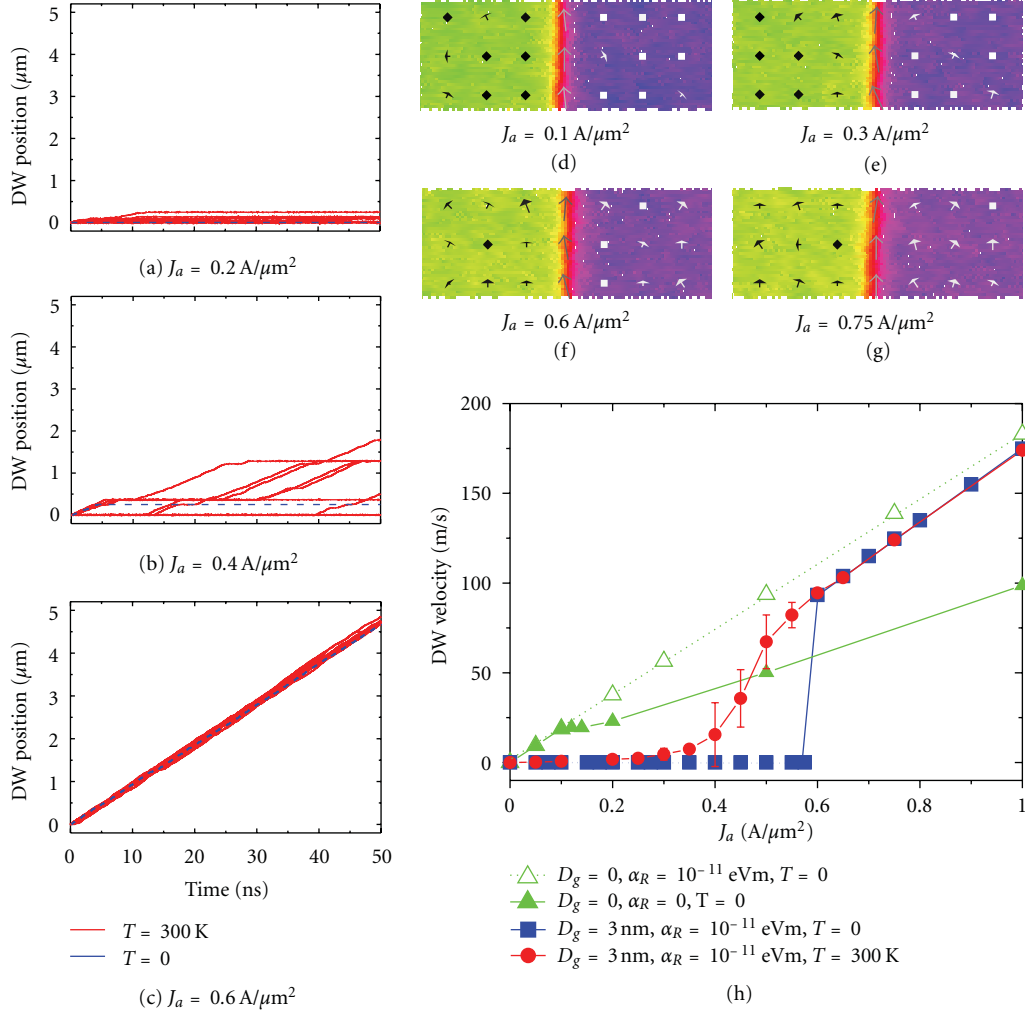


FIGURE 5: (a)–(c) $x(t)$ versus t along a rough strip ($D_g = 3 \text{ nm}$) for different j_a with $\alpha_R = 10^{-11} \text{ eVm}$ at zero (blue-dashed lines) and at room temperature (red-solid lines). (d)–(g) Typical DW configurations under different j_a . (h) DW velocity as a function of j_a . (Reprinted with permission From [71]. Copyright (2012), American Institute of Physics).

deviation. The results for $\xi = 0.4$ of former Figure 4(f) are also included for comparison. At $T = 0$, no sustained DW motion is achieved up to j_a overcomes the deterministic depinning threshold $j_d = 0.6 \text{ A}/\mu\text{m}^2$, and above it ($j_a \geq j_d$), the DW velocity increases linearly with j_a . The curve of $[\langle v \rangle]$ as a function of j_a at $T = 300 \text{ K}$ is in good qualitative agreement with recent experiments (see Figure 3 in [47] and in [55]). One observes (i) a slow regime ($j_a < j_d$) controlled by thermal activation and local pinning, where $[\langle v \rangle]$ increases exponentially, and (ii) a high-current flow regime ($j_a > j_d$) with a linear variation of $[\langle v \rangle]$. Note that the DW mobility at the high-current regime ($j_a > j_d$) is larger than the one achieved for $\vec{H}_R = 0$ because the transverse Rashba field SOI avoids the turbulent DW precession.

Due to the high computational effort, these types of full micromagnetic studies of realistic strips with edge roughness at room temperature are very time-consuming, and in order to describe experimental results, it is desirable to develop

the 1 DM given by (5) and (6) by including the effect of the Rashba field given by (7). The resulting 1 DM equations are

$$\begin{aligned}
 (1 + \alpha^2) \frac{\dot{X}}{\Delta} &= \alpha \gamma_0 (H_e + H_p(X) + H_{th}(t)) \\
 &\quad + \frac{1}{2} \gamma_0 (H_K \sin(2\Phi) - \pi H_R \sin(\Phi)) \\
 &\quad - (1 + \alpha \xi) \frac{1}{\Delta} \frac{\mu_B P}{e M_s} j_a \\
 (1 + \alpha^2) \Phi &= \gamma_0 (H_e + H_p(X) + H_{th}(t)) \\
 &\quad - \alpha \frac{1}{2} \gamma_0 (H_K \sin(2\Phi) - \pi H_R \sin(\Phi)) \\
 &\quad - (\xi - \alpha) \frac{1}{\Delta} \frac{\mu_B P}{e M_s} j_a,
 \end{aligned} \tag{8}$$

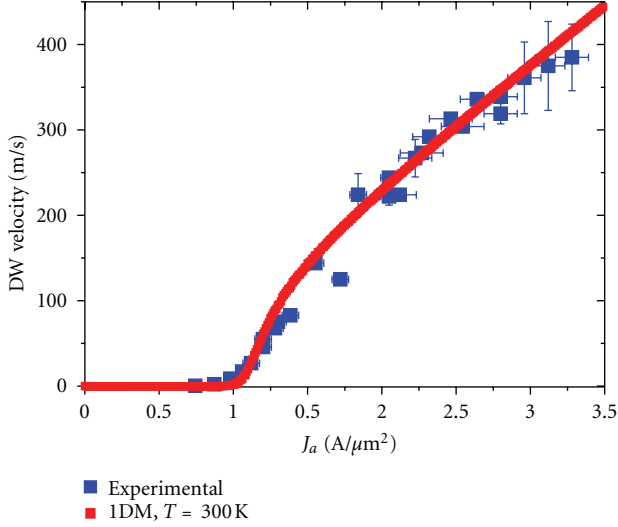


FIGURE 6: Comparison of the experimental results (see Figure 3 in [55]) and 1DM predictions for the current-induced DW dynamics along a Cobalt strip with high PMA sandwiched between two dissimilar nonmagnetic strips (Pt/Co/AlO) at room temperature ($T = 300$ K). All the 1DM parameters are enumerated in the text.

where $\vec{H}_R = H_R \vec{u}_y$ with $H_R = \alpha_R P j_a / \mu_0 \mu_B M_s$. Although it is not shown here for reasons of brevity, it was confirmed that the μ M results depicted in Figures 4(b), 4(c) and 4(f) are very accurately reproduced by these 1DM (8). Much more interesting is to show how this simple 1DM is able to reproduce the recent experimental results by Miron and coworkers [55]. In their experimental study, a cobalt strip with a cross-section of $L_y \times L_z = 500 \text{ nm} \times 0.6 \text{ nm}$ is sandwiched between two dissimilar nonmagnetic layers (Pt/Co/AlO). In order to reproduce these experimental results by using the 1DM (8), the following material parameters for the sandwiched Cobalt layer are considered: $M_s = 1.09 \times 10^6 \text{ A/m}$, $A = 10^{-11} \text{ J/m}$, $K = 1.19 \times 10^6 \text{ J/m}^3$, $\alpha = 0.2$, $P = 0.5$, $\xi = 1$, and $\alpha_R = 10^{-10} \text{ eVm}$. Note that these parameters are consistent with the ones which were used in [55, 79]. The DW width is $\Delta = \sqrt{A/K} = 3 \text{ nm}$, $H_K = 27852 \text{ A/m}$, and the effect of disorder is modeled by assuming a periodic pinning potential $V_{\text{pin}}(X) = V_0 \sin^2(\pi X/p)$ with a characteristic energy barrier of $V_0 = 1.8 \times 10^{-19} \text{ J}$, and a periodicity of $p = 30 \text{ nm}$.

The 1DM results for the average DW velocity at room temperature are compared to the experimental results (see Figure 3 in [55]) in Figure 6. In the low current regime, the DW exhibits a stochastic creep motion, and the DW velocity can be described by $v = v_0 \exp[-(j_d/j_a)^\mu (V_0/K_B T)]$ where v_0 is a prefactor, j_a is the applied current, and j_d is the critical depinning threshold. V_0 is the characteristic height of the pinning energy barrier induced by the surface roughness, and μ is a universal dynamics exponent. As in the field-driven case, the creep regime under current is consistent with an exponent of $\mu = 1/4$. When the driving density current j_a is well above the deterministic depinning threshold, thermal perturbations and surface roughness have a negligible effect on the DW velocity, which is found to

increase linearly on j_a similarly to the perfect strip case at zero temperature. As it clearly shown in Figure 6, the 1DM predictions are in very good agreement with the experimental measurements. This is a noticeable result, because a systematic experimental study of the DW velocity as function of the applied current along different strips with different materials, sizes, and configurations (single layer or asymmetric multilayer stacks) could be accurately reproduced by the 1DM simulations including both disorder and thermal effects, with low computational effort. By means of direct comparison with experimental measurements, it could be useful to gain information on the nonadiabatic parameter, for instance, by simply comparing with the high flow DW mobility. These type of comparative studies could be also used to extract the value of the Rashba parameter or the temperature dependence of the polarization factor. From a technological point of view, the SOI mediated by the Rashba field is a remarkable phenomenon because it promotes the high velocity and rigid DW propagation at relatively low current avoiding unwanted Joule heating.

4. DW Depinning from a Notch

The realization of DW-based devices for developing recording and logic technologies does not only require high velocity propagation with low current, but also an efficient control of the DW position. This can be done by means of constrictions or artificial notches which act as local pinning sites for the DW. The success of the applications require high stability against thermal fluctuations, and at the same time, low-current DW depinning. This section is dedicated to the analysis of the pinning potential due to artificial notches intentionally designed to control the DW position in a strip with high PMA, and to the study of the DW depinning processes driven by both magnetic field and/or currents.

4.1. Describing the Pinning Potential. Figure 7(a) shows the geometry of strip containing an artificial pinning site, which consists on two rectangular notches, each one of dimensions $n_x \times n_y$ and placed at both sides of the strip. In the rest of this review, the parameters for a typical CoPtCr alloy are considered: $M_s = 3 \times 10^5 \text{ A/m}$, $A = 10^{-11} \text{ J/m}$, $K = 2 \times 10^5 \text{ J/m}^3$, $P = 0.5$, $\alpha = 0.2$, and $\alpha_R = 0$, and the cross-section of the strip is fixed to $L_y \times L_z = 60 \text{ nm} \times 3 \text{ nm}$. Figure 7(b) depicts the pinned equilibrium state of a Bloch DW at rest for a pinning site with $n_x = 15 \text{ nm}$ and $n_y = 6 \text{ nm}$. In order to describe the pinning potential V_{pin} induced by the constriction, the temporal evolution of the DW position was micromagnetically computed under static fields $\vec{B}_e = B_e \vec{u}_z$ along the easy z -axis for three different widths (n_y : 3 nm, 6 nm, 9 nm) and fixed length ($n_x = 15 \text{ nm}$). After a few damped oscillations (not shown), the DW reaches final equilibrium position X_{eq} if the applied field is smaller than the depinning threshold ($B_e < B_d$), which depends on the length (n_x) and the width (n_y) of the notch. Figure 7(c) indicates that, except for fields close to the de-pin-nig threshold, the equilibrium DW position increases from the center of the constriction almost linearly with the applied field. The slope

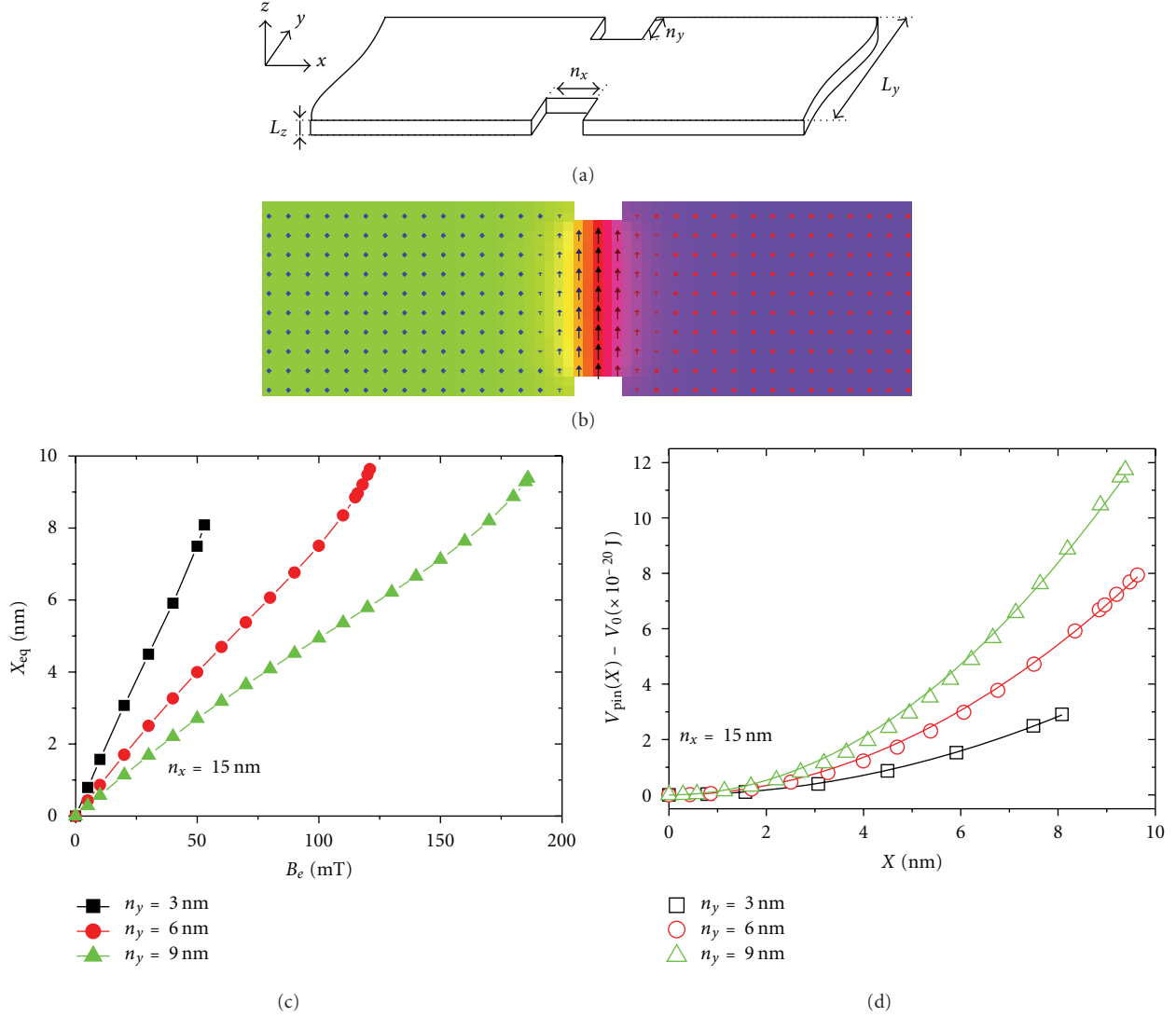


FIGURE 7: (a) Scheme of a pinning site consisting on two rectangular notches at both edges of the strip. (b) Equilibrium state of a pinned DW in a CoPtCr strip of $L_y \times L_z = 60 \text{ nm} \times 3 \text{ nm}$ with a constriction described by $n_x = 15 \text{ nm}$ and $n_y = 6 \text{ nm}$. (c) Equilibrium DW position as a function of the applied field B_e in the pinned regime. (d) Pinning potential V_{pin} as a function of the DW position. Dots correspond to micromagnetic results and the solid lines are the fittings to $V_{pin}(X) = (1/2)K_N X^2$. In these last graphs the length of the notch is fixed to $n_x = 15 \text{ nm}$, and three different widths are evaluated: $n_y : 3 \text{ nm}, 6 \text{ nm}, 9 \text{ nm}$.

of this increasing decreases with n_y . The pinning potential depicted in Figure 7(d) was computed from the total energy by subtracting the Zeemann contribution for each state [29]. In this pinned regime, the pinning potential can be fitted to a parabolic profile given by $V_{pin}(X) = (1/2)K_N X^2$ for $|X| \leq L_N$. K_N is the elastic constant of the constriction, and L_N is the half length of the pinning potential. From μM results of Figure 7(d), the following values are deduced for a constriction with $n_x = 15 \text{ nm}$ and $n_y = 6 \text{ nm}$: $K_N = 1.7 \times 10^{-3} \text{ N/m}$ and $L_N = 9.5 \text{ nm}$.

4.2. Field and Current-Driven DW Depinning. Once described the pinning potential, let us analyze the field and current DW depinning, in particular for a strip with $L_y \times L_z = 60 \text{ nm} \times 3 \text{ nm}$ with a constriction characterized by

$n_x = 15 \text{ nm}$ and $n_y = 6 \text{ nm}$. The goal is to evaluate how the depinning field B_d depends on the applied current j_a for several values of the nonadiabatic parameter ξ , firstly at zero temperature. The problem has been studied from both micromagnetic simulations (μM) and one-dimensional model (1DM). In the case of the 1DM, the DW width was obtained from equilibrium state of the pinned DW ($\Delta = 8.25 \text{ nm}$), and the hard-axis anisotropy field (H_K) of magnetostatic origin was deduced from the micromagnetically computed Walker breakdown field ($B_W = \mu_0 H_W \approx 0.33 \text{ mT}$), which results in $H_K = 2H_W/\alpha = 2626.06 \text{ A/m}$. The pinning potential is given by $V_{pin}(X) = (1/2)K_N X^2$ for $|X| \leq L_N$ with $K_N = 1.7 \times 10^{-3} \text{ N/m}$ and $L_N = 9.5 \text{ nm}$ ($V_{pin}(X) = 0$ for $|X| \geq L_N$). The results are depicted in Figure 8(a) for several values of the nonadiabatic parameter ξ . A good

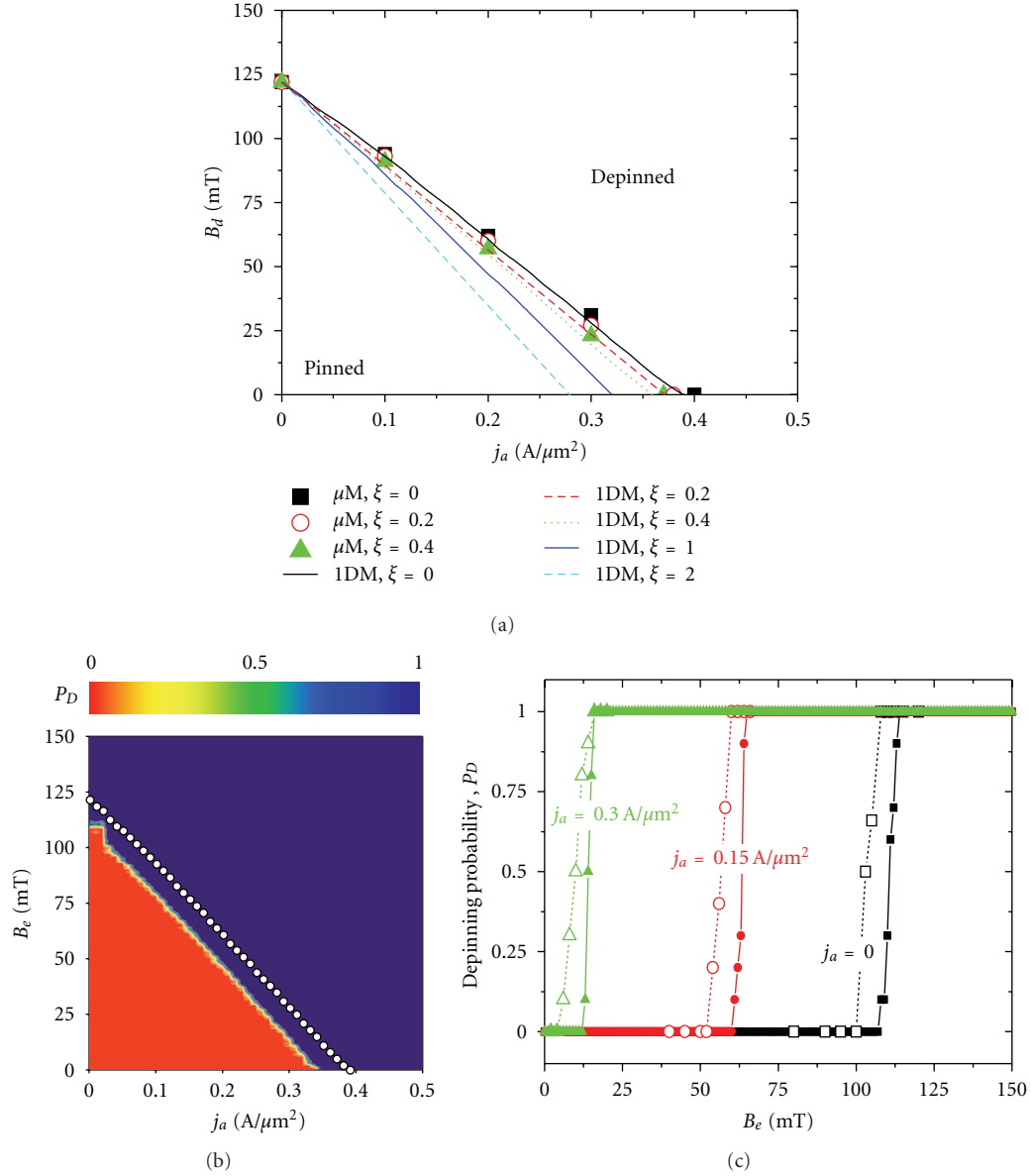


FIGURE 8: (a) Depinning field B_d as a function of j_a for several values of ξ for a CoPtCr strip with $L_y \times L_z = 60 \text{ nm} \times 3 \text{ nm}$ and $n_x = 15 \text{ nm}$ and $n_y = 6 \text{ nm}$. Dots correspond to μM results and lines correspond to the ones obtained from the 1 DM with $\Delta = 8.25 \text{ nm}$, $H_K = 2626.06 \text{ A/m}$, and a pinning potential given by $V_{\text{pin}}(X) = (1/2)K_N X^2$ for $|X| \leq L_N$ with $K_N = 1.7 \times 10^{-3} \text{ N/m}$ and $L_N = 9.5 \text{ nm}$ ($V_{\text{pin}}(X) = 0$ for $|X| \geq L_N$). (b) Probability of DW depinning (P_D) as a function of both (B_e, j_a) obtained from 1 DM with $\xi = 0$ at $T = 300 \text{ K}$. A temporal window of $t_w = 500 \text{ ns}$ was considered, and 100 stochastic realizations were evaluated. Open dots represent the deterministic ($T = 0$) depinning field $B_d(j_a)$. (c) Examples of P_D as a function of B_e under three different density currents: $j_a = 0$ (squares), $j_a = 0.15 \text{ A}/\mu\text{m}^2$ (circles) and $j_a = 0.3 \text{ A}/\mu\text{m}^2$ (triangles). Filled and open symbols correspond to 1 DM and μM results respectively (Reprinted with permission From [65]. Copyright (2012), American Institute of Physics).

quantitative agreement is observed between micromagnetic results (dots) and 1 DM predictions (lines). The depinning field $B_d(j_a, \xi)$ decreases linearly with the applied current j_a , and the diminution of B_d as a function of j_a becomes slightly stronger as the nonadiabatic parameter increases, but the linear behavior is preserved for all analysed values.

The results of Figure 8(a) were obtained at zero temperature ($T = 0$). In order to determine whether thermal fluctuations are likely to play an important role in the DW depinning process, the probability of DW depinning (P_D)

has been studied at $T = 300 \text{ K}$ by numerically solving the 1 DM (5) and (6). A temporal window of $t_w = 500 \text{ ns}$ was considered, and in order to present statistically meaningful results, 100 stochastic realizations were evaluated for each pair of (B_e, j_a) . The results for $\xi = 0$ are depicted in Figure 8(b), where open dots correspond to the deterministic ($T = 0$) depinning threshold. At $T = 0$, the DW depinning only occurs if the current and the field are sufficiently large. On the contrary, at $T = 300 \text{ K}$, the problem is no longer deterministic, and there is a non-null probability

of DW depinning for fields and currents smaller than the deterministic threshold. As it is observed, thermal fluctuations significantly reduces the depinning field B_d under a given current with respect to deterministic case. For instance, under zero current ($j_a = 0$), the depinning field at $T = 0$ is ≈ 123 mT, whereas the probability of DW depinning becomes 100% with a minimum field of 114 mT at room temperature. As it is shown in both Figures 8(b) and 8(c), the probability of DW depinning changes from 0% to 100% in a reduced range of fields, for example, from 60 mT to 65 mT under a current of $j_a = 0.15$ A/ μm^2 (see filled red circles in Figure 8(c)).

A similar analysis of thermal effects at $T = 300$ K was also carried by means of full micromagnetic modeling (μM , (1)) in the perfect adiabatic case. The probability of DW depinning (P_D) micromagnetically computed as a function of B_e is shown in Figure 8(c) by means of open symbols. Similarly to one-dimensional results, the transition from $P_D = 0$ to $P_D = 1$ is gradual and takes place in a narrow range of fields, but it is slightly anticipated toward smaller fields because the nonuniformities in the local magnetization assist the thermal depinning.

In summary, as it is desirable for memory applications, the field required to promote the DW depinning in absence of current is very high because the energy barrier required to overcome the pinning potential is around 19 times larger than the thermal energy at room temperature for a typical strip as the one studied here. The depinning field decreases linearly as the current is raised, and the slope of this declension slightly increases with the nonadiabaticity. Under zero field in the perfect adiabatic limit, the critical depinning density current is around 0.4 A/ μm^2 at zero temperature. This corresponds to a threshold current of 72 μA , which is small enough to minimize unwanted Joule heating effects. It was found that thermal fluctuations at room temperature play a significant role on the DW depinning by reducing the depinning field for a given current with respect to the deterministic case. These results are in good qualitative agreement with the experimental measurements by Ravelosona et al. [44] exploring the high pinning regime ($B_d \gg \mu_0 H_K / \alpha$), and they explain the linear decreasing of the depinning current with increasing field. In that experiment [44], the depinning current at zero field was found around 0.1 A/ μm^2 , which, in spite of the different materials and geometry, is in the same order of magnitude than our results. The Joule heating effect was estimated less than 20 K at the highest current densities applied, which is small enough to justify a Lagenvin description with constant temperature. By simulating the same geometry and materials than these experiments, the stochastic one-dimensional model can be directly adopted in order to gain a better description of the experimental observations by taking into account the effect of the constant temperature of the sample, and, therefore, a more accurate estimate of both the polarization factor and the nonadiabatic parameter, along with their dependence on the temperature could be addressed. On the other hand, the presented analysis also shows that the probability of the DW depinning under a given current changes abruptly from 0% to 100% in a narrow range of fields. This result

points out that the DW depinning is highly selective, which is also relevant for further technological applications. All these theoretical predictions indicate that engineering of pinning sites in thin strips of high perpendicular anisotropy provides an efficient pathway to achieve both high stability against thermal fluctuations, and at the same time, low-current-induced domain wall depinning.

5. DW-Based Nano-Oscillators

The theoretical studies of the current-driven DW dynamics along a strip with high PMA, and its pinning and depinning driven by fields and/or current, are relevant for further designing recording and logic devices based on DWs. However, these are not the only potential applications of DWs, which could be also useful in other branches of the nanotechnology. This last section is dedicated to the numerical study of the pinned DW oscillations driven by static currents, which could find application to develop novel DW-based nanoscillators.

5.1. Pinned DW Oscillations. Let us focus our attention on a CoPtCr strip ($M_s = 3 \times 10^5$ A/m, $A = 10^{-11}$ J/m, $K = 2 \times 10^5$ J/m³, $\alpha = 0.2$, and $P = 0.4$) with $L_y \times L_z = 60 \times 3$ nm² containing a single pinning site which consists on two rectangular notches ($n_x = 15$ nm long, $n_y = 6$ nm wide) symmetrically placed at both edges of the strip. The micromagnetically computed temporal evolution of the DW position $X(t)$ in the pinned regime ($j_a < j_d(\xi = 0, B_e = 0) = 0.4$ A/ μm^2) is depicted in Figure 9(a) for three values of the applied current j_a in the perfect adiabatic case ($\xi = 0$). For current smaller than Walker threshold ($j_a < j_W(0)$), the DW moves during the first nanoseconds, but after that it returns to its initial state where it finally rests. If the applied current surpasses the Walker value ($j_a \geq j_W(0) = 0.025$ A/ μm^2), and at the same time, it remains smaller than the critical depinning threshold ($j_a < j_d(\xi = 0, B_e = 0) = 0.4$ A/ μm^2), the DW develops pinned oscillations periodically rotating between Bloch and Neel configurations. Examples of these DW configurations are depicted in Figures 9(b)–9(e) in the adiabatic case for $j_a = 0.05$ A/ μm^2 . Under such low-density currents in the pinned regime (see Figures 9(b)–9(e)), the DW magnetization oscillates around the z -axis symmetrically with respect to the center of the notch, whereas under high density currents in the pinned regime (not shown) the central position of DW oscillations is pushed to the right-hand side due to the spin torque [40, 41]. The DW position $X_{\mu\text{M}}$ has two contributions: a static one X_{dc} , which represents the central position around which the DW oscillates, and a periodically oscillating contribution at a frequency f with an amplitude X_{ac} . The dependence of these three variables on the applied density current j_a is shown Figures 9(f), 9(g), and 9(h), respectively, for several values of the nonadiabatic parameter ($0 \leq \xi \leq 2\alpha$). Both X_{dc} and f increase almost linearly with j_a , but the amplitude of the DW oscillations X_{ac} decreases from the maximum value reached just above the Walker current. Except for a slight reduction of the critical depinning current $j_{\text{dep}}(\xi, B_e = 0)$, it is clear that

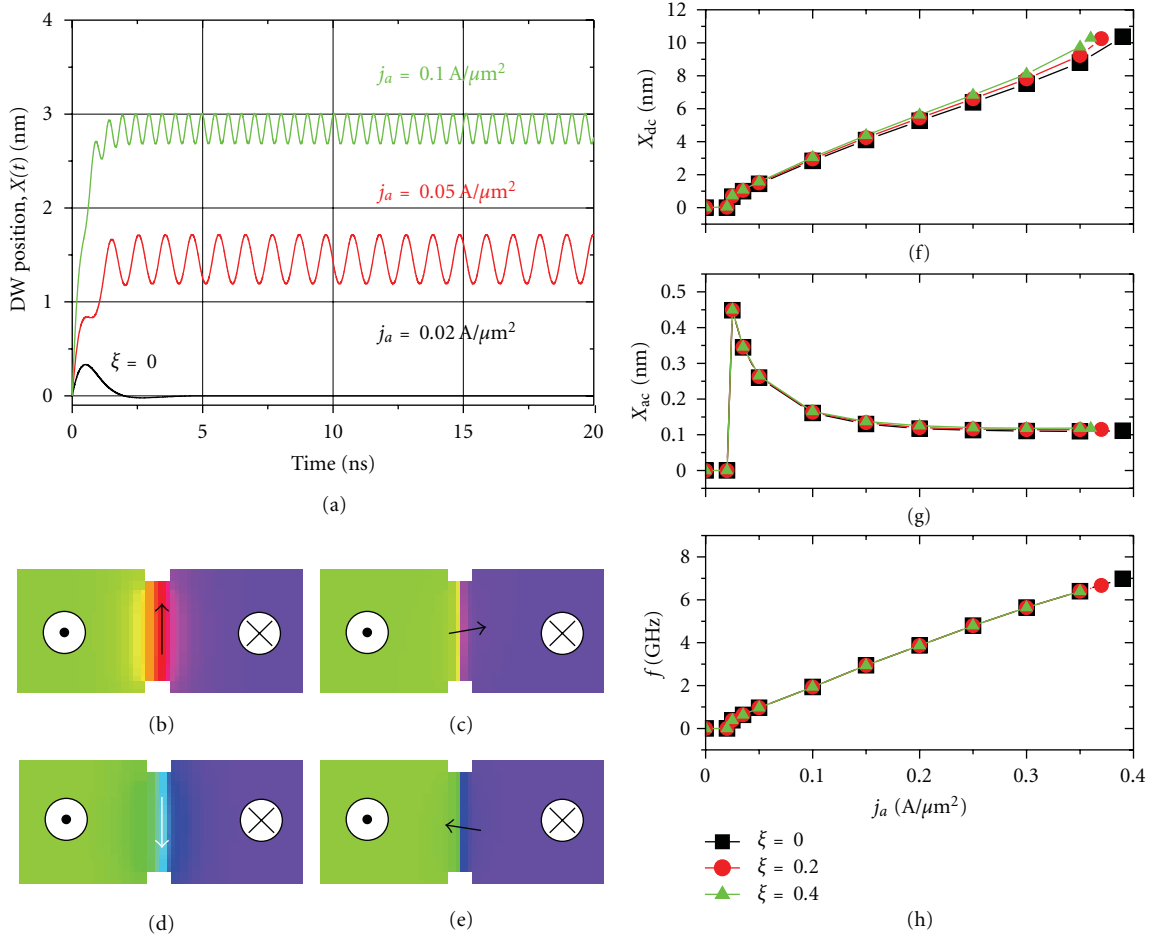


FIGURE 9: μM results for the DW dynamics under dcs in the pinned regime. The cross-section is $L_y \times L_z = 60 \text{ nm} \times 3 \text{ nm}$, and the dimensions of each rectangular notch are $n_x = 15 \text{ nm}$ and $n_y = 6 \text{ nm}$. (a) DW position $X(t)$ as a function of time under dcs in the perfect adiabatic case ($\xi = 0$). (b)–(e) depict the Bloch and Neel pinned DW configurations under $j_a = 0.05 \text{ A}/\mu\text{m}^2$. (f) Central DW position (X_{dc}), and (h) frequency f of DW oscillations as a function of j_a in the pinned regime. (From [41]).

the results do not depend significantly on the nonadiabaticity ξ . Although they are not shown here, it was also verified in [41] that the 1 DM results for the pinned DW oscillations are similar to the μM ones collected in Figures 9(a), 9(f)–9(h).

It is worthy to note that the complete analysis of the frequency of the localized DW oscillation requires either perform full micromagnetic simulations (as in Figure 9) or numerical solving the complete 1 DM (5) and (6) (as it was done in [41]). For instance, note from Figures 9(f) and 9(g) that although the time average of the DW velocity is zero, its instantaneous value is not exactly null. However, it is also possible to obtain some information from these 1 DM (5) and (6), which can be simplified by assuming some justified approximations. In particular, as the DW oscillations take place in the absence of driving field ($H_e = 0$) when the shape anisotropy is avoided ($H_K = 0$), and as the DW velocity is zero averaged over a period of the pinned oscillations ($\langle \dot{X} \rangle \approx 0$), it is possible to extract from (5) an expression for the pinning field $\gamma_0 H_p(X) = ((1 + \xi\alpha)/\Delta)(\mu_B P / e M_s) j_a$. Introducing this result in (6), we reach to

$$\Phi = -\frac{1}{\alpha \Delta} \frac{\mu_B P}{e M_s} j_a, \quad (9)$$

so the frequency of the pinned DW oscillations is $f = \Phi/\pi$ which is independent of the nonadiabatic parameter and increases linearly with j_a . This result is good quantitative agreement with the full micromagnetic results of Figure 9(f). Other 1 DM results and further micromagnetic details, such as the dependence of the pinned regime with the dimensions of the notches, can be seen in our former work [41].

5.2. Spin Pumping and Induced Voltage Signal. Results of former Figure 9 indicate that it is possible to achieve pinned DW oscillations just driven by dc via spin transfer torque. As electrons flow through the ferromagnetic strip, their spins tend to align with the magnetization. When they pass into the nonuniform magnetization region occupied by the DW, the electron spins rotate to stay aligned with the local magnetization. A reaction torque on the changing magnetization in the DW cause the pattern of magnetization at the DW to move in the direction of the electron flow. Considering perfect adiabatic conditions, the DW will move along a perfect strip if the applied density current is larger than the Walker breakdown ($j_a > j_W(0)$), and in its displacement, the DW experiences periodic transformations

between Bloch and Neel configurations. If the DW is trapped at a constriction, the spin transfer torque can promote pinned DW oscillations provided that the applied density current is above the Walker breakdown and below the critical depinning current ($j_W(0) < j_a < j_d$). The complementary effect, spin pumping [82], occurs when the pinned DW oscillation drives a spin current along the strip, which results in an induced voltage difference between the ends of the strip.

The rest of this section is dedicated to the analysis of the voltage signal produced by these pinned DW oscillations. It has been theoretically predicted that magnetization dynamics induces an electromotive and spin-motive force (emf/smf), which acts on the conduction electrons through the spin Berry phase [39, 83–87], and, therefore, magnetization dynamics can be a source of voltage signal for external circuits. Berger [39] provided the first theoretical prediction of this effect in terms of an analog of the Josephson effect: a static electric current larger than the Walker breakdown threshold can promote the DW rotation at a given frequency $f = (1/\pi)\Phi$. He also predicted that the DW oscillation gives rise to a voltage signal given by $V_{\text{smf}} = -(\hbar P/2e)\Phi$. Barnes and Maekawa [85] analyzed the generation of spin and charge current by a moving DW via electromotive forces considering the case that the spin is fully conserved. More recently, Duine [82, 88] pointed out that the voltage signal will be augmented by a nonadiabatic contribution, so it will be given by $V_{\text{smf}} = -(\hbar P/2e)(\dot{\Phi} - \xi(\ddot{X}/\Delta))$ in the 1 DM approach. The first experimental observation of the electromotive force induced by a moving DW was carried out recently by Yang and coworkers [89], where external fields larger than the Walker breakdown were used to drive a DW along a soft Permalloy strip, and the averaged induced voltage produced by its DW transformation between transverse and vortex configurations was $V_{\text{smf}} = -(\hbar P/e)(\gamma_0 H_e)$, where $H_e > H_W$.

Early theoretical predictions [39, 82, 85, 86, 88] for the voltage induced by DW oscillations considered an idealized rigid DW, where the DW width Δ remains fixed. However, as it was confirmed in Figure 2(a), the DW width changes above the Walker breakdown ($\Delta = \Delta(t)$), and these changes could play significant role in the induced voltage signal. Here, we will focus on describing the induced voltage signal due to the pinned DW oscillations driven by dc in a hard PMA strip from a full micromagnetic point of view, which straightforwardly accounts for the internal complexities of the dynamics changes of DW width. The effective electric field induced by a time-dependent magnetic texture is computed according to the formalism developed by Tserkovnyak and Mecklenburg [87]. The component of this field along the length of the strip (x -axis) is given by [87]

$$E_{\text{smf},x} = -\frac{\hbar P}{2e} \left[\vec{m} \cdot \left(\frac{\partial \vec{m}}{\partial t} \times \frac{\partial \vec{m}}{\partial x} \right) + \xi \left(\frac{\partial \vec{m}}{\partial t} \cdot \frac{\partial \vec{m}}{\partial x} \right) \right]. \quad (10)$$

The first term at the right hand side of (10) is the perfect adiabatic contribution to the electric field induced by a time-dependent magnetization texture, which was derived by considering that the exchange field provided by the localized magnetic d orbitals (local \vec{m}) is larger than the spin-diffusion

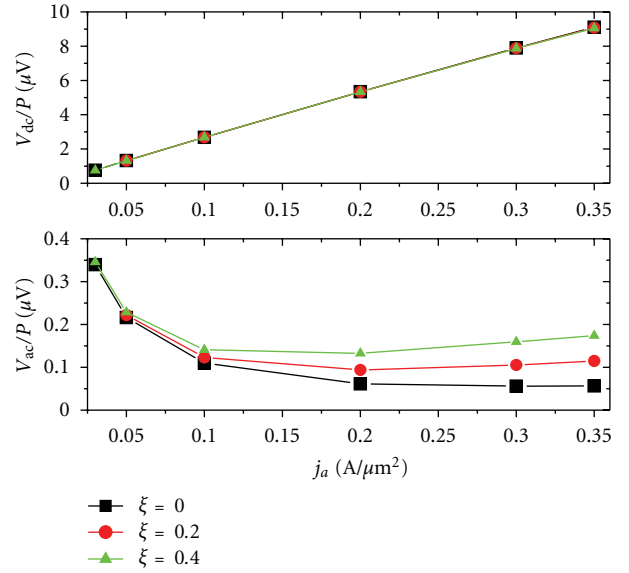


FIGURE 10: Voltage signal as due to the pinned DW oscillations driven dcs as computed from μM simulations. Static (V_{dc}) and oscillating (V_{ac}) contributions of the voltage signal $V_{\text{smf}}(t)$ are depicted in (top) and (bottom), respectively. (from [41]).

length, and, therefore, assumes that the spin of conduction electrons perfectly align with local magnetization [39, 86]. It is equally direct to interpret the first contribution to (10) in terms of the rate of the Berry-phase accumulation by spins adiabatically following the steady exchange field [85, 89]. The second term at the right hand side of (10) is proportional to the nonadiabatic parameter ξ . This correction is related to slight spin misalignment of electron propagating through an inhomogeneous magnetic texture with the local magnetization [87]. In the limit of infinite exchange field this misalignment vanished (and so should ξ), and only the adiabatic contributions would remain. The nonadiabatic corrections to the induced electric field by a time-dependent magnetic texture was firstly proposed by Duine [82] for a rigid DW. This nonadiabatic contribution can be viewed as a correction to the topological structure of the electron transport rigidly projected on the local magnetization texture. A more detailed description of the microscopic origin of (10) is far from the scope of this work, and they can be consulted in [39, 82, 85–88]. Once evaluated (10), the induced voltage between the ends of the strip is obtained by integrating over the strip length ($L_x = 1.2 \mu\text{m}$) as $V_{\text{smf}} = -\int_0^{L_x} E_{\text{smf},x} dx$.

The μM results of the induced voltage signal V_{smf} corresponding to the pinned DW oscillations described in former Figure 9 are depicted in Figure 10. They show that the induced voltage $V_{\text{smf}}(t)$ has also two contributions: a static one V_{dc} which increases linearly with j_a independently on the nonadiabatic parameter ξ (Figure 9(a)), and a periodic contribution with amplitude V_{ac} (see Figure 10(b)) oscillating at the same frequency f as the DW position oscillations of Figure 9(h). An interesting point from a fundamental point

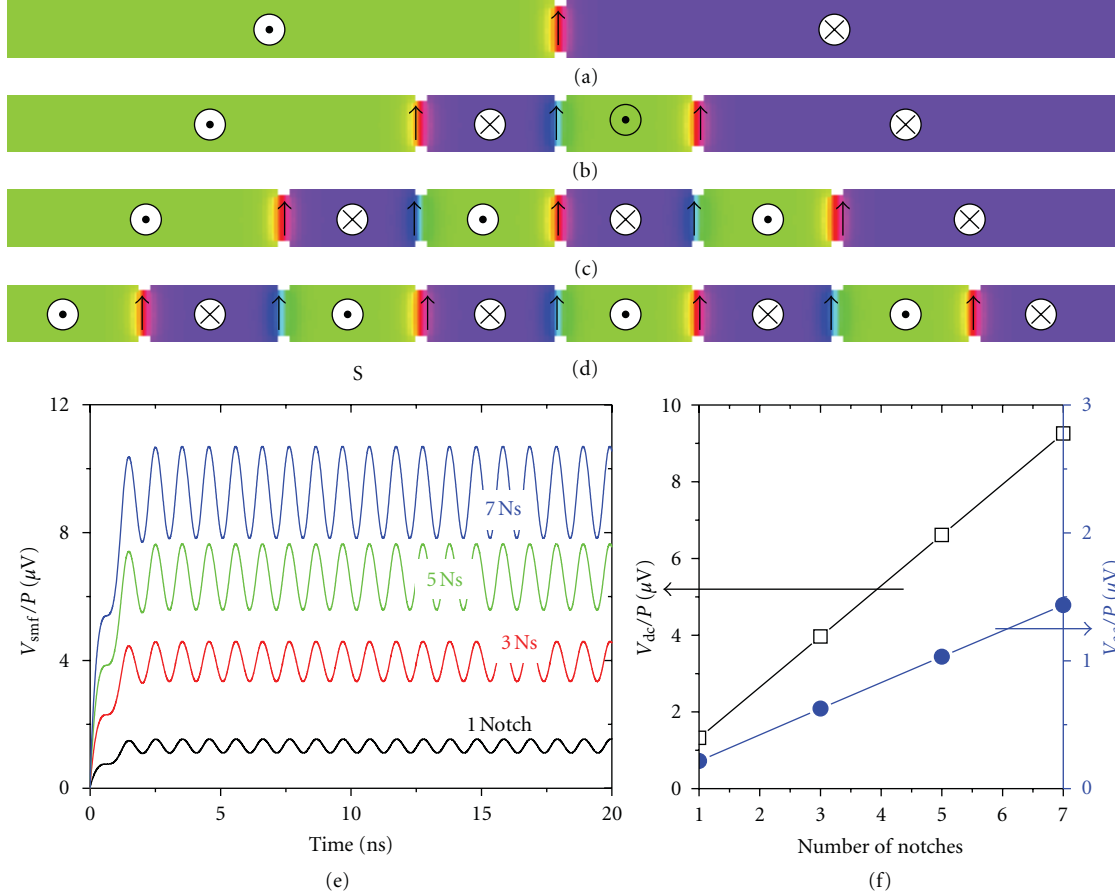


FIGURE 11: Equilibrium states with (a) one, (b) three, (c) five, and (d) seven Bloch DWs pinned at different notches separated each other by $S = 138$ nm. (e) Voltage signal as a function of time for a strip with different number of pinned DWs. The applied current is $j_a = 0.05 \text{ A}/\mu\text{m}^2$ and the perfect adiabatic case was considered. (f) Static (V_{dc}) and oscillating (V_{ac}) contributions of the voltage signal $V_{\text{smf}}(t)$ as a function of the number of pinned DWs. (from [41]).

of view is that, contrary to the V_{dc} case, the amplitude of the oscillating contribution V_{ac} shows a dependence on the nonadiabatic parameter ξ , and therefore, if this signal can be experimentally detected, it could give information on the nonadiabaticity of system.

5.3. Enhancing the Induced Voltage Signal. From a technological point of view, the voltage signals induced by the pinned DW oscillations might prove useful to design nanoscale microwave oscillators and generators, which could find application in several fields such as sensors, telecommunications, or rf assisted writing for memory devices. However, for a given strip with a given constriction the amplitude of the dc voltage signal V_{dc} is restricted to the values of the dc applied current densities of the oscillating pinned regime ($j_W < j_a < j_{\text{dep}}$). Moreover, the amplitude of the oscillating contribution V_{ac} decreases with j_a from j_W to j_{dep} , and it will be desirable to enhance and extend the operation regime towards higher values of both V_{dc} and V_{ac} with the aim of fulfilling further technological requirements. In order to do it, we proposed to introduce several pinned DWs along the strip [41].

Figure 11 shows the equilibrium state of a CoPtCr strip containing (a) one, (b) three, (c) five, and (d) seven Bloch DWs separated each other from $S = 138$ nm. The length and the cross-section of the strip, along with the shape and dimensions of each constriction are the same than in previous subsections: $L_x = 1.2 \mu\text{m}$, $L_y = 60$ nm, $L_z = 3$ nm, $n_x = 15$ nm, and $n_y = 6$ nm. Due to the magnetostatic interaction, the alternative pinned DWs adopt Bloch up ($\vec{m}_{\text{DW}} \propto +\vec{u}_y$) and Bloch down ($\vec{m}_{\text{DW}} \propto -\vec{u}_y$) magnetic configurations. A current source could be used to provide a fixed current along the strip. Under it, the central pinned DW rotates coherently counterclockwise. In the strip with three pinned DWs (Figure 11(b)), the ones at the left and at the right sides rotate clockwise. The same occurs for the strip containing five pinned DW (Figure 11(c)), where the ones at the left and the right extrema rotate similarly to the central one. Figure 11(e) depicts the temporal evolution of the induced voltage signal $V_{\text{smf}}(t)$ (in units of the polarization factor P) under a current density of $j_a = 0.05 \text{ A}/\mu\text{m}^2$ for strips with several pinned DWs in the perfect adiabatic case. For this system, where all constrictions are equal, both V_{dc} and V_{ac} increase linearly with the number of pinned DWs (see Figure 11(f)), and, therefore, if the voltage signal

can be experimentally detected, this proposed system could be useful to develop oscillators and/or amplifiers at the nanoscale.

However, there are a few aspects which have to be taken into account and controlled before going to the real device. The first one is the separation S between pinned DWs. When the constrictions are placed close to each other, the Bloch configurations are not stable, and the DWs adopt Neel configurations magnetized along the strip axis. This is what happens for three DWs pinned at similar constrictions separated $S \leq 45$ nm, and due to the magnetostatic coupling, a small current of $j_a = 0.05$ A/ μm^2 is not high enough to promote pinned DW oscillations. It was also verified that for separations $S \geq 130$ nm the induced voltage signal does not change. Other important challenge is the limitation of the available nanolithography techniques. Nowadays, fabricating identical notches in a strip at the nanoscale is a very difficult art. Therefore, the influence of different constrictions, with different shape and sizes, on the induced voltage signal has to be analyzed. It was verified that the linear increasing of the oscillating contribution to the induced voltage signal (V_{ac}) is not preserved with the number of pinned DWs at irregular constrictions, but the direct contribution (V_{dc}) increases almost linearly with the number of pinned DWs even in the case of different constrictions [41]. Thermal effects are also relevant. For instance, the coherent oscillation of the internal DW magnetization can be only achieved at very low temperatures ($T \approx 10$ K) for the constrictions analysed here. It was also confirmed, by means of preliminary simulations, that the internal DW structure is also coherently oscillating under injected static currents at room temperature if the constriction is made deeper. The challenging point consists on filtering the noise due to thermal fluctuations from the induced voltage signal. All these numerical predictions claim for a future experimental verification. Conceptually, it is straightforward to detect the induced voltage due to these pinned DW oscillations by simply measuring the voltage difference between the ends of the strip. In practice, however, this is not a trivial task, and nowadays only Yang et al. [89] have reported experimental measures of this signal. Indeed, the contribution of the spin-motive force to the voltage signal due to the pinned DW oscillations is only one of several voltages arising from different effects. For instance, an experimental challenge is to sort out the V_{smf} from other signals such as the voltage induced by the changing magnetic fluxes in the detection circuit as due to the classical Faraday's law. I hope that these theoretical predictions motivate experimental progress in this direction.

6. Conclusions and Final Remarks

The static and dynamics of DWs along thin rectangular cross-section strips with high PMA driven by spin-polarized currents has been theoretically studied from both micro-magnetic (μM) and one-dimensional (1 DM) models points of view. These materials are especially relevant for further technological applications because the intrinsic threshold current for current-induced DW motion can be drastically reduced with respect to soft materials such as Permalloy.

Thermal fluctuations and disorder (in particular, edge roughness) were both included in both models with the aim of providing a much more realistic description of experimental measurements. The current-induced DW propagation along a rough strip at room temperature was studied for both single layer strips and asymmetric multilayers stacks. In the former case, where the spin-orbit interaction (SOI) is negligible, the DW velocity increases firstly exponentially with current, following a creep regime which is governed by the pinning and thermal fluctuations. For very high currents, the DW mobility saturates reaching a value which approaches to the case of a perfect strip. It is interesting to note that, even when the nonadiabatic parameter is equal to the damping ($\xi = \alpha$), the DW propagates by transforming its internal structure between Bloch and Neel configurations in both the creep and high-current regimes. When a ferromagnetic strip with high PMA is sandwiched between two asymmetric nonmagnetic in a multilayer stack, the SOI on the conduction electrons allows for the transfer of orbital angular momentum from the crystal lattice to the local magnetization, and it is mediated by a Rashba field. This field is equivalent to a homogeneous transverse field, and for positive and negative currents, promotes the stabilization of one of the Bloch configurations, either up or down, by raising the energy barrier against Neel transformation. Therefore, in asymmetric stacks, the linear high mobility regime is extended to higher currents, and consequently, it allows to achieve rigid DW propagation with higher velocities than the ones achieved in single layer strips. Moreover, the extended 1 DM including the Rashba field along with thermal effects and disorder allows us to describe very recent experimental observations, not only qualitative but also quantitatively, with reduced computational effort. These architectures are promising for DW-based applications.

The pinning and depinning of an initially trapped DW in an artificial constrictions was also evaluated. Also in these processes the PMA strips present technological advantages over similar strips made of soft ferromagnetic materials. For the analysed geometry, the field required to promote the DW depinning in the absence of current is very high because the energy barrier required to overcome the pinning potential is around 19 times larger than the thermal energy at room temperature. Therefore, in the absence of driving force, the pinned DW remains stable against thermal fluctuations. The depinning field decreases linearly as the current is raised, and the slope of this declension slightly increases with the nonadiabaticity. On the other hand, under zero field in the perfect adiabatic limit, the critical depinning density current is around 0.4 A/ μm^2 at zero temperature. This corresponds to a threshold current of 72 μA , which is small enough to minimize unwanted Joule heating effects. The study also indicates that the probability of the DW depinning under a given current changes abruptly from 0% to 100% in a narrow range of fields. This result points out that the DW depinning is highly selective, which is also relevant for further technological applications. These results indicate that engineering of pinning sites in thin strips of high PMA provides an efficient pathway to achieve both high stability against thermal fluctuations and low

current-induced DW depinning and, therefore, it can find application on designing memory devices driven by static currents. Moreover, the theoretical formalism is also useful to elucidate the magnitude of the nonadiabatic parameter. In particular, our results are in good qualitative agreement with the experimental measurements by Ravelosona et al. [44] exploring the high pinning regime $B_d \gg \mu_0 H_K / \alpha$: the experimentally observed linear decreasing of the depinning current with increasing field is in good agreement with our simulations. In that experiment, the depinning current at zero field was found around $0.1 \text{ A}/\mu\text{m}^2$, which, in spite of the different materials and geometry, is in the same order of magnitude than our results. By simulating the same geometry and materials as these experiments, the stochastic 1DM can be directly adopted in order to gain a better description of the experimental observations by taking into account the effect of the constant temperature of the sample and, therefore, a more accurate estimate of both the polarization factor and the nonadiabatic parameter, along with their dependence on the temperature could be addressed. Much more experimental and numerical studies have to be done to address this issue.

Finally, the possibility of engineering nano-oscillator based on pinned DWs was explored from a theoretical point of view. The pinned DW oscillations driven by direct current were described. Both frequency and averaged DW position increase with the applied current in the pinned oscillating regime. However, the DW position has also another alternating contribution with an amplitude which decreases with the applied current. The contribution due to the spin-motive force to the voltage signal induced by these pinned DW oscillations has been also characterized. It consists of both static and oscillating contributions. The first one increases linearly with the applied current and it does not depend on the nonadiabaticity. However, the oscillating contribution depends on the nonadiabatic parameter, and, therefore, information on the strength of the nonadiabaticity could be obtained by means of experimental measurements which could detect such an oscillating voltage signal. The induced voltage signal due to the DW oscillations in a strip with several pinned domain walls was also analysed. The theoretical prediction that spin-motive force voltage signal can be linearly enhanced with the number of walls could be useful to develop DW-based nano-oscillators. Some of the possible experimental challenges, such as the limitation in the nanolithography and detection of the voltage signal, were also discussed.

Before ending this review, it is worthy to enumerate the limitations of the adopted theoretical formalism and numerical models, along with the future tasks to be performed in the framework of the current-induced DW dynamics.

- (i) The injected density current was assumed to be uniform along the strips. However, there must be an effect due to the spatial dependence of the injected current, specially in the analysis of the current-induced DW depinning from a constriction, where the current has to flow more densely than in the unconstricted zones. Taking into account the spatial dependence of

the injected current requires to numerically solve the Laplace equation for the electrostatic potential with the corresponding boundary conditions. This can be done in a preliminary simulation, which then has to be included in the full micromagnetic modeling in order to elucidate its effect for each specific case.

- (ii) The Oersted field due to the injected current has neither been taken into account. In the full micromagnetic model, this classical contribution can be straightforwardly introduced by numerically solving Biot-Savart's Law. When a uniform current density is injected along the axis ($\vec{j}_a = j_a \vec{u}_x$) of an infinitely long and perfect strip with thin rectangular cross-section ($L_z \ll L_y$), the Oersted field can be analytically evaluated. In this specific case, the Oersted field has a perpendicular z -component that is maximum at the strip edges and almost proportional to the strip thickness (L_z). The y -component of this Oersted field is slightly smaller, and changes sign across the strip thickness so that for thin nanostrips this field should have virtually no effect. The x -component field component is zero, so that it has no direct effect on the DW position. The influence of the Oersted field for imperfect samples, for example, with an edge roughness or even a notch that reduces locally the nanostrip width, should be investigated in each particular case. For this purpose, the current density cannot be assumed as uniform, and it requires a separate evaluation as it was already pointed out.
- (iii) It is also well known that the passage of an electric current through a conductor releases heat resulting in a rise of the temperature of the conductor. However, up to now this Joule heating as due to the injected current has not been included in the simulations because it involves theoretical problems. From a numerical point of view, it is needed to solve the heat diffusion equation in order to deduce the local value of the temperature as function of the space and the elapsed time. This could be done straight forwardly, but after that we will face a theoretical problem. On the one hand, all micromagnetic parameters are temperature dependent ($M_s(T)$, $A(T)$, or $P(T)$). However, the micromagnetic approach assumes that temperature is far from the Curie temperature, and it considers constant material parameters. On the other hand, thermal effects are commonly included in the micromagnetic formalism by adding a random thermal field [75, 76], which is assumed to be a Gaussian distributed and both spacial and temporal uncorrelated white noise (see (2) and (3)). This Langevin formalism assumes that the temperature of the system is the same for all points in the sample. Therefore, if the temperature depends on the position along the strip, an alternative theoretical formalism should be developed.

All these three phenomena (nonuniform current, the Oersted field and the Joule heating) cannot be taken into

account in the framework of the 1DM, and, therefore, the study of their role on the current-induced DW dynamics will require sophisticated and time-consuming micromagnetic simulations. Developing efficient micromagnetic tools including these fundamental effects would provide important steps towards the fully understanding of the DW dynamics driven by spin-polarized currents.

Acknowledgments

This work was supported by Project MAT2011-28532-C03-01 from Spanish government. The author thanks M. Miron and G. Gaudin for providing their experimental data of Figure 6.

References

- [1] A. Hubert and R. Schafer, *Magnetic Domains. The Analysis of Magnetic Microstructures*, Springer, 1998.
- [2] L. Berger, "Low-field magnetoresistance and domain drag in ferromagnets," *Journal of Applied Physics*, vol. 49, article 2156, 6 pages, 1978.
- [3] L. Berger, "Exchange interaction between ferromagnetic domain wall and electric current in very thin metallic films," *Journal of Applied Physics*, vol. 55, article 1954, 3 pages, 1984.
- [4] S. Zhang, P. M. Levy, and A. Fert, "Mechanisms of spin-polarized current-driven magnetization switching," *Physical Review Letters*, vol. 88, no. 23, Article ID 236601, 2004.
- [5] S. Zhang and Z. Li, "Roles of nonequilibrium conduction electrons on the magnetization dynamics of ferromagnets," *Physical Review Letters*, vol. 93, no. 12, Article ID 127204, 2004.
- [6] G. Tatara and H. Kohno, "Theory of current-driven domain wall motion: spin transfer versus momentum transfer," *Physical Review Letters*, vol. 92, no. 8, Article ID 086601, 2004.
- [7] X. Waintal and M. Viret, "Current-induced distortion of a magnetic domain wall," *Europhysics Letters*, vol. 65, no. 3, pp. 427–433, 2004.
- [8] A. Thiaville, Y. Nakatani, J. Miltat, and Y. Suzuki, "Micromagnetic understanding of current-driven domain wall motion in patterned nanowires," *Europhysics Letters*, vol. 69, no. 6, pp. 990–996, 2005.
- [9] J. Grollier, D. Lacour, V. Cros et al., "Switching the magnetic configuration of a spin valve by current-induced domain wall motion," *Journal of Applied Physics*, vol. 92, no. 8, p. 4825, 2002.
- [10] N. Vernier, D. A. Allwood, D. Atkinson, M. D. Cooke, and R. P. Cowburn, "Domain wall propagation in magnetic nanowires by spin-polarized current injection," *Europhysics Letters*, vol. 65, no. 4, pp. 526–532, 2004.
- [11] M. Kläui, C. A. F. Vaz, J. A. C. Bland et al., "Controlled and reproducible domain wall displacement by current pulses injected into ferromagnetic ring structures," *Physical Review Letters*, vol. 94, no. 10, Article ID 106601, 2005.
- [12] G. S. D. Beach, C. Knutson, C. Nistor, M. Tsoi, and J. L. Erskine, "Nonlinear domain-wall velocity enhancement by spin-polarized electric current," *Physical Review Letters*, vol. 97, no. 5, Article ID 057203, 2006.
- [13] M. Laufenberg, W. Buhrer, D. Bedau et al., "Temperature dependence of the spin torque effect in current-induced domain wall motion," *Physical Review Letters*, vol. 97, no. 4, Article ID 046602, 4 pages, 2006.
- [14] M. Hayashi, L. Thomas, C. Rettner, R. Moriya, X. Jiang, and S. S. P. Parkin, "Dependence of current and field driven depinning of domain walls on their structure and chirality in permalloy nanowires," *Physical Review Letters*, vol. 97, no. 20, Article ID 207205, 2006.
- [15] L. Thomas, M. Hayashi, X. Jiang, R. Moriya, C. Rettner, and S. S. P. Parkin, "Oscillatory dependence of current-driven magnetic domain wall motion on current pulse length," *Nature*, vol. 443, no. 7108, pp. 197–200, 2006.
- [16] M. Hayashi, L. Thomas, C. Rettner, R. Moriya, Y. B. Bazaliy, and S. S. P. Parkin, "Current driven domain wall velocities exceeding the spin angular momentum transfer rate in permalloy nanowires," *Physical Review Letters*, vol. 98, no. 3, Article ID 037204, 2007.
- [17] L. Thomas, M. Hayashi, X. Jiang, R. Moriya, C. Rettner, and S. Parkin, "Resonant amplification of magnetic domain-wall motion by a train of current pulses," *Science*, vol. 315, no. 5818, pp. 1553–1556, 2007.
- [18] D. Bedau, M. Kläui, S. Krzyk, U. Rudiger, G. Faini, and L. Vila, "Detection of current-induced resonance of geometrically confined domain walls," *Physical Review Letters*, vol. 99, no. 14, Article ID 146601, 2007.
- [19] G. Meier, M. Bolte, R. Eiselt, B. Kruger, P. Dong-Hyun, and K. Fischer, "Direct imaging of stochastic domain-wall motion driven by nanosecond current pulses," *Physical Review Letters*, vol. 98, no. 18, Article ID 187202, 2007.
- [20] S. Laribi, V. Cros, M. Muoz et al., "Reversible and irreversible current induced domain wall motion in CoFeB based spin valves stripes," *Physical Review Letters*, vol. 90, no. 23, Article ID 232505, 3 pages, 2007.
- [21] M. Y. Im, L. Bocklage, P. Fischer, and G. Meier, "Direct observation of stochastic domain-wall depinning in magnetic nanowires," *Physical Review Letters*, vol. 102, no. 14, Article ID 147204, 2009.
- [22] S. Lepadatu, A. Vanhaverbeke, D. Atkinson, R. Allenspanch, and C. H. Marrow, "Dependence of domain-wall depinning threshold current on pinning profile," *Physical Review Letters*, vol. 102, no. 12, Article ID 127203, 4 pages, 2009.
- [23] S. G. S. D. Beach, M. Tsoi, and J. L. Erskine, "Current-induced domain wall motion," *Journal of Magnetism and Magnetic Materials*, vol. 320, no. 7, pp. 1272–1281, 2008.
- [24] R. A. Duine, A. S. Nunez, and A. H. MacDonald, "Thermally assisted current-driven domain-wall motion," *Physical Review Letters*, vol. 98, no. 5, Article ID 056605, 2007.
- [25] A. Mougin, M. Cormier, J. P. Adam, P. J. Metaxas, and J. Ferre, "Domain wall mobility, stability and Walker breakdown in magnetic nanowires," *Europhysics Letters*, vol. 78, no. 5, Article ID 57007, 2007.
- [26] E. Martinez, L. Lopez-Diaz, L. Torres, C. Tristan, and O. Alejos, "Thermal effects in domain wall motion: Micromagnetic simulations and analytical model," *Physical Review B*, vol. 75, no. 17, Article ID 174409, 11 pages, 2007.
- [27] E. Martinez, L. Lopez-Diaz, O. Alejos, L. Torres, and C. Tristan, "Thermal effects on domain wall depinning from a single notch," *Physical Review Letters*, vol. 98, no. 26, Article ID 267202, 2007.
- [28] E. Martinez, L. Lopez-Diaz, O. Alejos, and L. Torres, "Resonant domain wall depinning induced by oscillating spin-polarized currents in thin ferromagnetic strips," *Physical Review B*, vol. 77, no. 14, Article ID 144417, 2008.
- [29] E. Martinez, L. Lopez-Diaz, O. Alejos, L. Torres, and M. Carpentieri, "Domain-wall dynamics driven by short pulses along thin ferromagnetic strips: micromagnetic simulations and

- analytical description," *Physical Review B*, vol. 79, no. 9, Article ID 094430, 14 pages, 2009.
- [30] O. Boulle, G. Malinowski, and M. Klaui, "Current-induced domain wall motion in nanoscale ferromagnetic elements," *Materials Science and Engineering R*, vol. 72, no. 9, pp. 159–187, 2011.
 - [31] D. A. Allwood, G. Xiong, M. D. Cooke et al., "Submicrometer ferromagnetic NOT gate and shift register," *Science*, vol. 296, no. 5575, pp. 2003–2006, 2002.
 - [32] D. A. Allwood, G. Xiong, C. C. Faulkner, D. Atkinson, D. Petit, and R. P. Cowburn, "Magnetic domain-wall logic," *Science*, vol. 309, no. 5741, pp. 1688–1692, 2005.
 - [33] P. Xu, K. Xia, C. Gu, L. Tang, H. Yang, and J. Li, "An all-metallic logic gate based on current-driven domain wall motion," *Nature Nanotechnology*, vol. 3, no. 2, pp. 97–100, 2008.
 - [34] S. S. P. Parkin, "Shiftable magnetic shift register and method of using the same," U.S. Patent No. 6834005, 2004.
 - [35] S. S. P. Parkin, M. Hayashi, and L. Thomas, "Magnetic domain-wall racetrack memory," *Science*, vol. 320, no. 5873, pp. 190–194, 2008.
 - [36] D. Atkinson, D. S. Eastwood, and L. K. Bogart, "Controlling domain wall pinning in planar nanowires by selecting domain wall type and its application in a memory concept," *Applied Physics Letters*, vol. 92, no. 2, Article ID 022510, 3 pages, 2008.
 - [37] J. He and S. Zhang, "Localized steady-state domain wall oscillators," *Applied Physics Letters*, vol. 90, no. 14, Article ID 142508, 2007.
 - [38] T. Ono and Y. Nakatani, "Magnetic domain wall oscillator," *Applied Physics Express*, vol. 1, Article ID 061301, 2008.
 - [39] L. Berger, "Possible existence of a Josephson effect in ferromagnets," *Physical Review B*, vol. 33, no. 3, pp. 1572–1578, 1986.
 - [40] A. Bisig, L. Heyne, O. Boulle, and M. Klaui, "Tunable steady-state domain wall oscillator with perpendicular magnetic anisotropy," *Applied Physics Letters*, vol. 95, Article ID 162504, 2009.
 - [41] E. Martinez, L. Torres, and L. Lopez-Diaz, "Oscillator based on pinned domain walls driven by direct current," *Physical Review B*, vol. 83, no. 17, Article ID 174444, 10 pages, 2011.
 - [42] E. Martinez, G. Finocchio, and M. Carpentieri, "Stochastic resonance of a domain wall in a stripe with two pinning sites," *Applied Physics Letters*, vol. 98, no. 7, Article ID 072507, 3 pages, 2011.
 - [43] D. Ravelosona, F. Caysol, J. Wunderlich et al., "Dynamics of magnetization reversal in a mesoscopic wire," *Journal of Magnetism and Magnetic Materials*, vol. 249, no. 1–2, pp. 170–174, 2002.
 - [44] D. Ravelosona, D. Lacour, J. A. Katine, B. D. Terris, and C. Chappert, "Nanometer scale observation of high efficiency thermally assisted current-driven domain wall depinning," *Physical Review Letters*, vol. 95, no. 11, Article ID 117203, 4 pages, 2005.
 - [45] D. Ravelosona, S. Mangin, J. A. Katine, E. E. Fullerton, and B. D. Terris, "Threshold currents to move domain walls in films with perpendicular anisotropy," *Applied Physics Letters*, vol. 90, no. 7, Article ID 072508, 3 pages, 2007.
 - [46] C. Burrowes, D. Ravelosona, C. Chappert et al., "Role of pinning in current driven domain wall motion in wires with perpendicular anisotropy," *Applied Physics Letters*, vol. 93, no. 17, Article ID 172513, 2008.
 - [47] T. A. Moore, I. M. Miron, G. Gaudin et al., "High domain wall velocities induced by current in ultrathin Pt/Co/AlO_x wires with perpendicular magnetic anisotropy," *Applied Physics Letters*, vol. 93, no. 26, Article ID 262504, 3 pages, 2008.
 - [48] O. Boulle, J. Kimling, P. Warnicke et al., "Nonadiabatic spin transfer torque in high anisotropy magnetic nanowires with narrow domain walls," *Physical Review Letters*, vol. 101, no. 21, Article ID 216601, 2008.
 - [49] T. Koyama, G. Yamada, H. Taniwaga et al., "Control of domain wall position by electrical current in structured Co/Ni wire with perpendicular magnetic anisotropy," *Applied Physics Express*, vol. 1, Article ID 101303, 3 pages, 2008.
 - [50] H. Tanigawa, K. Kondou, T. Koyama et al., "Current-driven domain wall motion in CoCrPt wires with perpendicular magnetic anisotropy," *Applied Physics Express*, vol. 1, no. 1, Article ID 011301, 2008.
 - [51] I. M. Miron, P. J. Zermatten, G. Gaudin, S. Auffret, B. Rodmacq, and A. Schuhl, "Domain wall spin torquemeter," *Physical Review Letters*, vol. 102, no. 13, Article ID 137202, 2009.
 - [52] L. San Emeterio Alvarez, K. Y. Wang, S. Lepadatu, S. Landi, S. J. Bending, and C. H. Marrows, "Spin-transfer-torque-assisted domain-wall creep in a Co/Pt multilayer wire," *Physical Review Letters*, vol. 104, no. 13, Article ID 137205, 2010.
 - [53] C. Burrowes, A. P. Mihai, D. Ravelosona et al., "Non-adiabatic spin-torques in narrow magnetic domain walls," *Nature Physics*, vol. 6, no. 1, pp. 17–21, 2010.
 - [54] H. Tanigawa, T. Koyama, G. Yamada et al., "Domain wall motion induced by electric current in a perpendicularly magnetized Co/Ni nano-wire," *Applied Physics Express*, vol. 2, no. 5, Article ID 053002, 2009.
 - [55] I. M. Miron, T. Moore, H. Szabolcs et al., "Fast current-induced domain-wall motion controlled by the Rashba effect," *Nature Materials*, vol. 10, no. 6, pp. 419–423, 2011.
 - [56] M. Cormier, A. Mougin, J. Ferre et al., "Fast propagation of weakly pinned domain walls and current-assisted magnetization reversal in He⁺-irradiated Pt/Co/Pt nanotracks," *Journal of Physics D*, vol. 44, no. 21, Article ID 215002, 2011.
 - [57] S. Fukami, T. Suzuki, Y. Nakatani et al., "Current-induced domain wall motion in perpendicularly magnetized CoFeB nanowire," *Applied Physics Letters*, vol. 98, no. 8, Article ID 082504, 3 pages, 2011.
 - [58] S. Fukami, T. Suzuki, Y. Nakatani et al., "Current-induced domain wall motion in perpendicularly magnetized CoFeB nanowire," *Applied Physics Letters*, vol. 98, no. 8, Article ID 082504, 2011.
 - [59] K. Ueda, T. Koyama, D. Chiba et al., "Current-induced magnetic domain wall motion in Co/Ni nanowire at low temperature," *Applied Physics Express*, vol. 4, no. 6, Article ID 063003, 2011.
 - [60] J. P. Adam, N. Vernier, J. Ferre et al., "Nonadiabatic spin-transfer torque in (Ga,Mn)As with perpendicular anisotropy," *Physical Review B*, vol. 80, no. 19, Article ID 193204, 4 pages, 2009.
 - [61] A. Kanda, A. Suzuki, F. Masukura, and H. Ohno, "Domain wall creep in (Ga,Mn)As," *Applied Physics Letters*, vol. 97, no. 3, Article ID 032504, 3 pages, 2010.
 - [62] S.-W. Jung, W. Kim, T.-D. Lee, K.-J. Lee, and H.-W. Lee, "Current-induced domain wall motion in a nanowire with perpendicular magnetic anisotropy," *Applied Physics Letters*, vol. 92, no. 20, Article ID 202508, 3 pages, 2008.
 - [63] T. Suzuki, S. Fukami, N. Ohshima, K. Nagahara, and N. Ishiwata, "Analysis of current-driven domain wall motion from pinning sites in nanostrips with perpendicular magnetic anisotropy," *Applied Physics Letters*, vol. 103, no. 11, Article ID 113913, 6 pages, 2008.
 - [64] S. Fukami, T. Suzuki, N. Ohshima, K. Nagahara, and N. Ishiwata, "Micromagnetic analysis of current driven domain

- wall motion in nanostrips with perpendicular magnetic anisotropy,” *Applied Physics Letters*, vol. 103, no. 7, Article ID 07E718, 2008.
- [65] J.-V. Kim and C. Burrowes, “Influence of magnetic viscosity on domain wall dynamics under spin-polarized currents,” *Physical Review B*, vol. 80, no. 21, Article ID 214424, 8 pages, 2009.
- [66] E. Martinez, L. Lopez-Diaz, O. Alejos, and L. Torres, “Thermally activated domain wall depinning in thin strips with high perpendicular magnetocrystalline anisotropy,” *Journal of Applied Physics*, vol. 106, no. 4, Article ID 043914, 5 pages, 2009.
- [67] F. Garcia-Sanchez, H. Szabolcs, A. P. Mihai et al., “Effect of crystalline defects on domain wall motion under field and current in nanowires with perpendicular magnetization,” *Physical Review B*, vol. 81, no. 13, Article ID 134408, 7 pages, 2010.
- [68] S. Emori and G. D. Beach, “Enhanced current-induced domain wall motion by tuning perpendicular magnetic anisotropy,” *Applied Physics Letters*, vol. 98, no. 13, Article ID 132508, 3 pages, 2011.
- [69] G. Consolo and E. Martinez, “The effect of dry friction on domain wall dynamics: a micromagnetic study,” *Journal of Applied Physics*, vol. 111, no. 7, Article ID 07D312, 3 pages, 2012.
- [70] E. Martinez, “The stochastic nature of the domain wall motion along high perpendicular anisotropy strips with surface roughness,” *Journal of Physics*, vol. 24, Article ID 024206, 2012.
- [71] E. Martinez, “The influence of the Rashba field on the current-induced domain wall dynamics: a full micromagnetic analysis, including surface roughness and thermal effects,” *Journal of Applied Physics*, vol. 111, no. 7, Article ID 07D302, 3 pages, 2012.
- [72] E. Martinez, “Micromagnetic analysis of the Rashba field on current-induced domain wall propagation,” *Journal of Applied Physics*, vol. 111, no. 3, Article ID 033901, 6 pages, 2012.
- [73] D. Weller, A. Moser, L. Folks et al., “High ku materials approach to 100 gbits/in²,” *IEEE Transactions on Magnetics*, vol. 36, no. 1, pp. 10–15, 2000.
- [74] P. J. Metaxas, J. P. Jamet, A. Mougin et al., “Creep and flow regimes of magnetic domain-wall motion in ultrathin Pt/Co/Pt films with perpendicular anisotropy,” *Physical Review Letters*, vol. 99, no. 21, Article ID 217208, 2007.
- [75] W. F. Brown, “Thermal fluctuations of a single-domain particle,” *Physical Review*, vol. 130, no. 5, pp. 1677–1686, 1963.
- [76] J. L. Garcia-Palacios and F. J. Lazaro, “Langevin-dynamics study of the dynamical properties of small magnetic particles,” *Physical Review B*, vol. 58, no. 22, pp. 14937–14958, 1998.
- [77] A. A. Thiele, “Steady-state motion of magnetic domains,” *Physical Review Letters*, vol. 30, no. 6, pp. 230–233, 1973.
- [78] T. W. Chiang, L. J. Chang, C. Yu et al., “Demonstration of edge roughness effect on the magnetization reversal of spin valve submicron wires,” *Applied Physics Letters*, vol. 97, no. 2, Article ID 022109, 3 pages, 2010.
- [79] I. M. Miron, G. Gaudin, S. Auffret et al., “Current-driven spin torque induced by the Rashba effect in a ferromagnetic metal layer,” *Nature Materials*, vol. 9, no. 3, pp. 230–234, 2010.
- [80] A. Manchon and S. Zhang, “Theory of nonequilibrium intrinsic spin torque in a single nanomagnet,” *Physical Review B*, vol. 78, no. 21, Article ID 212405, 4 pages, 2008.
- [81] A. Manchon and S. Zhang, “Theory of spin torque due to spin-orbit coupling,” *Physical Review B*, vol. 79, no. 9, Article ID 094422, 9 pages, 2009.
- [82] R. A. Duine, “Spin pumping by a field-driven domain wall,” *Physical Review B*, vol. 77, no. 1, Article ID 014409, 5 pages, 2008.
- [83] A. Stern, “Berry’s phase, motive forces, and mesoscopic conductivity,” *Physical Review Letters*, vol. 68, no. 7, pp. 1022–1025, 1992.
- [84] C.-M. Ryu, “Spin motive force and faraday law for electrons in mesoscopic rings,” *Physical Review Letters*, vol. 76, no. 6, pp. 968–970, 1996.
- [85] S. E. Barnes and S. Maekawa, “Generalization of faraday’s law to include nonconservative spin forces,” *Physical Review Letters*, vol. 98, no. 24, Article ID 246601, 4 pages, 2007.
- [86] W. M. Saslow, “Spin pumping of current in non-uniform conducting magnets,” *Physical Review B*, vol. 76, no. 18, Article ID 184434, 14 pages, 2007.
- [87] Y. Tserkovnyak and M. Mecklenburg, “Electron transport driven by nonequilibrium magnetic textures,” *Physical Review B*, vol. 77, no. 13, Article ID 134407, 4 pages, 2008.
- [88] R. A. Duine, “Effects of nonadiabaticity on the voltage generated by a moving domain wall,” *Physical Review B*, vol. 79, no. 1, Article ID 014407, 8 pages, 2009.
- [89] S. A. Yang, G. S. D. Beach, C. Knutson et al., “Universal electromotive force induced by domain wall motion,” *Physical Review Letters*, vol. 102, no. 6, Article ID 067201, 4 pages, 2009.

Research Article

Heterostructures for Realizing Magnon-Induced Spin Transfer Torque

P. B. Jayathilaka,¹ M. C. Monti,² J. T. Markert,² and Casey W. Miller¹

¹Department of Physics, University of South Florida, 4202 East Fowler Avenue, Tampa, FL 33620, USA

²Department of Physics, University of Texas at Austin, 1 University Station C1600, Austin, TX 78712, USA

Correspondence should be addressed to Casey W. Miller, millercw@usf.edu

Received 17 February 2012; Accepted 21 April 2012

Academic Editor: Giancarlo Consolo

Copyright © 2012 P. B. Jayathilaka et al. This is an open access article distributed under the Creative Commons Attribution License, which permits unrestricted use, distribution, and reproduction in any medium, provided the original work is properly cited.

This work reports efforts fabricating heterostructures of different materials relevant for the realization of magnon-induced spin transfer torques. We find the growth of high-quality magnetite on MgO substrates to be straightforward, while using transition metal buffer layers of Fe, Cr, Mo, and Nb can alter the structural and magnetic properties of the magnetite. Additionally, we successfully fabricated and characterized Py/Cr/Fe₃O₄ and Fe₃O₄/Cr/Fe₃O₄ spin valve structures. For both, we observe a relatively small giant magnetoresistance and confirm an inverse dependence on spacer layer thickness. Thus, we have shown certain materials combinations that may form the heterostructures that are the building blocks necessary to achieve magnon-induced spin transfer torque devices.

1. Introduction

The prediction [1, 2] and observation of “spin transfer” or “spin-transfer torque” in mechanical point contacts [3], and subsequently in lithographically defined point contacts [4], and nanopillars [5], revealed that spin-polarized currents can manipulate magnetization dynamics. The interest in this area is dominated by the potential for spin-torque-based magnetic random access memory to become a universal memory [6], as well as interesting high-frequency devices based on spin torque oscillators (STOs) [7, 8]. Spin torque research is one of the key areas of spintronics and nanomagnetism today [9], being relevant to both science and technology.

Theoreticians have recently promoted the idea of initiating spin transfer torque by thermal transport from magnons, initially in all-metal systems [11, 12] and recently with insulators [10]. Slonczewski's concept in [10] is based on the ability to convert the spin momentum of magnons in a magnetic insulator into a polarized current in a normal metal, which is then driven by a thermal gradient into a metallic ferromagnet. He showed that the quantum yield of heat-driven in-plane spin-transfer torque can exceed that from electric current in state-of-the-art spin-transfer devices

utilizing magnetic tunnel junctions by nearly two orders of magnitude. STOs would benefit greatly from the increased quantum yield deliverable from this magnon-induced spin transfer torque (MISTT) because increasing the usable torque would increase their output power, which is not yet compatible with applications [13–15]. Spin torque-based devices in general would benefit from replacing the high-current densities now necessary for operation, as this causes appreciable heating, as well as vortex nucleation in the free layer via the unavoidable Oersted field. MISTT could address both of these issues, allowing significant improvements in device performance, fabrication requirements, and reliability. The experimental realization of this magnonic spin torque may thus have transformative impact by essentially creating a new class of spin torque devices.

The significant difference between existing spin-transfer devices and Slonczewski's proposal is the origin of the torque on the free layer. Traditionally, the spin-transfer torque comes from direct electrical injection of electrons from a fixed metallic ferromagnet through a normal metal into the free layer [9]. The spin polarization of these electrons mimics that of the fixed ferromagnet, which results in an imposed torque on the free layer magnetization when the

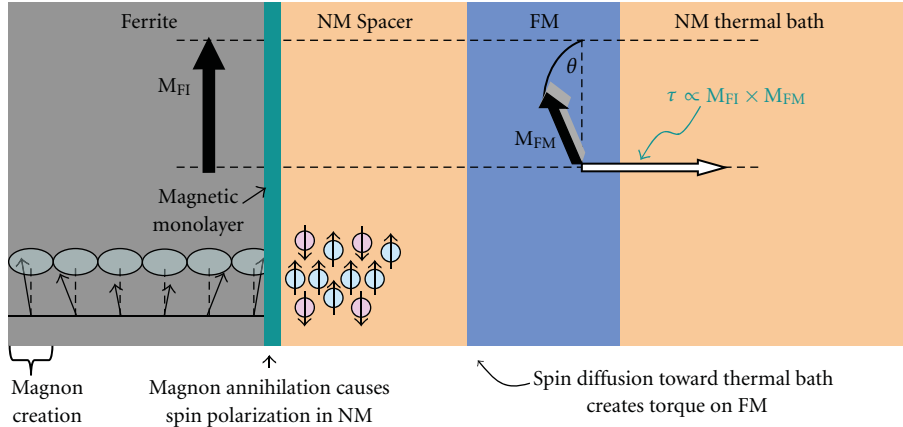


FIGURE 1: Magnon-induced spin transfer torque (MISTT) ala Slonczewski [10]. Magnons are created thermally in the magnetic insulator. Though these magnons are annihilated at the ferrite-normal metal (NM) interface (which contains a monolayer of ferromagnet metal atoms), their spin momentum is transferred to the electrons in the NM spacer. This creates spin accumulation in the NM, which then diffuses toward the NM thermal bath. The spin accumulation current density (more precisely, its time derivative) at the Py interface imposes a torque on the Py magnetization if its magnetization M_{FM} is at some angle relative to the ferrite's magnetization, M_{FI} .

spin polarization axes of the two ferromagnets are not co-linear. In the MISTT device concept (shown schematically in Figure 1), spin polarized electrons still impose a torque on the free layer via a normal metal spacer, but there are several critical differences. First, the electrons are driven by a thermal—not electrical—gradient. Second, because the fixed layer in MISTT is a resistive ferri or ferromagnet (such as spinel ferrites), electrons cannot be simply injected, so a more exotic mechanism for polarizing the electrons in the normal metal is required: magnon annihilation. The magnons within the ferrite carry spin momentum, and, being bosons, the magnon population can be increased dramatically through heating. Conversely, these magnons can also be annihilated when they reach the ferrite-normal metal interface. The spin momentum originally carried by the annihilated magnons can be transferred to electrons in the normal metal, causing them to become spin polarized. These spin-polarized electrons then diffuse into the free magnet, leading to a spin-transfer torque.

Given their great potential, we have been exploring the materials combinations that may lead to the successful fabrication of these devices. This article outlines our progress toward the production of structures that may be useful for realizing magnonic spin transfer torque devices.

2. Experimental Section

All the films were grown in an Ar ion sputtering system with a base pressure of 20 nTorr. Ultra-high-purity gases were used for all the deposition. Samples were rotated at a speed of 40 rotations per minute during the deposition to obtain uniform film thickness. To grow different thicknesses of the same material at a single deposition, the rotation of the sample holder was stopped, so that one sample closer to the gun sees more material flux and grows thicker and the samples away from the target get less material flux and grows thinner. This was used to grow “wedges” for

thickness-dependent studies. In this study, three different sets of samples were grown. Those are (a) Fe_3O_4 on MgO (100) substrates with transition metal buffer layers (Fe, Cr, Nb, Mo and No buffer), (b) Py/Cr/ Fe_3O_4 spin valve with different Cr thicknesses on Si (100) substrates, and (c) Fe_3O_4 /Cr/ Fe_3O_4 substrates with different Cr thicknesses on MgO (100) substrates. Fe_3O_4 was grown at 300C by rf reactive sputtering from an Fe target in an Ar and O_2 environment. The amount of Ar and O_2 were controlled by the adjusting the flow rates of those gases in to the deposition chamber (20 SCCM Ar and 0.75 SCCM O_2). The total deposition pressure was 10 mTorr and the deposition rate was 0.26 Å/s. Epitaxy was confirmed by X-ray diffraction, and the quality of the Fe_3O_4 was indicated by the quality of the Verwey transition. The Fe_3O_4 films we grew showed the Verwey transition in between 119 K to 125 K, which suggests the stoichiometry was Fe_3O_{4-x} , with x bounded above by 0.001 [16].

3. High-Quality Ferrite Films on MgO Substrates

Since magnetite and MgO have nearly perfect lattice matching (as do most spinel ferrites), it is hard to distinguish them using the principal reflections in XRD because the intensity of the substrate (002) peak drowns out the magnetite's (004) peak. We have used a combination of wide angle XRD to observe the (004) and (008) peaks of the substrate and film [17], along with in-plane XRD (i.e., phi scans) to distinguish the Fe_3O_4 from the substrate peaks. We carried out scans focusing on the (311) and (220) orientations. Figures 2(a) and 2(d) show the results of these scans, which confirm the epitaxial growth of the magnetite on the MgO. Using higher resolution in Figures 2(b), 2(c), 2(e), and 2(f) shows that the magnetite peaks are broadened slightly relative to those of the substrate, which may be expected from finite-size effects. The full width at half maximum (FWHM) for MgO (311),

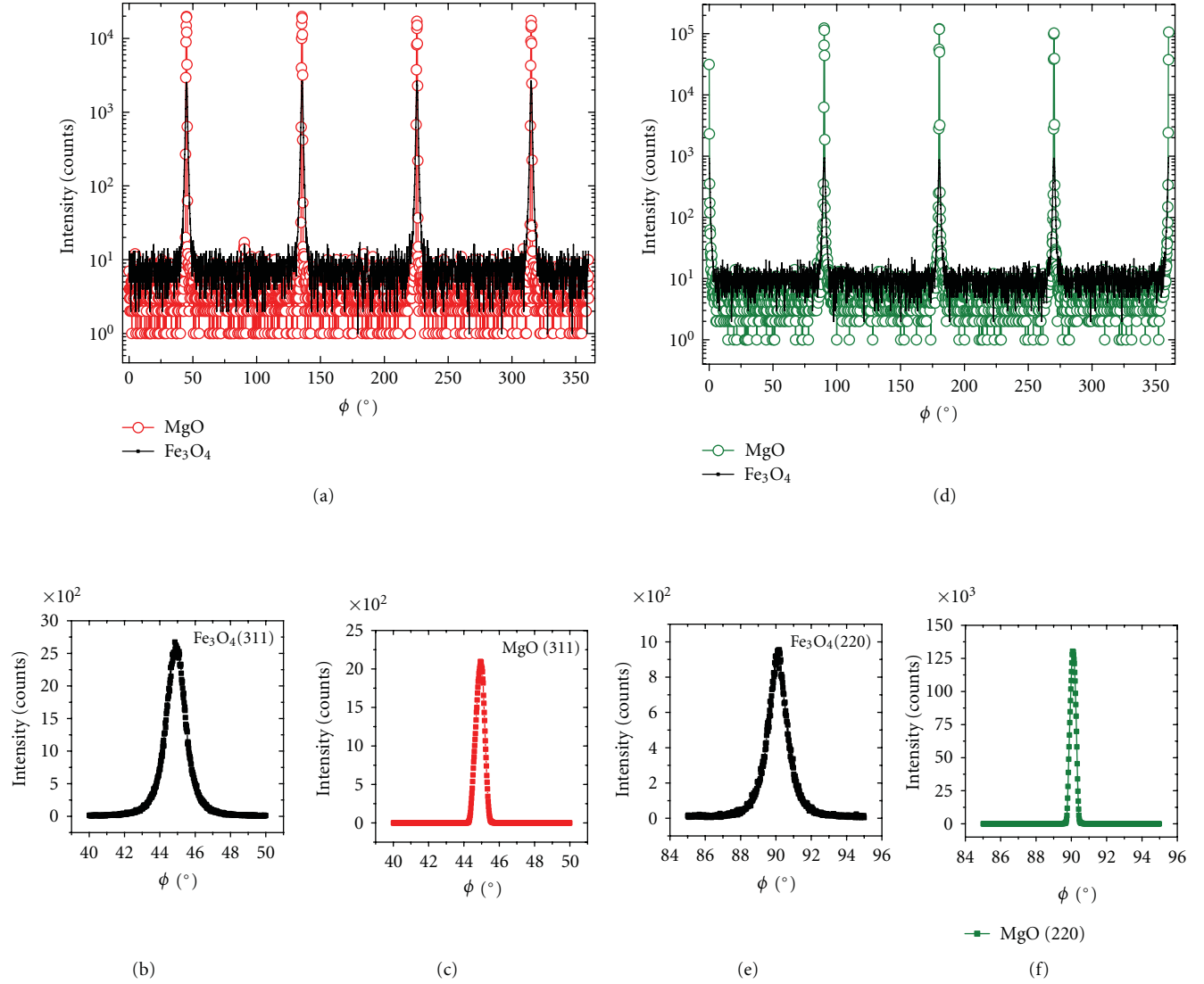


FIGURE 2: XRD Phi scans of Fe₃O₄ on MgO (100) substrates. (a) Complete scan on (220) plane, (b) complete scan on (311) plane, (c) MgO (220) peak, FWHM = 0.38°, (d) Fe₃O₄ (220) Peak, FWHM = 1.36° (e) MgO (311) peak, FWHM = 0.56° (f) Fe₃O₄ (311) peak, FWHM = 1.34°.

Fe₃O₄ (311), MgO (220), and Fe₃O₄ (220) was 0.56°, 1.34°, 0.38°, and 1.36° respectively.

4. Impact of Thin Buffer Layers on Magnetite

In a previous study, we showed that, the magnetite can be grown on 30 Å buffer layers of Fe, Mo, Nb, and Cr [17]. Fe, Mo, and Nb lend themselves to varying degrees of (100) texture, with Nb being the lowest quality; Cr leads to polycrystalline magnetite. The Mo-buffered magnetite has lattice parameters similar to magnetite grown directly on MgO, which is somewhat strained relative to bulk magnetite. The large lattice mismatch between Mo and magnetite appears to lead to the growth of magnetite nanoparticles, not a film per se. The Fe-buffered sample shows the least amount of strain of any sample. This reduced strain appears to reduce the density of antiphase boundaries, as inferred

from mobile magnetic domains observed with temperature-dependent MFM. This is in contrast to magnetite grown directly on MgO [18].

Resistivity measurements were carried out to determine the effect of the transition metal buffer layers on the Verwey transition, as shown in Figure 3. In growing, the magnetite on these buffer layers an in situ mask exchange system allowed us to grow the transition metals on separate MgO (100) substrates individually, and then to grow the magnetite simultaneously on all the samples in one deposition run (i.e., preparation took place entirely under vacuum). Since the magnetite is the same on all the samples, any differences in resistivities should be due to the buffer layer. In measuring the resistivity, we attached the samples to a measurement probe and dip the end into a liquid nitrogen bath, allowing the sample temperature to cool from 300 K down to about 100 K in about 30 minutes. Because of the

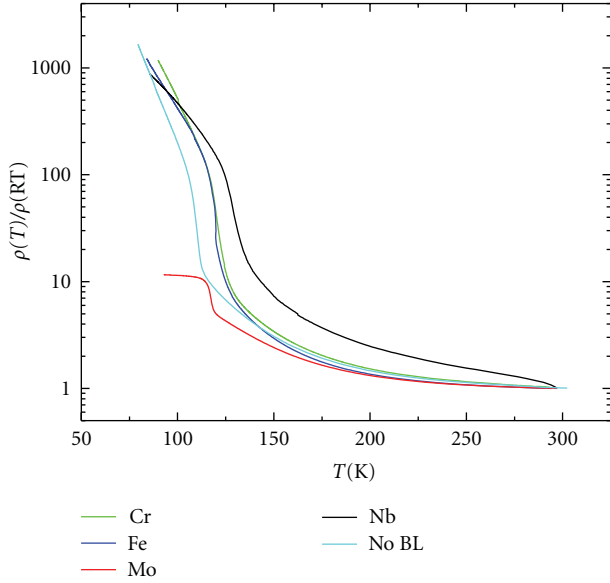


FIGURE 3: Change in resistivity as a function of temperature for magnetite simultaneously grown on different transition metal buffer layers, relative to the room temperature resistivity.

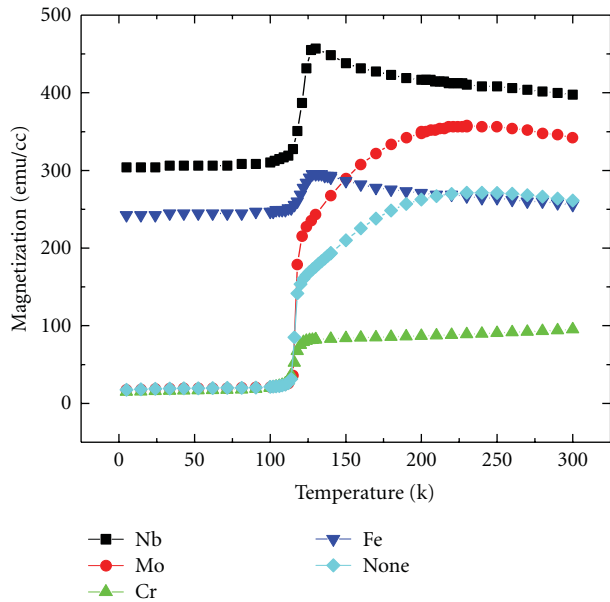


FIGURE 4: Temperature dependent magnetization of the Fe_3O_4 grown on top of different buffer layers. These SQUID magnetometry measurements were performed with a measurement field of 100 Oe applied along the (110) direction of the MgO .

high resistivity, we used 2 point resistivity measurements, making contact to the sample with pressed indium. The resistivity is measured as the sample cools down; the cooling rate is sufficiently slow that no thermal lag is noted with subsequent warming.

The unbuffered magnetite shows the sharpest Verwey transition, with an increase in resistivity of more than an order of magnitude in just a few degrees. Cr, Fe, and Nb

buffered samples showed little higher transition temperatures than the unbuffered magnetite, but the transition was not sharp. This shift in the transition temperature may be due to the stress created from these buffer layers on the magnetite layer, or possibly the formation of an interfacial layer between the buffer and the magnetite (e.g., if the buffer became oxidized by reducing the magnetite, then the interfacial magnetite may have its stoichiometry altered). The Mo-buffered sample showed a transition point closer to the unbuffered sample, but the resistance saturates, unlike any other samples we investigated. We hypothesize this being due to the formation of conduction paths at grain boundaries; indeed, force microscopy images show that the Mo-buffered sample's topography is quite granular due to the formation of magnetite nanoparticles rather than a film. Additionally, these grains appear to have magnetic switching events during magnetic force microscopy that are caused by sample-tip interactions. This indicates the formation of grains that are weakly coupled to their neighbors.

The Verwey transition can also be observed through magnetization measurements. Figure 4 shows the magnetization as a function of temperature with a 100 Oe applied field along the (110) direction (along the diagonal of the substrate plane) for each of the samples. We see each sample has a distinct drop in magnetization at the Verwey transition, which is the typical behavior. It is notable that the Fe and Nb-buffered samples' behavior is distinct from measurements made with the field along the (100) direction on the same samples. We previously observed anomalous magnetization peaks in these samples along (100) direction at the Verwey transition [17]. Thus, it seems that the magnetite anisotropy is temperature dependent, leading to a temperature-dependent rotation of the easy axis above and below the Verwey transition; this manifests itself as a peaking magnetization if the moment rotates into the direction sampled by the SQUID. Similar behavior was reported in bulk Magnetite [19]. Measurement with a vector magnetometer should clarify these observations.

Figure 5 shows hysteresis loops of buffered and unbuffered magnetite samples along the (100) direction at temperatures above (150 K) and below (10 K) the Verwey transition. The samples with no buffer, Mo, and Cr buffers all have similar behavior, showing enhanced coercive and saturation fields at low temperatures. There is also a shearing of the low-temperature loops. On the other hand, the Fe- and Nb-buffered samples show an increasing coercivity at low fields, but the loop shape is not as dramatically changed. This could be due to these buffer layers being more prone to oxidation than the other buffer materials used, which may cause the interfacial magnetite to be reduced.

5. Magnetite-Based Spin Valves

The magnetite was introduced into spin valve structures. The Cr spacer layers were grown as a wedge to study the thickness dependence. Current in-plane (CIP) magnetoresistance measurements were carried out at room temperature for $\text{Py/Cr/Fe}_3\text{O}_4$ and $\text{Fe}_3\text{O}_4/\text{Cr/Fe}_3\text{O}_4$ spin valve structures.

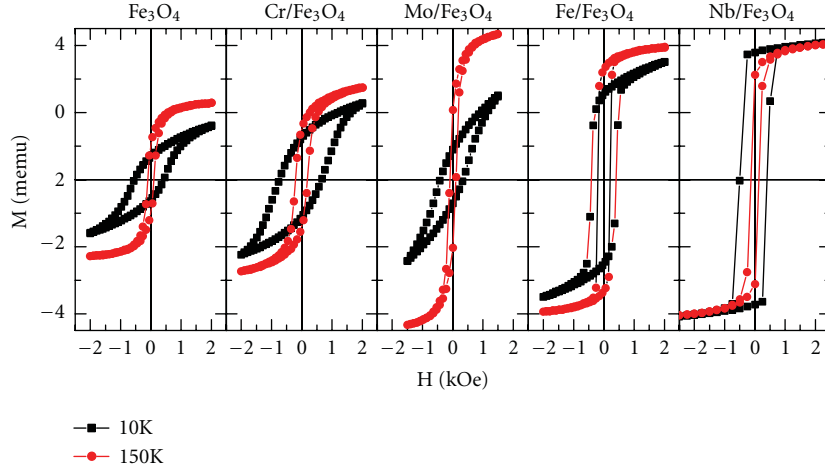


FIGURE 5: Hysteresis loops for Fe_3O_4 grown simultaneously on MgO (100) substrates with and without 30 Å transition metal buffer layers. The SQUID magnetometry measurements were performed with a measurement field of 100 Oe applied along the (100) direction of the MgO .

While CIP measurements are not typically used in spin-torque devices, this method can indicate that spin-dependent scattering is present in the structure. Note that MISTT does not even need current to flow in the device, as the magnons may be generated thermally (e.g., by optical means). We used pseudo-four-point resistance measurements, in which I^+ and V^+ leads are connected together at a single Indium contact (similarly for I^- and V^-) in order to remove effects related to the leads. In $\text{Py}/\text{Cr}/\text{Fe}_3\text{O}_4$ spin valves, the Cr thickness was varied from 41 Å to 107 Å and the Py and Fe_3O_4 thicknesses were kept constant at 300 Å (Figure 6). The GMR was calculated by subtracting the resistance of the saturated parallel state by the resistance of the shoulder in the antiparallel state. Then, the percentage was calculated with respect to the resistance of the saturated parallel state. The magnetoresistance showed a decrease with increasing spacer layer thickness in $\text{Py}/\text{Cr}/\text{Fe}_3\text{O}_4$. A fit of this thickness dependence reveals a decay constant of about 19 Å. This is less than the 45 Å reported for the spin diffusion length of Cr at 4.2 K [20]. Since the thicknesses used for the Cr spacer layer were relatively large, we did not observe any oscillatory coupling behavior as a function of spacer layer thickness. This ensured we were able to switch both ferromagnets separately, and it indicates the existence of a GMR signal, even for large thicknesses of normal metal spacer layers. In addition to the GMR signal there is also an anisotropic magnetoresistance (AMR) peak of Py due to the reversal of magnetization by the applied field. This AMR signal is essentially unavoidable because the metallic Py and Cr have much lower resistivity than the magnetite, so the current flows primarily through these layers. The intensity of this peak and its field range can be reduced by applying a magnetic field during the growth process, and likely by lithographic patterning to take advantage of shape anisotropy [21].

In $\text{Fe}_3\text{O}_4/\text{Cr}/\text{Fe}_3\text{O}_4$ spin valves (Figure 7), the Cr thickness was varied from 57 Å to 151 Å. To get different coercive

fields from the magnetite, the bottom layer was 500 Å and the top layer was 1000 Å. Here, there are no well-defined parallel and antiparallel states due to the butterfly-like AMR signal intrinsic to the magnetite layers [22]. Thus, we calculated the GMR by taking the shift of the signal relative to the AMR signal. In this case, the magnetoresistance signal also decays exponentially with the spacer layer thickness, but the decay constant is 33 Å. We did not observe any oscillatory coupling due to higher spacer layer thickness.

The GMR values are quite small for both spin valve varieties relative to all-metallic CIP spin valves [23], but fall in the range of GMR reports for magnetite-normal metal-ferromagnetic systems [22, 24]. This is most likely related to a combination of factors, which most likely includes possible oxidation of the Cr at the magnetite interface acting as a barrier to spin-dependent reflections necessary for large GMR, as well as the conductivity mismatch between the magnetite and the metals shunting much of the current in the Py-containing devices. The differences in the two decay constants observed in the two spin valves is probably related to impurities in the spacer (which may be due to residual oxygen from the reactive sputtering to form the magnetite), which are known to impact the spin diffusion length [20], and possibly uncertainty in the spacer layer thickness.

6. Conclusions

We have studied the growth of magnetite on transition metal buffer layers and the formation of magnetite-based spin valves. We found the structural and magnetic properties of magnetite to be strongly dependent on the buffer layer. Despite the differences noted for Cr buffer layers, we were able to grow spin valves that use Cr as a spacer layer and magnetite as the top layer. While these spin valves do not appear to have promise for GMR applications, this work shows we have successfully fabricated heterostructures with

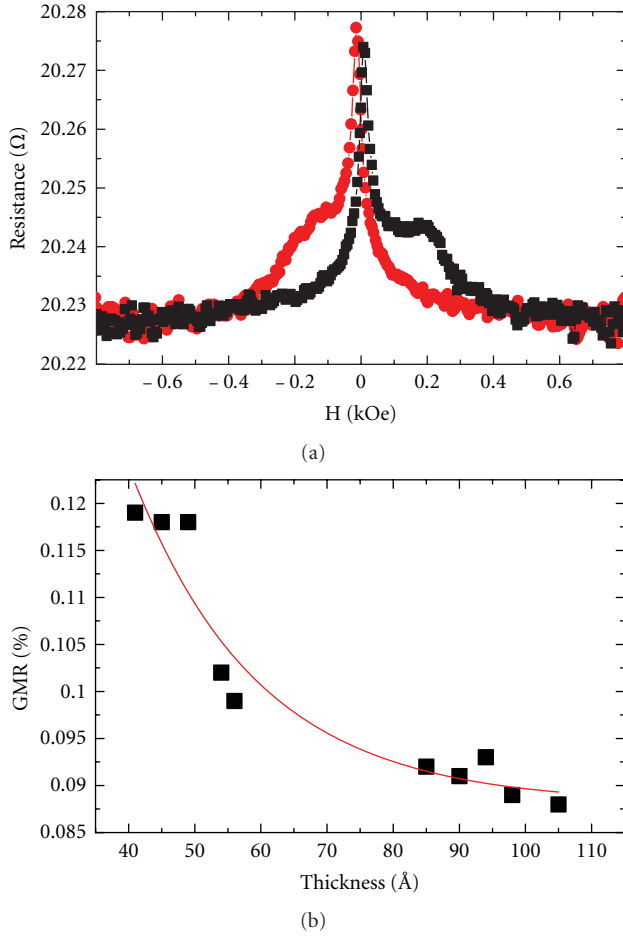


FIGURE 6: (a) Room temperature current in plane magnetoresistance measurements on Py(300 Å)/Cr(41 Å)/Fe₃O₄(300 Å) spin valves. The shoulders are the antiparallel state. The AMR peak of the Py is unavoidable because of the conductivity mismatch between the metals and the oxide. (b) GMR as a function of Cr spacer layer thickness.

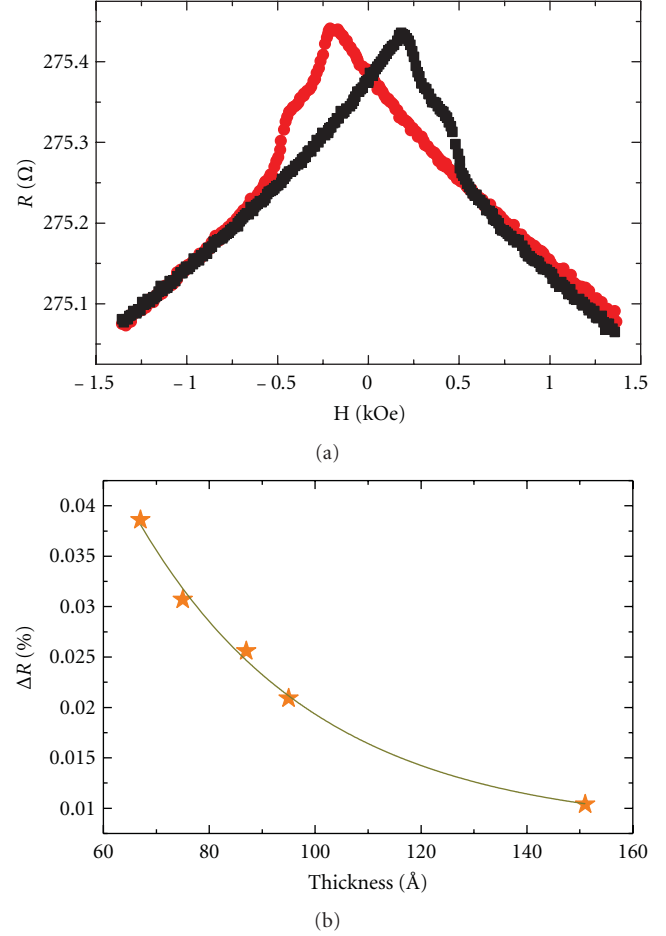


FIGURE 7: (a) Current in plane magnetoresistance measurements on Fe₃O₄(500 Å)/Cr(57 Å)/Fe₃O₄(1000 Å) spin valves. The black (red) data are measurements with increasing (decreasing) fields. (b) Change of GMR as a function of Cr spacer layer thickness; the line is a fit to an exponential decay, with a decay constant of 33 Å.

the potential for growing devices to realize magnon-induced spin transfer torques.

Acknowledgments

The work at USF was supported by the National Science Foundation; the work at UT was separately supported by the National Science Foundation, as well as the Welch Foundation. The authors thank C. Bauer and D. Williams for assistance with some of the measurements.

References

- [1] L. Berger, "Emission of spin waves by a magnetic multilayer traversed by a current," *Physical Review B*, vol. 54, no. 13, pp. 9353–9358, 1996.
- [2] J. C. Slonczewski, "Current-driven excitation of magnetic multilayers," *Journal of Magnetism and Magnetic Materials*, vol. 159, no. 1-2, pp. L1–L7, 1996.
- [3] M. Tsoi, A. G. M. Jansen, J. Bass et al., "Excitation of a magnetic multilayer by an electric current," *Physical Review Letters*, vol. 80, no. 19, pp. 4281–4284, 1998.
- [4] E. B. Myers, D. C. Ralph, J. A. Katine, R. N. Louie, and R. A. Buhrman, "Current-induced switching of domains in magnetic multilayer devices," *Science*, vol. 285, no. 5429, pp. 867–870, 1999.
- [5] J. A. Katine, F. J. Albert, R. A. Buhrman, E. B. Myers, and D. C. Ralph, "Current-driven magnetization reversal and spin-wave excitations in Co/Cu/Co pillars," *Physical Review Letters*, vol. 84, no. 14, pp. 3149–3152, 2000.
- [6] J. Åkerman, "Toward a universal memory," *Science*, vol. 308, no. 5721, pp. 508–510, 2005.
- [7] S. I. Kiselev, J. C. Sankey, I. N. Krivorotov et al., "Microwave oscillations of a nanomagnet driven by a spin-polarized current," *Nature*, vol. 425, no. 6956, pp. 380–383, 2003.
- [8] I. N. Krivorotov, N. C. Emley, J. C. Sankey, S. I. Kiselev, D. C. Ralph, and R. A. Buhrman, "Time-domain measurements of nanomagnet dynamics driven by spin-transfer torques," *Science*, vol. 307, no. 5707, pp. 228–231, 2005.

- [9] D. C. Ralph and M. D. Stiles, "Spin transfer torques," *Journal of Magnetism and Magnetic Materials*, vol. 320, no. 7, pp. 1190–1216, 2008.
- [10] J. C. Slonczewski, "Initiation of spin-transfer torque by thermal transport from magnons," *Physical Review B*, vol. 82, no. 5, Article ID 054403, 2010.
- [11] M. Hatami, G. E. W. Bauer, Q. Zhang, and P. J. Kelly, "Thermal spin-transfer torque in magnetoelectronic devices," *Physical Review Letters*, vol. 99, no. 6, Article ID 066603, 2007.
- [12] J. E. Wegrowe, "Spin transfer from the point of view of the ferromagnetic degrees of freedom," *Solid State Communications*, vol. 150, no. 11-12, pp. 519–523, 2010.
- [13] A. V. Nazarov, H. M. Olson, H. Cho et al., "Spin transfer stimulated microwave emission in MgO magnetic tunnel junctions," *Applied Physics Letters*, vol. 88, no. 16, Article ID 162504, 2006.
- [14] A. M. Deac, A. Fukushima, H. Kubota et al., "Bias-driven high-power microwave emission from MgO-based tunnel magnetoresistance devices," *Nature Physics*, vol. 4, no. 10, pp. 803–809, 2008.
- [15] D. Houssameddine, S. H. Florez, J. A. Katine et al., "Spin transfer induced coherent microwave emission with large power from nanoscale MgO tunnel junctions," *Applied Physics Letters*, vol. 93, no. 2, Article ID 022505, 2008.
- [16] M. G. Chapline and S. X. Wang, "Observation of the Verwey transition in thin magnetite films," *Journal of Applied Physics*, vol. 97, no. 12, Article ID 123901, 3 pages, 2005.
- [17] P. B. Jayathilaka, C. A. Bauer, D. V. Williams, M. C. Monti, J. T. Markert, and C. W. Miller, "Impact of ultrathin transition metal buffer layers on Fe₃O₄ thin films," *Journal of Applied Physics*, vol. 107, no. 9, Article ID 09B101, 2010.
- [18] A. K. H. Lee, P. B. Jayathilaka, C. A. Bauer et al., "Magnetic force microscopy of epitaxial magnetite films through the Verwey transition," *Applied Physics Letters*, vol. 97, no. 16, Article ID 162502, 2010.
- [19] K. Moloni, B. M. Moskowitz, and E. Dan Dahlberg, "Domain structures in single crystal magnetite below the Verwey transition as observed with a low-temperature magnetic force microscope," *Geophysical Research Letters*, vol. 23, no. 20, pp. 2851–2854, 1996.
- [20] J. Bass and W. P. Pratt Jr., "Spin-diffusion lengths in metals and alloys, and spin-flipping at metal/metal interfaces: an experimentalist's critical review," *Journal of Physics Condensed Matter*, vol. 19, no. 18, Article ID 183201, 2007.
- [21] P. B. Jayathilaka, C. A. Bauer, D. V. Williams, and C. W. Miller, "Influence of growth field on NiFe, Fe₃O₄, and NiFe/Cr/Fe₃O₄ spin-valves," *IEEE Transactions on Magnetics*, vol. 46, no. 6, pp. 1777–1779, 2010.
- [22] S. van Dijken, X. Fain, S. M. Watts, K. Nakajima, and J. M. D. Coey, "Magnetoresistance of Fe₃O₄/Au/Fe₃O₄ and Fe₃O₄/Au/Fe spin-valve structures," *Journal of Magnetism and Magnetic Materials*, vol. 280, no. 2-3, pp. 322–326, 2004.
- [23] M. N. Baibich, J. M. Broto, A. Fert et al., "Giant magnetoresistance of (001)Fe/(001)Cr magnetic superlattices," *Physical Review Letters*, vol. 61, no. 21, pp. 2472–2475, 1988.
- [24] D. Tripathy, A. O. Adeyeye, and S. Shannigrahi, "Effect of spacer layer thickness on the magnetic and magnetotransport properties of Fe₃O₄/Cu/Ni₈₀/Fe₂₀ spin valve structures," *Physical Review B*, vol. 75, no. 1, Article ID 012403, 2007.

Research Article

Thermodynamics of the Classical Planar Ferromagnet Close to the Zero-Temperature Critical Point: A Many-Body Approach

L. S. Campana,¹ A. Cavallo,² L. De Cesare,^{2,3} U. Esposito,¹ and A. Naddeo^{2,3}

¹*Dipartimento di Scienze Fisiche, Università degli Studi di Napoli "Federico II", Piazzale Tecchio 80, 80125 Napoli, Italy*

²*Dipartimento di Fisica "E.R. Caianiello", Università degli Studi di Salerno, Via Ponte don Melillo, 84084 Fisciano, Italy*

³*CNISM, Unità di Ricerca di Salerno, 84084 Fisciano, Italy*

Correspondence should be addressed to A. Cavallo, cavallo@sa.infn.it

Received 1 February 2012; Accepted 15 March 2012

Academic Editor: Giancarlo Consolo

Copyright © 2012 L. S. Campana et al. This is an open access article distributed under the Creative Commons Attribution License, which permits unrestricted use, distribution, and reproduction in any medium, provided the original work is properly cited.

We explore the low-temperature thermodynamic properties and crossovers of a d -dimensional classical planar Heisenberg ferromagnet in a longitudinal magnetic field close to its field-induced zero-temperature critical point by employing the two-time Green's function formalism in classical statistical mechanics. By means of a classical Callen-like method for the magnetization and the Tyablikov-like decoupling procedure, we obtain, for any d , a low-temperature critical scenario which is quite similar to the one found for the quantum counterpart. Remarkably, for $d > 2$ the discrimination between the two cases is found to be related to the different values of the shift exponent which governs the behavior of the critical line in the vicinity of the zero-temperature critical point. The observation of different values of the shift-exponent and of the related critical exponents along thermodynamic paths within the typical V-shaped region in the phase diagram may be interpreted as a signature of emerging quantum critical fluctuations.

1. Introduction

An intriguing aspect of quantum phase transitions (QPTs) [1] is that quantum critical fluctuations may play a relevant role also at finite temperature. This feature leads to a drastic modification of the expected properties of many systems within a wide region around their quantum critical point (QCP) [1–6].

Remarkably, the renormalization group framework (RG) [1, 7, 8] and Moriya's self-consistent renormalized approach [9, 10] have provided a well-defined scenario for this so-called quantum criticality giving qualitative and also quantitative agreement with a lot of experimental findings [1–6].

However, recent experiments seem to suggest that these theories fail in relevant practical situations (see [11–13] and references therein). Although several alternatives have been proposed to explain these unexpected behaviors, a completely convincing picture is still lacking. Hence, it becomes

crucial to provide nonambiguous criteria to determine accurately the range of temperatures where the QCP fluctuations survive against the thermal ones. On the ground of a comparison between the exactly solvable one-dimensional quantum transverse Ising model (QTIM) [1, 14–18] and its classical version (CTIM) (not to be confused with the standard Ising model) [19, 20], it was conjectured that [21], at least in selected cases, at finite temperature, close to the QCP, quantum critical fluctuations may not be so relevant as commonly believed. The emerging idea was that, to single out conventional quantum criticality, it is not sufficient to observe a power-law behavior of the correlation length or susceptibility decreasing temperature towards zero in the V-shaped quantum critical region of the phase diagram [1]; rather, the accurate determination of the critical exponents becomes the key ingredient to decide if we are in the influence domain of the QCP or the physics is governed by thermal fluctuations. Of course, to validate the previous

conjecture, more realistic many-body systems should be investigated, especially for dimensionalities where a finite-temperature critical line ends in a zero-temperature critical point.

A first step along this direction has been recently performed by exploring the low-temperature properties of the ($d > 1$)-dimensional CTIM [22]. On the ground of a suitable Ginzburg-Landau-Wilson functional and a momentum-shell RG approach around $d = 4$, this system is expected to have the same properties of the QTIM above a certain temperature.

Further insights will be provided in this paper where we investigate the low-temperature properties of the classical XXZ ferromagnetic model in presence of a longitudinal magnetic field when the longitudinal exchange interaction is smaller than the transverse one. Its quantum analogue, also called planar ferromagnet (PFM), has been extensively studied, in different physical contexts, using several methods. In particular, the spin-1/2 PFM has attracted great attention since, in the pioneering papers by Matsubara and Matsuda [23, 24] on superfluidity in ^4He , a quantum lattice gas of hard-core bosons with long-range attractive interactions has been proven to be just equivalent to the spin-1/2 PFM in a longitudinal field (see also [25]). Remarkably, the Wilson RG [26, 27], applied to a suitable functional representation of the spin-1/2 PFM, capturing the essential low-temperature physics, and the two-time Green's function technique [28], utilized to investigate the microscopic spin- S model, have provided a reliable scenario of the global phase diagram and crossovers in the vicinity of the QCP.

In the present work, we will study the corresponding d -dimensional classical XXZ spin model (CPFM) with particular attention to a field-induced quantum-like critical scenario for a direct comparison with the quantum counterpart. We will use the two-time Green's function method in classical statistical mechanics [29], developed and tested in [30–33], on microscopic classical spin model. This allows us to perform in parallel the quantum [28] and the classical analysis for any d , giving a transparent relation between the CPM and the spin- S QPFM, both exhibiting a zero-temperature critical point. Hence, new insights on quantum criticality, at least for a class of anisotropic magnetic systems, will be provided.

The paper is organized as follows. In Section 2 we will introduce the model and the equation of motion for the appropriate two-time Green function in the context of the classical Callen-like method [34] to calculate the magnetization within the Tyablikov decoupling procedure. The equations for the transverse susceptibility and the critical line will be presented in Section 3. The quantum-like scenario, with the global phase diagram and crossovers, close to the ($T = 0$)-critical point, will be analyzed in Section 4. In Section 5, concluding remarks will be drawn. At the end, for utility of reader, Appendix A is devoted to an outline of the two-time Green's function framework in classical statistical mechanics and Appendix B presents a method, alternative to the one employed in [22], to obtain the magnetization as the solution of the Callen-like method.

2. Spin Model and Callen-Like Method

The d -dimensional classical XXZ Heisenberg model in a longitudinal magnetic field $h \geq 0$ is described by the Hamiltonian:

$$\begin{aligned}\mathcal{H} &= -\frac{1}{2} \sum_{i,j=1}^N \left[J_{ij}^{\perp} (S_i^x S_j^x + S_i^y S_j^y) + J_{ij}^{\parallel} S_i^z S_j^z \right] - h \sum_{i=1}^N S_i^z \\ &= -\frac{1}{2} \sum_{i,j=1}^N \left[J_{ij}^{\perp} S_i^+ S_j^- + J_{ij}^{\parallel} S_i^z S_j^z \right] - h \sum_{i=1}^N S_i^z.\end{aligned}\quad (1)$$

Here $\{\mathbf{S}_j \equiv (S_j^x, S_j^y, S_j^z); j = 1, 2, \dots, N\}$ are classical spin- S vectors on an N -sites hypercubic lattice with unitary spacing, satisfying the identity $\mathbf{S}_j^2 = S_j^+ S_j^- + (S_j^z)^2 = S^2$ with $S_j^{\pm} = S_j^x \pm iS_j^y$. Besides, the transverse (J_{ij}^{\perp}) and longitudinal (J_{ij}^{\parallel}) exchange interactions (with $J_{ii}^{\perp} = J_{ii}^{\parallel} = 0$) between the spins at sites i and j are assumed to be symmetric, positive, and short ranged. As well known, it is perfectly legal in the classical context to put $S = 1$. However, for a more transparent and direct comparison with the quantum version [28], through this paper we will consider arbitrary S .

Many magnetic materials can be described by the Hamiltonian (1) and different cases may take place depending on the relative weight of the competing anisotropic exchange interactions. Indeed, one has a uniaxial ferromagnet (FM) if $J_{ij}^{\parallel} > J_{ij}^{\perp}$ with the extreme limit $J_{ij}^{\perp} = 0$ (Ising model); we recover the isotropic Heisenberg model when $J_{ij}^{\perp} = J_{ij}^{\parallel}$ and the PFM if $J_{ij}^{\parallel} < J_{ij}^{\perp}$ whose extreme limit $J_{ij}^{\parallel} = 0$ is the XY model in a transverse field (TXYM). In the following, we will focus on the classical PFM which exhibits a field-driven zero-temperature critical point as it happens in the quantum case.

The classical model (1) can be described in terms of the $2N$ canonical variables $\phi \equiv \{\phi_j\}$ and $S^z \equiv \{S_j^z\}$, where ϕ_j is the angle between the projection of the spin vector \mathbf{S}_j in the xy -plane and the x -axis. The Poisson bracket of two generic classical dynamical variables $A = A(\phi, S^z)$ and $B = B(\phi, S^z)$ is then defined by

$$\{A, B\} = \sum_{j=1}^N \left(\frac{\partial A}{\partial \phi_j} \frac{\partial B}{\partial S_j^z} - \frac{\partial A}{\partial S_j^z} \frac{\partial B}{\partial \phi_j} \right). \quad (2)$$

It is easy to show that, with this prescription, the Poisson brackets for the spin components are given by

$$\begin{aligned}\{S_i^z, S_j^{\pm}\} &= \mp i S_i^{\pm} \delta_{ij}, \\ \{S_i^+, S_j^-\} &= -2i S_i^z \delta_{ij}, \\ \{S_i^{\alpha}, S_j^{\beta}\} &= \epsilon_{\gamma}^{\alpha\beta} S_i^{\gamma} \delta_{ij} \quad (\alpha, \beta, \gamma = x, y, z),\end{aligned}\quad (3)$$

where $\epsilon_{\gamma}^{\alpha\beta}$ is the Levi-Civita tensor.

Following the Callen procedure developed for the quantum Heisenberg FM [35], we introduce now the retarded two-time GF [29, 33] (see Appendix A):

$$G_{ij}(t-t') = \theta(t-t') \left\langle \left\{ S_i^+(t-t'), e^{aS_j^z} S_j^- \right\} \right\rangle = \left\langle \left\{ S_i^+(t-t'); e^{aS_j^z} S_j^- \right\} \right\rangle, \quad (4)$$

where $\theta(x)$ is the usual step function, a denotes the Callen-like parameter, $\langle \dots \rangle = \mathcal{Z}^{-1} \prod_{j=1}^N \int_0^{2\pi} d\phi_j \int_{-S}^S \dots dS_j^z \dots \exp\{-\beta \mathcal{H}(\phi, S^z)\}$ stands for the classical ensemble average, $\beta = 1/T$ is the inverse temperature, and $X(t) = e^{iLt} X$, $L = i\{\mathcal{H}, \dots\}$ is the Liouville operator. Here, e^{iLt} acts as a classical time-evolution operator which transforms the dynamical variable $X = X(0) \equiv X(\phi(0), S^z(0))$ at the initial time $t = 0$ into $X(t) \equiv X(\phi(t), S^z(t))$ at the time t . The physics will be of course obtained setting $a = 0$ at the end of the calculations.

The equation of motion (EM) for the GF (4) is given by (with $\tau = t - t'$)

$$\frac{dG_{ij}(\tau)}{d\tau} = \delta(\tau) \left\langle \left\{ S_i^+, e^{aS_j^z} S_j^- \right\} \right\rangle + \left\langle \left\{ S_i^+(\tau), \mathcal{H}; e^{aS_j^z} S_j^- \right\} \right\rangle, \quad (5)$$

which, in the frequency- ω Fourier space, becomes

$$\omega G_{ij}(\omega) = i \left\langle \left\{ S_i^+, e^{aS_j^z} S_j^- \right\} \right\rangle + i \left\langle \left\{ S_i^+(\tau), \mathcal{H}; e^{aS_j^z} S_j^- \right\} \right\rangle_\omega, \quad (6)$$

with $G_{ij}(\omega) = \langle \langle S_i^+(\tau); e^{aS_j^z} S_j^- \rangle \rangle_\omega$ and $\langle \langle A(\tau); B \rangle \rangle_\omega = \int_{-\infty}^{+\infty} d\tau e^{i\omega\tau} \langle \langle A(\tau); B \rangle \rangle$. From the basic Poisson brackets (2), a simple algebra yields

$$i \left\langle \left\{ S_i^+, e^{aS_j^z} S_j^- \right\} \right\rangle = \psi(a) \delta_{ij}, \quad (7)$$

where

$$\psi(a) = -a\Omega(a) + 2\Omega'(a) + a\Omega''(a), \quad (8)$$

with

$$\Omega(a) = \langle e^{aS_i^z} \rangle. \quad (9)$$

Notice that, for the magnetization per spin $m = \langle S_i^z \rangle$, the relevant exact relation is fulfilled:

$$m = \frac{1}{2} \psi(0) = \Omega'(0). \quad (10)$$

On the other hand, in (6), we have also

$$\{S_i^+, \mathcal{H}\} = i \sum_h \left[J_{ih}^+ S_i^z S_h^+ - J_{ih}^{\parallel} S_i^+ S_h^z \right] - i h S_i^+. \quad (11)$$

Then, (6) becomes (again without approximations)

$$\begin{aligned} (\omega - h) G_{ij}(\omega) &= \psi(a) \delta_{ij} \\ &- \sum_h \left[J_{ih}^+ \left\langle \left\{ S_i^z(\tau) S_h^+(\tau); e^{aS_j^z} S_j^- \right\} \right\rangle_\omega \right. \\ &\quad \left. - J_{ih}^{\parallel} \left\langle \left\{ S_i^+(\tau) S_h^z(\tau); e^{aS_j^z} S_j^- \right\} \right\rangle_\omega \right]. \end{aligned} \quad (12)$$

The next step consists in performing an appropriate decoupling to close (12). Here we will use the classical version of the Tyablikov decoupling (TD) which, for the quantum case, has been proven [28] to give near-exact results close to the QCP. This decoupling procedure consists in neglecting transverse correlations in (12) so that one can assume that

$$\begin{aligned} \left\langle \left\{ S_h^z(\tau) S_k^+(\tau); e^{aS_j^z} S_j^- \right\} \right\rangle_\omega &\simeq \langle S_h^z \rangle \left\langle \left\{ S_k^+(\tau); e^{aS_j^z} S_j^- \right\} \right\rangle_\omega \\ &\simeq m \left\langle \left\{ S_k^+(\tau); e^{aS_j^z} S_j^- \right\} \right\rangle_\omega, \end{aligned} \quad (13)$$

providing

$$\left[\omega - h - m J^{\parallel}(0) \right] G_{ij}(\omega) = \psi(a) \delta_{ij} - m \sum_h J_{ih}^+ G_{hj}(\omega), \quad (14)$$

where $\sum_h J_{ih}^{\parallel} = J^{\parallel}(0)$ is the ($\mathbf{k} = 0$)-component of the \mathbf{k} -wave vector Fourier transform in the first Brillouin zone (1BZ) $J_{ij}^{\parallel} = (1/N) \sum_{\mathbf{k}} e^{i\mathbf{k} \cdot (\mathbf{r}_i - \mathbf{r}_j)} J^{\parallel}(\mathbf{k})$. Finally, using the Fourier transforms in the \mathbf{k} -space

$$\begin{aligned} G_{ij}(\omega) &= \frac{1}{N} \sum_{\mathbf{k}} e^{i\mathbf{k} \cdot (\mathbf{r}_i - \mathbf{r}_j)} G_{\mathbf{k}}(\omega), \\ J_{ij}^{\alpha} &= \frac{1}{N} \sum_{\mathbf{k}} e^{i\mathbf{k} \cdot (\mathbf{r}_i - \mathbf{r}_j)} J^{\alpha}(\mathbf{k}), \quad \alpha = \perp, \parallel, \end{aligned} \quad (15)$$

with $\delta_{ij} = (1/N) \sum_{\mathbf{k}} e^{i\mathbf{k} \cdot (\mathbf{r}_i - \mathbf{r}_j)}$, (14) reduces to an algebraic equation for $G_{\mathbf{k}}(\omega)$ with solution

$$G_{\mathbf{k}}(\omega) = \frac{\psi(a)}{\omega - \omega_{\mathbf{k}}}, \quad (16)$$

where

$$\omega_{\mathbf{k}} = h + m \left[J^{\parallel}(0) - J^{\perp}(\mathbf{k}) \right]. \quad (17)$$

This equation represents the dispersion relation, at Tyablikov-like decoupling (TD) level, of undamped oscillations for the PFM, expressed as a function of \mathbf{k} in terms of the Fourier transform $J^{\perp}(\mathbf{k})$ of the transverse exchange interaction J_{ij}^{\perp} . The key step is to determine the function $\psi(a)$ or $\Omega(a)$ and hence $m = (1/2)\psi(0) = \Omega'(0)$. For utility of the reader, we outline here in after the classical version of the Callen procedure used to solve this problem for isotropic quantum [35] and classical [34] Heisenberg FMs and for QPFM [28].

From the expression (16) for $G_{\mathbf{k}}(\omega)$ and the exact relation between $G_{\mathbf{k}}(\omega)$ and the corresponding spectral density $\Lambda_{\mathbf{k}}(\omega)$ (see Appendix A)

$$\Lambda_{\mathbf{k}}(\omega) = i[G_{\mathbf{k}}(\omega + i\epsilon) - G_{\mathbf{k}}(\omega - i\epsilon)]_{\epsilon \rightarrow 0^+}, \quad (18)$$

one easily finds

$$\Lambda_{\mathbf{k}}(\omega) = 2\pi \psi(a) \delta(\omega - \omega_{\mathbf{k}}). \quad (19)$$

Then, the spectral density $\Lambda_{ij}(\omega)$ corresponding to $G_{ij}(\omega)$ can be obtained via its Fourier transform:

$$\begin{aligned} \Lambda_{ij}(\omega) &= \frac{1}{N} \sum_{\mathbf{k}} e^{i\mathbf{k} \cdot (\mathbf{r}_i - \mathbf{r}_j)} \Lambda_{\mathbf{k}}(\omega) \\ &= 2\pi \psi(a) \frac{1}{N} \sum_{\mathbf{k}} e^{i\mathbf{k} \cdot (\mathbf{r}_i - \mathbf{r}_j)} \delta(\omega - \omega_{\mathbf{k}}). \end{aligned} \quad (20)$$

Now, with these ingredients, we are in position to obtain the correlation function $\langle BA \rangle = \langle e^{aS_j^z} S_j^- S_i^+ \rangle$ related to the original GF $G_{ij}(\omega) = \langle \langle A(\tau); B \rangle \rangle_\omega = \langle \langle S_i^+(\tau); e^{aS_j^z} S_j^- \rangle \rangle_\omega$.

From the classical spectral theorem (see Appendix A, (A.13) and (A.14)), one immediately gets

$$\langle e^{aS_j^z} S_j^- S_i^+ \rangle = T \int_{-\infty}^{+\infty} \frac{d\omega}{2\pi} \frac{\Lambda_{ij}(\omega)}{\omega} \simeq T\psi(a) \frac{1}{N} \sum_{\mathbf{k}} \frac{e^{i\mathbf{k} \cdot (\mathbf{r}_i - \mathbf{r}_j)}}{\omega_{\mathbf{k}}}, \quad (21)$$

and hence also

$$\langle e^{aS_i^z} S_i^- S_i^+ \rangle = \Phi\psi(a). \quad (22)$$

Here, the quantity

$$\Phi = \frac{T}{N} \sum_{\mathbf{k}} \frac{1}{\omega_{\mathbf{k}}} \stackrel{N \rightarrow \infty}{=} T \int_{\text{1BZ}} \frac{d^d k}{(2\pi)^d} \frac{1}{\omega_{\mathbf{k}}} \quad (23)$$

is independent of the Callen parameter a .

On the other hand, from the relation $S_i^+ S_i^- = S_i^- S_i^+ = S^2 - (S_i^z)^2$, we can also write

$$\langle e^{aS_i^z} S_i^- S_i^+ \rangle = S^2 \Omega(a) - \Omega''(a). \quad (24)$$

Then, combining (22) and (24), where $\psi(a)$ is given by (8), we obtain the following differential equation for $\Omega(a)$:

$$\Omega''(a) + 2\left(\frac{1}{\Phi} + a\right)\Omega'(a) - S^2\Omega(a) = 0, \quad (25)$$

to be solved with the initial condition $\Omega(0) = 1$ and the additional one $\Omega(a) = \int_{-S}^S dS^z f(S^z) e^{aS^z}$, arising from the ensemble-average definition of e^{aS^z} .

With these conditions we have obtained in [34] the physical solution of (25):

$$\Omega(a) = \frac{S/\Phi}{S/\Phi + a} \frac{\sinh(S/\Phi + a)}{\sinh(S/\Phi)}. \quad (26)$$

This key result (26) represents the classical analogue of the famous Callen formula for quantum spin- S models [35]. An alternative and very instructive method to obtain the solution (26) is presented in Appendix B.

Taking into account the exact relation (10), (26) gives the the remarkable expression:

$$m = S \left[\coth\left(\frac{S}{\Phi}\right) - \frac{\Phi}{S} \right] = SL\left(\frac{S}{\Phi}\right), \quad (27)$$

which is valid for any d , T , and h . Here, $L(x) = \coth x - 1/x$ is the well-known Langevin function and Φ is expressed by (23) in terms of the dispersion relation $\omega_{\mathbf{k}}$. If we use the TD, $\omega_{\mathbf{k}}$ is given by (17) which is in turn a function of m . Hence, (27) is a self-consistent equation for m and T . The longitudinal magnetic field h and the anisotropy enter into the problem via the function Φ .

Of course, in the spirit of the Callen method for the calculation of m , it is possible to introduce more elaborate decoupling procedures which preserve its validity.

For instance, we could adopt the Callen decoupling (CD) [35], with its classical variant [34],

$$\langle \langle S_h^z(\tau) S_k^+(\tau); e^{aS_j^z} S_j^- \rangle \rangle_\omega \simeq m \left[G_{kj}(\omega) - \frac{\langle S_h^- S_k^+ \rangle}{2S^2} G_{hj}(\omega) \right], \quad (28)$$

which takes into account the transverse correlations to the leading order and implies the dispersion relation:

$$\omega_{\mathbf{k}}^{(\text{CD})} = \omega_{\mathbf{k}}^{(\text{TD})} + \frac{m}{2S^2} \frac{1}{N} \sum_{\mathbf{k}'} [J^\perp(\mathbf{k}') - J^\parallel(\mathbf{k} - \mathbf{k}')] C(\mathbf{k}') \quad (29)$$

with

$$C(\mathbf{k}) = \sum_i e^{-i\mathbf{k} \cdot (\mathbf{r}_i - \mathbf{r}_j)} \langle S_i^+ S_j^- \rangle. \quad (30)$$

However, in the present case, the TD and the CD (28) provide essentially identical results close to the ($T = 0$)-critical point where m is near the full polarized-state value S .

Given the magnetization m , the thermodynamics of our CPFM will be derived using the general formalism of the classical two-time Green functions (see Appendix A and [33]).

3. Transverse Susceptibility and Critical Line

We have now all the elements to extract the physics of interest setting $a = 0$ in the previous results and solving the set of self-consistent equations:

$$\sigma = \coth\left(\frac{S}{\Phi}\right) - \frac{\Phi}{S} = L\left(\frac{S}{\Phi}\right), \quad (31)$$

$$\Phi = T \int_{\text{1BZ}} \frac{d^d k}{(2\pi)^d} \frac{1}{\omega_{\mathbf{k}}(\sigma)},$$

$$\omega_{\mathbf{k}}(\sigma) = \omega_0(\sigma) + \sigma S [J^\perp(0) - J^\perp(\mathbf{k})] \geq 0,$$

where $\omega_0(\sigma) = h + S\sigma [J^\parallel(0) - J^\perp(0)]$. Here we have conveniently introduced the reduced magnetization per spin $\sigma = m/S$, with $0 \leq \sigma \leq 1$. Equations (31) will give σ as a function of T and h and hence the GF (16), also at $a = 0$.

For our aim, the relevant quantity to be calculated is the transverse GF:

$$G_\perp(\mathbf{k}, \omega) = \langle \langle S_i^+(\tau); S_j^- \rangle \rangle_{\mathbf{k}, \omega} \equiv G_{\mathbf{k}}(\omega)|_{a=0}. \quad (32)$$

This allows to determine the dynamical transverse susceptibility for CPFM:

$$\chi_\perp(\mathbf{k}, \omega) = -G_\perp(\mathbf{k}, \omega) \equiv -G_{\mathbf{k}}(\omega)|_{a=0}, \quad (33)$$

where, at the TD level,

$$G_\perp(\mathbf{k}, \omega) = \frac{2S\sigma}{\omega - \omega_{\mathbf{k}}(\sigma)}. \quad (34)$$

In particular, the thermodynamic transverse susceptibility is given by

$$\chi_\perp(T, h) \equiv \chi_\perp(\mathbf{k} = \mathbf{0}, \omega = 0) = \frac{2S\sigma}{\omega_0(\sigma)} = \frac{2S\sigma(T, h)}{h + S\sigma[J^\parallel(0) - J^\perp(0)]}. \quad (35)$$

Using (35) it is also possible to obtain the transverse correlation length via the following relation [36]:

$$\xi_{\perp}^2 = -\frac{1}{2}\chi_{\perp}^{-1}(0,0) \left[\frac{d^2(\chi_{\perp}(\mathbf{k},0))}{d\mathbf{k}^2} \right]_{\mathbf{k}=0}, \quad (36)$$

where $\chi_{\perp}(\mathbf{k},0) = 2S\sigma/\omega_{\mathbf{k}}$. The longitudinal susceptibility will be simply given by $\chi_{\parallel}(T,h) = S(\partial\sigma(T,h)/\partial h)$. Of course, the stability condition $\chi_{\perp} \geq 0$ requires that, in (35), the inequality $\omega_0(\sigma) = h + S\sigma(T,h)[J^{\parallel}(0) - J^{\perp}(0)] \geq 0$ must be fulfilled. The equality is physically possible for $h > 0$ and $\sigma > 0$ only if $J^{\parallel}(0) < J^{\perp}(0)$, which is the regime characterizing the CPFM of interest to us.

Here in after we will focus on quantum-like criticality related to the field-driven easy-plane ordering whose key quantities are ω_0 and χ_{\perp} and the related ones as functions of T and h . However, in some relevant cases which may have physical interest, we will calculate also the longitudinal quantities $\sigma(T,h)$ and $\chi_{\parallel}(T,h)$. Other expressions can be obtained by means of known thermodynamic relations [33].

We start exploring the main features of the CPFM phase diagram in the (h,T) -plane. These results will be used as a basis for next developments. At zero temperature with $h \neq 0$, (31) provides the solution $\sigma = 1$ for the reduced magnetization, characterizing a fully polarized state. This implies that the dispersion relation is given by $\omega_{\mathbf{k}} = \omega_0 + S[J^{\perp}(0) - J^{\perp}(\mathbf{k})]$, where $\omega_0 = h - S[J^{\perp}(0) - J^{\parallel}(0)]$ is the frequency gap. Hence the transverse susceptibility, which has physical meaning for $h \geq S[J^{\perp}(0) - J^{\parallel}(0)] > 0$, becomes

$$\chi_{\perp} = \frac{2S}{h - S[J^{\perp}(0) - J^{\parallel}(0)]}. \quad (37)$$

Remarkably, (37) suggests that, despite the classical nature of our anisotropic spin model, there exists, as in the quantum case [26–28], a $(T = 0)$ -critical point at the value $h_c = S[J^{\perp}(0) - J^{\parallel}(0)]$ of the longitudinal magnetic field. Then, crossing this point, decreasing h to h_c , a field-induced second-order $(T = 0)$ -phase transition arises from a fully polarized state with $\sigma = 1$ to a transverse-ordered phase. However, the latter phase is unaccessible by the present analysis due to the absence in the Hamiltonian (1) of an in-plane symmetry breaking magnetic field.

From (37), with $\omega_0 = h - h_c \geq 0$, we have $\chi_{\perp} = 2S(h - h_c)^{-1}$ as $h \rightarrow h_c^+$, defining the mean field exponent $\gamma_h = 1$. (Through the paper we will use the indices h and T to denote the horizontal (isothermal) and the vertical trajectories approaching a critical point in the (h,T) -plane, resp.)

For arbitrary temperature we can write $\omega_0(\sigma) = h - \sigma h_c \geq 0$ (so that $\omega_{\mathbf{k}} = (h - \sigma h_c) + S\sigma[J^{\perp}(0) - J^{\perp}(\mathbf{k})]$). Hence the transverse susceptibility can be conveniently written as

$$\chi_{\perp}(T,h) = \frac{2S\sigma(T,h)}{h - \sigma(T,h)h_c}, \quad (38)$$

with $h \geq \sigma(T,h)h_c$ or $\sigma(T,h) \leq h/h_c$ for stability reasons. Equation (38) establishes an interesting relation between the transverse physics and the longitudinal one.

In the (h,T) -plane, where $\chi_{\perp} = \infty$ ($\omega_0(\sigma) = 0$), the general equation which determines the possible critical points is

$$h - \sigma(T,h)h_c = 0, \quad (39)$$

or, in view of the equation for σ ,

$$\frac{h}{h_c} = L\left(\frac{S}{\Phi_c}\right). \quad (40)$$

Here,

$$\Phi_c = \Phi\left(T,h;\sigma = \frac{h}{h_c}\right) = \frac{T}{J^{\perp}(0)S} \frac{h_c}{h} F_d(-1), \quad (41)$$

where $\omega_{\mathbf{k}}^{(c)} = \omega_{\mathbf{k}}(\sigma = h/h_c) = S(h/h_c)J^{\perp}(0)(1 - \gamma_{\mathbf{k}}^{\perp})$ at the critical points and

$$F_d(-1) = \int_{\text{1BZ}} \frac{d^d k}{(2\pi)^d} \frac{1}{(1 - \gamma_{\mathbf{k}}^{\perp})}, \quad (42)$$

with $\gamma_{\mathbf{k}}^{\perp} = J^{\perp}(\mathbf{k})/J^{\perp}(0) \leq 1$. More explicitly, (40) can be also written as

$$h + F_d(-1) \frac{T}{J^{\perp}(0)S^2} \frac{h_c^2}{h} - h_c \coth \left[\left(F_d(-1) \frac{T}{J^{\perp}(0)S^2} \frac{h_c}{h} \right)^{-1} \right] = 0. \quad (43)$$

The quantity $F_d(-1)$ is one of the so-called structure sums $F_d(n) = (1/N) \sum_{\mathbf{k}} (1 - \gamma_{\mathbf{k}}^{\perp})^n \stackrel{N \rightarrow \infty}{\rightarrow} \int_{\text{1BZ}} (d^d k / (2\pi)^d) (1 - \gamma_{\mathbf{k}}^{\perp})^n$ depending only on the lattice structure of the spin model. Accurate numerical values of $F_d(n)$ can be found in the literature for different d and lattice structures [34, 35, 37]. Previous results suggest that, while a $(T = 0)$ -CP with $\sigma = 1$ exists for any d , a critical line with $0 \leq \sigma \leq 1$, ending in such a point, may occur only for dimensionalities for which the integral (42) converges.

If we consider short-range interactions and an hypercubic lattice $J^{\alpha}(\mathbf{k}) = 2J^{\alpha} \sum_{\nu=1}^d \cos k_{\nu} \simeq J^{\alpha}(0) - J^{\alpha}k^2$ ($\alpha = \perp, \parallel$) as $k \rightarrow 0$ with $J^{\alpha}(0) = 2dJ^{\alpha}$, from (42) it immediately follows that for $d \leq 2$ only the $(T = 0)$ -CP exists, while for $d > 2$ a finite-temperature critical line, ending in the $(T = 0)$ -CP ($h_c, T = 0$), occurs consistently with the Mermin-Wagner theorem [38]. The same result has been obtained in the quantum case [28].

For $d > 2$, the critical line equation (42) (or (43)) can be solved numerically with respect to h or T providing the representation $h_c(T)$ or $T_c(h)$. Notice that, along the critical line, the reduced magnetization $\sigma(T, h_c(T)) = \sigma(T)$ is simply given by $\sigma(T) = h_c(T)/h_c$ when $h_c(T)$ is known. The critical line in the plane (h,T) for $d = 3$ is plotted in Figure 1.

Starting from (40) or (43) we can easily derive the analytical expression of the zero-field critical temperature T_c ($h = 0 \equiv T_c$ where $\sigma = 0$ irrespective of the specific structure of $\gamma_{\mathbf{k}}^{\perp}$ in (37) (as in the case of short-range interactions for which $\gamma_{\mathbf{k}}^{\perp} = J^{\perp}(\mathbf{k})/J^{\perp}(0) = (2J^{\perp}/J^{\perp}(0)) \sum_{\nu=1}^d \cos k_{\nu} = (1/d) \sum_{\nu=1}^d \cos k_{\nu}$).

From the expansion $\coth x \simeq 1/x + (1/3)x + O(x^3)$, and hence $L(x) = \coth x - 1/x \simeq x/3 + O(x^3)$, for $x = S/\Phi_c \ll 1$, (40) provides, for $\Phi_c \rightarrow \infty$ as $h \rightarrow 0$ at finite T (see (41)),

$$\frac{T_c}{J^{\perp}(0)S^2} = \frac{1}{3F_d(-1)}. \quad (44)$$

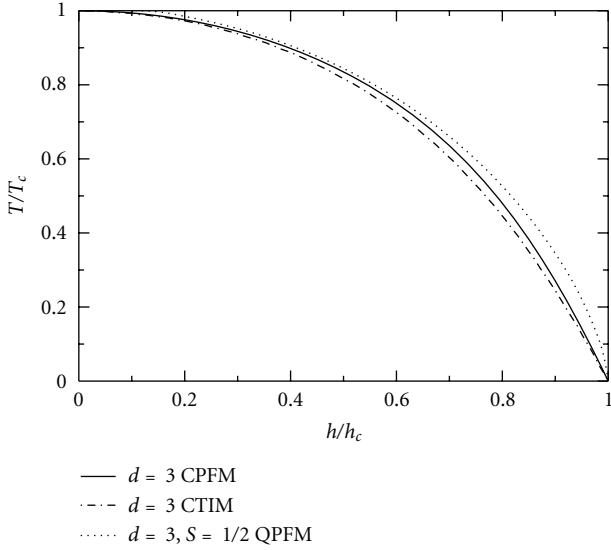


FIGURE 1: Critical line of the classical planar ferromagnet (CPFM) with short-range interactions on a three-dimensional cubic lattice (present work). Here T_c denotes the critical temperature at $h = 0$ and h_c the critical magnetic field at $T = 0$. A comparison is shown with the corresponding curves for the classical transverse Ising model (CTIM), obtained by RG calculations, and for the spin-1/2 quantum planar ferromagnet (QPFM). The critical line for the spin- S QPFM with long-range interactions in the classical limit $S \rightarrow \infty$ has been also obtained at the Tyablikov decoupling level, and, as expected, it coincides with the one calculated for the CPMF.

It is worth noting that for QPFM, within the TD it was found that [28] $T_c^{\text{QPFM}}/J^\perp(0)S(S+1) = 1/3F_d(-1)$, which reproduces, as expected, (44) in the classical limit for $S \rightarrow \infty$.

For short-range interactions and an hypercubic lattice, estimates for $d > 2$ can be obtained assuming $1 - \gamma_k^\perp \simeq k^2/2d$ as $k \rightarrow 0$.

Now we explore the behavior of the critical line in the low-temperature regime close to the $(T = 0)$ -CP where $\Phi_c \ll 1$. With $L(S/\Phi_c) \simeq 1 - \Phi_c/S + 2e^{-2S/\Phi_c}$, (40) becomes

$$\frac{h}{h_c} \simeq 1 - F_d(-1) \frac{T}{J^\perp(0)S^2} \frac{h_c}{h} + O\left(e^{-(2/F_d(-1))(J^\perp(0)S^2/T)}\right). \quad (45)$$

Solving the equation with respect to h or T , we find

$$h_c(T) \simeq h_c \left\{ 1 - F_d(-1) \frac{T}{J^\perp(0)S^2} + O\left(e^{-(2/F_d(-1))(J^\perp(0)S^2/T)}\right) \right\}, \quad T \rightarrow 0, \quad (46)$$

or

$$T_c(h) \simeq \frac{J^\perp S^2}{F_d(-1)h_c} (h_c - h) + O\left(\left(e^{-(2(F_d(-1))^2 h_c)/(h_c - h)}\right)\right), \quad h \rightarrow h_c^-. \quad (47)$$

Along this branch of the critical line we have also

$$\sigma(T) \simeq 1 - F_d(-1) \frac{T}{J^\perp(0)S^2} + O\left(e^{-(2/F_d(-1))(J^\perp(0)S^2/T)}\right). \quad (48)$$

From the low-temperature representations (46) and (47) for the critical line we can extract the shift exponent $\psi = 1$, which determines the shape of the phase boundary close to the $(T = 0)$ -CP. It has to be stressed that the value of ψ is independent of d , in contrast with the result ($\psi = d/2$) known for the QPFM [27, 28].

4. Low-Temperature Critical Properties

In this section we study the low-temperature properties and crossovers of our CPMF within the easy-plane-disordered phase, close to the field-induced $(T = 0)$ -CP where $\sigma \approx 1$, $h \simeq h_c$ (nearly polarized state), and $\omega_0(\sigma) = h - \sigma h_c$ is very small. Under these conditions, in (31) $\Phi(\sigma)/S \ll 1$; therefore, the equation for σ becomes

$$\sigma \simeq 1 - \frac{\Phi(\sigma)}{S} + 2e^{-(2S/\Phi(\sigma))}. \quad (49)$$

The quantity $\Phi(\sigma) \equiv \Phi(\omega_0)$ near criticality can be suitably estimated assuming, for the oscillation spectrum $\omega_{\mathbf{k}}$, the low- \mathbf{k} expression $\omega_{\mathbf{k}} \simeq \omega_0 + S\sigma J^\perp k^2$. This provides

$$\Phi \simeq \frac{d}{2} \left(\frac{T}{\omega_0} \right) \int_0^1 dx \frac{x^{d/2-1}}{1 + (\tau/\omega_0)}, \quad (50)$$

where $\tau \approx SJ^\perp \Lambda_{\text{IBZ}}^2 = (SJ^\perp(0)/2d)\Lambda_{\text{IBZ}}^2$ and Λ_{IBZ} is a natural wave-vector cut-off related to the first Brillouin zone and determined by $(1/N)\sum_{\mathbf{k}} = 1$ or (as $N \rightarrow \infty$) $\Lambda_{\text{IBZ}} = (d/K_d)^{1/d}$, with $K_d = 2^{1-d}\pi^{-d/2}/\Gamma(d/2)$.

As a consequence, to the leading order in Φ , the self-consistent equation for σ can be written as (except for exponentially small terms)

$$\sigma \simeq 1 - \frac{1}{S} \left(\frac{T}{\omega_0(\sigma)} \right) F\left(1, \frac{d}{2}; \frac{d}{2} + 1; -\frac{\tau}{\omega_0(\sigma)}\right), \quad (51)$$

where $F(\alpha, \beta; \gamma; z)$ is the hypergeometric function.

For our purposes, it is convenient to transform (51) for the longitudinal physics into a self-consistent equation for the oscillation gap ω_0 , strictly related to χ_\perp and hence to the transverse physics.

Since $\sigma = h/h_c - \omega_0/h_c$, straightforward calculations provide the following expression for (51) in terms of the natural variable ω_0/T :

$$\frac{\omega_0}{T} = \frac{g}{T} + \frac{h_c}{S\tau} \left(\frac{\tau}{\omega_0} \right) F\left(1, \frac{d}{2}; \frac{d}{2} + 1; -\frac{\tau}{\omega_0}\right). \quad (52)$$

Here $g = h - h_c$ and $\omega_0/T = 2S\sigma/T\chi_\perp \simeq 2S/T\chi_\perp \propto (T\chi_\perp)^{-1} \propto (T\xi_\perp^2)^{-1}$. Notice that since $\chi_\perp(\mathbf{k}, 0) \simeq 2S\sigma/[\omega_0 + \sigma SJ^\perp k^2]$, from (37), one gets $\xi_\perp \simeq J^\perp \chi_\perp^{1/2}$.

Of course, once ω_0 has been determined as a function of (T, h) , one can directly calculate $\chi_\perp(T, h)$ and, using the relation between ω_0 and σ , it is possible to determine $\sigma(T, h)$ and, therefore, the longitudinal physics near the polarized state in the low-temperature critical regime.

Adopting the asymptotic expansions of the hypergeometric function $F(1, \nu; \nu + 1; -(1/z))$ for $z \ll 1$,

$$F\left(1, \nu; \nu + 1; -\frac{1}{z}\right) \approx \begin{cases} \frac{\pi\nu}{\sin \pi\nu} z^\nu, & \nu < 1, \\ z \ln \frac{1}{z}, & \nu = 1, \\ \frac{\nu}{\nu - 1} z - \frac{\pi\nu}{|\sin \pi\nu|} z^\nu, & 1 < \nu < 2, \end{cases} \quad (53)$$

now, we can systematically explore the thermodynamics of the CPM close to the $(T = 0)$ -CP for different values of the dimensionality d of the system. Bearing this in mind, in strict analogy with the quantum case [28, 39], in the following subsections we will show the asymptotic solutions of (52) in the classical $\omega_0/T \ll 1$ ($\Leftrightarrow T\xi_\perp^2 \gg 1$ or $T\chi_\perp \gg 1$) and quantum-like ($\omega_0/T \gg 1 \Leftrightarrow T\xi_\perp^2 \ll 1$ or $T\chi_\perp \ll 1$) regimes, respectively, and the estimates of the related crossovers for different values of d .

4.1. $d < 2$. Replacing the expansions (53) in the self-consistent equation (52) for ω_0 , we get

$$\frac{\omega_0}{T} \simeq \frac{g}{T} + \frac{\pi d/2}{\sin(\pi d/2)} \frac{h_c}{S\tau} \left(\frac{T}{\tau}\right)^{(d-2)/2} \left(\frac{\omega_0}{T}\right)^{(d-2)/2}, \quad (54)$$

In the regime $\omega_0/T \ll 1$ ($T\xi_\perp^2 \gg 1$), classical regime in the quantum critical scenario near the isolated $(T = 0)$ -CP, (54) admits a solution only for $h < h_c$, which reads

$$\omega_0 \simeq \left[\frac{\pi d/2}{\sin(\pi d/2)} \frac{h_c}{S\tau^{d/2}} \right]^{2/(2-d)} \left(\frac{T}{h_c - h} \right)^{2/(2-d)}. \quad (55)$$

Under the consistency condition $T \ll (h_c - h)^{2/d}$. Then, for $h < h_c$ within the region $T \ll (h_c - h)^{2/d}$, in the (h, T) -plane, the transverse and longitudinal susceptibilities are given by

$$\begin{aligned} \chi_\perp &\simeq 2S \left[\frac{\pi d/2}{\sin(\pi d/2)} \frac{h_c}{S\tau^{d/2}} \right]^{-2/(2-d)} \left(\frac{T}{h_c - h} \right)^{-2/(2-d)}, \\ \chi_\parallel &\simeq \frac{S}{h_c} \left\{ 1 - \left[\frac{\pi d/2}{\sin(\pi d/2)} \frac{h_c}{S\tau^{d/2}} \right]^{2/(2-d)} \left(\frac{h_c}{h_c - h} \right)^{2/(2-d)} \right. \\ &\quad \left. \times \left(\frac{T}{h_c - h} \right)^{2/(2-d)} \right\}, \end{aligned} \quad (56)$$

where the reduced magnetization near polarization is immediately given as $\sigma(T, h) \simeq 1 - \omega_0/h_c$.

It is worth noting that, for fixed $h < h_c$ and $T \rightarrow 0$, the transverse susceptibility diverges with the critical exponent $\gamma_T = 2/(2 - d)$, while the longitudinal one remains finite.

In the regime $\omega_0/T \gg 1$ ($T\xi_\perp^2 \ll 1$), named here quantum-like regime again in analogy with the corresponding quantum scenario, different terms in (54) may enter in competition and different asymptotic behaviors are expected to occur close to the isolated $(T = 0)$ -CP. For $h < h_c$ in the region $(h_c - h)^{2/d} \ll T \ll (h_c - h)^{(4-d)/2}$, where $1 \ll \omega_0/T \ll g/T$, (54) provides, to the leading order, a solution

which is formally identical to (55) but now the condition $\omega_0/T \gg 1$ should hold. The same occurs for the thermodynamic quantities (56) and the related ones.

For $h = h_c$, decreasing T along a vertical trajectory which corresponds to the quantum critical one in the phase diagram of the QPFM [28], (54) yields, with $\omega_0(T, h_c) \equiv \omega_{0c}(T)$,

$$\omega_{0c}(T) \simeq \tau \left[\frac{\pi d/2}{\sin(\pi d/2)} \frac{h_c}{S\tau} \right]^{2/(4-d)} \left(\frac{T}{\tau} \right)^{2/(4-d)}. \quad (57)$$

Then, we get

$$\chi_\perp(T, h_c) \simeq 2 \left(\frac{S}{\tau} \right) \left[\frac{\pi d/2}{\sin(\pi d/2)} \frac{h_c}{S\tau} \right]^{-2/(4-d)} \left(\frac{T}{\tau} \right)^{-2/(4-d)}, \quad (58)$$

which defines the critical exponent $\gamma_T = 2/(4 - d)$, with $1/2 < \gamma_T < 1$. For the nearly polarized state (with $\sigma(T, h) \lesssim 1$), a simple algebra yields

$$\sigma(T, h_c) \simeq 1 - \frac{\tau}{h_c} \left[\frac{\pi d/2}{\sin(\pi d/2)} \frac{h_c}{\tau} \right]^{2/(4-d)} \left(\frac{T}{\tau} \right)^{2/(4-d)}, \quad (59)$$

which increases towards unity decreasing T according to the power-law $\sim T^{\gamma_T}$.

Now we consider the region which is more relevant from the experimental point of view, namely, the V-shaped region $T \gg |h - h_c|^{(4-d)/2}$, around the vertical trajectory $h = h_c$ (for both $h \lesssim h_c$ and $h \gtrsim h_c$). Under this condition, from (54) a straightforward algebra gives

$$\omega_0(T, h) \simeq \omega_{0c}(T) \left\{ 1 + \frac{2}{4 - d} \frac{h - h_c}{\omega_{0c}(T)} \right\}. \quad (60)$$

This expression suggests that, within the V-shaped region, the thermodynamics is essentially identical to the one along the trajectory $h = h_c$, except for a small correction $\sim |h - h_c|$.

Finally, for $h > h_c$ and sufficiently far from the quantum-like critical trajectory, within the region $T \ll (h - h_c)^{(4-d)/2}$, we have

$$\omega_0(T, h) \simeq (h - h_c) \left\{ 1 + \frac{\pi d/2}{\sin(\pi d/2)} \frac{h_c}{S\tau^{d/2}} \frac{T}{(h - h_c)^{(4-d)/2}} \right\}. \quad (61)$$

This implies that

$$\chi_\perp(T, h) \simeq 2S(h - h_c)^{-1} \left\{ 1 - \frac{\pi d/2}{\sin(\pi d/2)} \frac{h_c}{S\tau^{d/2}} \frac{T}{(h - h_c)^{(4-d)/2}} \right\}, \quad (62)$$

which differs from the MF result $\chi_\perp \simeq 2S(h - h_c)^{-1}$, found before at $T = 0$, for a small power-law correction in temperature, in contrast with the exponentially small correction which occurs in the quantum counterpart [28]. Besides, for the nearly polarized state, we obtain

$$\begin{aligned} \sigma(T, h) &\simeq 1 - \frac{\pi d/2}{\sin(\pi d/2)} \frac{1}{S\tau^{d/2}} \frac{T}{(h - h_c)^{(2-d)/2}}, \\ \chi_\parallel(T, h) &\simeq \frac{2 - d}{2} \frac{\pi d/2}{\sin(\pi d/2)} \frac{1}{\tau^{d/2}} \frac{T}{(h - h_c)^{(4-d)/2}}. \end{aligned} \quad (63)$$

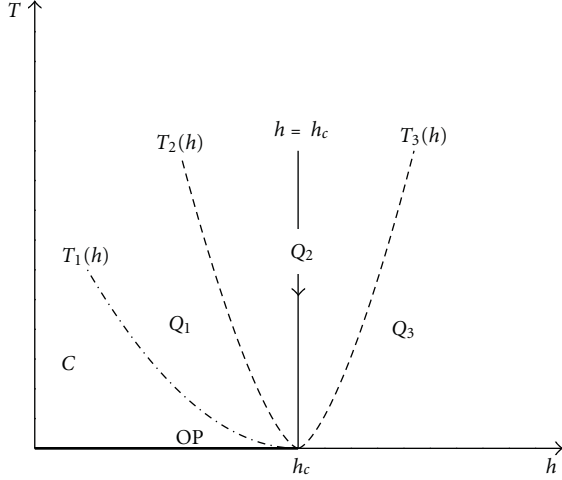


FIGURE 2: Qualitative phase diagram of CPMF with short-range interactions for $d < 2$, close to the zero-temperature critical point. The line $T_1(h)$ marks the crossover between the regimes $T\chi_\perp \propto T\xi_\perp^2 \gg 1$ (region C) and $T\chi_\perp \propto T\xi_\perp^2 \ll 1$ (region Q $\equiv (Q_1, Q_2, Q_3)$) increasing h . The lines $T_2(h)$ and $T_3(h)$, symmetric with respect to the vertical line $h = h_c$, signal the crossovers among the subregimes Q_1, Q_2 , and Q_3 . Finally, the heavy line OP represents the zero-temperature-ordered phase.

In summary, the previous results suggest, for $d < 2$, a very rich phase diagram around the isolated $(T = 0)$ -CP, qualitatively reported in Figure 2, where different low- T regimes and crossover lines are presented. It appears divided in two main regions (named in analogy with the quantum case [28]): C, where $\omega_0/T \ll 1$ ($T\chi_\perp \propto T\xi_\perp^2 \gg 1$), and Q $\equiv (Q_1, Q_2, Q_3)$, where $\omega_0/T \gg 1$ ($T\xi_\perp^2 \ll 1$). The line $T_1 \simeq (h_c - h)^{2/d}$ for $h < h_c$ signals the crossover between the regimes C and Q; the lines $T_2(h) \sim (h_c - h)^{(4-d)/2}$ and $T_3(h) \sim (h - h_c)^{(4-d)/2}$, symmetric to the vertical trajectory $h = h_c$, provide the signature of crossovers among three distinct subregimes Q_1, Q_2 , and Q_3 with different asymptotic behaviors of the thermodynamic quantities as functions of T and h . We stress that, within the V-shaped region Q_2 , delimited by the crossover lines $T_2(h)$ and $T_3(h)$, the T -dependent behaviors are essentially identical to those along the trajectory $h = h_c$ except for different a small power law corrections $\sim |h - h_c|$. Besides, in the regime Q_3 , decreasing T at fixed $h > h_c$, the transverse susceptibility deviates from the one at $T = 0$ except for a small power law correction as a function of T and $h - h_c$. The latter feature differs crucially from the QPFM scenario where the correction to the $(T = 0)$ -behavior of χ_\perp is an exponentially small function of T and $h - h_c$ [28, 39].

In any case, below two dimensions, the global phase diagram and the crossovers of the CPMF and QPFM are quite similar. This similarity represents a very interesting ingredient for experimental studies in the sense specified in the introductory section.

4.2. $d = 2$. For the two-dimensional CPMF, which also exhibits only a $(T = 0)$ -CP, a low-temperature scenario similar

to the one derived for $d < 2$ takes place. But now, logarithmic corrections to the leading power-law behavior arise. This peculiarity has been also found for the analogous quantum system [28].

With the expansion (53), close to the $(T = 0)$ -CP the general self-consistent equation (52) reduces to

$$\frac{\omega_0}{T} \simeq \frac{g}{T} + \frac{h_c}{S\tau} \ln\left(\frac{\tau}{\omega_0}\right). \quad (64)$$

First, we consider the regime $\omega_0/T \ll 1$. If $h \geq h_c$, no solution exists while, for $h < h_c$, (64) provides

$$\omega_0 \simeq \tau \exp\left(-\frac{S\tau}{h_c} \frac{h_c - h}{T}\right), \quad (65)$$

which has to be compared with the corresponding result achieved for the QPFM, $\omega_0 \simeq T e^{-(S\tau/h_c)((h_c - h)/T)}$ [28]. Then, for the transverse susceptibility we have the exponentially divergent behavior $\chi_\perp \simeq (2S/\tau) \exp[(S\tau/h_c)((h_c - h)/T)]$ as $T \rightarrow 0$ (corresponding to a critical exponent $\gamma_T = \infty$). For the nearly polarized state we immediately find $\sigma(T, h) \simeq 1 - (\tau/h_c) \exp[-(S\tau/h_c)((h_c - h)/T)]$ and $\chi_\parallel \simeq (S/h_c) \{1 - (S\tau/h_c)(\tau/T) e^{-(S\tau/h_c)((h_c - h)/T)}\}$.

Let us consider now the regime $\omega_0/T \gg 1$. For $h = h_c$, (64) gives

$$\omega_0(T, h_c) \simeq \frac{h_c T}{S\tau} \ln\left(\frac{S\tau^2}{h_c T}\right), \quad (66)$$

and $\chi_\perp(T, h_c)$ diverges as $T^{-1} \ln^{-1}(1/T)$ when $T \rightarrow 0$. Moreover, around this vertical line for $T \gg |h - h_c| \ln^{-1}(1/|h - h_c|)$, we find

$$\omega_0(T, h) \simeq \frac{h_c T}{S\tau} \ln\left(\frac{S\tau^2}{h_c T}\right) \left\{1 + \frac{S\tau}{h_c T} \frac{h - h_c}{\ln(S\tau^2/h_c T)}\right\}, \quad (67)$$

which signals the same leading behavior of $\omega_{0c}(T)$ and related thermodynamic quantities in the limit $T \rightarrow 0$, except for small corrections in $h - h_c$.

Finally, for $h > h_c$ and $T \ll (h - h_c) \ln^{-1}(1/(h - h_c))$, the frequency gap behaves as

$$\omega_0(T, h) \simeq (h - h_c) \left\{1 - \frac{T}{S\tau} \frac{h_c}{h - h_c} \ln\left(\frac{\tau}{Sh_c} \frac{h_c}{h - h_c}\right)\right\}, \quad (68)$$

providing a thermodynamics very similar to the one found for $d < 2$ except for logarithmic corrections in $h - h_c$ with respect to the $T = 0$ MF results.

In conclusion, for the two-dimensional CPMF close to $(T = 0)$ -CP, we have a qualitative phase diagram which is very similar to the one shown in Figure 2, presenting three regions C, Q_1 , and Q_2 . In this case the sector corresponding to previous Q_1 is absent and the V-shaped region is delimited by the lines $T_{1,2}(h) \sim |h - h_c| \ln^{-1}(1/|h - h_c|)$ which, in contrast to the ones shown in Figure 2, exhibit small logarithmic corrections.

4.3. $d > 2$. For such dimensionalities the CPMF exhibits a critical line ending in the $(T = 0)$ -CP. To explore the low-temperature critical properties it is convenient to rewrite (52)

in terms of $g(T) = h - h_c(T) \geq 0$ (for the disordered phase). We will focus on dimensionalities $2 < d < 4$ (the case $d \geq 4$ is rather trivial although completely consistent with the general theory of critical phenomena) for which, given the expansions (53), (52) assumes the form

$$\frac{\omega_0}{T} \simeq \frac{g(T)}{T} - \frac{\pi d/2}{|\sin(\pi d/2)|} \left(\frac{h_c}{S\tau} \right) \left(\frac{T}{\tau} \right)^{(d-2)/2} \left(\frac{\omega_0}{T} \right)^{(d-2)/2}, \quad (69)$$

where the right-hand side must be positive for stability reasons.

In this paper we will present only explicit results related to the transverse thermodynamics which plays a direct role for our purposes. However, the relevant longitudinal quantities near the polarized state may be simply obtained from the general relations $\sigma = h/h_c - \omega_0/h_c$ and $\chi_{\parallel} = S(\partial\sigma/\partial h)$.

We start calculating the asymptotic solutions of (69) where the critical region around the $(T = 0)$ -CP in the (h, T) -plane is approached in two ways: (i) along horizontal trajectories, as $h \rightarrow h_c^+(T)$ (with $h_c(T) \simeq h_c - (d/(d-2))(h_c/S)(T/\tau)$) at fixed T (isothermal trajectories); and (ii) along vertical trajectories, as $T \rightarrow T_c^+(h)$ (with $T_c(h) \simeq ((d-2)/d)(S\tau/h_c)(h_c - h)$) at fixed $h \leq h_c$ or $T \rightarrow 0$ for $h > h_c$.

We first consider the regime $\omega_0/T \ll 1$ ($T\xi_{\perp}^2 \gg 1$). The right-hand side of (69) suggests that two subregimes $\omega_0/T \ll \theta$ and $\omega_0/T \gg \theta$ should be investigated, with

$$\theta = \frac{\pi d/2}{|\sin(\pi d/2)|} \left(\frac{h_c}{S\tau} \right) \left(\frac{T}{\tau} \right)^{(d-2)/2} \left(\frac{\omega_0}{T} \right)^{(d-2)/2}, \quad (70)$$

where $\omega_0/T \simeq \theta$ signals the crossover between them. For isothermal trajectories, in the subregime $\omega_0/T \ll \theta$, one finds for ω_0 the asymptotic solution

$$\omega_0(T, h) \simeq \tau \left[\frac{\pi d/2}{|\sin(\pi d/2)|} \frac{h_c}{S} \right]^{-2/(d-2)} \left(\frac{T}{\tau} \right)^{-2/(d-2)} \times (h - h_c(T))^{(d-2)/2}, \quad (71)$$

which provides for transverse susceptibility $\chi_{\perp} \sim (h - h_c(T))^{-\gamma_h}$ the nontrivial non-MF critical exponent $\gamma_h = 2/(d-2)$. This spherical-model incorrect result is typical of the Tyablikov-like decoupling also for the quantum model at finite temperature [28, 39, 40].

When $\omega_0/T \gg \theta$, (69) yields simply $\omega_0 \simeq h - h_c(T)$ which corresponds to the MF exponent $\gamma_h = 1$. The crossover between the two previous regimes ($\omega_0/T \simeq \theta$) is indicated by the Ginzburg-like line for horizontal trajectories:

$$h_{Gi}(T) \simeq h_c(T) + h_c \left[\frac{1}{S} \frac{\pi d/2}{|\sin(\pi d/2)|} \right]^{2/(4-d)} \times \left(\frac{h_c}{\tau} \right)^{(d-2)/(4-d)} \left(\frac{T}{\tau} \right)^{2/(4-d)}. \quad (72)$$

Notice that $h_{Gi}(T) \rightarrow h_c$ as $T \rightarrow 0$; that is, the two lines $h_c(T)$ and $h_{Gi}(T)$ merge at the $(T = 0)$ -CP.

For vertical trajectories at fixed $h < h_c$ ($T_c(h) \neq 0$), setting $g(T) \simeq (d/(d-2))(h_c/S\tau)(T - T_c(h))$ in (69), we easily obtain the asymptotic solutions.

$$\omega_0 \simeq \begin{cases} \tau \left[\frac{d-2}{2} \frac{|\sin(\pi d/2)|}{\pi d/2} \right]^{2/(d-2)} \left(\frac{T - T_c(h)}{T_c(h)} \right)^{2/(d-2)}, & \frac{\omega_0}{T} \ll \theta, \\ \frac{d}{d-2} \frac{h_c}{S} \left(\frac{T_c(h)}{\tau} \right) \left(\frac{T - T_c(h)}{T_c(h)} \right), & \frac{\omega_0}{T} \gg \theta. \end{cases} \quad (73)$$

All the macroscopic quantities of interest can be now determined in the previous regimes for $T \rightarrow T_c^+(h)$. In particular, for χ_{\perp} , we find the critical exponents $\gamma_T \equiv \gamma_h = 2/(d-2)$ for $\omega_0/T \ll \theta$ and $\gamma_T = \gamma_h = 1$ for $\omega_0/T \gg \theta$. The crossover between these two asymptotic sub-regimes for $h < h_c$ occurs crossing the conventional Ginzburg-Landau line (with $\omega_0/T \simeq \theta$):

$$T_{Gi}(h) \simeq T_c(h) + \frac{d-2}{d} \tau \left[\frac{\pi d/2}{|\sin(\pi d/2)|} \right]^{2/(4-d)} \times \left(\frac{h_c}{S\tau} \right)^{(d-2)/(4-d)} \left(\frac{T_c(h)}{\tau} \right)^{2/(4-d)}. \quad (74)$$

Of course, also for vertical trajectories within the region of the (h, T) -plane between the critical and Ginzburg lines, with $h < h_c$, the TD quantitatively fails.

Let us consider now the behavior of ω_0 , and hence of χ_{\perp} , along the line $h = h_c$, decreasing T , which is of most experimental interest in view of the problematics discussed in Section 1.

Since in this case $T_c(h_c) = 0$, one can immediately see that, to leading order in T , a self-consistent solution of (69), under the condition $\omega_0/T = O(1)$, is given by

$$\omega_{0c}(T) \simeq \frac{d}{d-2} \left(\frac{h_c}{S} \right) \left(\frac{T}{\tau} \right). \quad (75)$$

This result is strictly connected with the shift exponent $\psi = 1$ and in drastic contrast with the corresponding relation obtained for the QPFM [27, 39], which, due to the presence of quantum fluctuations, shows that $\psi = d/2$. Equation (75) predicts that $\chi_{\perp} \sim T^{-1}$ as $T \rightarrow 0$ along the vertical line $h = h_c$, providing the exponent $\gamma_T = \psi = 1$, in contrast with the quantum result $\gamma_T = \psi = d/2$ for the QPFM [28, 39].

From (69), under condition $h - h_c \ll (d/(d-2))(h_c/S)(T/\tau)$, we get

$$\omega_0(T, h) \simeq \omega_{0c}(T) \left\{ 1 + \frac{d-2}{d} \left(\frac{S\tau}{h_c} \right) \frac{(h - h_c)}{T} \right\}. \quad (76)$$

This means that, within the V-shaped region delimited by the critical line for $h < h_c$ and the symmetric one $T^X(h) \simeq ((d-2)/d)(S\tau/h_c)(h - h_c)$ for $h > h_c$, the spectrum gap, the transverse susceptibility, and other macroscopic quantities behave essentially as along the line $h = h_c$, except for negligible corrections in $h - h_c$.

Increasing $h - h_c > 0$ and crossing the line $T^X(h)$, a crossover to the regime $\omega_0/T \gg 1$ ($T\xi_{\perp}^2 \ll 1$) takes place

a crossover between the classical thermally activated regime, with $\chi_\perp \sim T^{-1}$ ($\psi = 1$), and the quantum one, with $\chi_\perp \sim T^{-d/2}$ ($\psi = d/2$). This feature agrees with the RG predictions for the same quantum spin model near and below four dimensions [27].

It is worth mentioning that within our many-body framework one can also extract the basic quantum-like dynamics by variation of dimensionality. In particular, relevant information can be easily obtained from the scaling structure of the transverse dynamic susceptibility $\chi_\perp(\mathbf{k}, \omega) = -G_\perp(\mathbf{k}, \omega)$ for small values of the arguments. Indeed, from (33)-(34) close to the ($T = 0$)-CP we find

$$\chi_\perp(\mathbf{k}, \omega) \simeq 2S\xi_\perp^2 \left\{ \left[SJ^+(k\xi_\perp)^2 + 1 \right] - \omega\xi_\perp^2 \right\}^{-1}, \quad (79)$$

where $\xi_\perp \simeq (SJ^\perp)^{1/2}(h - h_c)^{-1/2} \propto \chi_\perp^{1/2}$ defines the transverse correlation length at zero temperature for $h \geq h_c$. Then, comparing (79) with the general dynamic scaling relation $\chi(\mathbf{k}, \omega) \simeq \xi^{2-\eta} W(k\xi, \omega\xi^z)$ we immediately get $\eta = 0$ and $z = 2$ for the Fisher η and dynamic z critical exponents, and $W(x, y) = 2S[SJ^+(x^2 + 1) - y]^{-1}$.

In conclusion, our results are in agreement with the statements made in [21] for the CTIM chain and in [28] for $d > 1$. Our analysis suggests that reliable measurements of the shift exponent (or related ones) close to the QCP of magnetic systems with PFM symmetry may provide a signature of the presence of quantum critical fluctuations. We believe also that this feature is rather general and not limited to TIM-like and PFM-like systems.

Appendices

A. An Outline of the Two-Time Green's Function Framework in Classical Statistical Mechanics

In this section, for utility of the reader, we briefly review the basic ingredients of the two-time retarded ($\nu = r$) and advanced ($\nu = a$) GF's framework in classical statistical mechanics in a form strictly parallel to the quantum counterpart [40–44]. For two arbitrary dynamical variables A and B , they are defined as [29]

$$G_{AB}^{(\nu)}(t, t') = \theta_\nu(t - t') \langle \{A(t), B(t')\} \rangle \equiv \langle \langle A(t); B(t') \rangle \rangle_\nu, \quad (\nu = r, a), \quad (A.1)$$

where $\theta_r(t - t') = \theta(t - t')$, $\theta_a(t - t') = -\theta(t' - t)$, $\theta(x)$ is the usual step function, $\langle \dots \rangle$ denotes an equilibrium ensemble average, and $\{A, B\}$ is the Poisson bracket of A and B .

In (A.1), the dynamical variables A and B depend on time via the conjugate canonical coordinates $(q(t), p(t)) \equiv (q_1(t), \dots, q_N(t); p_1(t), \dots, p_N(t))$, (N is the number of degrees of freedom of the classical system under study), $X(t) = e^{iLt}X(0)$ with $X = A, B, q, p$, $L = i\{\mathcal{H}, \dots\}$ is the Liouville operator, and \mathcal{H} is the Hamiltonian of the system and $X(0) \equiv X(q(0), p(0))$ at the initial time $t = 0$. Of course, the time evolution of the generic dynamical variable $X(t)$ is

governed by the well-known Liouville equation of motion (EM):

$$\frac{dX(t)}{dt} = \{X(t), \mathcal{H}\}. \quad (A.2)$$

One can easily prove that the two-time GFs (A.1) depends on times t, t' only through the difference $t - t'$, that is

$$G_{AB}^{(\nu)}(t - t') = \langle \langle A(t - t'); B \rangle \rangle_\nu = \langle \langle A; B(t' - t) \rangle \rangle_\nu, \quad (A.3)$$

and the two-time correlation function $F_{AB}(t, t') = F_{AB}(t - t') = \langle A(t)B(t') \rangle = \langle A(\tau)B \rangle = \langle AB(-\tau) \rangle$, with $\tau = t - t'$, is related to the classical GFs (A.3) by the following relation [29]:

$$G_{AB}^{(\nu)}(\tau) = \beta\theta_\nu(\tau) \frac{d}{d\tau} \langle A(\tau)B \rangle = \beta\theta_\nu(\tau) \langle \{A(\tau), \mathcal{H}\}B \rangle, \quad (A.4)$$

where $\beta = (K_B T)^{-1}$, T is the temperature, and K_B is the Boltzmann constant (we assume $K_B = 1$). In particular, we have also

$$\langle \{A(\tau), B\} \rangle = \beta \frac{d}{d\tau} \langle A(\tau)B \rangle = \beta \langle \{A(\tau), \mathcal{H}\}B \rangle. \quad (A.5)$$

For $G_{AB}^{(\nu)}(\tau)$ and $F_{AB}(\tau)$ one can introduce the Fourier transforms:

$$G_{AB}^{(\nu)}(\tau) = \int_{-\infty}^{+\infty} \frac{d\omega}{2\pi} G_{AB}^{(\nu)}(\omega) e^{-i\omega\tau}, \quad (A.6)$$

$$F_{AB}(\tau) = \int_{-\infty}^{+\infty} \frac{d\omega}{2\pi} F_{AB}(\omega) e^{-i\omega\tau},$$

where $G_{AB}^{(\nu)}(\omega) = \langle \langle A(\tau); B \rangle \rangle_{\nu, \omega}$ and $F_{AB}(\omega) = \langle A(\tau)B \rangle_\omega$ are called the ν -GF of A and B in the ω -representation and the classical spectral intensity of the time-dependent correlation function $F_{AB}(\tau)$, respectively, with $f(\omega) = \int_{-\infty}^{+\infty} d\tau e^{i\omega\tau} f(\tau)$. Then, using (A.4) and the integral representations

$$\theta(\tau) = i \int_{-\infty}^{+\infty} \frac{dx}{2\pi} \frac{e^{-ix\tau}}{x + i\varepsilon}, \quad \varepsilon \rightarrow 0^+; \quad (A.7)$$

$$\delta(x) = \int_{-\infty}^{+\infty} \frac{d\tau}{2\pi} e^{ix\tau},$$

for the step function and the Dirac δ -function, $G_{AB}^{(\nu)}(\omega)$ can be expressed in terms of the corresponding spectral intensity as

$$G_{AB}^{(\nu)}(\omega) = \int_{-\infty}^{+\infty} \frac{d\omega'}{2\pi} \frac{\beta\omega' F_{AB}(\omega')}{\omega - \omega' + (-1)^\nu i\varepsilon}, \quad \varepsilon \rightarrow 0^+, \quad (A.8)$$

where the symbol $(-1)^\nu$ means +1 if $\nu = r$ and -1 if $\nu = a$. It is interesting to compare (A.8) with the quantum corresponding expression for two operators A and B [40–44]:

$$G_{AB}^{(\nu)}(\omega) = \int_{-\infty}^{+\infty} \frac{d\omega'}{2\pi} \frac{(1 + \eta e^{-\beta\hbar\omega'}) F_{AB}(\omega')}{\omega - \omega' + (-1)^\nu i\varepsilon}, \quad \varepsilon \rightarrow 0^+, \quad (A.9)$$

where $\eta = -1$ and $\eta = +1$ by definition of quantum two-time GFs with commutator or anticommutator, respectively,

and \hbar is the reduced Planck constant. Notice that formally, as expected for internal consistency, the function $C(\omega) = \beta\omega$ or $Q_\eta(\omega) = (1 + \eta e^{-\beta\hbar\omega})/\hbar$ characterizes the classical or quantum nature of the problem under study, respectively.

In analogy with the quantum case [45–47], we now introduce the time-dependent classical spectral density (CSD) for A and B [31, 37, 48, 49]:

$$\Lambda_{AB}(\tau) = i\langle\{A(\tau), B\}\rangle, \quad (\text{A.10})$$

with the Fourier transform:

$$\Lambda_{AB}(\omega) = i\langle\{A(\tau), B\}\rangle_\omega = \int_{-\infty}^{+\infty} d\tau e^{i\omega\tau} \Lambda_{AB}(\tau) = \beta\omega F_{AB}(\omega). \quad (\text{A.11})$$

Hence, from (A.8), one immediately obtains the spectral representation:

$$G_{AB}^{(\nu)}(\omega) = \int_{-\infty}^{+\infty} \frac{d\omega'}{2\pi} \frac{\Lambda_{AB}(\omega')}{\omega - \omega' + (-1)^\nu i\varepsilon}, \quad \varepsilon \rightarrow 0^+, \quad (\text{A.12})$$

for the two-time GFs (A.1) in terms of the corresponding CSD $\Lambda_{AB}(\omega)$ in the ω -representation. Also the dynamical correlation function $\langle A(\tau)B \rangle$ can be easily expressed in terms of $\Lambda_{AB}(\omega)$. From (A.5), (A.10), and (A.11), we obtain indeed (classical spectral theorem)

$$\langle A(\tau)B \rangle \equiv \langle BA(\tau) \rangle = \int_{-\infty}^{+\infty} \frac{d\omega}{2\pi} \frac{\Lambda_{AB}(\omega)}{\beta\omega} e^{-i\omega\tau}. \quad (\text{A.13})$$

From (A.10)–(A.13) some formally exact results can be easily obtained. First, (A.10) and (A.11) yield

$$\int_{-\infty}^{+\infty} \frac{d\omega}{2\pi} \Lambda_{AB}(\omega) = i\langle\{A, B\}\rangle. \quad (\text{A.14})$$

Besides, from (A.13), it follows

$$\int_{-\infty}^{+\infty} \frac{d\omega}{2\pi} \frac{\Lambda_{AB}(\omega)}{\beta\omega} = \langle AB \rangle. \quad (\text{A.15})$$

The relations (A.14) and (A.15) constitute useful examples of the so-called *sum rules* of the CSD, $\Lambda_{AB}(\omega)$, which have great relevance for physical consistency of practical calculations and approximations. Combining now (A.12) and (A.14), one can easily obtain another general result which plays an important role for calculation of the GFs. As $\omega \rightarrow \infty$ we have indeed [33]

$$G_{AB}^{(\nu)}(\omega) = \begin{cases} \frac{i\langle\{A, B\}\rangle}{\omega} \sim \omega^{-1}, & \text{if } \langle\{A, B\}\rangle \neq 0, \\ \sim \omega^{-\alpha} \ (\alpha \geq 2), & \text{if } \langle\{A, B\}\rangle = 0, \end{cases} \quad (\text{A.16})$$

which provide a relevant boundary condition for the ν -GFs.

Let us come back now to the relations (A.12) for classical retarded and advanced GFs in the ω -representation. As in the quantum counterpart [40–42], one can prove that $G_{AB}^{(r)}(\omega)$ and $G_{AB}^{(a)}(\omega)$, analytically continued in the ω -complex plane, are analytical functions in the upper and lower half-plane, respectively. Then, combining these two analytical

functions, one can construct a single function $G_{AB}(\omega) = \int_{-\infty}^{+\infty} dt e^{i\omega t} G_{AB}(t)$ of complex ω such that

$$G_{AB}(\omega) = \begin{cases} G_{AB}^{(r)}(\omega), & \text{Im } \omega > 0, \\ G_{AB}^{(a)}(\omega), & \text{Im } \omega < 0. \end{cases} \quad (\text{A.17})$$

Hence, (A.12) provides for $G_{AB}(\omega)$ the spectral representation:

$$G_{AB}(\omega) = \int_{-\infty}^{+\infty} \frac{d\omega'}{2\pi} \frac{\Lambda_{AB}(\omega')}{\omega - \omega'}. \quad (\text{A.18})$$

This function is analytical in the whole complex ω -plane with a cut along the real axis where singularities for $G_{AB}(\omega)$ may occur. It is worth noting that, in terms of $\Lambda_{AB}(\omega)$, no formal differences exist for the spectral representations of $G_{AB}^{(\nu)}(\omega)$ and $G_{AB}(\omega)$ in the classical and quantum context. Hence, all the developments already known in the quantum framework remain formally valid for the classical one. In particular, one has the important exact relation

$$\Lambda_{AB}(\omega) = i[G_{AB}(\omega + i\varepsilon) - G_{AB}(\omega - i\varepsilon)], \quad (\text{A.19})$$

which expresses the CSD in terms of the related two-time GFs in the ω -representation. This allows us to state also that the cut for $G_{AB}(\omega)$ along the real axis in ω -complex plane is determined by (A.19) and its singularities are the points of the real axis where the condition $\Lambda_{AB}(\omega) \neq 0$ is satisfied. For the spectral intensity of classical systems, (A.11) and (A.19) yield

$$F_{AB}(\omega) = \langle A(\tau)B \rangle_\omega = i \frac{G_{AB}(\omega + i\varepsilon) - G_{AB}(\omega - i\varepsilon)}{\beta\omega}. \quad (\text{A.20})$$

Of course, other known quantum relations are formally valid for classical many-body theory. Besides, when $\Lambda_{AB}(\omega)$ is real, the classical Kramers-Kronig relations (classical dispersion relations) between the real and imaginary parts of $G_{AB}^{(\nu)}(\omega)$ are true:

$$\text{Re } G_{AB}^{(\nu)}(\omega) = \frac{(-1)^\nu}{\pi} \wp \int_{-\infty}^{+\infty} d\omega' \frac{\text{Im } G_{AB}^{(\nu)}(\omega')}{\omega' - \omega}, \quad (\text{A.21})$$

where the symbol \wp denotes the main part of the integral. We have also

$$\Lambda_{AB}(\omega) = -2(-i)^\nu \text{Im } G_{AB}^{(\nu)}(\omega), \quad (\text{A.22})$$

and, in particular,

$$\Lambda_{AB}(\omega) = -2 \text{Im } G_{AB}^{(r)}(\omega). \quad (\text{A.23})$$

Differentiating (A.3) with respect to $\tau = t - t'$, with EM (A.2) for dynamical variables and $d\theta_\nu(\tau)/d\tau = \delta(\tau)$, yields

$$\frac{d}{d\tau} \langle\langle A(\tau); B \rangle\rangle_\nu = \delta(\tau) \langle\{A, B\}\rangle + \langle\langle A(\tau), \mathcal{H} \rangle\rangle_\nu, \quad (\text{A.24})$$

which is the basic EM for the GF $\langle\langle A(\tau); B \rangle\rangle_\nu$. This, however, is not a closed differential equation since in the right-hand side of (A.24) a new higher-order ν -GF occurs involving Poisson brackets of a greater number of dynamical variables.

Then, one needs to consider a new EM for the two-time ν -GF $\langle\langle\{A(\tau), \mathcal{H}\}; B\rangle\rangle_\nu$. The τ -derivative of this function provides an additional equation, formally identical to (A.24) with $A(\tau)$ replaced by $\{A(\tau), \mathcal{H}\}$, the right-hand side of which contains the new ν -GF $\langle\langle\{A(\tau), \mathcal{H}\}, \mathcal{H}\}; B\rangle\rangle_\nu$. By iteration of this procedure, we obtain the infinite chain of coupled EMs for GFs of increasing order:

$$\begin{aligned} \frac{d}{d\tau} \langle\langle \mathcal{L}_{\mathcal{H}}^m A(\tau); B \rangle\rangle_\nu &= \delta(\tau) \langle\{ \mathcal{L}_{\mathcal{H}}^m A, B \}\rangle_\nu \\ &+ \langle\langle \mathcal{L}_{\mathcal{H}}^{m+1} A(\tau); B \rangle\rangle_\nu \quad (m=0, 1, 2, \dots). \end{aligned} \quad (\text{A.25})$$

Here $\mathcal{L}_{\mathcal{H}} = iL = \{\dots, \mathcal{H}\}$ and $\mathcal{L}_{\mathcal{H}}^m A$ means $\mathcal{L}_{\mathcal{H}}^0 A = A$, $\mathcal{L}_{\mathcal{H}}^1 A = \{A, \mathcal{H}\}$, $\mathcal{L}_{\mathcal{H}}^2 A = \{\{A, \mathcal{H}\}, \mathcal{H}\}$, and so on. Notice that the chain of EMs (A.25) is formally the same for different types of GFs and hence one can eliminate the index ν when the physical context is clear.

In the practical calculations it is more convenient to work in the ω -Fourier space. With $i \int_{-\infty}^{+\infty} d\tau e^{i\omega\tau} (df(\tau)/d\tau) = \omega f(\omega)$, the chain of equations, in the ω -representation, assumes the following form:

$$\begin{aligned} \omega \langle\langle \mathcal{L}_{\mathcal{H}}^m A(\tau); B \rangle\rangle_{\nu, \omega} &= i \langle\{ \mathcal{L}_{\mathcal{H}}^m A, B \}\rangle_{\nu, \omega} \\ &+ i \langle\langle \mathcal{L}_{\mathcal{H}}^{m+1} A(\tau); B \rangle\rangle_{\nu, \omega} \quad (m=0, 1, 2, \dots), \end{aligned} \quad (\text{A.26})$$

which has to be solved with appropriate boundary conditions (A.17). Since an exact solution is, of course, impossible, in practical calculations one must resort to decoupling procedures, and hence to approximate methods, to reduce the infinite chain of coupled equations to a finite closed one. Unfortunately, systematic and controllable decouplings are not easy to find and one must check for the reliability of a given approximation for each specific problem, by comparing the results with experiments, simulations, or other types of approaches.

B. Callen-Like Approach for Magnetization: A Classical Moment Problem

In this appendix we present an instructive method to solve the differential equation (25) for $\Omega(a)$ via a classical moment problem. The differential equation is the following:

$$\Omega''(a) + 2 \left(\frac{1}{\Phi} + a \right)^{-1} \Omega'(a) - S^2 \Omega(a) = 0, \quad (\text{B.1})$$

for which the initial condition $\Omega(0) = 1$ is valid by definition. This is, of course, insufficient to find the physical solution of (25) and one should add a supplementary condition to be searched properly. Unfortunately, there is not classical analogue of the operatorial identity $\Pi_{p=-S}^S (S^z - p) = 0$ which is the key ingredient of the Callen approach for the quantum HM [35]. In the following, we will show that, at our level of approximation, the additional condition

$$\Omega(a) = \int_{-S}^S dS^z f(S^z) e^{aS^z}, \quad (\text{B.2})$$

which follows formally from the definition of the canonical ensemble average of the dynamical variable e^{aS^z} , combined

with $\Omega(0) = 1$, allows to determine $\Omega(a)$ as a classical moment problem [50–53]. In view of the structure of the differential equation (25) for $\Omega(a)$, it is convenient to define

$$f(S^z) = g(S^z) e^{S^z/\Phi}, \quad (\text{B.3})$$

so that, we can write

$$\begin{aligned} \Omega(a) &= \int_{-S}^S dS^z g(S^z) e^{(1/\Phi+a)S^z} \\ &= S \int_{-1}^1 dx g(Sx) e^{S(1/\Phi+a)x}. \end{aligned} \quad (\text{B.4})$$

Replacing this expression and its derivatives in (25), we have for $g(S^z)$ the following:

$$\int_{-1}^1 dx (yx^2 + 2x - y) g(Sx) e^{yx} = 0, \quad (\text{B.5})$$

where $y = S(1/\Phi + a)$. Then, with $e^{yx} = \sum_{n=0}^{\infty} (y^n/n!) x^n$, (B.5) provides

$$\sum_{n=0}^{\infty} \frac{y^n}{n!} [y(I_{n+2} - I_n) + 2I_{n+1}] = 0, \quad (\text{B.6})$$

with

$$I_k = \int_{-1}^1 dx g(Sx) x^k. \quad (\text{B.7})$$

It is now simple to show that the moments (B.7) of $g(Sx) \equiv \mathcal{G}(x)$ are determined by the recursion relations:

$$I_1 = 0, \dots, I_{n+1} = \frac{n}{n+2} I_{n-1}, \quad n = 1, 2, \dots \quad (\text{B.8})$$

These provide

$$I_k = \begin{cases} \frac{I_0}{k+1}, & k = 2n, \\ 0, & k = 2n+1, \quad n \geq 0, \end{cases} \quad (\text{B.9})$$

where, at this stage, the moment I_0 is unknown. From (B.9), it is immediate to see that the solution of the moment problem for $g(Sx)$ is given by $g(Sx) = I_0/2$.

However, for the univocal determination of $\Omega(a)$ it is not necessary to have the explicit form of $g(Sx) = g(S^z)$ but rather its moments (B.9). From the integral representation (B.4), we have indeed

$$\begin{aligned} \Omega(a) &= S \sum_{k=0}^{\infty} \frac{y^k}{k!} \int_{-1}^1 dx g(Sx) x^k \\ &= \frac{SI_0}{y} \sum_{n=0}^{\infty} \frac{y^{2n+1}}{(2n+1)!} = \frac{SI_0}{y} \sinh y, \end{aligned} \quad (\text{B.10})$$

or, explicitly,

$$\Omega(a) = SI_0 \frac{\sinh[S(1/\Phi + a)]}{S(1/\Phi + a)}. \quad (\text{B.11})$$

Finally, the boundary condition $\Omega(0) = 1$ yields $I_0 = (1/\Phi)(1/\sinh(S/\Phi))$ so that we obtain the following solution:

$$\Omega(a) = \frac{1/\Phi}{1/\Phi + a} \frac{\sinh[S(1/\Phi + a)]}{\sinh(S/\Phi)}. \quad (\text{B.12})$$

This is the central result of this appendix which constitutes the classical analogue [34] of the quantum Callen formula [35]. It provides the required expression for m , which is valid for any d , T , and h .

Acknowledgments

A. Cavallo acknowledges the MIUR (Italian Ministry of Research) for financial support within the program “Incentivazione alla mobilità di studiosi stranieri e italiani residenti all'estero.”

References

- [1] S. Sachdev, *Quantum Phase Transitions*, Cambridge University Press, Cambridge, UK, 1999.
- [2] G. R. Stewart, “Non-fermi-liquid behavior in d- and f-electron metals,” *Reviews of Modern Physics*, vol. 73, no. 4, pp. 797–855, 2001.
- [3] H. V. Löhneysen, A. Rosch, M. Vojta, and P. Wölfle, “Fermi-liquid instabilities at magnetic quantum phase transitions,” *Reviews of Modern Physics*, vol. 79, no. 3, pp. 1015–1075, 2007.
- [4] P. Gegenwart, Q. Si, and F. Steglich, “Quantum criticality in heavy-fermion metals,” *Nature Physics*, vol. 4, no. 3, pp. 186–197, 2008.
- [5] S. Roy and A. M. S. Tremblay, “Scaling and commensurate-incommensurate crossover for the $d=2$, $z=2$ quantum critical point of itinerant antiferromagnets,” *Europhysics Letters*, vol. 84, no. 3, Article ID 37013, 6 pages, 2008.
- [6] J. Kroha, M. Klein, A. Nuber, F. Reinert, O. Stockert, and H. V. Löhneysen, “High-temperature signatures of quantum criticality in heavy-fermion systems,” *Journal of Physics Condensed Matter*, vol. 22, no. 16, Article ID 164203, 2010.
- [7] J. A. Hertz, “Quantum critical phenomena,” *Physical Review B*, vol. 14, no. 3, pp. 1165–1184, 1976.
- [8] A. J. Millis, “Effect of a nonzero temperature on quantum critical points in itinerant fermion systems,” *Physical Review B*, vol. 48, no. 10, pp. 7183–7196, 1993.
- [9] T. Moriya, *Spin Fluctuations in Itinerant Electron Magnetism*, Springer, Berlin, Germany, 1985.
- [10] T. Moriya and T. Takimoto, “Anomalous properties around magnetic instability in heavy electron systems,” *Journal of the Physical Society of Japan*, vol. 64, no. 3, pp. 960–969, 1995.
- [11] S. Takashima, M. Nohara, H. Ueda et al., “Robustness of non-Fermi-liquid behavior near the ferromagnetic critical point in clean ZrZn_2 ,” *Journal of the Physical Society of Japan*, vol. 76, no. 4, Article ID 043704, 2007.
- [12] R. A. Borzi, S. A. Grigera, J. Farrell et al., “Formation of a nematic fluid at high fields in $\text{Sr}_3\text{Ru}_2\text{O}_7$,” *Science*, vol. 315, no. 5809, pp. 214–217, 2007.
- [13] T. Misawa, Y. Yamaji, and M. Imada, “Spin fluctuation theory for quantum tricritical point arising in proximity to first-order phase transitions: applications to heavy-fermion systems, YbRh_2Si_2 , CeRu_2Si_2 , and $\beta\text{-YbAlB}_4$,” *Journal of the Physical Society of Japan*, vol. 78, no. 8, Article ID 084707, 2009.
- [14] P. Pfeuty, “The one-dimensional Ising model with a transverse field,” *Annals of Physics*, vol. 57, no. 1, pp. 79–90, 1970.
- [15] P. Pfeuty, “The quantum-classical crossover critical behaviour of the Ising model in a transverse field,” *Journal of Physics C*, vol. 9, no. 21, pp. 3993–4001, 1976.
- [16] B. K. Chakrabarty, A. Dutta, and P. Sen, *Quantum Ising Phases and Transitions in Transverse Ising Model*, Springer, Berlin, Germany, 1986.
- [17] A. K. Chandra, J. I. Inoue, and B. K. Chakrabarti, “Quantum phase transition in a disordered long-range transverse Ising antiferromagnet,” *Physical Review E*, vol. 81, no. 2, Article ID 021101, 2010.
- [18] A. Dutta, U. Divakaran, D. Sen, B. K. Chakrabarty, T. F. Rosenbaum, and G. Aeppli, “Transverse field spin models: from Statistical Physics to Quantum Information,” *Statistical Mechanics*. In press. <http://arxiv.org/abs/1012.0653>.
- [19] P. Prelovsek and I. Sega, “Numerical simulation of the classical Ising model in a transverse field statical properties,” *Journal of Physics C*, vol. 11, no. 10, pp. 2103–2113, 1978.
- [20] P. Prelovek and I. Sega, “Molecular-dynamics study of the classical Ising model in a transverse field,” *Physical Review B*, vol. 17, no. 11, pp. 4416–4425, 1978.
- [21] A. Cuccoli, A. Taiti, R. Vaia, and P. Verrucchi, “Extracting signatures of quantum criticality in the finite-temperature behavior of many-body systems,” *Physical Review B*, vol. 76, no. 6, Article ID 064405, 2007.
- [22] A. Caramico D’Auria, L. De Cesare, M. T. Mercaldo, and I. Rabuffo, “Quantum-like criticality for a classical transverse Ising model in $4-\epsilon$ dimensions,” *European Physical Journal B*, vol. 77, no. 3, pp. 419–427, 2010.
- [23] T. Matsubara and H. Matsuda, “A lattice model of liquid Helium, I,” *Progress of Theoretical Physics*, vol. 16, p. 569, 1956.
- [24] T. Matsubara and H. Matsuda, “A lattice model of liquid helium, II,” *Progress of Theoretical Physics*, vol. 17, p. 19, 1957.
- [25] M. E. Fisher, “The theory of equilibrium critical phenomena,” *Reports on Progress in Physics*, vol. 30, no. 2, article 306, pp. 615–730, 1967.
- [26] D. K. Dacol, “Low-temperature critical phenomena in the spin-1/2 planar ferromagnet,” *Journal of Low Temperature Physics*, vol. 41, no. 3–4, pp. 349–373, 1980.
- [27] M. T. Mercaldo, A. Caramico D’Auria, L. De Cesare, and I. Rabuffo, “Low-temperature critical properties and crossovers of a spin-1/2 planar ferromagnet in $4-\epsilon$ dimensions,” *Physical Review B*, vol. 77, no. 18, Article ID 184424, 2008.
- [28] L. S. Campana, L. De Cesare, U. Esposito, M. T. Mercaldo, and I. Rabuffo, “Field-induced quantum critical point in planar Heisenberg ferromagnets with long-range interactions: two-time Green’s function framework,” *Physical Review B*, vol. 82, no. 2, Article ID 024409, 2010.
- [29] N. N. Bogoliubov and B. I. Sadovnikov, “Green’s functions and distribution functions in the statistical mechanics of classical systems,” *Journal of Experimental and Theoretical Physics*, vol. 16, p. 482, 1963.
- [30] L. S. Campana, A. C. D’Auria, M. D’Ambrosio, U. Esposito, L. De Cesare, and G. Kamieniarz, “Spectral-density method for classical systems: heisenberg ferromagnet,” *Physical Review B*, vol. 30, no. 5, pp. 2769–2775, 1984.
- [31] A. Cavallo, F. Cosenza, and L. De Cesare, “Classical Heisenberg ferromagnetic chain with long-range interactions: a spectral density approach,” *Physical Review B*, vol. 66, no. 17, Article ID 174439, 2002.
- [32] A. Cavallo, F. Cosenza, and L. De Cesare, “Thermodynamic properties of a classical d-dimensional spin-S Heisenberg ferromagnet with long-range interactions via the spectral density method,” *Physica A*, vol. 332, no. 1–4, pp. 301–317, 2004.

- [33] A. Cavallo, F. Cosenza, and L. De Cesare, "The classical spectral density method at work: the heisenberg ferromagnet," in *New Developments in Ferromagnetism Research*, V. N. Murray, Ed., Nova Science Publishers, New York, NY, USA, 2006.
- [34] L. S. Campana, A. Cavallo, L. De Cesare, U. Esposito, and A. Naddeo, "Callen-like method for the classical Heisenberg ferromagnet," *Physica A*, vol. 391, no. 4, pp. 1087–1096, 2012.
- [35] H. B. Callen, "Green function theory of ferromagnetism," *Physical Review*, vol. 130, no. 3, pp. 890–898, 1963.
- [36] S. K. Ma, *Modern Theory of Critical Phenomena*, Benjamin, London, UK, 1976.
- [37] L. S. Campana, A. C. D'Auria, M. D'Ambrosio, U. Esposito, L. De Cesare, and G. Kamieniarz, "Spectral-density method for classical systems: heisenberg ferromagnet," *Physical Review B*, vol. 30, no. 5, pp. 2769–2775, 1984.
- [38] N. D. Mermin and H. Wagner, "Absence of ferromagnetism or antiferromagnetism in one- or two-dimensional isotropic Heisenberg models," *Physical Review Letters*, vol. 17, no. 22, pp. 1133–1136, 1966.
- [39] L. S. Campana, L. De Cesare, U. Esposito, and M. T. Mercaldo, "Two-time Green's function treatment of field-induced quantum criticality of a d-dimensional easy-plane ferromagnet with longitudinal uniform interactions," *Physica A*, vol. 388, no. 8, pp. 1446–1462, 2009.
- [40] S. V. Tyablikov, *Methods in the Quantum Theory of Magnetism*, Plenum Press, New York, NY, USA, 1967.
- [41] D. N. Zubarev, "2-Time green functions in statistical physics," *Uspekhi Fizicheskikh Nauk*, vol. 71, no. 1, pp. 71–116, 1960.
- [42] D. N. Zubarev, "Double-time green functions in statistical physics," *Soviet Physics Uspekhi*, vol. 3, no. 3, p. 320, 1960.
- [43] N. Majlis, *The Quantum Theory of Magnetism*, World Scientific, Singapore, 2000.
- [44] D. N. Zubarev, *Nonequilibrium Statistical Thermodynamics*, Consultants Bureau, New York, NY, USA, 1974.
- [45] O. K. Kalashnikov and E. S. Fradkin, *Zhurnal Eksperimentalnoi i Teoreticheskoi Fiziki*, vol. 55, p. 607, 1968.
- [46] O. K. Kalashnikov and E. S. Fradkin, "The method of spectral densities in quantum statistical mechanics," *Journal of Experimental and Theoretical Physics*, vol. 28, p. 317, 1969.
- [47] O. K. Kalashnikov and E. S. Fradkin, "Spectral density method applied to systems showing phase transitions," *Physica Status Solidi B*, vol. 59, no. 1, pp. 9–46, 1973.
- [48] A. C. D'Auria, L. De Cesare, and U. Esposito, "Spectral density method in classical statistical mechanics," *Physics Letters A*, vol. 85, no. 4, pp. 197–200, 1981.
- [49] L. S. Campana, A. C. D'Auria, M. D'Ambrosio, L. De Cesare, and U. Esposito, "A proposal to include damping effects in the spectral density approach," *Journal of Physics C*, vol. 16, no. 17, pp. L549–L553, 1983.
- [50] N. I. Akhiezer, *The Classical Moment Problem and Some Related Questions in Analysis*, Hafner Publishing, New York, NY, USA, 1965.
- [51] T. M. Pham Ngoc, "A statistical minimax approach to the Hausdorff moment problem," *Inverse Problems*, vol. 24, no. 4, Article ID 045018, 1996.
- [52] G. D. Lin, "On the moment problems," *Statistics & Probability Letters*, vol. 35, no. 1, pp. 85–90, 1997.
- [53] R. Mnatsakanov, "Hausdorff moment problem: reconstruction of distributions," *Statistics & Probability Letters*, vol. 78, no. 12, pp. 1612–1618, 2008.

Research Article

Spin-Wave Band Structure in 2D Magnonic Crystals with Elliptically Shaped Scattering Centres

Sławomir Mamica, Maciej Krawczyk, and Jarosław Wojciech Kłos

Nanomaterials Physics Division, Faculty of Physics, Adam Mickiewicz University, 61-614 Poznań, Poland

Correspondence should be addressed to Sławomir Mamica, mamica@amu.edu.pl

Received 2 February 2012; Accepted 2 March 2012

Academic Editor: Roberto Zivieri

Copyright © 2012 Sławomir Mamica et al. This is an open access article distributed under the Creative Commons Attribution License, which permits unrestricted use, distribution, and reproduction in any medium, provided the original work is properly cited.

Spin waves in 2D periodic magnetic nanocomposites are studied by means of the plane wave method. The effect of the ellipticity and in-plane rotation of the scattering centers on the band structure is investigated, to indicate new possibilities of fine tuning of spin-wave filter passbands.

1. Introduction

Magnetic composites with a structure modulated periodically on the nanoscale are the subject of a very intensive research activity, and the interest in their properties is increasing [1–7]. By analogy to photonic crystals (PCs), they are referred to as magnonic crystals (MCs) [8], since the role of information carriers in these materials is played by magnons, or spin-wave quanta. Magnonic crystals have properties that cannot be reduced to those of their constituent materials, as manifested, among others, by the band structure of their spin-wave spectrum. The periodic structure given to a magnetic composite strictly determines the possible occurrence of magnonic gaps, or energy ranges forbidden to propagating spin waves [9–11]. The anticipated full control over the spin waves propagating in MCs, similar to that of the electromagnetic waves in PCs, combined with a long-term stability of the programmable magnetic state makes MCs excellent for both research and application purposes [12, 13]. Moreover, the wavelength of spin waves is much shorter than that of electromagnetic waves of the same frequency. This provides additional possibilities in the miniaturization of MC-based devices [14–16]. For a broad survey of the current state of both the experimental and theoretical research in MCs and their potential applications, please refer to review papers [17, 18].

The most frequently mentioned of the numerous potential applications of MCs include microwave resonators,

magnonic waveguides, spin-wave emitters, and filters [19]. These potential applications, along with the possibility of modeling the energy spectrum of spin-wave excitations propagating in MCs, are the very reason of the intensification of the research on new magnonic materials with so far unknown properties and functionalities [14, 16]. In particular, two-dimensional (2D) MCs with band gaps in the spin-wave spectrum have potential applications in diverse magnonic devices, such as spin-wave filters or switches, or current-controlled delay lines [20]. For example, the latest results of micromagnetic simulations [21] indicate the occurrence of wide magnonic gaps, implying a possible application in spin-wave filters, in 2D Fe/YIG MCs, two-component magnetic composites with iron scattering centers embedded in a matrix of yttrium iron garnet. A particular role in the modeling of magnonic gaps is played by the deformation of the scattering centers in the plane of spin-wave propagation [22].

In this study we examine the possibilities of modeling the spin-wave spectrum of 2D MCs that could be used for fine tuning of spin-wave filter passbands [23]. We present the results of calculations of the magnonic band structure of a Co/Fe composite with scattering centers in the shape of elliptic cylinders. We find that for different filling fraction values there are specific in-plane rotation angles for which modifying the rod ellipticity can alter the position of the allowed band without changing its width or

cause a substantial shrinking of two adjacent bands without changing the width of the gap between them.

2. The Model

Figure 1(a) depicts schematically a section of the system under consideration in the plane perpendicular to the rod axis (the x - y plane), which is the plane of spin-wave propagation. The system includes cobalt rods (scattering centers), which are assumed to be parallel to each other and have an infinite length. The rods are arranged in sites of a 2D square lattice and embedded in an iron matrix. The system is infinite in the plane of periodicity. The filling fraction ff , describing the proportion of the rod material in the whole volume of the system, in the case of elliptic cylinders is given as $ff = \pi R_a R_b / a^2$, where R_a and R_b are the semiaxes of the rod cross section, and a is the lattice constant. Let us define the ellipticity RR of the rods as the semiaxis ratio: $RR = R_a / R_b$. The angle α between the major semiaxis R_a and the x -axis of the crystallographic system is the angle of rotation of the rods (in the plane of periodicity). Applied to the system, an external magnetic field perpendicular to the plane of periodicity is assumed to be strong enough to enforce a uniform magnetization throughout the system.

We shall consider in-plane propagation of spin waves, that is, their propagation in the plane of periodicity, in 2D MCs as described above. Thus, the wave vectors to be considered are limited to the Brillouin zone of the 2D lattice. Figure 1(b) shows the high-symmetry line in such a 2D Brillouin zone. In the case of square lattice the line starts at the zone center (point Γ) to pass through X and M and return to Γ (segments C , D , and E in Figure 1(b)). The introduction of rods with elliptical cross section breaks the symmetry of the square lattice. If the semiaxes of the ellipse follow the axes of the 2D crystallographic system, the structure has the symmetry of a rectangular lattice. Points X and X' are not equivalent anymore, and the high-symmetry line in this case leads from M to X' , Γ , X , and back to M (segments A , B , C , and D). For an ellipse rotated by 45° points, X and X' are equivalent symmetry points, whereas M and M' are not. Thus, the high-symmetry line leads from Γ to X , M , Γ , M' , and X (segments C , D , E , F , G). In the general case, that is, for any angle of rotation of the ellipse, the full line shown in Figure 1(b) must be considered.

Our theoretical approach is based on a set of equations including the linearized Landau-Lifshitz equation and Maxwell's magnetostatic equations [24]. When the applied magnetic field is parallel to the rods, the internal static magnetic field is uniform, which allows us to only take into account the exchange and dynamic dipolar interactions. The ferromagnetic materials of the rods and the matrix are characterized by two quantities: the spontaneous magnetization M_s and the exchange stiffness constant A . For the materials considered in this study the specific values of these two magnetic parameters are for iron $M_s = 1.752e6$ A/m and $A = 2.1e-11$ J/m, and for cobalt $M_s = 1.390e6$ A/m and $A = 2.8e-11$ J/m [25]. Crucial for the magnonic nature of the structure under consideration is the assumption that these two material parameters are periodic functions of

position, with the same periodicity as the 2D lattice on which the magnonic crystal is built. With this assumption our equations can be solved by the plane wave method. The main point of this method is the Fourier expansion of the material parameters. Bloch theorem is applied to the dynamic functions, such as the demagnetizing field potential and the dynamic component of magnetization. Thus, the equations are transformed to the reciprocal space, where their solution is equivalent to the diagonalization of a $2N \times 2N$ matrix, N being the number of plane waves used in the Fourier expansion (for more details, see [24] and references therein).

3. The Role of Magnetostatic Interactions

Figure 2 shows examples of the so-called magnonic spectra, represented by the spin-wave spectra of 2D Co/Fe magnetic composites, calculated along the high-symmetry line in the 2D Brillouin zone. The spectra shown in Figures 2(a) and 2(b) have been obtained for lattice constants $a = 50$ nm and $a = 100$ nm, respectively. A circular cross section of the rods ($RR = 1$) and a filling fraction $ff = 0.5$ are assumed in both cases. For small lattice constants the exchange interactions play a dominant role; however, as the lattice constant grows, their importance diminishes to the advantage of the magnetostatic interactions [26, 27]. As a result, the spin-wave frequency range lowers; for the lattice constant of 50 nm the frequency of the ten lowest modes is below 80 GHz (Figure 2(a)), but only ranges from 10 GHz to 35 GHz for $a = 100$ nm (Figure 2(b)). The flattening of successive bands results in the opening of a magnonic gap: for $a = 50$ nm all the bands overlap, while for $a = 100$ nm a gap occurs between the lowest band and the rest of the spectrum.

4. The Ellipticity and Rotation of the Rods

Figure 3 presents the effect of the cross-sectional ellipticity of the scattering centers and their rotation in the plane of spin-wave propagation on the magnonic spectrum in a Co/Fe composite with a lattice constant of 300 nm and a filling fraction of 0.3. For unrotated rods (Figure 3(a)) the maximum ellipticity (corresponding to touching rods) is $RR = 2.6$, which means the major and minor semiaxes R_a and R_b can range from 92.7 nm up to 149.8 nm and down to 57.4 nm, respectively. In the whole range of rod ellipticity the bottom of the lowest band is nearly constant, remaining between 10.84 GHz and 10.89 GHz. Also the top of the second band varies very slightly, only ranging from 12.04 GHz to 12.15 GHz. However, the width of both bands grows rapidly, as the top of the first band and the bottom of the second one converge. Consequently, the gap between the bands shrinks to vanish completely for $RR = 2.1$ ($R_a = 134.3$ nm, $R_b = 64.0$ nm). The two bands merge to form a single wide band, separated from the rest of the spectrum by a third gap, the width of which varies from 1.26 GHz for right circular cylinders ($RR = 1.0$) to 0.79 GHz for $RR = 2.1$ (the closing of the second gap) to 0.37 GHz for $RR = 2.6$ (the

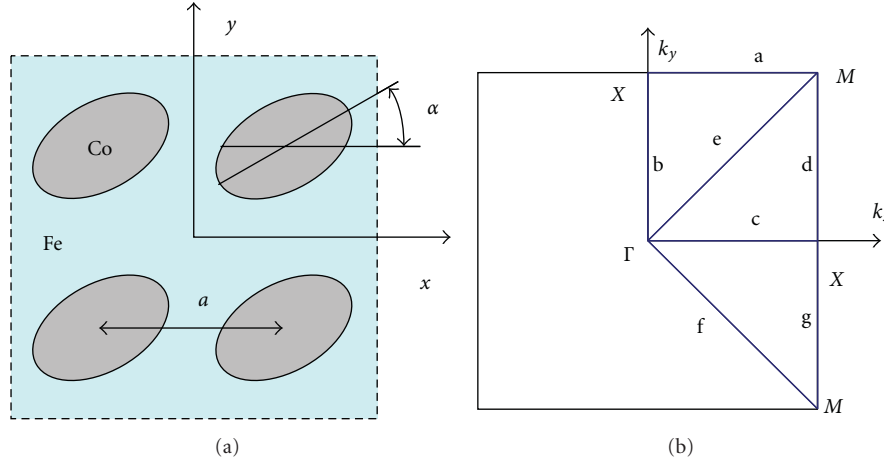


FIGURE 1: (a) Schematic view of the 2D MC under consideration, section in the plane of periodicity. (b) High-symmetry line over the 2D Brillouin zone for ellipses arranged in a square lattice.

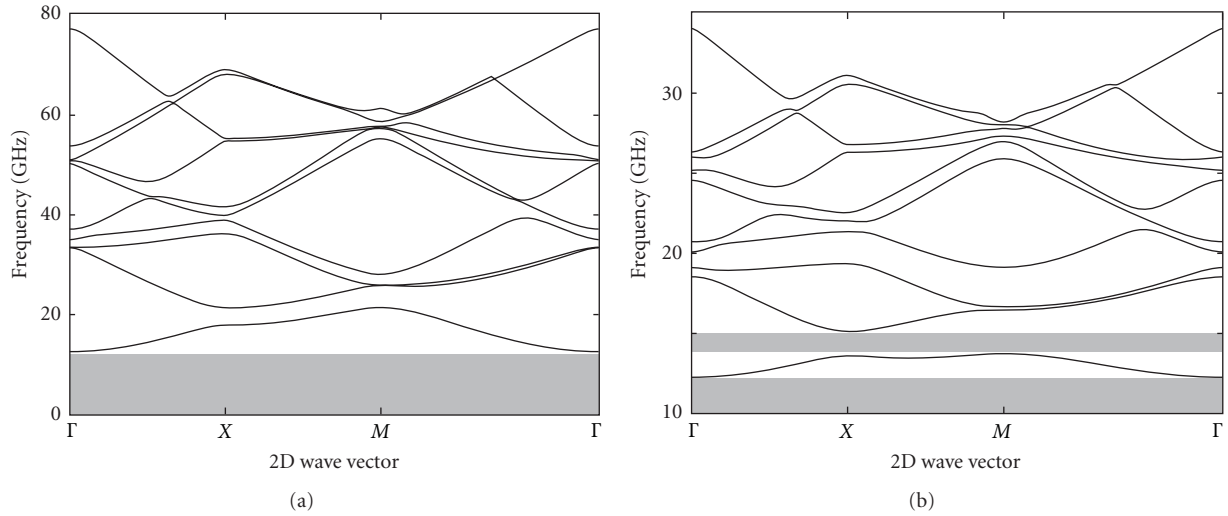


FIGURE 2: Ten lowest bands in the spin-wave spectrum of a 2D Co/Fe composite with lattice constant (a) 50 nm and (b) 100 nm, calculated along the high-symmetry line in the 2D Brillouin zone (cf. Figure 1(b)). Circular cross section of the rods ($RR = 1$) and filling fraction $ff = 0.5$ are assumed in both cases. Shaded areas represent magnonic gaps. Note the plots differ in frequency range: 0 GHz to 80 GHz in (a), and 10 GHz to 35 GHz in (b).

maximum ellipticity). Figure 3(b) shows the band and gap widths plotted versus the rod ellipticity.

Also for rods rotated by 45° (Figure 3(c)) the second gap is seen to shrink, though not as rapidly as in the case of unrotated rods. The gap closes for $RR = 3.45$, which corresponds to $R_a = 212.0$ nm and $R_b = 40.5$ nm. A significant difference with respect to the composite with unrotated rods is seen in the behavior of the second band, which moves down the frequency scale with nearly constant width as RR grows from 1.0 to 2.8 (cf. Figure 3(d)).

In a Co/Fe composite with a filling fraction of 0.5 and rods unrotated in the plane of periodicity (the major semiaxis following the x direction), the rod ellipticity can range from 1.0 (circular cross section) to 1.57, which for the assumed lattice constant $a = 300$ nm corresponds to the major semiaxis ranging from 119.7 nm up to 150.0 nm, and

the minor semiaxis from 119.7 nm down to 95.5 nm. As the ellipticity of the cylinders grows, the gaps are seen to shrink and the bands to widen (Figure 4(a)). Although the bottom of the lowest band at first moves towards higher frequencies, the change is slight to compensate the concurrent rising of the top. In the second band the top is seen to descend slightly, while the bottom moves much faster in the same direction. As a consequence, the second gap, between the first and second bands, shrinks rapidly with growing ellipticity to vanish completely for $RR = 1.2$ ($R_a = 131.1$ nm, $R_b = 109.3$ nm). The first and second bands merge to form one relatively wide band (of width ranging from 1.17 GHz for $RR = 1.2$ to 1.32 GHz for $RR = 1.57$), separated from the rest of the spectrum by a third gap, which has a maximum width of 0.65 GHz for $RR = 1.2$, and a minimum width of 0.25 GHz for $RR = 1.57$ (cf. Figure 4(b)).

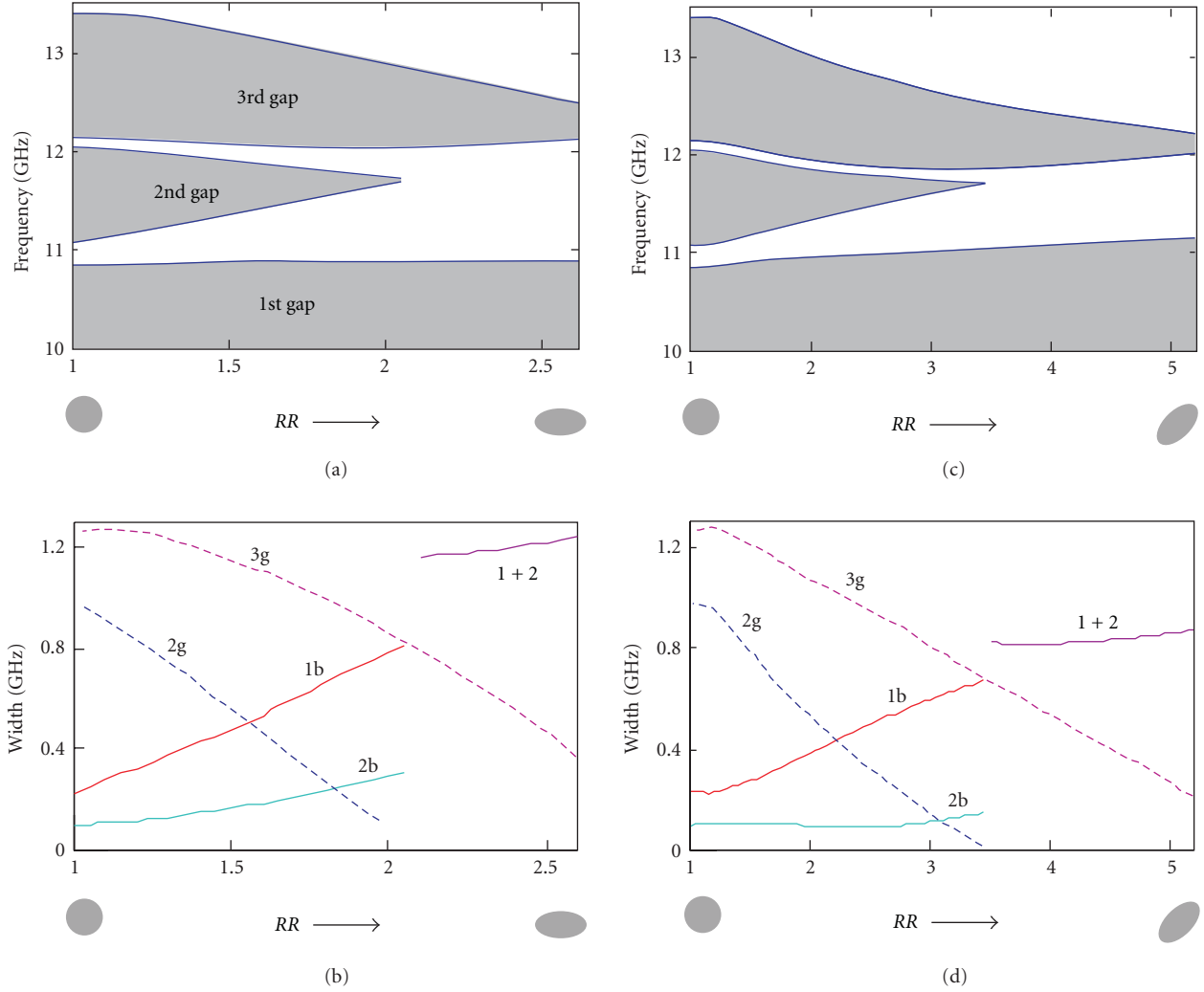


FIGURE 3: (a), (c) Three lowest magnonic gaps (shaded) versus rod ellipticity RR for 2D Co/Fe MCs with lattice constant 300 nm, filling fraction 0.3, and two angles of in-plane rotation of the rods: (a) $\alpha = 0^\circ$ and (c) $\alpha = 45^\circ$. (b), (d) The width of the lowest gaps and bands versus RR in (a) and (c), respectively. The width of the second (2g) and third (3g) gaps is plotted with dashed line. Solid line represents the width of the lowest bands: the first (1b), the second (2b), and, in the range of RR values in which the gap between them does not occur, the band resulting from their merging (1 + 2).

A completely different behavior of the spin-wave spectrum is seen for the same filling fraction ($ff = 0.5$), but with rods rotated by 45° in the plane of periodicity (Figure 4(c)). Two ranges of RR can be distinguished in this case. In the first range, from 1.0 to 2.0 (the major semiaxis growing from 0.52 GHz to 0.28 GHz, and the minor semiaxis shrinking from 119.7 nm to 84.6 nm), the width of both lowest bands decreases substantially, the first one shrinking from 0.52 GHz to 0.28 GHz, and the second from 0.34 GHz to 0.22 GHz (Figure 4(d)). At the same time, the midlevels of both bands move, from 11.0 GHz to 11.1 GHz in the case of the first band, and from 11.7 GHz to 11.6 GHz for the second. Interestingly, in this range of RR the second gap remains nearly unchanged, its width only ranging from 0.29 GHz to 0.30 GHz. In the other part of the RR dependence the spectrum behaves as in the cases considered previously: the bands widen and the gaps shrink rapidly. However, in this

case even for the maximum ellipticity of the rods ($RR = 3.14$) the second gap will not close completely, though its width falls as low as 0.02 GHz.

5. Conclusions

In the 2D magnetic composites considered in this paper, with Co rods embedded in an Fe matrix, the increase in importance of the magnetostatic interactions results in the formation of band gaps in the spin-wave spectrum. These magnonic gaps are destroyed as the exchange interactions begin to play a dominant role. On the other hand, the increase in importance of the exchange interactions not only results in a widening of the bands, but also, consequently, causes the possible gaps to move towards higher frequencies. In contrast, when the magnetostatic interactions gain in importance at the cost of the exchange interactions, the

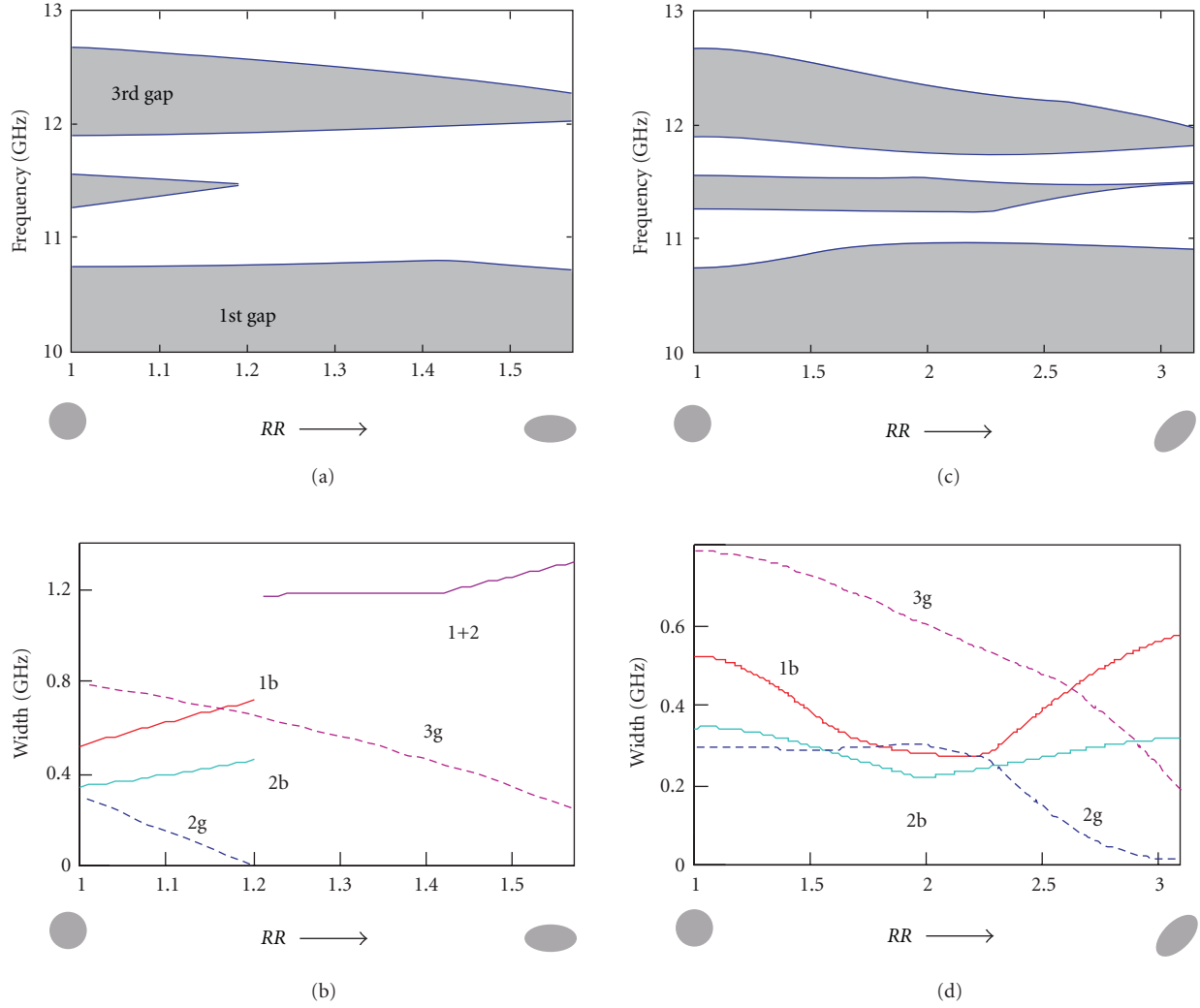


FIGURE 4: The same as in Figure 3, but for filling fraction 0.5.

frequency range in which magnonic gaps will occur lowers substantially. This finding is consistent with the results obtained for 2D composites with an EuO matrix [28]. However, an entirely different behavior is observed in 3D magnonic crystals, in which absolute magnonic gaps are destroyed by the magnetostatic interactions [29].

The use of rods in the shape of elliptic cylinders as scattering centers in 2D magnetic composites implies the introduction of two additional structural parameters: the cross-sectional ellipticity of the rods and the angle of their rotation in the plane perpendicular to the rod axis (the plane of spin-wave propagation). In contrast to the lattice constant, a change of which will strongly modify the spin-wave spectrum, these new parameters allow fine tuning of the width and position of the bands and gaps. For specific in-plane rotation angles, changing the rod ellipticity will modify the position of a band without changing its width or cause two adjacent bands to shrink substantially without affecting the width of the gap between them. Thus, an appropriate use of rods of elliptical cross section offers

additional possibilities in the design of spin-wave filters with precisely adjusted passband.

Acknowledgments

Those results were presented at 18th International Conference on Composite Materials, Jeju Island, Korea. The research leading to these results has received funding from the European Community's Seventh Framework Programme (FP7/2007-2013) under Grant Agreement no. 228673 for MAGNONICS project.

References

- [1] A. V. Chumak, A. A. Serga, B. Hillebrands, and M. P. Kostylev, "Scattering of backward spin waves in a one-dimensional magnonic crystal," *Applied Physics Letters*, vol. 93, no. 2, Article ID 022508, 2008.
- [2] Z. K. Wang, V. L. Zhang, H. S. Lim et al., "Observation of frequency band gaps in a one-dimensional nanostructured

- magnonic crystal,” *Applied Physics Letters*, vol. 94, no. 8, Article ID 083112, 2009.
- [3] S. L. Vysotskii, S. A. Nikitov, E. S. Pavlov, and Y. A. Filimonov, “The spectrum of the spin-wave excitations of the tangentially magnetized 2D hexagonal ferrite magnonic crystal,” *Journal of Communications Technology and Electronics*, vol. 55, no. 7, pp. 800–809, 2010.
 - [4] S. Neusser, G. Duerr, H. G. Bauer et al., “Anisotropic propagation and damping of spin waves in a nanopatterned antidot lattice,” *Physical Review Letters*, vol. 105, no. 6, Article ID 067208, 2010.
 - [5] Y. Cao, G. Yun, X. Liang, and N. Bai, “Band structures of two-dimensional magnonic crystals with different shapes and arrangements of scatterers,” *Journal of Physics D*, vol. 43, no. 30, Article ID 305005, 2010.
 - [6] J. W. Klos, M. Krawczyk, and M. Sokolovskyy, “Bulk and edge modes in two-dimensional magnonic crystal slab,” *Journal of Applied Physics*, vol. 109, no. 7, Article ID 07D311, 2011.
 - [7] R. Zivieri, S. Tacchi, F. Montoncello et al., “Bragg diffraction of spin waves from a two-dimensional antidot lattice,” *Physical Review B*, vol. 85, no. 1, Article ID 012403, pp. 1–6, 2012.
 - [8] S. A. Nikitov, P. Tailhades, and C. S. Tsai, “Spin waves in periodic magnetic structures—magnonic crystals,” *Journal of Magnetism and Magnetic Materials*, vol. 236, no. 3, pp. 320–330, 2001.
 - [9] M. Krawczyk and H. Puzskarski, “Magnonic excitations versus three-dimensional structural periodicity in magnetic composites,” *Crystal Research and Technology*, vol. 41, no. 6, pp. 547–552, 2006.
 - [10] S. Neusser, H. G. Bauer, G. Duerr et al., “Tunable metamaterial response of a Ni80Fe20 antidot lattice for spin waves,” *Physical Review B*, vol. 84, no. 18, Article ID 184411, 2011.
 - [11] S. Tacchi, F. Montoncello, M. Madami et al., “Band diagram of spinwaves in a two-dimensional magnonic crystal,” *Physical Review Letters*, vol. 107, no. 12, Article ID 127204, pp. 1–5, 2011.
 - [12] J. Topp, D. Heitmann, M. P. Kostylev, and D. Grundler, “Making a reconfigurable artificial crystal by ordering bistable magnetic nanowires,” *Physical Review Letters*, vol. 104, no. 20, Article ID 207205, 2010.
 - [13] S. Tacchi, M. Madami, G. Gubbiotti et al., “Analysis of collective spin-wave modes at different points within the hysteresis loop of a one-dimensional magnonic crystal comprising alternative-width nanostripes,” *Physical Review B*, vol. 82, no. 18, Article ID 184408, 2010.
 - [14] S. Tacchi, M. Madami, G. Gubbiotti et al., “Anisotropic dynamical coupling for propagating collective modes in a two-dimensional magnonic crystal consisting of interacting squared nanodots,” *Physical Review B*, vol. 82, no. 2, Article ID 024401, 2010.
 - [15] G. Duerr, M. Madami, S. Neusser et al., “Spatial control of spin-wave modes in Ni80Fe20 antidot lattices by embedded Co nanodisks,” *Applied Physics Letters*, vol. 99, no. 20, Article ID 202502, 2011.
 - [16] S. Neusser, G. Duerr, S. Tacchi et al., “Magnonic minibands in antidot lattices with large spin-wave propagation velocities,” *Physical Review B*, vol. 84, no. 9, Article ID 094454, pp. 1–9, 2011.
 - [17] V. V. Kruglyak, S. O. Demokritov, and D. Grundler, “Magnonics,” *Journal of Physics D*, vol. 43, no. 26, Article ID 264001, 2010.
 - [18] S. Neusser and D. Grundler, “Magnonics: spin waves on the nanoscale,” *Advanced Materials*, vol. 21, no. 28, pp. 2927–2932, 2009.
 - [19] S. Choi, K. S. Lee, K. Y. Guslienko, and S. K. Kim, “Strong radiation of spin waves by core reversal of a magnetic vortex and their wave behaviors in magnetic nanowire waveguides,” *Physical Review Letters*, vol. 98, no. 8, Article ID 087205, 2007.
 - [20] A. B. Ustinov, A. V. Drozdovskii, and B. A. Kalinikos, “Multi-functional nonlinear magnonic devices for microwave signal processing,” *Applied Physics Letters*, vol. 96, no. 14, Article ID 142513, 2010.
 - [21] F. S. Ma, H. S. Lim, Z. K. Wang, S. N. Piramanayagam, S. C. Ng, and M. H. Kuok, “Micromagnetic study of spin wave propagation in bicomponent magnonic crystal waveguides,” *Applied Physics Letters*, vol. 98, no. 15, Article ID 153107, 2011.
 - [22] H. T. Nembach, J. M. Shaw, T. J. Silva et al., “Effects of shape distortions and imperfections on mode frequencies and collective linewidths in nanomagnets,” *Physical Review B*, vol. 83, no. 9, Article ID 094427, 2011.
 - [23] S. Mamica and M. Krawczyk, “Tuning of the spin-wave band structure in 2d magnetic composites,” in *Proceedings of the 18th International Conference on Composite Materials*, P4-34, Jeju Island, Republic of Korea, 2011.
 - [24] M. Krawczyk, J. Klos, M. L. Sokolovskyy, and S. Mamica, “Materials optimization of the magnonic gap in three-dimensional magnonic crystals with spheres in hexagonal structure,” *Journal of Applied Physics*, vol. 108, no. 9, Article ID 093909, 2010.
 - [25] C. A. F. Vaz, J. A. C. Bland, and G. Lauhoff, “Magnetism in ultrathin film structures,” *Reports on Progress in Physics*, vol. 71, no. 5, Article ID 056501, 2008.
 - [26] V. S. Tkachenko, V. V. Kruglyak, and A. N. Kuchko, “Spectrum and reflection of spin waves in magnonic crystals with different interface profiles,” *Physical Review B*, vol. 81, no. 2, Article ID 024425, 2010.
 - [27] M. Krawczyk, “Magnetostatic waves in one-dimensional magnonic crystals with magnetic and nonmagnetic components,” *IEEE Transactions on Magnetics*, vol. 44, no. 11, pp. 2854–2857, 2008.
 - [28] J. O. Vasseur, L. Dobrzynski, B. Djafari-Rouhani, and H. Puzskarski, “Magnon band structure of periodic composites,” *Physical Review B*, vol. 54, no. 2, pp. 1043–1049, 1996.
 - [29] M. Krawczyk and H. Puzskarski, “Plane-wave theory of three-dimensional magnonic crystals,” *Physical Review B*, vol. 77, no. 5, Article ID 054437, 2008.

Research Article

Gap Structure and Gapless Structure in Fractional Quantum Hall Effect

Shosuke Sasaki

KYOKUGEN (Center for Quantum Science and Technology under Extreme Conditions), Osaka University, 1-3 Machikaneyama, Toyonaka, Osaka 560-8531, Japan

Correspondence should be addressed to Shosuke Sasaki, sasaki@ns.sist.ac.jp

Received 14 November 2011; Revised 9 January 2012; Accepted 24 January 2012

Academic Editor: Roberto Zivieri

Copyright © 2012 Shosuke Sasaki. This is an open access article distributed under the Creative Commons Attribution License, which permits unrestricted use, distribution, and reproduction in any medium, provided the original work is properly cited.

Higher-order composite fermion states are correlated with many quasiparticles. The energy calculations are very complicated. We develop the theory of Tao and Thouless to explain them. The total Hamiltonian is $(H_D + H_I)$, where H_D includes Landau energies and classical Coulomb energies. We find the most uniform electron configuration in Landau states which has the minimum energy of H_D . At $\nu = (2j - 1)/(2j)$, all the nearest electron pairs are forbidden to transfer to any empty states because of momentum conservation. Therefore, perturbation energies of the nearest electron pairs are zero in all order of perturbation. At $\nu = j/(2j - 1)$, $j/(2j + 1)$, all the nearest electron (or hole) pairs can transfer to all hole (or electron) states. At $\nu = 4/11, 4/13, 5/13, 5/17, 6/17$, only the specific nearest hole pairs can transfer to all electron states. For example, the nearest-hole-pair energy at $\nu = 4/11$ is lower than the limiting energies from both sides (the left side $\nu = (4s + 1)/(11s + 3)$ and the right side $\nu = (4s - 1)/(11s - 3)$ for infinitely large s). Thus, the nearest-hole-pair energy at specific ν is different from the limiting values from both sides. The property yields energy gap for the specific ν . Also gapless structure appears at other filling factors (e.g., at $\nu = 1/2$).

1. Introduction

Precise experiments on ultra-high-mobility samples revealed many local minima of diagonal resistivity ρ_{xx} [1, 2]. Therein small local minima are detected at the filling factors of $\nu = 3/8, 3/10, 7/11, 4/11, 4/13, 5/13, 5/17$, and $6/17, \dots$. These states cannot be understood by use of the standard composite fermion (CF) model [3, 4]. Jain has originally considered multiflavor composite fermion picture with coexistence of composite fermions carrying different numbers of fluxes. Wójs et al. [5, 6], Smet [7], and Peterson and Jain [8] and Pashitskii [9] investigated these states and described the states in their extended systematics. Smet has explained these states in terms of the multiflavor composite fermion picture. Pashitskii presented expanded systematics based on Halperin's conjecture of coexistence of free electrons and bound electron pairs, with predicted new exotic fractions of $\nu = 5/14, 5/16$, and $3/20$. These investigations are complicated to explain the stability of expanded states with $\nu = 3/8, 3/10, 7/11, 4/11, 4/13, 5/13, 5/17$, and $6/17, \dots$, because many quasiparticles are correlated with each others.

The results of various theories depend upon what kinds of quasi-particles are combined with each others. Therefore, it is preferable that the same logic is applied to any kind of filling factors (including both standard and nonstandard filling factors).

We study the other description in order to remove these ambiguities. Tao and Thouless [10, 11] examined the case that the lowest Landau levels are partially filled with electrons. They cannot lead which states are stable in comparison with the other states. However, their method is very important to investigate the FQH states. We have carefully examined the Coulomb interactions and develop their theory [12, 13]. Then the Coulomb transitions conserve the x component of the total momentum where the x direction indicates the current direction. This property produces energy gaps for the specific filling factors. Also the momentum conservation produces no binding energy for some filling factors. We study these gap structure or gapless structure for various filling factors, respectively. Quantum hall devices have an ultra thin layer of electron conducting channel as in Figure 1.

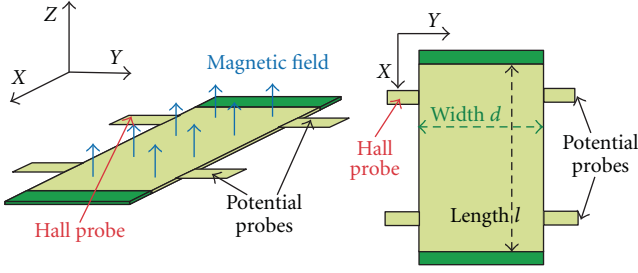


FIGURE 1: Quantum hall device.

That is to say the potential well in the z direction is deep and extremely narrow. Then the electron state of the z -direction is the ground state $\phi(z)$ at a low temperature because the probability of excited states is negligibly small caused by large excitation energy. The remaining freedoms are the x and y directions. If we neglect the Coulomb interactions between electrons, the single-electron eigenstates are the Landau states. Although these states are well known, we shortly write them for applying them below. Landau wave function is given as follows:

$$\psi_{L,j}(x, y, z) = \sqrt{\frac{1}{\ell}} \exp(ikx) u_L H_L \left(\sqrt{\frac{m\omega}{\hbar}} (y - \alpha_j) \right) \times \exp \left(-\frac{m\omega}{2\hbar} (y - \alpha_j)^2 \right) \phi(z). \quad (1)$$

Therein, L is the Landau level number, k is the angular wave-number, and α_j is the central position in the y -direction which is related as

$$\alpha_j = \frac{2\pi\hbar J}{(eB\ell)} \quad k = \frac{2\pi J}{\ell}, \quad (2)$$

where J indicates the integer assigned to each momentum of the x -direction. The eigen energy is

$$E_L = \lambda + \hbar\omega \left(L + \frac{1}{2} \right) \quad (L = 0, 1, 2, 3, \dots), \quad (3)$$

where λ is the ground state energy of the z -direction. We count the number of states with a fixed value of L by (2)

$$0 \leq \alpha_j \leq d \longrightarrow 0 \leq \frac{2\pi\hbar J}{(eB\ell)} \leq d \longrightarrow 0 \leq J \leq \frac{eB\ell d}{(2\pi\hbar)}, \quad (4)$$

where d is the width of the device in Figure 1. Then the total number of Landau states with the same value of L is equal to $eB\ell d/(2\pi\hbar)$.

Next we consider the many electron states $\Psi(L_1, \dots, L_N; p_1, \dots, p_N)$ described by the Slater determinant where L_j and p_j indicate the Landau level number and the momentum of j th electron, respectively. All the states composed of $\Psi(L_1, \dots, L_N; p_1, \dots, p_N)$ make the complete set. The total Hamiltonian is rewritten by use of this complete set. The diagonal part is described by H_D which is given as

$$H_D = \sum_{L_1, \dots, L_N} \sum_{p_1, \dots, p_N} |\Psi(L_1, \dots, L_N; p_1, \dots, p_N)\rangle \times W(L_1, \dots, L_N; p_1, \dots, p_N) \times \langle \Psi(L_1, \dots, L_N; p_1, \dots, p_N) |, \quad (5)$$

where $W(L_1, \dots, L_N; p_1, \dots, p_N)$ is the diagonal matrix element defined by

$$W(L_1, \dots, L_N; p_1, \dots, p_N) = \sum_{i=1}^N E_{L_i} + C(L_1, \dots, L_N; p_1, \dots, p_N). \quad (6)$$

Therein, E_{L_i} is the eigen-energy (3) of single electron with Landau level number L_i . Also C is the expectation value of Coulomb interactions which is defined by

$$C(L_1, \dots, L_N; p_1, \dots, p_N) = \int \dots \int \Psi(L_1, \dots, L_N; p_1, \dots, p_N)^* \times \sum_{i=1}^{N-1} \sum_{j>i}^N \frac{e^2}{4\pi\epsilon \sqrt{(x_i - x_j)^2 + (y_i - y_j)^2 + (z_i - z_j)^2}} \times \Psi(L_1, \dots, L_N; p_1, \dots, p_N) \times dx_1 dy_1 dz_1 \dots dx_N dy_N dz_N. \quad (7)$$

Hereafter, we call $C(L_1, \dots, L_N; p_1, \dots, p_N)$ “classical Coulomb energy.” The total Hamiltonian is divided into two parts H_D and H_I . The residual part H_I is obtained by

$$H_I = H_T - H_D, \quad (8)$$

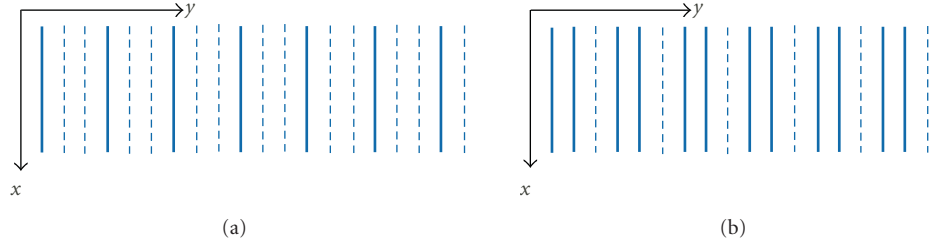
where H_I is constructed only by the off-diagonal elements. The residual Hamiltonian H_I is the interaction between two electrons depending upon only the relative coordinate. Therefore, the total momentum of the x -direction conserves in this system. That is to say the sum of the initial momenta p_i and p_j is equal to the sum of the final momenta p'_i and p'_j via Coulomb transition as follows:

$$p'_i + p'_j = p_i + p_j. \quad (9)$$

At a filling factor smaller than 1, the ground state of H_D is the following many-electron state as:

- (1) N electrons exist in the lowest Landau levels of $L_1 = L_2 = \dots = L_N = 0$.
- (2) The electrons should most uniformly occupy the lowest Landau levels so that the classical Coulomb energy has the lowest value. The electron momenta p_1, p_2, \dots, p_N are related to each centre positions as in (2). Therefore, the most uniform electron configuration determines the electron momenta p_1, p_2, \dots, p_N for each filling factor ν .

In the next section we will schematically draw the most uniform electron configuration at several filling factors. Then it is clarified that the most uniform electron configuration is unique. The most uniformity yields the minimum eigen energy of H_D , and the uniqueness produces a nondegenerate ground state although the ground states of the single electron Hamiltonian H_0 are degenerate. The electron configurations are examined in Section 2.

FIGURE 2: (a) Electron configuration at $\nu = 1/3$. (b) Configuration at $\nu = 2/3$.

We can estimate the perturbation energy via the Coulomb transitions by using the usual perturbation method of nondegenerate case. Electron (or hole) pairs in the nearest Landau orbitals are most affected by the Coulomb interaction. The perturbation energies of the nearest electron (or hole) pairs are sensitively dependent upon each electron configurations. The sensitivity is caused by Fermi-Dirac statistics and the momentum conservation of the x -direction. The most uniform electron configuration produces the following properties: all the *nearest electron* (or *hole*) pairs are allowed to transfer to all vacant (or filled) states at the filling factors of $\nu = j/(2j \pm 1)$. The property produces energy gap structure. For example, the perturbation energy of the *nearest electron pair* at $\nu = j/(2j - 1)$ is lower than the limiting value from both sides as $s \rightarrow \nu \pm \varepsilon$ where ε is an infinitesimally small value. The energy gap is defined as

$$\text{Energy gap} = \Delta E_{\text{nearest pair}} = \left(E(\nu) - \lim_{s \rightarrow \nu \pm \varepsilon} E(s) \right). \quad (10)$$

The ratio of the energy gap and the original nearest electron pair energy is equal to

$$\begin{aligned} \frac{\Delta E_{\text{nearest pair}}}{E(\nu)} &= \frac{(E(\nu) - \lim_{s \rightarrow \nu \pm \varepsilon} E(s))}{E(\nu)} \\ &= \frac{1}{2(j-1)} \quad \text{for } \nu = \frac{j}{2j-1}. \end{aligned} \quad (11)$$

It is noteworthy that both the energy $E(\nu)$ and the energy gap $E(\nu) - \lim_{s \rightarrow \nu \pm \varepsilon} E(s)$ are negative values. This mechanism is clarified in Section 3.

All the *nearest electron* (or *hole*) pairs are forbidden to transfer to any vacant (or filled) state at the filling factors of $\nu = (2j - 1)/(2j)$ (or $\nu = 1/(2j)$). This mechanism is examined in Section 4.

At the filling factors of $\nu = 7/11, 4/11, 4/13, 5/13, 5/17$, and $6/17$, some of the *nearest electron* (or *hole*) pairs are allowed to transfer to all vacant (or filled) states. This case yields small energy gaps, for example,

$$\begin{aligned} \frac{\Delta E_{\text{nearest pair}}}{E(\nu)} &= \frac{(E(\nu) - \lim_{s \rightarrow \nu \pm \varepsilon} E(s))}{E(\nu)} \\ &\approx \frac{0.006493}{0.103896} \quad \text{for } \nu = \frac{7}{11} \end{aligned} \quad (12)$$

which is investigated in Section 5. Thus, the present theory produces a gap structure or a gapless structure for each

fractional filling factor. The theoretical results are in a good agreement with the experimental data.

We examine another type of gap which indicates the excitation energy gap from the ground state to excited states. This new gap is highly correlated with the gap in the spectrum of energy versus filling factor. The mechanism is studied in Section 6.

2. Most Uniform Configuration of Electrons

We can find out the many-electron states with the minimum energy of H_D for any filling factor. As most easy examples, we show the case of $\nu = 1/3$ and $\nu = 2/3$. Figures 2(a) and 2(b) indicate the configurations of electrons with the minimum classical Coulomb energy at $\nu = 1/3$ and $2/3$, respectively.

Therein the bold line indicates a Landau state filled with electron, and the dashed line means an empty state. It is noteworthy that the current direction is described by the x -direction, and the Hall voltage direction is described by the y -direction (same as in Figure 1). Figure 2(a) shows the electron configuration with repeating of the arrangement (empty, filled, empty). This filling way is the most uniform configuration at $\nu = 1/3$ and then has the minimum classical Coulomb energy. The filling way in Figure 2(b) also has the minimum classical Coulomb energy at $\nu = 2/3$. It is easily seen that Figures 2(a) and 2(b) indicate the most uniform filling ways at $\nu = 1/3$ and $\nu = 2/3$, respectively.

We explain the searching method to find the electron configuration with the minimum Coulomb energy, because it is nontrivial to find the filling way for any fractional filling factor $\nu < 1$. In order to clarify the explanation, we consider one example of $\nu = 3/5$. We compare the classical Coulomb energies of the following two cases.

Case 1. In the whole region, three electrons exist inside every 5 sequential Landau states. Then the filling factor becomes $3/5$.

Case 2. Two electrons exist in 5 sequential Landau states for some parts, and four electrons exist in 5 sequential Landau states for some other parts. And the average filling factor is equal to $3/5$.

The Coulomb energy of Case 1 is smaller than one of Case 2 because the filling way of Case 1 is more uniform than one of Case 2. Therefore, it is sufficient to consider all the

filling ways inside 5 sequential states. They are 10 filling ways as shown in Figure 3.

The five filling ways (a-1, a-2, a-3, a-4, and a-5) give the same electron configuration A by numerous repeating of themselves except both end parts. The electron configuration A is shown in Figure 4(a). The both end parts can be neglected for macroscopic number of electrons in a quantum Hall device.

Similarly the five filling ways (b-1, b-2, b-3, b-4, and b-5) in Figure 3 give the same electron configuration B as Figure 4(b). It is clear that the electron configuration A of Figure 4(a) has the classical Coulomb energy smaller than one of configuration B at $\nu = 3/5$.

It is noteworthy to examine the connections between different arrangements in Figure 3. We draw the connections of (a-1 and a-2), (a-1 and a-3), (a-1 and a-4), and (a-1 and a-5) in Figure 5 where the first filling way is red coloured, and the second filling way is blue coloured. All the connections include green areas where 2 electrons or 4 electrons exist inside five sequential Landau states as in Figure 5.

Therefore, these connections belong to Case 2 and then have a classical Coulomb energy larger than one of configuration A in Figure 4(a).

For any filling factor $\nu = r/q$, r electrons should exist in q sequential Landau states everywhere. All filling ways have the number of $q!/(r!(q-r)!)$. We can draw all the filling ways and then find out the most uniform configuration of electrons. This procedure is applied to the cases with denominator $q = 2, 3, 4, 5, 6, 7, 8$. Then, we get the filling ways with the minimum classical Coulomb energy as drawn in Figure 6 (We abbreviate equivalent filling ways. For example only the filling way a-1 is drawn, and other filling ways a-2, a-3, a-4, a-5 are abbreviated for $\nu = 3/5$). These filling ways are called unit arrangements for each filling factors.

When we repeat the unit arrangement in Figure 6, we obtain the electron configuration with the minimum classical Coulomb energy at each filling factor.

We draw some examples with higher Coulomb energy for the denominator $q = 7, 8$ in Figure 7. Comparison of Figure 6 with Figure 7 reveals the fact that the unit arrangements in Figure 6 have more uniformity than ones in Figure 7.

Thus only one configuration has the minimum classical Coulomb energy among the enormous many configurations. The whole-electron configuration is created by repeating of only one unit arrangement of electron at any fractional number of ν .

3. Gap Structure in the Neighbourhood of $\nu = j/(2j \pm 1)$

3.1. Calculation of Binding Energy at $\nu = j/(2j - 1)$. The shape of Landau wave function with $L = 0$ is schematically drawn by a straight line. We draw the most uniform electron configuration at $\nu = j/(2j - 1)$ in Figure 8 where solid lines indicate the Landau orbitals filled with electron, and dashed lines indicate the vacant Landau orbitals. Therein, *nearest electron pairs* are red-coloured, and single electrons are blue-coloured. The Coulomb transitions from the nearest electron

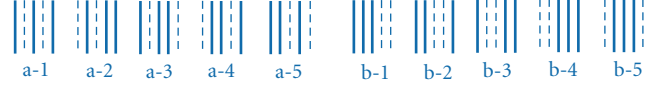


FIGURE 3: All unit arrangements of electron configurations for $\nu = 3/5$.

pair AB are illustrated by black arrows in Figure 8. The x and y directions are drawn in the upper left corner.

The electron configurations in Figure 8 have the minimum classical Coulomb energy for each filling factors. In order to explain the calculation of the second-order perturbation energy, we draw again the most uniform electron configuration of $\nu = 2/3$ in Figure 9. Therein the first transition is expressed by black arrows, and the second transition is expressed by green arrows and so on.

The momenta of the *nearest electron pair* AB are described by p_A, p_B , respectively. When electron A transfers to the first orbital to the left, the initial momentum p_A decreases by $2\pi\hbar/\ell$ according to (2). After the transition, the electron A has a new momentum p'_A as

$$p'_A = p_A - \frac{2\pi\hbar}{\ell}. \quad (13)$$

The other electron B transfers to the momentum p'_B . Then the total momentum conservation in the x -direction gives the following relation:

$$p'_A + p'_B = p_A + p_B. \quad (14)$$

Substitution of (13) into (14) yields the momentum p'_B as

$$p'_B = p_B + \frac{2\pi\hbar}{\ell}. \quad (15)$$

This momentum increment means that the electron B should transfer from its original orbital to the first orbital to the right because of (2) and (15). This transition is allowed because the right orbital is empty as in Figure 9.

Similarly the *nearest electron pair* AB can transfer to the other empty states, and the momenta after the transition are given by

$$\begin{aligned} p'_A &= p_A - \Delta p, \\ p'_B &= p_B + \Delta p, \end{aligned} \quad (16)$$

where the momentum transfer Δp at $\nu = 2/3$ has the values as

$$\Delta p = \frac{(3j+1)2\pi\hbar}{\ell} \quad \text{for } j = 0, \pm 1, \pm 2, \pm 3, \dots \quad (17)$$

because the electrons are possible to transfer to empty orbitals only. (In this paper we investigate the case that all the electron spins have an opposite direction of magnetic field. Another case is discussed in the other articles [14–16]). The second-order perturbation energy of the *nearest electron pair* AB is given by

$$\begin{aligned} \zeta_{\nu=2/3} &= \sum_{\Delta p=(3j+1)2\pi\hbar/\ell \text{ for } j=0,\pm 1,\pm 2,\dots}^R \\ R &= \frac{\langle p_A, p_B | H_I | p'_A, p'_B \rangle \langle p'_A, p'_B | H_I | p_A, p_B \rangle}{W_G - W_{\text{excite}}(p_A \rightarrow p'_A, p_B \rightarrow p'_B)}. \end{aligned} \quad (18)$$

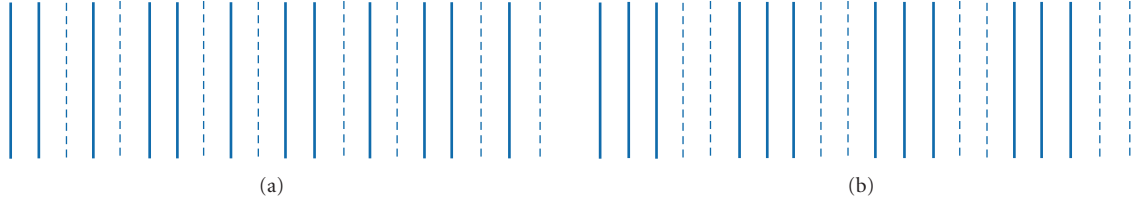
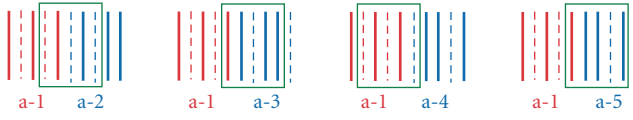
FIGURE 4: (a) Configuration A at $\nu = 3/5$. (b) Configuration B at $\nu = 3/5$.

FIGURE 5: Connections between different arrangements.

We introduce the following summation Z as

$$Z = - \sum_{\Delta p \neq 0, -2\pi\hbar/\ell}^{\text{all}} \frac{\langle p_A, p_B | H_I | p'_A, p'_B \rangle \langle p'_A, p'_B | H_I | p_A, p_B \rangle}{W_G - W_{\text{excite}}(p_A \rightarrow p'_A, p_B \rightarrow p'_B)}, \quad (19)$$

where the momentum transfer Δp takes all values $(2\pi\hbar/\ell) \times$ integer except $\Delta p = 0$ and $\Delta p = -2\pi\hbar/\ell$. The transferred states with $\Delta p = 0$ and $\Delta p = -2\pi\hbar/\ell$ are the same state as the initial state. This state is eliminated in the summation of (19) because the diagonal matrix element of H_I is zero. Therefore, the denominator is not zero and has a negative value. The definition of Z includes (-1) in the right-hand side, and the denominator is a negative value. Accordingly the value of Z is positive.

We can systematically describe the perturbation energies at any filling factors by using the value of Z . We compare Z with the perturbation energy $\zeta_{\nu=2/3}$ of (18). The interval of the momentum transfer is $3 \times 2\pi\hbar/\ell$ in the summation $\zeta_{\nu=2/3}$. On the other hand, the summation Z is performed by the momentum interval $2\pi\hbar/\ell$. The interval value is very small for a quantum Hall device with a macroscopic size and then we get

$$\zeta_{\nu=2/3} = -\frac{1}{3}Z. \quad (20)$$

Thus, we can express the perturbation energy $\zeta_{\nu=2/3}$ of the *nearest electron pair* by the summation Z . The perturbation energies depend upon ℓ and B , namely, device size and magnetic field strength. These dependences are included in the summation Z .

The number of *nearest electron pairs* is $(1/2)N$ at $\nu = 2/3$, where N is the total number of electrons. Accordingly the total perturbation energy $E_{\text{nearest pair}}$ of all *nearest electron pairs* is obtained as

$$E_{\text{nearest pair}} = \frac{1}{2}N \times \zeta_{\nu=2/3} = -\frac{1}{6}ZN, \quad \text{for } \nu = \frac{2}{3}. \quad (21)$$

Similar calculation leads the second order perturbation energy of *nearest electron pairs* at any filling factor of $\nu = j/(2j-1)$ as follows [16].

Therein, j electrons partially occupy each sequential $(2j-1)$ Landau states, and then $(j-1)$ Landau states are empty for each sequential $(2j-1)$ Landau states. Any *nearest electron pair* can transfer to all the empty states as in Figure 8. The number of transitions is equal to $(j-1)$ for each $(2j-1)$ Landau states. Therefore, the second-order perturbation energy per pair is given by

$$\zeta_{\nu=j/(2j-1)} = -\frac{j-1}{2j-1}Z, \quad \text{for } \nu = \frac{j}{(2j-1)}. \quad (22)$$

The number of *nearest electron pairs* is $(1/j)N$ at $\nu = j/(2j-1)$, where N is the total number of electrons. Accordingly the total perturbation energy $E_{\text{nearest pair}}$ from all *nearest electron pairs* is obtained as

$$\begin{aligned} E_{\text{nearest pair}} &= \frac{N}{j} \zeta_{\nu=j/(2j-1)} \\ &= -\frac{j-1}{j(2j-1)}ZN, \quad \text{for } \nu = \frac{j}{(2j-1)}. \end{aligned} \quad (23)$$

The *nearest electron pair* energy per electron is given by

$$\chi\left(\nu = \frac{j}{2j-1}\right) = -\frac{(j-1)Z}{(j(2j-1))}, \quad \text{for } \nu = \frac{j}{(2j-1)}. \quad (24)$$

3.2. Gap Structure at $\nu = j/(2j-1)$. It has been clarified in the previous subsection that all the *nearest electron pairs* can transfer to all empty Landau orbitals at the filling factor of $\nu = j/(2j-1)$. We next examine the perturbation energies in the neighbourhood of $\nu = j/(2j-1)$. The fraction $\nu = (j(2s)-1)/((2j-1)(2s)-2)$ approaches $\nu = j/(2j-1)$ in the limit of infinitely large s . In the case of $j=4, s=2$, the fraction is equal to

$$\nu = \frac{(j(2s)-1)}{((2j-1)(2s)-2)} = \frac{15}{26}. \quad (25)$$

The most uniform electron configuration is illustrated in Figure 10.

It is noteworthy that some *nearest electron pairs* cannot transfer to some empty states because of momentum conservation and Pauli's exclusion principle. We take this prohibition of the transitions into consideration and obtain the perturbation energy of *nearest electron pairs* as follows:

$$\begin{aligned} E_{\text{nearest pair}} &= \left[-2 \times \left(\frac{8}{26} \right) Z - 2 \times \left(\frac{10}{26} \right) Z \right] \\ &\times \left(\frac{1}{15} \right) N = -\frac{36}{26 \times 15} ZN, \quad \text{for } \nu = \frac{15}{26}. \end{aligned} \quad (26)$$

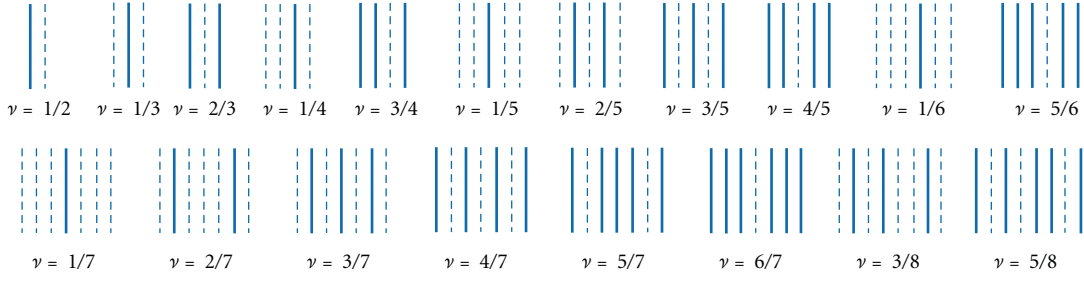


FIGURE 6: Most uniform unit arrangements of electron configuration.

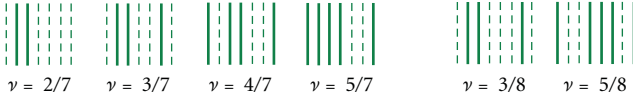
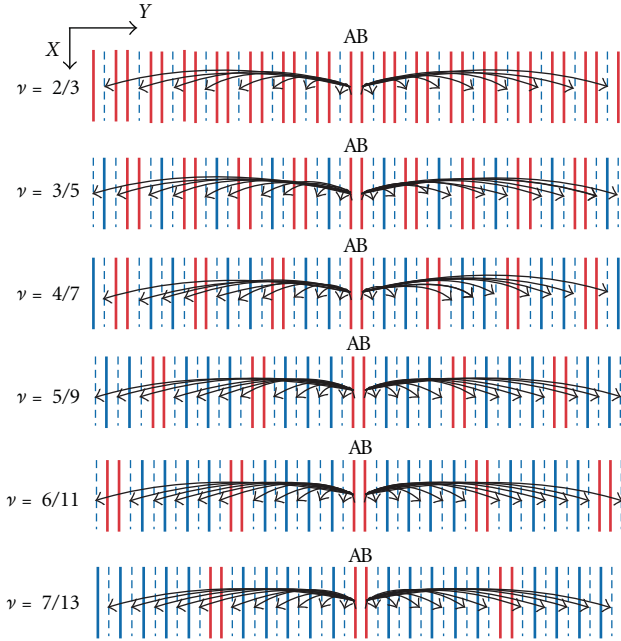


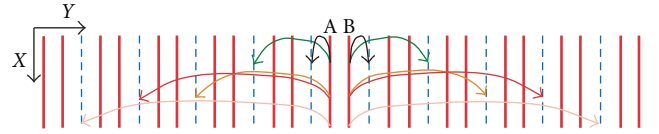
FIGURE 7: Filling ways with higher classical Coulomb energy.

FIGURE 8: Allowed transitions of nearest electron pair at $\nu = j/(2j - 1)$.

This calculation process can be extended to any integer s as follows:

$$E_{\text{nearest pair}} = \left[-2 \times \left(\frac{4s}{(14s-2)} \right) Z - 2 \times \left(\frac{(4s+2)}{(14s-2)} \right) Z \dots \right. \\ \left. \dots - 2 \times \left(\frac{(6s-2)}{(14s-2)} \right) Z \right] \times \frac{N}{(8s-1)}. \quad (27)$$

The result indicates the perturbation energy of nearest electron pairs in the neighbourhood of $\nu = 4/7$.

FIGURE 9: Coulomb transitions from nearest electron pair AB at $\nu = 2/3$. (The electric current flows along the x -direction. The momentum value is related to its central position of the y direction as in (2)).

Next we examine the neighbourhood of $\nu = j/(2j - 1)$ for any integer of j . That is to say we consider the filling factor of $\nu = (j(2s) - 1)/((2j - 1)(2s) - 2)$. We introduce new three parameters as follows:

$$\alpha = ((2j - 1)(2s) - 2), \quad \beta = (j(2s) - 1), \quad (28) \\ \gamma = ((j - 1)(2s) - 1).$$

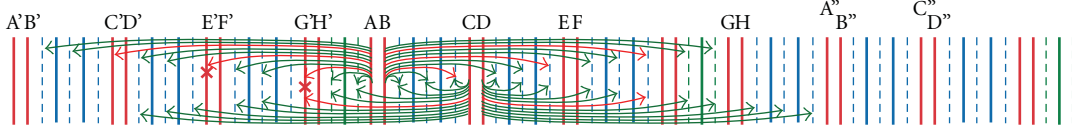
The parameter α is the number of orbitals in unit arrangement, β is the number of electrons in unit arrangement, and γ is the number of empty orbitals in unit arrangement. Accordingly we replace $(8s - 1)$ into β and also replace $(14s - 2)$ into α in (27). Then we get

$$E_{\text{nearest pair}} = \left[-2 \times \left(\frac{(4s)}{\alpha} \right) Z - 2 \times \left(\frac{(4s+2)}{\alpha} \right) Z \dots - 2 \times \left(\frac{(6s-2)}{\alpha} \right) Z \right] \times \frac{N}{\beta}, \quad (29)$$

where $(6s - 2)$ indicate $\gamma - 1$. Accordingly $(4s)$ is replaced to $\gamma + 1 - 2s$, and then we obtain that

$$E_{\text{nearest pair}} = \left[-2 \times \left(\frac{(\gamma + 1 - 2s)}{\alpha} \right) Z - 2 \times \left(\frac{(4s+2)}{\alpha} \right) Z \dots - 2 \times \left(\frac{(\gamma-1)}{\alpha} \right) Z \right] \times \frac{N}{\beta}, \\ E_{\text{nearest pair}} = [-2 \times (\gamma + 1 - 2s) - 2 \times (\gamma + 3 - 2s) \dots - 2 \times (\gamma - 1)] \frac{Z}{\alpha} \times \frac{N}{\beta},$$

$$E_{\text{nearest pair}} = [-(2\gamma - 2s)s] \frac{Z}{\alpha} \times \frac{N}{\beta} \quad \text{at } \nu = \frac{\beta}{\alpha}. \quad (30)$$

FIGURE 10: Transitions from nearest electron pairs for $\nu = 15/26$.

Substitution of (28) into (30) yields

$$E_{\text{nearest pair}} = -\frac{((2j-3)2s-2)s}{((2j-1)(2s)-2)} \frac{ZN}{(j(2s)-1)} \quad (31)$$

$$\text{at } \nu = \frac{(j(2s)-1)}{((2j-1)(2s)-2)}.$$

Thus, we have obtained the perturbation energy of the nearest electron pairs for any integers of j and s . Equation (31) gives the limiting value from the right for $s \rightarrow \infty$ because $\nu = \beta/\alpha$ is larger than $j/(2j-1)$. We have

$$\nu = \frac{\beta}{\alpha} = \frac{(j(2s)-1)}{((2j-1)(2s)-2)} \xrightarrow{s \rightarrow \infty} \frac{j}{(2j-1)}, \quad (32a)$$

$$E_{\text{nearest pair}} = -\frac{((2j-3)2s-2)s}{((2j-1)(2s)-2)} \frac{ZN}{(j(2s)-1)} \xrightarrow{s \rightarrow \infty} -\frac{(2j-3)ZN}{2j(2j-1)}$$

$$\text{at } \nu = \frac{j}{2j-1} + \epsilon, \quad (32b)$$

where ϵ indicates an infinitesimally small positive value. Equation (23) indicates the perturbation energy of nearest electron pairs at $\nu = j/(2j-1)$ as

$$E_{\text{nearest pair}} = -\frac{(j-1)ZN}{j(2j-1)} \quad \text{at } \nu = \frac{j}{2j-1}, \quad (33)$$

$$\chi\left(\frac{j}{2j-1}\right) = \frac{E_{\text{nearest pair}}}{N} = -\frac{(j-1)Z}{(j(2j-1))}. \quad (34)$$

Equation (32b) means the limiting value of *nearest pair* perturbation energy from the right at $\nu = j/(2j-1)$. The perturbation energy (33) at $\nu = j/(2j-1)$ is lower than the limiting value (32b), and, therefore, the energy gap is equal to

$$\Delta E_{\text{nearest pair}} = E(\nu) - \lim_{s \rightarrow \nu+\epsilon} E(s)$$

$$= -\frac{ZN}{2j(2j-1)} \quad \text{for } \nu = \frac{j}{2j-1}. \quad (35)$$

Next we calculate the limiting value from the left. We consider the fraction $\nu = (j(2s)+1)/((2j-1)(2s)+2)$ which is smaller than $\nu = j/(2j-1)$. New three parameters α' , β' , and γ' are defined as

$$\alpha' = ((2j-1)(2s)+2), \quad \beta' = (j(2s)+1), \quad (36)$$

$$\gamma' = ((j-1)(2s)+1).$$

The parameter α' is the number of orbitals in unit arrangement, β' is the number of electrons in unit arrangement, and γ' is the number of empty orbitals in unit arrangement. The filling factor is given by $\nu = \beta'/\alpha'$ as

$$\nu = \frac{\beta'}{\alpha'} = \frac{(j(2s)+1)}{((2j-1)(2s)+2)}. \quad (37)$$

The total transition energy from all the *nearest electron pairs* is equal to

$$E_{\text{nearest pair}} = [-(2\gamma' - 2s)s] \frac{Z}{\alpha'} \times \frac{N}{\beta'} \quad \text{at } \nu = \frac{\beta'}{\alpha'}. \quad (38)$$

Limiting values of (37) and (38) are

$$\nu = \frac{(j(2s)+1)}{((2j-1)(2s)+2)} \xrightarrow{s \rightarrow \infty} \frac{j}{(2j-1)},$$

$$E_{\text{nearest pair}} = -\frac{((2j-3)2s+2)s}{((2j-1)(2s)+2)} \frac{ZN}{(j(2s)+1)} \quad (39)$$

$$\xrightarrow{s \rightarrow \infty} -\frac{(2j-3)ZN}{2j(2j-1)} \quad \text{at } \nu = \frac{j}{2j-1} - \epsilon.$$

This limiting value from the left is compared with the original value at $\nu = j/(2j-1)$, and then the original value is lower than the limiting value from the left as

$$\Delta E_{\text{nearest pair}} = E(\nu) - \lim_{s \rightarrow \nu-\epsilon} E(s)$$

$$= -\frac{ZN}{2j(2j-1)} \quad \text{for } \nu = \frac{j}{2j-1}. \quad (40)$$

Equations (35) and (40) indicate that the limiting values from both sides of $\nu = j/(2j-1)$ are higher than the original value at $\nu = j/(2j-1)$.

The gap structure is produced from the property that all the *nearest electron pairs* are possible to transfer to all empty states at $\nu = j/(2j-1)$. When the filling factor ν changes from $j/(2j-1)$ by an infinitesimally small value, some of the transitions are forbidden. That is to say the number of allowed transitions decreases drastically. This property is caused by the most uniform electron configuration, Fermi-Dirac statistics, and momentum conservation. The drastic change also appears in higher order of the perturbation energy. The higher-order perturbations are studied in the other article.

Table 1 shows the discontinuous structure of the perturbation energies at the filling factors of $\nu = j/(2j-1)$, where ϵ expresses an infinitesimally small positive value. Therefore, $+\epsilon$ indicates the limiting process from the right, and $-\epsilon$ indicates the limiting process from the left.

TABLE 1: Energy gaps of *nearest electron pairs* per electron at $\nu = j/(2j - 1)$.

ν	$E_{\text{nearest pair}}/N$	ν	$\lim(E_{\text{nearest pair}}/N)$	$\Delta\epsilon_+(\nu) = \Delta\epsilon_-(\nu)$
2/3	$-(1/6)Z$	$(2/3) \pm \epsilon$	$-(1/12)Z$	$-(1/12)Z$
3/5	$-(2/15)Z$	$(3/5) \pm \epsilon$	$-(3/30)Z$	$-(1/30)Z$
4/7	$-(3/28)Z$	$(4/7) \pm \epsilon$	$-(5/56)Z$	$-(1/56)Z$
5/9	$-(4/45)Z$	$(5/9) \pm \epsilon$	$-(7/90)Z$	$-(1/90)Z$
6/11	$-(5/66)Z$	$(6/11) \pm \epsilon$	$-(9/132)Z$	$-(1/132)Z$
7/13	$-(6/91)Z$	$(7/13) \pm \epsilon$	$-(11/182)Z$	$-(1/182)Z$
8/15	$-(7/120)Z$	$(8/15) \pm \epsilon$	$-(13/240)Z$	$-(1/240)Z$

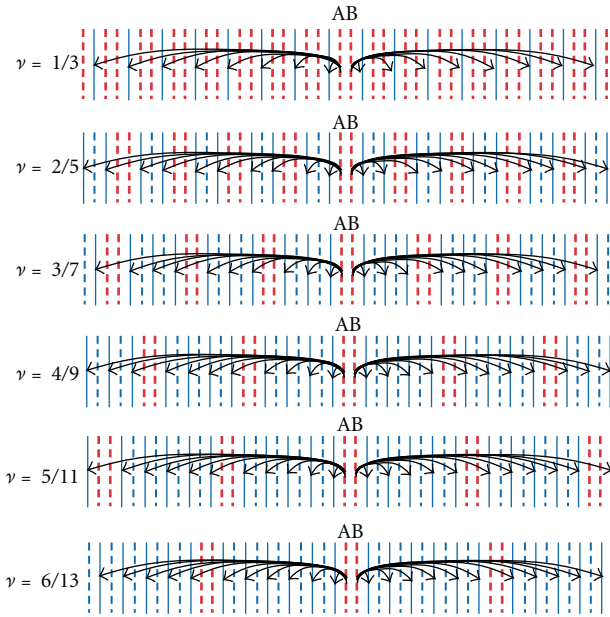


FIGURE 11: Coulomb transitions from nearest hole pair AB.

3.3. *Gap Structure at $\nu = j/(2j + 1)$.* We draw the most uniform electron configuration at $\nu = j/(2j + 1)$ in Figure 11.

Therein, solid lines indicate the Landau orbitals filled with electron, and dashed lines indicate the vacant Landau orbitals. *Nearest hole pairs* are red coloured, and single holes are blue coloured. The Coulomb transitions from the *nearest hole pair* AB are drawn by black arrows in Figure 11. Using the same method as in the previous section, we can estimate the perturbation energies of the *nearest hole pairs* $E_{\text{nearest hole pair}}$. The result is as follows:

$$E_{\text{nearest hole pair}} = -\frac{j}{(j+1)(2j+1)}Z_H N_H \quad \text{at } \nu = \frac{j}{2j+1}, \quad (41)$$

where N_H is the total number of holes. We obtain the pair energy per hole as

$$\frac{E_{\text{nearest hole pair}}}{N_H} = -\frac{j}{(j+1)(2j+1)}Z_H \quad \text{at } \nu = \frac{j}{2j+1}. \quad (42)$$

The energy per electron is

$$\frac{E_{\text{nearest hole pair}}}{N} = -\frac{1}{(2j+1)}Z_H \quad \text{at } \nu = \frac{j}{2j+1}. \quad (43)$$

We also calculate the perturbation energies in the neighbourhood of $\nu = j/(2j + 1)$, and the results are

$$E_{\text{nearest hole pair}} = -\frac{((2j-1)2s-2)s}{((2j+1)(2s)-2)} \frac{Z_H N_H}{((j+1)(2s)-1)} \quad \text{at } \nu = \frac{((j)(2s)-1)}{((2j+1)(2s)-2)},$$

$$E_{\text{nearest hole pair}} = -\frac{((2j-1)2s+2)s}{((2j+1)(2s)+2)} \frac{Z_H N_H}{((j+1)(2s)+1)} \quad \text{at } \nu = \frac{((j)(2s)+1)}{((2j+1)(2s)+2)}. \quad (44)$$

The limiting values are obtained as

$$\frac{E_{\text{nearest hole pair}}}{N} \xrightarrow{s \rightarrow \infty} -\frac{2j-1}{2j(2j+1)}Z_H \quad \text{for } \nu = \frac{j}{2j+1} \pm \epsilon. \quad (45)$$

We summarize the energy gaps of the *nearest hole pairs* at $\nu = j/(2j + 1)$ in Table 2. The rightmost column means the energy gap per electron (not per hole).

Tables 1 and 2 show the gap structure of the fractional filling states at $\nu = j/(2j \pm 1)$ because the perturbation energy is lower than one of each neighbourhood.

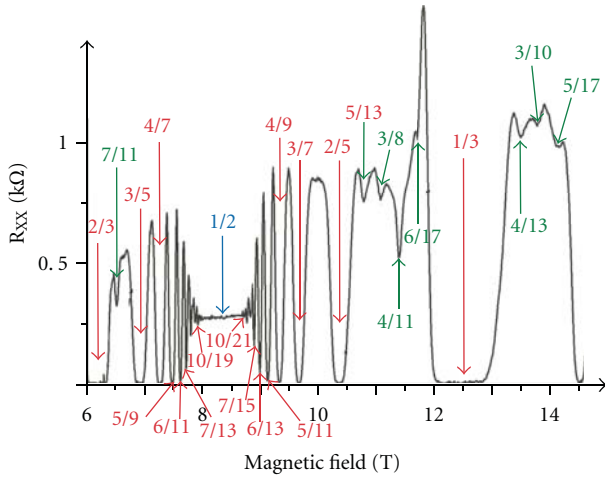
3.4. *Comparison between Experimental Data and Nearest Pair Energy at $\nu = j/(2j \pm 1)$.* Many electrons in the electric current are scattered by impurities and thermal vibrations. These scatterings yield the diagonal resistance of the x direction.

At $\nu = j/(2j \pm 1)$, we have theoretically estimated the energy gaps in the spectrum of energy versus filling factor in Sections 3.2 and 3.3. The energy gaps in the spectrum produce the plateaus in Hall resistance curve (confinements of Hall resistance). The excitation-energy gap from the ground state is highly correlated with the energy gap in the spectrum as discussed in Section 6.

The excitation-energy gaps suppress the electron scatterings. Then the diagonal resistance becomes small. This

TABLE 2: Energy gaps of *nearest hole pairs* per electron at $\nu = j/(2j + 1)$.

ν	$E_{\text{nearest pair}}/N_H$	$E_{\text{nearest pair}}/N$	ν	$\lim(E_{\text{nearest pair}}/N)$	$\Delta\epsilon_+(\nu) = \Delta\epsilon_-(\nu)$
1/3	$-(1/6)Z_H$	$-(1/3)Z_H$	$(1/3) \pm \epsilon$	$-(1/6)Z_H$	$-(1/6)Z_H$
2/5	$-(2/15)Z_H$	$-(1/5)Z_H$	$(2/5) \pm \epsilon$	$-(3/20)Z_H$	$-(1/20)Z_H$
3/7	$-(3/28)Z_H$	$-(1/7)Z_H$	$(3/7) \pm \epsilon$	$-(5/42)Z_H$	$-(1/42)Z_H$
4/9	$-(4/45)Z_H$	$-(1/9)Z_H$	$(4/9) \pm \epsilon$	$-(7/72)Z_H$	$-(1/72)Z_H$
5/11	$-(5/66)Z_H$	$-(1/11)Z_H$	$(5/11) \pm \epsilon$	$-(9/110)Z_H$	$-(1/110)Z_H$
6/13	$-(6/91)Z_H$	$-(1/13)Z_H$	$(6/13) \pm \epsilon$	$-(11/156)Z_H$	$-(1/156)Z_H$
7/15	$-(7/120)Z_H$	$-(1/15)Z_H$	$(7/15) \pm \epsilon$	$-(13/210)Z_H$	$-(1/210)Z_H$

FIGURE 12: Many local minima of the diagonal resistance in the region of $2/3 \geq \nu \geq 1/3$. This experimental result has been obtained in [2].

mechanism produces local minima in the diagonal resistance curve. The theoretical results in Tables 1 and 2 are in a good accordance with the experimental data of Figure 12.

The local minima appear at the filling factors of $\nu = 2/3, 3/5, 4/7, 5/9, 6/11, 7/13, 8/15, \dots$ and $\nu = 7/15, 6/13, 5/11, 4/9, 3/7, 2/5, 1/3$ which are indicated by red colour in Figure 12. Furthermore, there are small local minima in the curve of diagonal resistance versus magnetic field strength. The fractions are $7/11, 5/13, 3/8, 4/11, 6/17, 4/13, 3/10$, and $5/17$ which are coloured by green in Figure 12. We will examine the FQH states with $\nu = 7/11, 4/11, 4/13, 5/13, 5/17, 6/17$ in the later Section 5. The remaining FQH states with $\nu = 3/8, 5/8, 3/10$ have even denominators and have been already investigated in [17].

4. Gapless Structure of Nearest Pair Energy at $\nu = 1/(2j)$ and $\nu = (2j - 1)/(2j)$

The most uniform electron configurations are illustrated in Figure 13 at $\nu = (2j - 1)/(2j)$. The filling factors have even number of the denominator. As an example, we examine the case of $\nu = 3/4$. When electron A transfers to the fifth orbital to the left, electron B should transfer to the fifth orbital to the right. However, the fifth orbital is already filled with electron. Therefore, this transition is forbidden. Similarly all

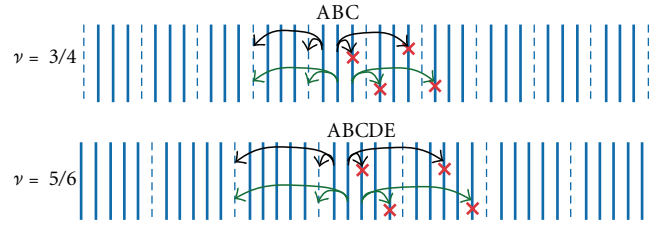


FIGURE 13: All Coulomb transitions from nearest electron pairs are forbidden.

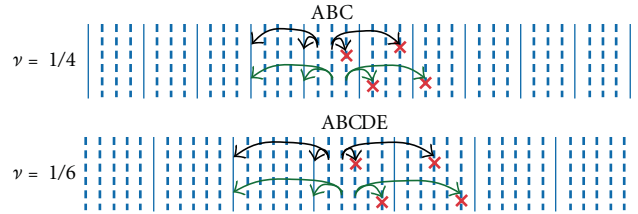


FIGURE 14: All Coulomb transitions from nearest hole pairs are forbidden.

the nearest electron pairs cannot transfer to empty states at $\nu = (2j - 1)/(2j)$.

Next we draw the most uniform electron configuration for $\nu = 1/(2j)$ in Figure 14. The hole pairs AB and BC cannot transfer to any filled orbitals at $\nu = 1/4$ as in Figure 14. All the nearest hole pairs cannot transfer to any filled orbitals at $\nu = 1/(2j)$ for any integer of j . Therefore, the perturbation energies of the nearest electron (or hole) pairs are zero for all order perturbations at $\nu = (2j - 1)/(2j)$ (or $\nu = 1/(2j)$).

That is to say we obtain the following relations:

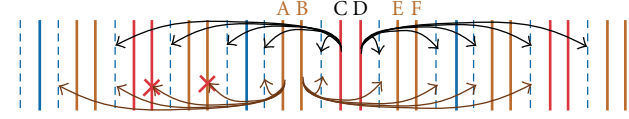
$$\begin{aligned} \frac{E_{\text{nearest electron pair}}}{N} &= 0, \quad \text{for } \nu = \frac{(2j - 1)}{(2j)}, \\ \frac{E_{\text{nearest hole pair}}}{N_H} &= 0, \quad \text{for } \nu = \frac{1}{(2j)}. \end{aligned} \quad (46)$$

We show the perturbation energies of *nearest electron pairs* and *nearest hole pairs* in Table 3.

Consequently the states with $\nu = (2j - 1)/(2j)$ (and $\nu = 1/(2j)$) are not confined in the Hall resistance curve [18–23].

TABLE 3: Nearest pair energies at $\nu = (2j - 1)/(2j)$ and $\nu = 1/(2j)$.

ν	$E_{\text{nearest pair}}/N$	ν	$E_{\text{nearest pair}}/N_H$
1/2	0		
3/4	0	1/4	0
5/6	0	1/6	0
7/8	0	1/8	0

FIGURE 15: Coulomb transitions of nearest electron pairs at $\nu = 7/11$.

5. Special States with Several Fractional Filling Factors

In this section we examine the states with the filling factors $\nu = 7/11, 4/11, 4/13, 5/13, 5/17$, and $6/17$. The most uniform electron configuration with $\nu = 7/11$ is schematically drawn in Figure 15. There are three pairs of nearest electrons in every unit arrangement, namely, (filled, empty, filled, filled, empty, filled, filled, empty, filled, filled, empty). The orbitals filled with electron are illustrated by solid lines, and the empty orbitals are illustrated by dashed lines.

The nearest electron pair CD can transfer to all empty orbitals. Then the perturbation energy of the pair CD is equal to

$$\zeta_{CD} = -\left(\frac{4}{11}\right)Z. \quad (47)$$

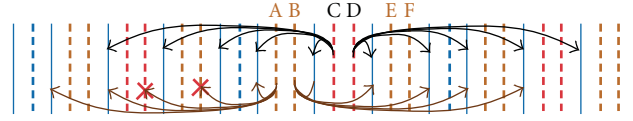
The nearest electron pairs AB and EF transfer to two empty states per unit arrangement and have the perturbation energies ζ_{AB} and ζ_{EF} as

$$\zeta_{AB} = \zeta_{EF} = -\left(\frac{2}{11}\right)Z, \quad (48)$$

$$\begin{aligned} \left(\frac{E_{\text{nearest pair}}}{N}\right)_{\nu=7/11} &= \left(-\frac{4}{11}Z - \frac{2}{11}Z - \frac{2}{11}Z\right)\frac{1}{7}N, \\ &= -\frac{8}{77}ZN, \quad \text{for } \nu = \frac{7}{11}, \end{aligned} \quad (49)$$

$$\left(\frac{E_{\text{nearest pair}}}{N}\right)_{\nu=7/11} = -\frac{8}{77}Z \approx -0.103896 \times Z, \quad \text{for } \nu = \frac{7}{11}. \quad (50)$$

We examine the neighbourhood of $\nu = 7/11$ which are $\nu = (7s - 2)/(11s - 3)$ and $\nu = (7s + 2)/(11s + 3)$. The most uniform electron configuration at $\nu = (7s \pm 2)/(11s \pm 3)$ is systematically produced by modulation of the configuration as Figure 15. Then the perturbation energy of the nearest

FIGURE 16: Coulomb transitions of nearest hole pairs at $\nu = 4/11$.

electron pairs is calculated by the use of the computer program. The calculation results for $s = 100$ are

$$\begin{aligned} \left(\frac{E_{\text{nearest pair}}}{N}\right)_{\nu=698/1097} &= -\frac{74601}{765706}Z = -0.0974277 \times Z, \quad \text{for } \nu_- = \frac{698}{1097}, \\ \left(\frac{E_{\text{nearest pair}}}{N}\right)_{\nu=702/1103} &= -\frac{75401}{774306}Z = -0.0973788 \times Z, \quad \text{for } \nu_+ = \frac{702}{1103}. \end{aligned} \quad (51)$$

We also calculate the case of $s = 1000$ the results of which are

$$\begin{aligned} \left(\frac{E_{\text{nearest pair}}}{N}\right)_{\nu=6998/10997} &= -\frac{7496001}{76957006}Z = -0.097405 \times Z, \quad \text{for } \nu_- = \frac{6998}{10997}, \\ \left(\frac{E_{\text{nearest pair}}}{N}\right)_{\nu=7002/11003} &= -\frac{7504001}{77043006}Z = -0.0974002 \times Z, \quad \text{for } \nu_+ = \frac{7002}{11003}. \end{aligned} \quad (52)$$

We compare the case of $s = 100$ with $s = 1000$ and find that the energies (51)–(52) are nearly equal to each other. Then the limiting values from both sides are approximately equal to

$$\lim_{\nu \rightarrow (7/11) \pm \epsilon} \left(\frac{E_{\text{nearest pair}}}{N}\right) \approx -0.097403 \times Z, \quad \text{for } \nu_{\pm} = \frac{7}{11} \pm \epsilon. \quad (53)$$

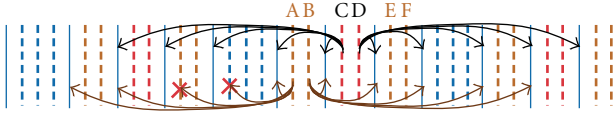
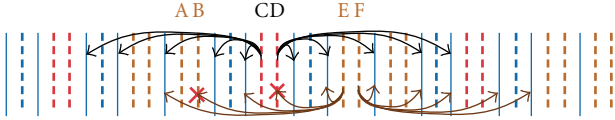
The perturbation energy per electron is $(-0.103896 \times Z)$ at $\nu = 7/11$, and therefore the energy gap appears at $\nu = 7/11$ as in (50) and (53)

$$\left(\frac{E_{\text{nearest pair}}}{N}\right)_{\nu=7/11} - \lim_{\nu \rightarrow (7/11) \pm \epsilon} \left(\frac{E_{\text{nearest pair}}}{N}\right) \approx -0.006493 \times Z. \quad (54)$$

Next we examine the case of $\nu = 4/11$. We schematically draw the most uniform electron configuration of $\nu = 4/11$ in Figure 16.

Then the perturbation energy of the nearest hole pairs is obtained as

$$\begin{aligned} \left(\frac{E_{\text{nearest pair}}}{N_H}\right)_{\nu=4/11} &= -\frac{8}{77}Z_H N_H, \quad \text{for } \nu = \frac{4}{11}, \\ \left(\frac{E_{\text{nearest pair}}}{N_H}\right)_{\nu=4/11} &= -\frac{8}{77}Z_H, \quad \text{for } \nu = \frac{4}{11}, \\ \left(\frac{E_{\text{nearest pair}}}{N}\right)_{\nu=4/11} &= -\frac{8}{11 \times 4}Z_H = -\frac{2}{11}Z_H, \quad \text{for } \nu = \frac{4}{11}. \end{aligned} \quad (55)$$

FIGURE 17: Coulomb transitions of nearest hole pair at $\nu = 4/13$.FIGURE 18: Coulomb transitions of nearest hole pair at $\nu = 5/13$.

If the configuration continues infinitely (it is a good approximation for macroscopic size of a device), then Figure 16 has the left-right symmetry for the centre of the hole pair CD. These pairs like CD are coloured red. All the red pairs can transfer to all the electron states. On the other hand, there is no left-right symmetry for the centre of the pair AB or EF. The pairs are coloured brown. They cannot transfer to some electron states because of momentum conservation. The perturbation energy of the nearest hole pairs has the energy gap at $\nu = 4/11$ as in the case of $\nu = 7/11$.

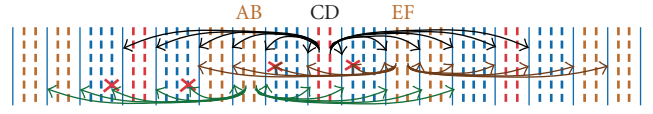
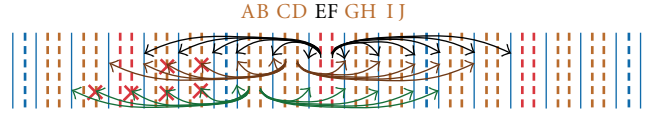
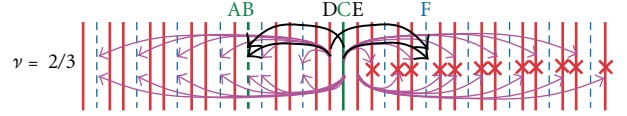
Similar configurations are schematically drawn in Figures 17, 18, 19 and 20 for $\nu = 4/13, 5/13, 5/17, 6/17$.

All the red hole pairs can transfer to all electron states as in Figures 15–20. This property is violated by infinitesimally small changing of the value ν . When the value of ν varies from the original values $\nu = 4/13, 5/13, 5/17$, and $6/17$, the number of allowed transitions becomes small. Therefore, these states with $\nu = 4/13, 5/13, 5/17, 6/17$ are stable. This property is in accordance with the experimental data as it is shown by green colour in Figure 12. (The fractions $\nu = 3/8, 5/8, 3/10$ have been studied in [17].)

6. Excitation Energy of FQHS

We have used the term “energy gap” for the gap in the spectrum of energy versus filling factor in the previous sections. This gap produces the plateau in the Hall resistance curve [18–23]. There is another gap which indicates the minimum value of all excitation energies from the ground state to excited states with the same filling factor ν . We call it “excitation-energy-gap.” We examine the excitation-energy-gap for three filling factors in this section.

We first consider one of excited states at $\nu = 2/3$ which is illustrated in Figure 21. The electron configuration is created by the excitation from the ground state as follows: one electron in the orbital B transfers to the orbital C. This excitation from the ground state is shown by green color in Figure 21. The electron configuration expresses one of eigen states for the Hamiltonian H_D . This excited state #1 has new nearest-electron pairs CE and DC which have the perturbation energies via residual Coulomb transitions. As in Figure 21, no transition is allowed from the pair CE, and only two transitions are allowed from the pair DC. Forbidden

FIGURE 19: Coulomb transitions of nearest hole pair at $\nu = 5/17$.FIGURE 20: Coulomb transitions of nearest hole pair at $\nu = 6/17$.FIGURE 21: Electron configuration in excited state #1 at $\nu = 2/3$.

transitions are drawn by pink color, and allowed transitions are drawn by black color.

The perturbation energies of the pairs CE and DC are described by the symbols ζ'_{CE} and ζ'_{DC} , respectively. The symbol ζ' (symbol prime) means the perturbation energy for the excited state #1. The second-order perturbation energy ζ'_{DC} is obtained as

$$\zeta'_{DC} = \sum_{\Delta p = 6(2\pi\hbar/\ell), -7(2\pi\hbar/\ell)} \frac{\langle p_D, p_C | H_I | p'_D, p'_C \rangle \langle p'_D, p'_C | H_I | p_D, p_C \rangle}{W_{\text{state}\#1} - W_{\text{excite}}(p_D \rightarrow p'_D, p_C \rightarrow p'_C)}. \quad (56)$$

We introduce the following summation Z' as:

$$Z' = - \sum_{\Delta p \neq 0, -2\pi\hbar/\ell}^{\text{all}} \frac{\langle p_D, p_C | H_I | p'_D, p'_C \rangle \langle p'_D, p'_C | H_I | p_D, p_C \rangle}{W_{\text{state}\#1} - W_{\text{excite}}(p_D \rightarrow p'_D, p_C \rightarrow p'_C)}. \quad (57)$$

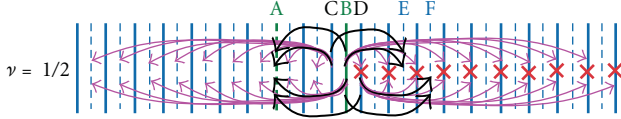
This definition is similar to (19). We count the number of effective transitions which have the overlapping region between the initial Landau wave function and the final wave function. If the momentum transfer becomes larger than some critical value, then the transition matrix element becomes negligibly small.

The spreading width of Landau state is denoted by Δy , the value of which is about 10.5 nm for the case of $B \approx 6$ [T].

$$\hbar \approx 1.0546 \times 10^{-34} \text{ J s}, \quad e \approx 1.6022 \times 10^{-19} \text{ C}, \quad (58) \\ \Delta y \approx 10.5 \text{ [nm]}, \quad \text{for } B \approx 6 \text{ [T]}.$$

The interval width between nearest Landau orbitals is estimated as

$$\Delta\alpha = \frac{2\pi\hbar}{eB\ell} \approx 6.5 \times 10^{-4} \text{ [nm]}, \quad \text{for } \ell = 1 \text{ [mm]} = 10^6 \text{ [nm]}, \quad (59)$$

FIGURE 22: Electron configuration in excited state #2 at $\nu = 1/2$.

where we have applied $\ell = 1$ [mm] for the length of quantum Hall device. Then there are enormous many single-electron states inside the spreading width Δy . The number is

$$\frac{\Delta y}{\Delta \alpha} \approx \frac{\ell}{2\pi} \sqrt{\frac{eB}{\hbar}} \approx 2 \times 10^4. \quad (60)$$

Accordingly the effective momentum transfers satisfy the following relation:

$$|p'_C - p_C| \leq \frac{2\pi\hbar}{\ell} \times 2 \times 10^4. \quad (61)$$

Only two transitions are allowed from the pair DC, and therefore the ratio $-\zeta'_{DC}/Z'$ is about 10^{-4} as follows:

$$\frac{-\zeta'_{DC}}{Z'} \approx \frac{2}{(2 \times 10^4)} = 10^{-4}, \quad \text{for } \ell = 1 \text{ [mm]}. \quad (62)$$

Because this value is negligibly small, we can use the following approximation:

$$\zeta'_{DC} \approx -10^{-4} \times Z' \approx 0. \quad (63)$$

All the transitions from the pair CE are forbidden, and then the perturbation energy of the nearest pair CE is zero

$$\zeta'_{CE} = 0. \quad (64)$$

Furthermore, the nearest pair AB disappears by the excitation in Figure 21, and therefore the excitation-energy $\Delta E_{\text{excitation \#1}}$ is given by

$$\Delta E_{\text{excitation \#1}} = \zeta'_{DC} + \zeta'_{CE} - \zeta_{AB}, \quad (65)$$

where ζ_{AB} indicates the summation (18) the result of which is equal to (20)

$$\zeta_{AB} = -\left(\frac{1}{3}\right)Z. \quad (66)$$

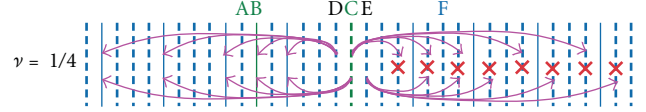
Substitution of (63), (64), and (66) into (65) yields the excitation energy as

$$\Delta E_{\text{excitation \#1}} = \zeta'_{DC} + \zeta'_{CE} - \zeta_{AB} \approx \left(\frac{1}{3}\right)Z. \quad (67)$$

It is noteworthy that the excitation energy is a positive value.

The second example is shown in Figure 22 where the electron A transfers to the orbital B at $\nu = 1/2$. The excited state #2 has two nearest electron pairs CB and BD. The excitation energy $\Delta E_{\text{excitation \#2}}$ from ground state to the state #2 is given by

$$\Delta E_{\text{excitation \#2}} = \zeta'_{CB} + \zeta'_{BD} \approx 0. \quad (68)$$

FIGURE 23: Electron configuration in excited state #3 at $\nu = 1/4$.

The third example is the case of $\nu = 1/4$. The hole B transfers to the orbital C and, then, the transition yields the excited state #3 as in Figure 23. Then the nearest hole pairs DC and CE are produced additionally. However, all the quantum transitions are forbidden from the hole pairs DC and CE. Accordingly the excitation energy $\Delta E_{\text{excitation \#3}}$ is zero as

$$\Delta E_{\text{excitation \#3}} = \zeta''_{DC}{}^{\text{hole}} + \zeta''_{CE}{}^{\text{hole}} - 2 \times \zeta_{\nu=1/4}^{\text{hole}} = 0, \quad (69)$$

where $\zeta_{\nu=1/4}^{\text{hole}}$ is the nearest hole pair energy. It is noteworthy that two nearest-hole pairs disappear by the excitation of the state #3. The value of $\zeta_{\nu=1/4}^{\text{hole}}$ is zero derived from the estimation in Section 4.

Thus the excitation-energy gap has a correlation with the energy gap in the spectrum.

When the device size is very small, the ratio $\Delta y/\Delta \alpha$ becomes small. Therein, the energy gaps also become small for any fractional (not integer) filling factor. The size effect appears in a quantum Hall device with ultrasmall size (such as about 50 nm size for length ℓ).

7. Conclusion

We have developed the theory of Tao and Thouless. Then we have found the momentum conservation of the x direction for the Coulomb transitions. The momentum conservation law, Fermi-Dirac statistics, and the most uniform electron configuration produce gap structure at the filling factors $\nu = j/(2j \pm 1)$, $1/(2j + 1)$, $(2j)/(2j + 1)$ and gapless structure at the filling factors $\nu = 1/(2j)$, $(2j - 1)/(2j)$. Furthermore small energy gaps are estimated for examples of $\nu = 7/11$ and $4/11$ by the use of computer program. Thus, we have applied the same procedure to FQH states with arbitrary fractional filling factors, and then we have obtained various types of energy spectra for nearest electron pairs and nearest hole pairs. It is important to use the same logic for investigation of all FQH states. This paper has explained FQH states with various filling factors by using usual quantum mechanics and usual electrons without any quasiparticle.

Acknowledgments

The author would like to acknowledge Professor H. Hori and Professor K. Oto for useful discussions. The author expresses his heartfelt appreciation for the comments of the referee and the editor. This paper has been improved and revised by the comments.

References

- [1] W. Pan, H. L. Stormer, D. C. Tsui, L. N. Pfeiffer, K. W. Baldwin, and K. W. West, "Transition from an electron solid to the

- sequence of fractional quantum Hall states at very low Landau level filling factor,” *Physical Review Letters*, vol. 88, no. 17, Article ID 176802, pp. 1–4, 2002.
- [2] W. Pan, H. L. Stormer, D. C. Tsui, L. N. Pfeiffer, K. W. Baldwin, and K. W. West, “Fractional quantum hall effect of composite fermions,” *Physical Review Letters*, vol. 90, no. 1, Article ID 016801, pp. 1–4, 2003.
- [3] J. K. Jain, “Composite-fermion approach for the fractional quantum Hall effect,” *Physical Review Letters*, vol. 63, no. 2, pp. 199–202, 1989.
- [4] J. K. Jain, “Theory of the fractional quantum Hall effect,” *Physical Review B*, vol. 41, no. 11, pp. 7653–7665, 1990.
- [5] A. Wójs and J. J. Quinn, “Quasiparticle interactions in fractional quantum Hall systems: justification of different hierarchy schemes,” *Physical Review B*, vol. 61, no. 4, pp. 2846–2854, 2000.
- [6] A. Wójs, K. S. Yi, and J. J. Quinn, “Fractional quantum Hall states of clustered composite fermions,” *Physical Review B*, vol. 69, no. 20, Article ID 205322, 13 pages, 2004.
- [7] J. H. Smet, “Wheels within wheels,” *Nature*, vol. 422, no. 6930, pp. 391–392, 2003.
- [8] M. R. Peterson and J. K. Jain, “Flavor altering excitations of composite fermions,” *Physical Review Letters*, vol. 93, no. 4, Article ID 046402, 4 pages, 2004.
- [9] E. A. Pashitskii, “New quantum states in the fractional quantum Hall effect regime,” *Low Temperature Physics*, vol. 31, no. 2, pp. 171–178, 2005.
- [10] R. Tao and D. J. Thouless, “Fractional quantization of Hall conductance,” *Physical Review B*, vol. 28, no. 2, pp. 1142–1144, 1983.
- [11] R. Tao, “Fractional quantization of hall conductance—II,” *Physical Review B*, vol. 29, no. 2, pp. 636–644, 1984.
- [12] S. Sasaki, “Energy gap in fractional quantum Hall effect,” *Physica B*, vol. 281–282, pp. 838–839, 2000.
- [13] S. Sasaki, “Binding energy and polarization of fractional quantum Hall state,” in *Proceedings of the 25th International Conference on the Physics of Semiconductors*, pp. 925–926, Springer, 2011.
- [14] S. Sasaki, “Spin polarization in fractional quantum Hall effect,” in *Proceedings of the 21nd European Conference on Surface Science*, vol. 532–535, pp. 567–575, June 2003.
- [15] S. Sasaki, “Spin-Peierls effect in spin-polarization of fractional quantum Hall states,” in *Proceedings of the 22nd European Conference on Surface Science*, vol. 566–568, pp. 1040–1046, September 2004.
- [16] S. Sasaki, *Surface Science: New Research*, chapter 4, Nova Science, 2006.
- [17] S. Sasaki, “Calculation of binding energies for fractional quantum Hall states with even denominators,” In press, <http://arxiv.org/abs/cond-mat/0703360>.
- [18] S. Sasaki, “Energy gaps in fractional quantum Hall states,” *Journal of Physics*, vol. 100, Article ID 042021, 4 pages, 2008.
- [19] S. Sasaki, “Energy spectra for fractional quantum Hall states,” In press, <http://arxiv.org/abs/0708.1541>.
- [20] S. Sasaki, “Movement of diagonal resistivity in fractional quantum Hall effect via periodic modulation of magnetic field strength,” *Journal of Physics*, vol. 100, Article ID 042022, 4 pages, 2008.
- [21] S. Sasaki, “Frequency dependence of diagonal resistance in fractional quantum Hall effect via periodic modulation of magnetic field,” In press, <http://arxiv.org/abs/0803.0615>.
- [22] S. Sasaki, “Consideration of ac Josephson effect in fractional quantum Hall states,” In press, <http://arxiv.org/abs/0807.0288>.
- [23] S. Sasaki, “Tunneling effect in quantum Hall device,” *Journal of Surface Science and Nanotechnology*, vol. 8, pp. 121–124, 2010.

Research Article

Semiclassical Description of Anisotropic Magnets for Spin $S = 1$

Khikmat Muminov and Yousef Yousefi

Physical-Technical Institute Named after S. U. Umaro, Academy of Sciences of Republic of Tajikistan, Aini Avenue 299/1, Dushanbe, Tajikistan

Correspondence should be addressed to Yousef Yousefi, yousof54@yahoo.com

Received 10 August 2011; Revised 13 September 2011; Accepted 15 September 2011

Academic Editor: Roberto Zivieri

Copyright © 2012 K. Muminov and Y. Yousefi. This is an open access article distributed under the Creative Commons Attribution License, which permits unrestricted use, distribution, and reproduction in any medium, provided the original work is properly cited.

Nonlinear equations describing one-dimensional non-Heisenberg ferromagnetic model are studied by the use of generalized coherent states in a real parameterization. Also, dissipative spin wave equation for dipole and quadruple branches is obtained if there is a small linear excitation from the ground state.

1. Introduction

In the past decades, magnets with spin value $s = 1/2$ have been studied completely. There are dipoles, quadruples and higher-order branches that affect the behavior of magnet crystal. However, the only necessary tool for describing the behavior of this kind of magnets is dipole branch effect, and the order branches are not necessary. This results in linear approximation for describing the magnet behavior.

Indeed, only dipole branch effect has been used for describing magnets with spin value $s \geq 1$, and the effect of quadrupole and higher-order branches has been ignored. Recently, however, due to the new developments in mathematics and technology and also due to the great potential of quadrupole branch in description of nanoparticles, its important role cannot be ignored [1, 2].

Using the effects of both dipole and quadrupole branches results in a nonlinear approximation. The use of higher-order multipole effects yields more accurate approximations which demand more complicated equations. In this paper, only the effect of quadruple branch for Hamiltonians described by (1) is considered. Study of isotropic and anisotropic spin Hamiltonian with non-Heisenberg terms are complicated due to quadruple excitation dynamics [3–5]. Antiferromagnetic property of this excitation in states near the ground proves the existence of it. The effect of this calculation has been studied by Dzyaloshinskii [6]. The results obtained through the quadrupole excitation in nanoparticles

Fe_8 and Mn_{12} are more in line with numerical calculations and laboratory results [7, 8].

In classical physics term, the number of parameters required for a full macroscopic description of the magnet behavior is equal to $4s$, where s is the spin value. Also real-parameterized coherent states based on related group is used to obtain classical equation of motion and to describe multipole dynamics [9, 10]. Here, Heisenberg ferromagnets with anisotropic term as described by (1) are considered:

$$\hat{H} = -J \sum_i \left(\vec{\hat{S}}_i \vec{\hat{S}}_{i+1} + \delta \hat{S}_i^z \hat{S}_i^z \right). \quad (1)$$

Here, \hat{S}_i^x , \hat{S}_i^y , and \hat{S}_i^z are the spin operators acting at a site i , and δ is the anisotropy coefficient. This Hamiltonian is related to a one-dimensional ferromagnetic spin chains, and the coefficient J is positive.

In order to calculate the effect of quadrupole excitation, first, the classical equivalent of Hamiltonian (1) is obtained and then, by analyzing such equation for small linear excitation from the ground states, the spin wave solution is found. This process requires the following steps.

- (1) Obtaining coherent states for spin $s = 1$ which are coherent states of $\text{SU}(3)$ group.
- (2) Calculating the average values of spin operator.
- (3) Obtaining classical spin Hamiltonian equation using previously calculated values.

- (4) Computing Lagrangian equation by the use of Feynman path integral over coherent states and then computing classical equations of motion.
- (5) For finding nonlinear equations of magnet behavior, it is necessary to substitute resulted Hamiltonian in classical equations of motion. Solutions of these nonlinear equations result in soliton description of magnet that is not needed here.
- (6) Calculating ground states of magnet and then linearizing the nonlinear equations around the ground states for small excitation.
- (7) At the end, calculating spin wave equation and dispersion equation.

In what follows, the mathematical descriptions of the above steps are presented.

2. Theory and Calculation

In quantum mechanics, coherent states are special kind of quantum states that their dynamics are very similar to their corresponding classical system. These states are obtained by act of Weil-Heisenberg group operator on vacuum state. Vacuum state of SU(3) group is $(1, 0, 0)^T$, and coherent state is introduced as [11]

$$|\psi\rangle = D^{1/2}(\theta, \phi) e^{-iy\widehat{S}} e^{2ig\widehat{Q}^{xy}} |0\rangle$$

$$= C_0|0\rangle + C_1|1\rangle + C_2|2\rangle, \quad (2)$$

where $D^{1/2}(\theta, \phi)$ is Wigner function and Q^{xy} is quadruple moment which is written in the following form:

$$\widehat{Q}^{xy} = \frac{i}{2} \begin{pmatrix} 0 & 0 & 1 \\ 0 & 0 & 0 \\ -1 & 0 & 0 \end{pmatrix}. \quad (3)$$

Coefficients C_0 to C_2 are computed from these equations

$$C_0 = e^{i\phi} \left(e^{-iy} \sin^2\left(\frac{\theta}{2}\right) \cos g + e^{iy} \cos^2\left(\frac{\theta}{2}\right) \sin g \right),$$

$$C_1 = \frac{\sin \theta}{\sqrt{2}} (e^{-iy} \cos g - e^{iy} \sin g), \quad (4)$$

$$C_2 = e^{-i\phi} \left(e^{-iy} \cos^2\left(\frac{\theta}{2}\right) \cos g + e^{iy} \sin^2\left(\frac{\theta}{2}\right) \sin g \right).$$

Two angles, θ and ϕ , determine the direction of classical spin vector in spherical coordinate system. The angle γ determines the direction of quadruple moment around the spin vector, and parameter g shows change of the magnitude of spin vector.

In order to obtain the classical equivalent of Hamiltonian (1), the classical equivalent of spin vector and its corresponding products should be computed. So, consider

$$\vec{S} = \langle \psi | \vec{S} | \psi \rangle \quad (5)$$

as classical spin vector, and also consider

$$Q^{ij} = \langle \psi | \widehat{S}^i \widehat{S}^j | \psi \rangle \quad (6)$$

as components of quadruple moment. Spin operators can be commute in different lattices; so

$$\langle \psi | \widehat{S}_n^i \widehat{S}_{n+1}^j | \psi \rangle = \langle \psi | \widehat{S}_n^i | \psi \rangle \langle \psi | \widehat{S}_{n+1}^j | \psi \rangle, \quad (7)$$

where $|\psi\rangle = |\psi\rangle_n |\psi\rangle_{n+1}$.

The average spin values in SU(3) group are defined as [12]

$$S^+ = e^{i\phi} \cos(2g) \sin \theta,$$

$$S^- = e^{-i\phi} \cos(2g) \sin \theta,$$

$$S^z = \cos(2g) \cos \theta, \quad (8)$$

$$S^2 = \cos^2(2g).$$

Classical Hamiltonian can be obtained from the average calculation of Hamiltonian (1) over coherent states. The classical continuous limit of Hamiltonian in SU(3) group is

$$H_{cl}$$

$$= -J \int \frac{dx}{a_0} \left(\cos^2(2g) \right.$$

$$+ \frac{\delta}{2} (\cos^2 \theta + \sin(2g) \cos(2\gamma) \sin^2 \theta)$$

$$\left. - \frac{a_0^2}{2} ((\theta_x^2 + \phi_x^2 \sin^2 \theta) \cos^2(2g) + 4g_x^2 \sin^2(2g)) \right). \quad (9)$$

The above classical Hamiltonian is substituted in equation of motion that was obtained from the Lagrangian, and the result is classical equations of motion:

$$\frac{1}{\omega_0} \phi_t = \delta \cos \theta (\sec(2g) - \cos(2\gamma) \tan(2g))$$

$$+ a_0^2 \cos(2g) (\theta_{xx} \csc \theta + \phi_x^2 \cos \theta),$$

$$\frac{1}{\omega_0} \theta_t = \frac{\delta}{2} \sin(2\theta) \sin(2\gamma) \tan(2g) - a_0^2 \phi_{xx} \cos(2g) \sin \theta,$$

$$\frac{1}{\omega_0} g_t = -\frac{\delta}{2} \sin(2\gamma) \sin^2 \theta,$$

$$\frac{1}{\omega_0} \gamma_t = (4 \cos(2g)$$

$$- \delta (\cos(2\gamma) (\cot(4g) - \cos(2\theta) \csc(4g))$$

$$+ \cos^2 \theta \sec(2g)))$$

$$+ \left(\cos(2g) (8g_x^2 - 2\theta_x^2 \right.$$

$$+ \frac{1}{2} \phi_x^2 (-3 + \cos(2\theta)) - \theta_{xx} \cot \theta$$

$$\left. + 4g_{xx} \sin(2g) \right) a_0^2. \quad (10)$$

These equations describe nonlinear dynamics of non-Heisenberg ferromagnetic chain completely. Solutions of these equations are magnetic solitons that are not studied in this paper.

In this paper, only the linearized form of (10) for small excitation from the ground states is considered. To this end, first, classical ground states must be calculated. therefore in the above Hamiltonian, only nonderivative part is taken into account:

$$H_0 = -J \int \frac{dx}{a_0} \left(\cos^2(2g) + \frac{\delta}{2} (\cos^2 \theta + \sin(2g) \cos(2\gamma) \sin^2 \theta) \right). \quad (11)$$

It is necessary to calculate derivative of (11) with respect to all variables to find out minimum of H_0 . As a result, if $\delta < 0$, ground states are at these points

$$\theta = \frac{\pi}{2}, \quad \gamma = \frac{\pi}{2}, \quad \sin 2g_0 = \frac{|\delta|}{4}, \quad |\delta| < 4. \quad (12)$$

In this paper, only dispersion of spin wave in neighborhood of the ground states is studied. For this purpose, small linear excitations from the ground states, as shown in (13), are defined:

$$\begin{aligned} \theta &\longrightarrow \frac{\pi}{2} - \theta, \\ 2\gamma &\longrightarrow \pi + \gamma, \\ 2g &\longrightarrow g_0 + g. \end{aligned} \quad (13)$$

In this situation, the linearized classical equations of motion are

$$\begin{aligned} \frac{1}{\omega_0} \phi_t &= \delta (\sec g_0 + \tan g_0) \theta + a_0^2 \cos g_0 \theta_{xx}, \\ \frac{1}{\omega_0} \theta_t &= -a_0^2 \phi_{xx} \cos g_0, \\ \frac{1}{\omega_0} g_t &= -\frac{\delta}{2} \gamma, \end{aligned} \quad (14)$$

$$\frac{1}{\omega_0} \gamma_t = -2 \left(2 \sin g_0 + \frac{\delta}{\cos g_0} \right) g + 4a_0^2 g_{xx} \sin g_0.$$

Consider functions θ , ϕ , γ , and g as plane waves to obtain dispersion equation:

$$\begin{aligned} \phi &= \phi_0 e^{i(\omega t - kx)} + \bar{\phi}_0 e^{-i(\omega t - kx)}, \\ \theta &= \theta_0 e^{i(\omega t - kx)} + \bar{\theta}_0 e^{-i(\omega t - kx)}, \\ g &= g_0 e^{i(\omega t - kx)} + \bar{g}_0 e^{-i(\omega t - kx)}, \\ \gamma &= \gamma_0 e^{i(\omega t - kx)} + \bar{\gamma}_0 e^{-i(\omega t - kx)}. \end{aligned} \quad (15)$$

Substitute of these equations in (14), then

$$\begin{aligned} \omega_1^2 &= \omega_0^2 k^2 a_0^2 (\delta (1 + \sin g_0) + k^2 a_0^2 \cos^2 g_0), \\ \omega_2^2 &= \omega_0^2 \left[2 \sin g_0 k^2 a_0^2 + \delta \left(\frac{4\delta}{\sin^2 g_0} - 2 \sin g_0 \right) \right]. \end{aligned} \quad (16)$$

These equations are dispersion equations of spin wave near the ground states in SU(3) group.

3. Conclusions

In this paper, describing equations of one-dimensional anisotropic non-Heisenberg Hamiltonians are obtained using real-parameter coherent states. It was indicated that both dipole and quadruple excitations have different dispersion if there is small linear excitation from the ground state.

In addition, it was indicated, that for anisotropic ferromagnets, the magnitude of average quadruple moment is not constant and its dynamics consists of two parts. One part is rotational dynamics around the classical spin vector ($\gamma_i \neq 0$) and the other related to the change of the magnitude of quadruple moment ($g_i \neq 0$).

References

- [1] E. L. Nagaev, "Anomalous magnetic structures and phase transitions in non-Heisenberg magnetic materials," *Soviet Physics Uspekhi*, vol. 25, p. 31, 1982.
- [2] E. L. Nagaev, *Magnets with Nonsimple Exchange Interactions*, Nauka, Moscow, Russia, 1988.
- [3] Kh. O. Abdulloev and Kh. Kh. Muminov, "Semiclassical description of anisotropic magnets acted upon by constant external magnetic fields," *Physics of the Solid State*, vol. 36, no. 1, pp. 93–97, 1994.
- [4] B. A. Ivanov, A. Yu. Galkin, R. S. Khymyn, and A. Yu. Merkulov, "Nonlinear dynamics and two-dimensional solitons for spin $S = 1$ ferromagnets with biquadratic exchange," *Physical Review B*, vol. 77, no. 6, Article ID 064402, 2008.
- [5] Yu. A. Fridman, O. A. Kosmachev, A. K. Kolezhuk, and B. A. Ivanov, "Spin nematic and antinematic states in a spin-3/2 isotropic non-Heisenberg magnet," *Physical Review Letters*, vol. 106, no. 9, Article ID 097202, 4 pages, 2011.
- [6] I. Dzyaloshinskii, "External magnetic fields of antiferromagnets," *Solid State Communications*, vol. 82, no. 7, pp. 579–580, 1992.
- [7] G. Bellessa, E. Del Barco, N. Vernier et al., "Quantum coherence in Fe₈ molecular nanomagnets," *Europhysics Letters*, vol. 47, no. 6, pp. 722–728, 1999.
- [8] M. S. Foss-Feig and J. R. Friedman, "Geometric-phase-effect tunnel-splitting oscillations in single-molecule magnets with fourth-order anisotropy induced by orthorhombic distortion," *Europhysics Letters*, vol. 86, no. 2, Article ID 27002, 2009.
- [9] V. S. Ostrovskii, *Soviet Physics JETP*, vol. 64, no. 5, p. 999, 1986.
- [10] N. A. Mikushina and A. S. Moskvina, "Dipole and quadrupole skyrmions in $S = 1$ (pseudo)spin systems," *Physics Letters A*, vol. 302, no. 1, pp. 8–16, 2002.
- [11] Kh. O. Abdulloev and Kh. Kh. Muminov, "Coherent states of SU(4) group in real parameterization and Hamiltonian equations of motion," *Reports of Tajikistan Academy of science*, vol. 36, no. 6, 1993 (Russian).
- [12] Kh. O. Abdulloev and Kh. Kh. Muminov, "Accounting of quadrupole dynamics of magnets with spin," *Proceedings of Tajikistan Academy of Sciences*, no. 1, pp. 28–30, 1994 (Russian).